HIGH RESOLUTION CROSS-WELL IMAGING OF A WEST TEXAS CARBONATE RESERVOIR: McELROY FIELD

Final Report

submitted to

Chevron Oil Field Research Company

La Habra, CA

STP Volume 3, No. 4

April 1993

Prepared by

Jerry M. Harris

Principal Investigator

with contributions from

Richard Nolen-Hoeksema

Spyros K. Lazaratos

James W. Rector

Mark Van Schaack

INTRODUCTION

A pilot project is being conducted in Section 205 of the McElroy field to evaluate the performance of a hybrid CO_2-injection scheme. Stanford University's Seismic Tomography Project (STP) is a participant in this project through a demonstration field experiment (DFE) sponsored by Chevron Oil Field Research Company (COFRC; now Chevron Petroleum Technology Company or CPTC). The sponsored activities include acquisition of a crosswell seismic survey and tomography data processing. In addition, STP's co-sponsored research activities include reflection processing of crosswell data and the use of crosswell seismic techniques for (1) reservoir characterization and (2) monitoring CO_2 injection. Stanford University gathered two crosswell seismic profiles in late 1991. Profile 1 was between Wells J. T. McElroy (JTM) 1068 and JTM-1202 and had a nominal well-to-well distance of 184 feet. Profile 2 was between Wells JTM-1080 and JTM-1202, with a nominal well-to-well distance of 600 feet. Well JTM-1202 was the receiver well for both profiles. Here, we summarize the main accomplishments and results from Profile 1.

The project was co-funded by COFRC, the Gas Research Institute (GRI), the Seismic Tomography Project, and the Packard Foundation. COFRC provided cash in the amount of $111,000 to cover data acquisition and tomographic data processing. GRI made available the downhole tools. STP provided student support in the amount of approximately $30,000. The Packard Foundation, through a Fellowship to Prof. Jerry M. Harris, provided cash (~$50,000) for field operations, student and staff support, and equipment to support the field operations.

Notes on Accompanying Reports

The first 5 reports that accompany this summary appeared earlier as Papers A-E in STP-3 (1992). The last report (Paper F) contains core-analysis results in support of the project.

We have altered the field location and well names for purposes of presentation in Papers A-F. Well A refers to JTM-1202, Well B to JTM-1068, and Well C to JTM-1080. We altered the reservoir depths and reduced them by 1,000 feet in Papers A-E.

SITE DESCRIPTION

Reservoir Geology

McElroy field is located on the eastern edge of the Central Basin Platform in Crane and Upton Counties, Texas (Harris et al., 1984; Ward et al., 1986). The reservoir is a stratigraphic-structural trap. Oil production comes primarily from shelf dolomites of the Grayburg formation. The Grayburg is capped and sealed conformably by terrigenous sediments and evaporites of the Lower Queen formation. It unconformably overlies San Andres formation evaporitic dolomites. The structure of the reservoir is a NNW trending, asymmetric anticline that has a steeply dipping eastern limb, a gently dipping western limb, and provides about 250 feet of structural closure. The eastern limit of the field is determined by an oil-water contact.

The reservoir is 2,900 feet deep, and oil production comes from a gross pay zone with an average thickness of 275 feet. Oil recovery varies across the field, with the highest production coming from the central area of the field and lowest from the flanking areas. The lower recovery in the flanking areas results from low reservoir quality (e.g., low permeabilities, high water saturations). Up dip to the west, porosity and reservoir quality decrease because pore space is filled with evaporite minerals, for example, gypsum ($CaSO_4 \cdot 2H_2O$) or anhydrite ($CaSO_4$). Down dip to the east, reservoir quality decreases because of high water saturation as the oil-water contact is approached.

The CO_2-injection pilot project is being conducted in Section 205, in the southwest portion of the field (Lemen et al., 1990). The top of the Grayburg formation occurs at a depth of about 2,700 feet and the top of the San Andres formation occurs at about 3,040 feet. Within the Grayburg, reservoir zones occur in the E, D5 and M units, whose tops occur at electric-log markers at about 2,780, 2,860 and 2,950 feet, respectively. The principal reservoir is the D5 unit. Porosity, permeability and, consequently, reservoir quality generally increase from west to east in Section 205. However, these general trends mask the high spatial variability of these reservoir properties and lack of spatial correlation between porosity and permeability (Lemen et al., 1990).

Lemen and coworkers (1990) highlight the difficulty of well-to-well correlation of reservoir zones. One purpose of the demonstration field experiment is to investigate the use of crosswell seismic techniques for reservoir characterization, an important component of which is well-to-well stratigraphic correlation.

Well Descriptions

In 1991, Chevron drilled Well JTM-1202 as an observation well for the CO_2-injection pilot project. The well was drilled to a depth of 3260 feet. A total of 285 feet of 3.25-inch diameter, unoriented core was cut between 2,775 and 3,060 feet. Well JTM-1202 was cased using fiberglass tubing. The well was used as the receiver well for both crosswell seismic profiles.

Wells JTM-1068 and JTM-1080 were drilled in 1988, as infill wells for a waterflood-realignment project in Section 205 (Lemen et al., 1990). JTM-1068 was drilled as an injection well and JTM-1080 as a production well. Well JTM-1068 was the source well for crosswell profile 1 and well JTM-1080 was the source well for profile 2.

We concentrate on Profile 1 between wells JTM-1068 and JTM-1202 in this summary report. The reports exceed the contractual obligations of the project sponsored by COFRC. Although work on Profile 2 is underway, it has not been completed and is not presented as part of this final report but will be delivered to Chevron as part of the ongoing research activities by the STP.

MAJOR ACCOMPLISHMENTS AND RESULTS FROM PROFILE 1

Profile 1 was gathered between source well JTM-1068 and receiver well JTM-1202. The nominal well-to-well distance was 184 feet. Profile 1 covers depths from 2,650 to 3,150 feet, was sampled uniformly at 2.5 feet source and receiver spacing, and contains the main Grayburg reservoir zone (D5 unit) in the middle of the survey between 2,850 and 2,950 feet (cf. Paper A, figure 1).

Stanford proposed to do standard acquisition and tomographic processing. At the time, the STP was aggressively researching reflection processing under sponsorship of GRI and STP. We chose to use McElroy as a site for testing the reflection processing algorithms. From the beginning, we realized that our then current acquisition methods were not capable of recording data suitable for reflection processing. As a result, we worked, before McElroy, to improve acquisition and reflection processing methods. Although these developments described below were not part of the COFRC sponsored project, they were critical to its success.

Data Acquisition On-the-Fly

Paper A gives a description of data acquisition and field operations. There were three principal data acquisition accomplishments from profile 1. These accomplishments result

from our new ability to record data on-the-fly. Recording on-the-fly involves positioning the receiver string at a fixed depth. The source is lowered to the lowermost source position and then pulled continuously up the well, while it fires at specified depth intervals. This on-the-fly method affords us three advantages. First, the depth of the source is known more accurately because there is constant tension on its wireline. The smear in the source location introduced by the moving source is under 2 inches. Second, we are able to gather data much more quickly than by more conventional methods. We were able to record about 36,000 traces in just under 48 hours (Profile 1) and about 37,000 traces in 40 hours (Profile 2). Finally, the significant speedup in data acquisition allowed us to record densely sampled profiles. This is important to reduce spatial aliasing of low phase-velocity events and thus increase the likelihood for wavefield separation (cf. Papers B and D). Both crosswell traveltime tomography (Paper C) and crosswell reflection imaging (Paper E) are enhanced by dense sampling. In particular, reliable crosswell reflection imaging requires that spatial aliasing be minimized and wavefield separation possible. Data acquisition on-the-fly made possible these accomplishments and the impressive crosswell results that we summarize below. Before this survey, STP had not recorded a survey using this acquisition method. A preliminary "test" experiment was run at the Devine test site as a dry run for McElroy before McElroy.

Wavefield Separation and Modeling

An important result from Profile 1 is our ability to recognize and separate the many varieties of modes in the crosswell seismic data. In Paper B, we show how the raw data contain a rich variety of wave modes (cf. Paper B, figures 1 & 22). This is unprecedented in crosswell data. In addition to the usually recognized direct P, head wave, and tube wave modes, we can recognize direct S waves, primary P reflections, primary S reflections, S-wave multiples, P-S conversions, S-P conversions, and P-S-P conversions. We have modeled these wave modes (Paper B, except tube waves). We have separated these wave modes from the full wavefield (Paper D) to produce crosswell tomograms from the P traveltimes (Paper C) and high-resolution crosswell reflection images from the primary P and S reflections (Paper E). It is also possible to produce other views of the data. For example, a P/S ratio image would give insight into the interwell variation of Poisson's ratio in these rocks. High resolution cross-well seismology combines rapid data acquisition and dense sampling. It opens up new ways of investigating the interwell region. In the next two sections, we highlight results of improved interwell imaging from Profile 1.

Traveltime Tomography

The principal objective of this crosswell demonstration field experiment was to assess the capability of crosswell tomography to assist with reservoir delineation and characterization. Indeed, Lemen et al. (1990) emphasize the difficulty of correlation of individual high-permeability layers from one well to the next. We used crosswell seismic tomography and reflection imaging to demonstrate crosswell seismic capabilities. In this section, we summarize the tomography results.

Paper C describes the P-wave traveltime inversion used to produce the traveltime tomogram for Profile 1 (cf. Paper C, figure 12). The tomogram produces a low resolution (15-30 feet) image of the reservoir volume. It provides an image of seismic velocity and of large-scale reservoir structural and stratigraphic variations. It indicates how associated reservoir properties (e.g., porosity, Poisson's ratio) may vary, if the appropriate velocity-to-property translation can be found.

In figure 12 of Paper C, the tomogram is oriented more-or-less west-to-east from source to receiver well (right to left). The tomogram is divided into 5 layers. The boundaries of these layers correlate very well with known markers defined from gamma-ray, neutron, and sonic well-logs (Lemen et al., 1990; pers. comm., Bill Dees and Leon Roe, Chevron U.S.A., 1992). From bottom to top these markers are:

1. Top of the San Andres formation at 3,050 feet.
2. Top of Grayburg M unit at 2,950 feet.
3. Top of Grayburg D5 unit at 2,860 feet. The D5 unit is the main reservoir zone.
4. Top of Grayburg Formation at 2,750 feet or higher.
5. Top of McElroy marker zone at 2,700 feet. Above this is the Queen formation.

Admittedly, it is difficult to pick out structure and stratigraphy from this tomogram. In fact, velocity variations below about 2% raise questions in our minds. Some may result from reservoir property variations. Some may result from seismic anisotropy. We assumed seismic isotropy to produce figure 12. And, some variation may result from artifacts in the inversion process. The tomographic results are very sensitive to survey geometry, i.e., depth control (knowing how deep the source and receivers are) and well spacing (knowing where the wells are). The geometry is especially critical for these closely spaced wells. A 2% error in well offset is less than five feet for this survey and would introduce errors in the tomogram comparable to the small artifacts mentioned above.

We are confident, however, that the zonation of the Grayburg reservoir in the tomogram reflects geology. This confidence comes from synthetic modeling. A model of the interwell reservoir volume was developed based on well-to-well log correlations. The

model was used to produce a synthetic tomogram. The agreement between the field and synthetic tomograms was very good (cf. Paper C, figures 12 and 14).

Some prominent features occur in the tomogram.

1. The low-velocity (blue) zone from 2,710 to 2,730 feet correlates with a low sonic velocity and high gamma-ray zone known from well logs near the top of the Grayburg formation in the McElroy field (Harris et al., 1984).
2. The slower (yellow) zone around 2,780 feet correlates with the Grayburg E marker, a gamma-ray peak, sonic-velocity low and porosity peak (Lemen et al., 1990).
3. As indicated above, the transitions in velocity near 2,850, 2,950 and 3,050 feet all correlate with well-log markers for the D5 unit, M unit and San Andres formation, respectively.

All these features can be carried from well-to-well in Profile 1.

Other features are less obvious. For example, the two sonic-velocity lows (gamma-ray peaks) between 3,080 and 3,100 feet in the receiver well (left in figure 12, Paper C) appear as one velocity low (gamma-ray peak) at 3,080 in the source well (right in figure 12, Paper C). Nothing is very apparent in the tomogram. However, reflection imaging adds detail to this information.

Reflection Imaging

Paper E describes the reflection processing used to produce the P and S reflection images for Profile 1 (cf. Paper E, figures 4 and 5). The reflection images produce higher resolution details of the structure within the well-to-well reservoir volume. At this time, however, we are not able to extract information of the impedance contrasts at these reflectors. We are only able to map the reflectors. These are not zero-offset seismic sections of the type produced by surface seismics.

In figures 4 and 5 of Paper E, the major reflections correlate to well-log markers and to the major velocity transitions seen in the tomogram (Paper C, figure 12). From bottom to top these markers are:

1. Top of the San Andres formation at 3,050 feet.
2. Top of Grayburg M unit at 2,950 feet.
3. Top of Grayburg D5 unit at 2,860 feet.
4. Top of Grayburg Formation at 2,750 feet or higher.
5. Top of McElroy marker zone at 2,700 feet.

Furthermore, there is fine-scale detail not seen in the tomogram. The San Andres-to-Grayburg boundary is known to be an unconformity (Harris et al., 1984; Walker and Harris, 1986) corresponding to a regression or low stand of sea-level that exposed the underlying San Andres carbonate platform. This unconformity occurs near 3,050 feet in the reflection images. The images also show that this unconformity to be an angular unconformity. The San Andres strata dip from west to east towards the Midland Basin, while the overlying Grayburg strata are more flat lying. The reflection images reveal that the reflector corresponding to the sonic-velocity low (gamma-ray peak) at 3,080 feet at the receiver well terminates up dip at the San Andres to Grayburg unconformity near the source well (Paper E, figures 4-5 and 9-10). The reflector corresponding to the sonic-velocity low (gamma-ray peak) at 3,100 feet at the receiver well ties to the 3,080-foot velocity low in the source well. These relations could not be resolved using the tomogram (Paper C, figure 12), only using the reflection images.

This kind of stratigraphic and structural information is unprecedented in exploration and production geophysics. This detail seen in the crosswell reflection images cannot be matched by surface seismic or vertical seismic profiling methods. The interwell correlations observed in the images can only be inferred when using well logs alone. The detail and information in the crosswell reflection images should be invaluable to reservoir engineers and geologists who need to achieve a better understanding of their reservoirs to solve hydrocarbon production problems (Nolen-Hoeksema, 1990).

A second example is found between 2,750 and 2,775 feet in the reflection images (Paper E, figures 4-5 and 11-12). Here a small pinchout is shown to occur near the top of the Grayburg E unit. Well logs clearly show a lateral variation in log character between the source and receiver wells. The Grayburg E marker at 2,780 feet can be carried from well to well using both well logs and reflection images. The reflector corresponding to the sonic-velocity low at 2,770 feet in the receiver well appears to pinchout or downlap near the Grayburg E marker. This depth range corresponds to the relatively slow (yellow) zone in the tomogram, but these relations cannot be resolved there. The two crosswell seismic methods complement each other. The reflection images show dipping beds, while the tomogram shows lowered velocity in this depth interval. The lowered velocity may result in part from the dipping beds and the local anisotropy that this produces in this depth interval.

Within the main Grayburg (D5 unit) reservoir zone we observe both obvious and subtle variations in the reflection images (Paper E, figures 4-5 and 6-7). The reflection images clearly show vertical heterogeneity that is not evident in the tomogram. The strata are flat. Many of these reflectors carry right across the profile and provide confidence to the well-to-

well correlation of porosity zones. There are subtle suggestions of reflection terminations that may be amenable to seismic stratigraphy analysis, where interwell stratigraphic relations are resolved (e.g., Mitchum et al., 1977). An example of this may occur at 2,930 feet near the receiver well in the P-wave image (Paper E, figure 6). This feature, however, is not apparent in the S-wave image (Paper E, figure 7). Although in this depth range, there is more curvature in the S-wave image than in the P-wave image.

If the P- and S-wave reflection images are stacked to enhance the coherent effects in both images (Paper E, figure 8), then the main reservoir horizon appears to be zoned. The "D5" reflector is strong at 2,850 feet and the "M" reflector is strong at 2,950 feet. There is a third strong reflector at 2,880 feet. In the lower part of the reservoir horizon, reflectors are strong and coherent in the west (right side) and discontinuous in the east (left side). We are not sure what this means yet. This may simply reflect that over this depth range in the separate P- and S-wave images the reflectors on the right half of the images appear more continuous and coherent than on the left (Paper E, figures 6-7). As explained in Paper E, the two halves of each reflection image were processed independently and then spliced together. The continuous and discontinuous nature of the reflectors may be artifacts of this processing. Stacking then enhances these artifacts.

To conclude these last two sections, high-resolution crosswell seismology is able to assist with reservoir delineation and characterization. We have shown how traveltime tomography provides information on the larger-scale zones within the reservoir and reflection imaging provides finer-scale information on structure within these zones. Crosswell seismology provides information on the continuity and coherency of reflectors. It complements other reservoir characterization tools. It provides much finer-scale information than surface-reflection seismology (cf. Paper A, figure 5) and gives confidence to well-to-well correlation of well logs. In time, crosswell reflection images may assist with resolving stratigraphic relations in the interwell region through seismic stratigraphy analysis.

The traveltime tomography and reflection images do not appear to provide information about the permeability continuity of reservoir zones, as is needed by reservoir geologists and engineers (Lemen et al., 1990). We cannot tell whether a laterally-continuous porosity zone is actually discontinuous in permeability because of plugging by anhydrite or gypsum. In time, this difficulty may be overcome through better correlations of crosswell seismic results to rock properties.

Core Analysis

Another principal objective of this crosswell demonstration field experiment was to assess the capability of crosswell seismology to monitor the movement of CO_2 after injection. As part of this program of research, we conducted a core-analysis program to see if it is be feasible to identify seismic property changes in response to CO_2 flooding.

Paper F describes the core-analysis program, ultrasonic velocity data, and methods used to estimate sonic and seismic properties from core data. We matched the P- and S-wave sonic logs from Well JTM-1202 with synthetic logs calculated from the core data. After obtaining a satisfactory match to the sonic logs, we estimated the effects of CO_2 flooding on the seismic properties of the Grayburg formation. These estimates suggest that the contrast between a CO_2-swept zone and an unswept zone is a small 2% if one uses P-wave velocities. The contrast is somewhat better for P-wave and bulk-wave impedances, being 3% and 4.5%, respectively. The best contrast comes from the bulk moduli where the estimated contrast is about 8%.

Our P-wave traveltime tomography results indicate that we should be able to see changes in the velocity field that are greater than 1% (cf. Paper C, p. C13). We predict P-wave velocities will change by 2% in response to CO_2 flooding. Providing we can repeat a baseline survey with variations of less than 1% from one time to the next, we are hopeful that we can detect CO_2-induced changes in seismic velocity and monitor the movement of CO_2 after injection.

CONCLUSIONS

We have shown how crosswell seismology can be used to reveal the interwell structure of the Grayburg reservoir in Section 205 of McElroy Field. Our data acquisition on-the-fly allows us to record a densely sampled data set (40,000 traces) in a reasonable amount of time (2 days). The high density of these data sets minimizes problems of spatial aliasing and allows for decomposition of the full wavefield into its various wave modes. It also allows for direct synthetic-to-data comparisons, which enhances data acquisition planning and data interpretation. We have demonstrated that we can handle these large data sets—the reflection imaging was the computational equivalent of imaging 1516 offset vertical seismic profiles (VSPs).

Using Profile 1, we have shown how traveltime tomography reveals the large-scale zonation of the reservoir. Reflection imaging provides information of the finer-scale internal structure within these zones and of the continuity and coherency of strata

(reflectors). Crosswell seismology complements other reservoir characterization tools. It provides much finer-scale information than surface-reflection seismology and gives confidence to well-to-well correlation of well logs. In time, crosswell reflection images may assist with resolving stratigraphic relations in the interwell region through seismic stratigraphy analysis.

We have investigated the feasibility of detecting seismic-property changes in response to CO_2 flooding. Our traveltime tomography results indicate we are capable of detecting velocity changes greater than 1%. Our core analysis results suggest that seismic properties can vary from 2% (P-wave velocity) to 8% (bulk modulus) as a result of CO_2 flooding. Together, these data give us confidence that we shall be able to monitor the movement of CO_2 after injection.

Profile 2 is being processed now. Our plans include a repeat baseline survey to test the repeatability of our data in these wells. This will be the baseline for the post-CO_2 profile and the link between 1991 and future activities. After CO_2 injection, we plan a second survey to try to monitor the movement of CO_2 or any changes in response to CO_2.

ACKNOWLEDGMENTS

The results reported here were cooperatively supported by Chevron (COFRC), the Seismic Tomography Project (STP), the Packard Foundation, and the Gas Research Institute (GRI). Thanks to Don Paul and Bjorn Paulsson for initiating this project with Stanford. Our COFRC project leader, Robert Langan, was instrumental in facilitating project activities and coordinating with Chevron, USA. The project could not have been completed without the planning and support of Chevron's Midland office, especially the field team lead by Ronnie Brumfield. Leon Roe, Ron Genter, Jim Flis, and others of Midland provided data and advice at appropriate times.

REFERENCES

Harris, P. M., Dodman, C. A., and Bliefnick, D. M., 1984, "Permian (Guadalupian) reservoir facies, McElroy Field, west Texas: in Carbonate Sands—A Core Workshop," in Harris, P. M. (ed.), SEPM Core Workshop No. 5, pp. 136-174.

Nolen-Hoeksema, R. C., 1990, "The future role of geophysics in reservoir engineering," Geophysics: The Leading Edge of Exploration, **9** (12), 89-97.

Lemen, M. A., Burlas, T. C., and Roe, L. M., 1990, "Waterflood pattern realignment at the McElroy field—Section 205 case history," SPE Paper 20120 presented at the 1990 Permian Basin Oil & Gas Recovery Conference, Midland, Texas, March 8-9.

Mitchum, R. M., Jr., Vail, P. R., and Thompson, S., III, 1977, "Seismic stratigraphy and global changes of sea level, Part 2, The depositional sequence as a basic unit for stratigraphic analysis," in Seismic Stratigraphy—Applications to Hydrocarbon Exploration, AAPG Memoir **26**, pp. 53-62.

STP-3, 1992, Seismic Tomography Project, **3** (1), July 1992.

Walker, S. D., and Harris, P. M., 1986, "McElroy Field—Development of a dolomite reservoir, Permian Basin of west Texas," Permian Basin/SEPM Publication **86-26**, 127-132.

Ward, R. F., Kendall, C. G. St. C., and Harris, P. M., "Upper Permian (Guadalupian) facies and their association with hydrocarbons—Permian Basin, west Texas and New Mexico," AAPG Bulletin, **70** (3), 239-262.

PAPER A

HIGH RESOLUTION CROSS-WELL IMAGING OF A WEST TEXAS CARBONATE RESERVOIR

Part 1 - Project Overview and Data Acquisition

Jerry M. Harris, Richard Nolen-Hoeksema, James W. Rector III[#], Mark Van Schaack, and Spyros K. Lazaratos
Seismic Tomography Project

ABSTRACT

Cross-well traveltime tomography and reflection imaging were combined to produce high resolution images of a West Texas carbonate reservoir. The cross-well project reported on here represented the geophysical component of a miscible CO_2 flood pilot study. The project objectives were to (1) evaluate the effectiveness of the high frequency piezoelectric source, (2) assess the capability of cross-well seismology to assist with reservoir delineation and characterization prior to CO_2 injection, and (3) monitor movement of CO_2 after injection. Data were acquired using the piezoelectric source and a hydrophone array. Field operations were distinguished by the fact that nearly 80,000 seismic traces were recorded in approximately four days using the technique of recording with the source moving, i.e., on-the-fly. Initial tomography and reflection results illustrate vividly how high frequency cross-well seismology can be used for imaging subtle velocity variations and bed geometry inside a thin reservoir. Moreover, the results demonstrate the great potential of cross-well seismology to meet the needs of high resolution reservoir description. Data from two cross-well profiles are described, one between wells 184 feet apart, the other between wells 600 feet apart. In this paper, Part 1 of 5, we present an overview of the project, review data acquisition, and summarize the results. We discuss the hardware used, data gathering method, then summarize the results to date. The four companion papers present additional details.

Now with the University of California, Berkeley

SITE DESCRIPTION

This area of West Texas has been under production since the mid 1930s. Our particular field has undergone significant infill drilling dating back to the late 1950s when waterflood patterns were introduced. The profile area is part of three 20-acre five spot patterns in a CO_2 pilot study. An observation well, used for the cross-well profiling, was drilled for the CO_2 study. This observation well has a large suite of logs and core samples that will be used later for interpretation. The field location, reservoir depths, and names of wells have been altered for purposes of presentation in this paper.

The target of the cross-well profiles was the Permian-aged San Andres/Grayburg formation. The depositional sequence consists of a series of upwardly shallowing and prograding carbonate units. Production is mainly from the Grayburg where several distinct depositional groups and lithofacies can be identified. Structurally, the region is flat although mildly increasing dips can be found toward the bottom of the surveyed section. The dominant lithologies encountered are dolomite and anhydrite. Reservoir rocks are primarily dolomitized carbonates. Overall, the reservoir is characterized by irregular geometry and significant variations in both porosity and permeability. Average porosity throughout the field is about 10% but varies higher due to solution enhancement and lower because of evaporites. Permeability is also quite variable averaging only a few millidarcies throughout the main pay, but increasing to a few hundred millidarcies in thin high permeability streaks that can cause significant fluid channeling.

Seismic properties of the sequences are approximately known from well logs run throughout the field and at the observation well. Compressional wave velocities range from about 14,000 ft/sec to over 21,000 ft/sec. Density values range from slightly less than 2.6 gm/cm3 in the reservoir to over 3 gm/cm3. The composite reservoir zone is approximately 100 feet thick. Its thickness and large seismic contrast (>20%) with the surrounding formations represent an easily visible target for either seismic tomography or reflection imaging.

DATA ACQUISITION

Two cross-well profiles were run with the geometry shown in Figure 1. Well A, the observation well, was used for the receivers during both surveys. The well spacings were 184 feet and 600 feet, respectively. Profile #1, recorded between wells A and B, consisted of nearly 36,000 traces. Profile #2, acquired between wells A and C, consisted of over 37,000 traces. Receiver positions were approximately centered about the reservoir as

shown in the figure. Profile #1 was uniformly sampled at 2.5 ft. source and receiver spacing, Profile #2 at 5.0 ft.

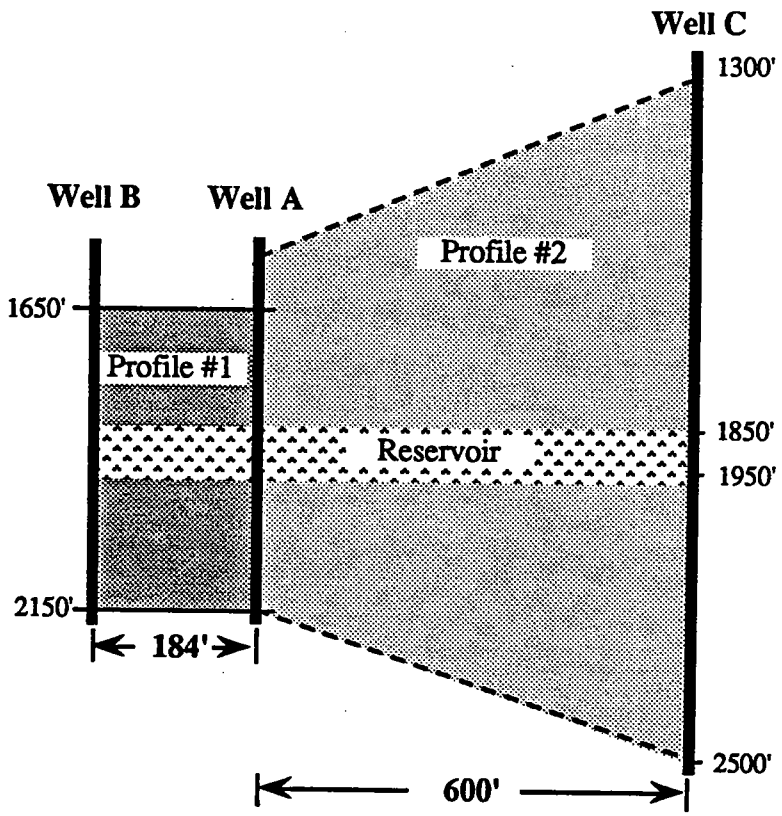

Figure 1. Profile #1 (201 sources x 178 receivers) was recorded between wells A and B. Profile #2 (240 sources x 153 receivers) was recorded between wells A and C. Receivers are in Well A.

Prior to these surveys, high frequency datasets recorded primarily for tomography were not suitable for reflection processing because of severe spatial aliasing of events with low phase velocity, e.g., reflected arrivals and tube waves (Rector, 1992a). Partly in response to our interest to create high resolution reflection images from cross-well data, we focused attention on improving data acquisition, namely finer sampling and faster field operations. The West Texas profiles described here were the first run using the new acquisition method of recording on-the-fly, where the source is continuously moving while being fired. This technique significantly improved both depth control and acquisition speed.

Field Operations

The data were acquired as common-receiver gathers or receiver fans. For each simultaneous group of receiver fans (usually 7 or 8 elements), the hydrophone array was positioned in the well and set up for recording. The source was then logged up the well at approximately 500 feet per hour. As the source moved continuously, it and the hydrophome array would receive trigger signals from the wireline depth system at regular depth intervals. The trigger initiated the vertical stack, two sweeps for Profile #1 and four sweeps for Profile #2. The stack was initiated at 2.5 foot source intervals for Profile #1 was recorded and 5.0 foot intervals for Profile #2. With the low stacking depth, shot point smear was minimized. in fact, the bottleneck in this procedure was the uplink time required by the hydrophone array to transmit its digital data up hole. The major advantage of shooting "on-the-fly" in this manner was that the depth interval between shot points was accurately maintained throughout the survey due primarily to operating the source wireline under steady tension. The source wireline was marked so that a depth tie could be made before and after each scan of the source. Also, the receiver wireline was also marked. Receiver depth was checked by lowering the array at regular intervals, checking the mark, then pulling up to the desired depth. As a result, depth control was excellent. With this procedure, data were collected at a rate of nearly 1400 traces per hour. Profile #1 (36,000 traces) took a little more than 48 hours to complete despite some downtime for minor repairs. Profile #2 (37,000 traces) took only 40 hours to complete including time for the rig up on well C.

Identical sweeps were used in both surveys, i.e., a 250-2000 Hz linear upsweep of 200 mS duration. A listen time of 300 mS and 500 mS were used for Profiles #1 and #2, respectively. The data were sampled at 200 uS with low cut filters (-3 dB) set to 250 Hz and the high cuts at 2000 Hz. A representative common-receiver gather from each profile is shown in Figure 3.

A schematic outline of Stanford's data acquisition system is shown in Figure 2. The system consists of a three-element piezoelectric downhole source, a nine-level hydrophone array, and of course, two logging trucks with associated surface equipment and instruments to control the downhole tools. Both the source and receiver systems are installed in standard logging truck. All field operations are directed from the source truck. Receiver signals are interfaced via a multi-conductor ground line between the source truck and the receiver wireline. Both downhole source and receiver wireline depths are electronically monitored and recorded to the segy header along with the data. The data are transferred to a DEC 5000 workstation running ProMAX for correlation and in-field quality control and processing. A brief description of the hardware systems is given below.

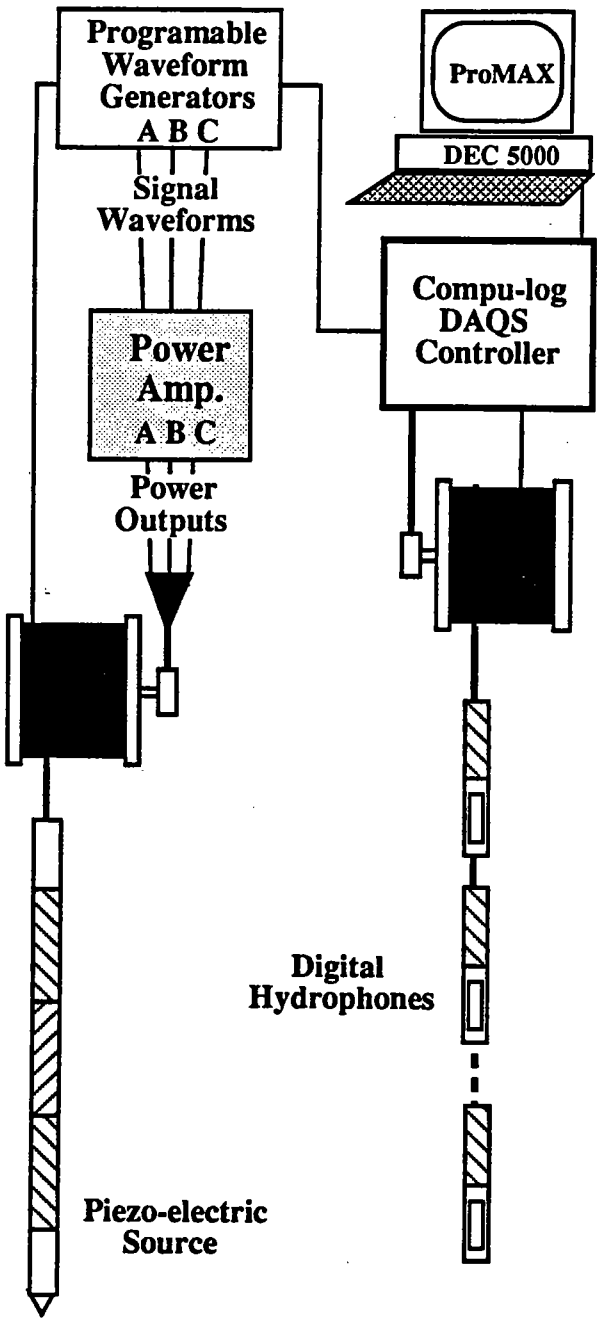

Figure 2. Diagram of the STP data acquisition system.

The Piezoelectric Downhole Source

The source consists of three active elements, symmetrically placed into the downhole tool to form a mass balanced downhole source. Two banks of power transformers are mounted above and below the active transducers for symmetry. The balance is intended to reduce spurious modes of structural vibration, thus creating more radiation from the desired monopole mode. The transducers are wired as an adjacent array, capable of being operated independently for purposes of beamsteering. The elements may be driven as three independent sources or as a single unit for increased coherent output. No beamsteering was used while recording the West Texas profiles discussed here. Source signatures are generated by three 12-bit D-to-A phase-coherent waveform generators. Arbitrarily defined waveforms including sweeps, pulses, and pulse sequences can be used. The source is powered by a three-channel 24 kVA linear power amplifier. This power is delivered via 12,000 feet of 7-conductor armored wireline. The 0.579-inch diameter cable has the standard 7-conductor armored configuration but uses lower resistance conductors and special insulation for better power transfer.

The Hydrophone Receiver System

The receiver system consists of a nine-level array of hydrophones. Each level is independently digitized downhole to sixteen bits of resolution. A surface computer, located in the source truck, provides control of recording parameters - sampling rate, downhole analog and digital gain, vertical stacking depth, and high and low pass filter settings. The hydrophones are interfaced to the surface via a telemetry sonde that controls communications and data transfer. Data are stacked downhole in order to reduce transmission throughput. Though only four conductors are required, the entire system is run on 17, 000 feet of standard seven-conductor wireline. Recording parameters are saved to segy headers along with the trace data.

PROCESSING AND INTERPRETATION

As shown schematically in Figure 4, our data processing scheme combines traveltime tomography and reflection imaging . For details, the reader is referred to the four companion papers in this volume: (Van Schaak, et al, 1992a), (Van Schaak, et al, 1992b), (Rector, et al,1992b), and (Lazaratos, et al, 1992). Initial results for Profile #1 are discussed below.

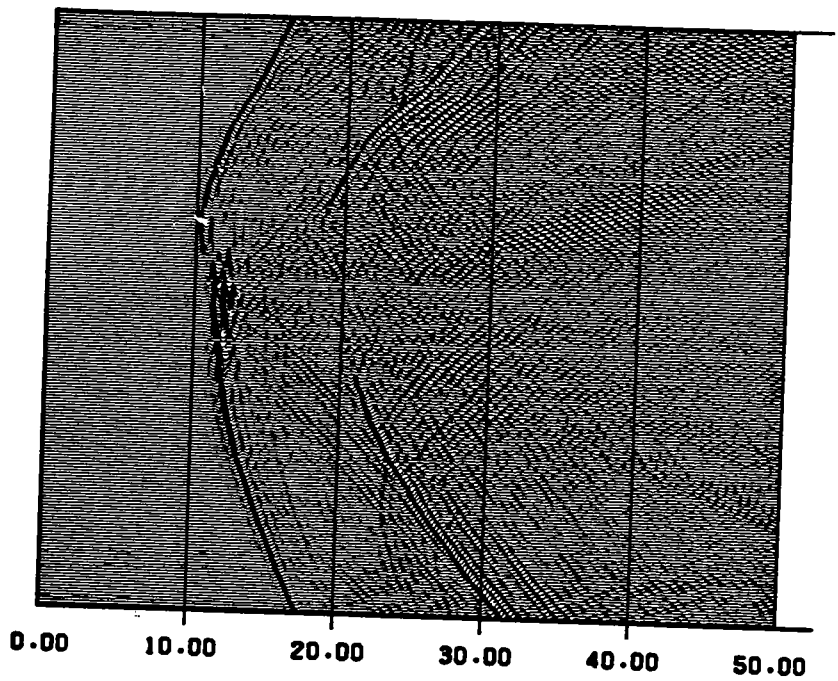

(a)

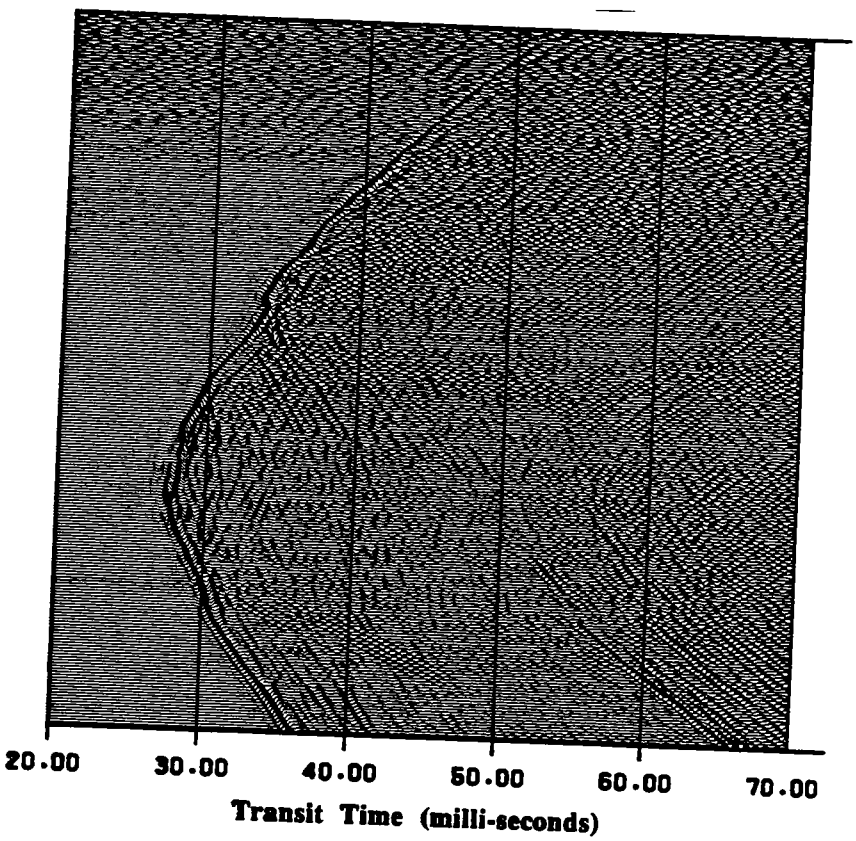

(b)

Figure 3. Common-receiver gathers: (a) Profile #1, 2.5 ft. source spacing; Wells A-B. (b) Profile #2, 5.0 ft. source spacing; Wells A-C.

Initial images generated by the processing are shown in Figure 5. The P-wave tomogram (Fig. 5a) provides a very good quantitative image of interval velocity. Resolution is better vertically than laterally as is well known for the limited view cross-well geometry. Van Schaack, et al (1992b) compares the velocities estimated from the tomography with those obtained form sonic logs. Based on the smoothing parameters used on the logs, he estimate the vertical resolution of the cross-well velocity tomogram at about 10-20 feet. Overall, the tomography is extremely successful at imaging the transition zones above and below the reservoir and even the subtle variations inside the reservoir. For example, we see excellent imaging of the sharp transition in velocity from about 20,000 ft/s above the reservoir to 16,500 ft/s inside the reservoir near the depth of 1850 feet. Similarly, below the reservoir, the tomography successfully delineates the more gradual transition out of the reservoir into faster rocks. Subtle lateral variations inside the reservoir are indicated but are not yet interpretable as geology or reconstruction artifacts. A constant velocity starting model was used to initiate the tomography results shown in Figure 5a.

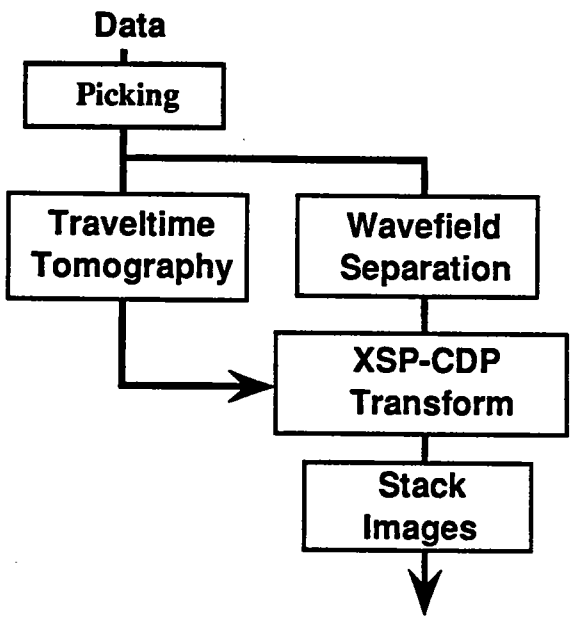

Figure 4. Schematic flow of cross-well data processing for tomography and reflections.

The reflection image general from data for Profile #1, shown in Figure 5b, was generated by a pre-stack XSP-CDP mapping algorithm (Lazaratos, et al, 1992). Though the reflection image is qualitative in nature, it gives 2-3 times better resolution than the tomography. Wavefield separation (Rector, 1992b) played an important part in data preparation before imaging. The volume of data and sorts available from the cross-well geometry provide more opportunity for reflection enhancement. Although the imaging method is similar to offset VSP imaging, the XSP-CDP transform uses many more gathers of data and combines upgoing and downgoing reflections, in this case over 750 gathers. The image shown here is a "brute stack." Each common-source and common-receiver gather was mapped, then the independent images stacked. Reflectors imaged *inside* the reservoir (1850 ft - 1950 ft) provide an unambiguous measure of bed continuity, at a vertical resolution better than 5 feet. Aside from this excellent resolution, the image also provides other remarkable ties to the logs. See, for example, the twin features marked near 2100 feet in well A to the single feature marked in Well B. The reflection image may be used to guide connecting these features, thus delineating the geological framework of the interwell region.

For comparison, we show a typical surface seismic section from the West Texas study area (Figure 5c). (Absolute times and parts of the overburden have been removed.) These data were recorded with 250-foot shot-point spacing with about 50 Hz of bandwidth (e.g., 5-55 Hz). At reservoir depth, the wavelength approaches 300 feet; therefore, the entire 100-foot thick reservoir is visible only as a single event. Reservoir structure is unresolved. That is, no separate identification of the top, bottom, or internal structure is possible. Also, the entire lateral section imaged by cross-well is less than two surface seismic CDP points wide - as illustrated. Clearly, cross-well seismology, whether tomography or reflections, offers complementary high resolution advantages to surface seismic. And, unlike surface seismic, which is often presented as a time section, cross-well reflection images are true depth images with higher spatial resolution.

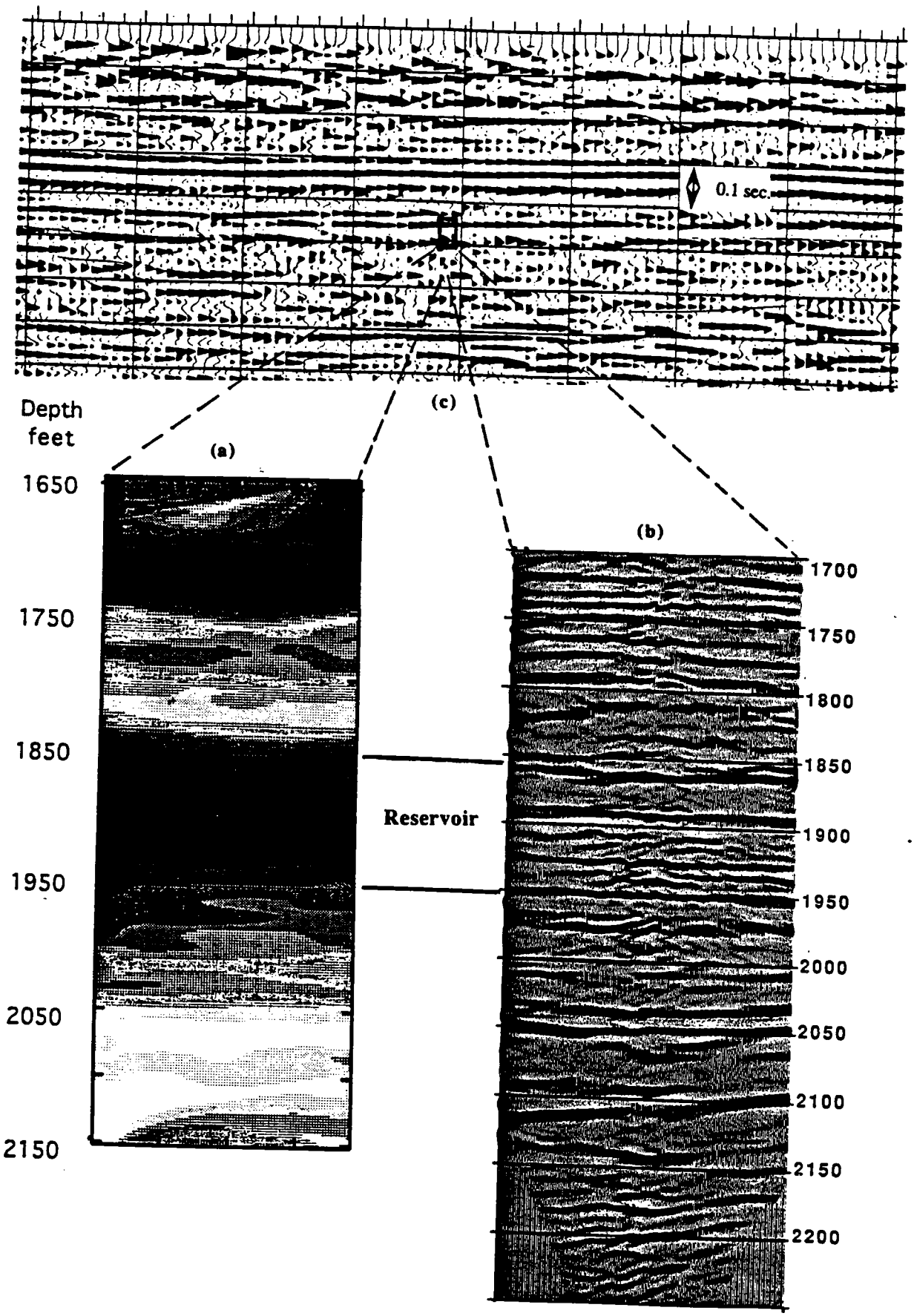

Figure 5. Complementary images of the reservoir. (a) Cross-well traveltime tomogram; (b) Cross-well P-to-P reflection image; (c) Surface seismic reflection image.

CONCLUSIONS

We have shown how cross-well direct wave traveltimes and reflections are combined to image the internal structure of a West Texas carbonate reservoir. The high resolution images result from the cooperation of new data acquisition and data processing techniques. Though at small scale, only 184 feet between wells for Profile #1, we believe our results illustrate the enormous potential of cross-well seismology to usefully address reservoir delineation and characterization problems. As illustrated in Figure 5, one role for cross-well imaging is to complement the low resolution but large coverage already available from surface reflection seismology. Although Profile #2 has yet to be processed, the initial results discussed for Profile #1 are only the beginning of a new high resolution technology. Also, much work remains to be done for this particularly study, including processing S-wave tomograms and S-to-S reflection images from both profiles. In addition, our plans include using logs, cores, and an anticipated 3D surface survey to make quantitative estimates of reservoir properties throughout the field. We believe that these results will be extremely useful in reservoir characterization for the CO_2 injection study. A post CO_2 injection survey is planned for late 1992 to attempt monitoring.

ACKNOWLEDGMENTS

The authors are grateful to Chevron Oil Field Research Company for providing the field site and co-sponsoring this study with Stanford University. We also thank the Gas Research Institute and the Packard Foundation for their continuing support of the Seismic Tomography Project (STP) at Stanford University.

REFERENCES

Van Schaack, M., J.M. Harris, J.W. Rector, and S. Lazaratos, 1992a, High resolution imaging of a West Texas carbonate reservoir: Part 2 - wavefield analysis, STP-3, Paper B.

Van Schaack, M., J.M. Harris, J.W. Rector, and S. Lazaratos, 1992b, High resolution imaging of a West Texas carbonate reservoir: Part 3 - tomography, STP-3, Paper C.

Rector, J.W., S. Lazaratos, J.M. Harris and M. Van Schaack, 1992b, High resolution imaging of a West Texas carbonate reservoir: Part 4 - wavefield separation, STP-3, Paper D.

Lazaratos, S., J.W. Rector, J.M. Harris and M. Van Schaack, 1992, High resolution imaging of a West Texas carbonate reservoir: Part 5 - reflection imaging, STP-3, Paper E.

Rector, J., S. Lazaratos, J. Harris and M. Van Schaack, 1992a, Wavefield separation of cross-well seismic data, STP-3, Paper L.

PAPER B

HIGH RESOLUTION CROSS-WELL IMAGING OF A WEST TEXAS CARBONATE RESERVOIR

Part 2 – Wavefield Modeling and Analysis

Mark Van Schaack, Jerry Harris, James Rector III#, and Spyros Lazaratos
Seismic Tomography Project

ABSTRACT

Crosswell seismic data containing a rich variety of wave modes has been collected from a producing carbonate field in West Texas. Among the easily identifiable modes are; direct p-wave, direct s-wave, reflected p-wave, reflected s-wave, p-s conversions, s-p conversions, head waves, and of course, tube waves. Despite the intimidating complexity of the seismic records many wave modes (except tube waves) can be simulated very effectively. This is accomplished with a radial point force and the radial (horizontal) stress component to model a cylindrical piezoelectric bender source and hydrophone receivers respectively. A blocked sonic well log is used as a 1-D velocity model.

Wavefield analysis is achieved using synthetic shot records run with a viscoelastic 3-D modeling code with an equivalent bandwidth to our field data. This code supports full wave modeling of p-wave and s-wave direct arrivals, reflections, conversions, multiples and head waves. In addition we can add and subtract conversions and multiples, separate p-waves from the mixed compressional and shear wavefield, and to switch between radial point force and explosive sources. This flexibility allows us to identify and particular seismic events and determine their origin. We believe simulations of this sort lead not only to a better understanding of the crosswell wavefield but also provide a solid foundation to develop and modify processing and acquisition schemes.

INTRODUCTION

Crosswell seismic data can be incredibly rich in wave modes even in the simplest geologic settings. A common shot gather fan across a single acoustic bed boundary will

Now with the University of California, Berkeley

generate eight distinct body wave arrivals for a source generating both p and s waves. These arrivals consist of direct p, direct s, reflected p, reflected s, p-s converted and reflected, s-p converted and reflected, and finally p-s and s-p transmitted conversions. In addition to these basic body waves, our single boundary model can also result in the formation of tube waves, various secondary waves arising from them, Mach waves and head waves. These are the expected modes for a geologic model containing a single layer. With additional layers more complicated wave modes are possible, including channel waves and multiples.

Although a great number of wave modes are predicted for crosswell data far fewer can usually be distinguished in field data. In many cases this can accounted for by low signal levels, inadequate spatial sampling, and the dominance of tube wave arrivals in the seismic record. Often, complex geology can lead to records that are virtually indecipherable. It is in the simplest geologic structures that we can first expect to make progress in wavefield analysis.

Two crosswell surveys were shot in a producing West Texas carbonate field. Hardware, acquisition technique and simple geology have led to datasets of truly remarkable character. In particular, in the near offset survey, virtually all of the above described wave modes can be clearly observed. This is supported by simulations made possible by the simple structure of the surveyed area. These simulations permit us to identify and trace the origin of many of the various modes with confidence.

In this paper we use a simple source, receiver, and geologic model to identify the many wave modes observed in the field data. Despite the absence of source and receiver boreholes in our simulations we find a remarkable similarity between our field data and the simulated data. Discrepancies between the field and synthetic data suggest further analysis of wave modes not simulated by our simple model.

DESCRIPTION OF THE DATASET

The crosswell data were collected at a producing carbonate field in West Texas. The site and acquisition techniques used for collecting the data are described in more detail in Harris, et al (1992) and Van Schaack et al (1992). Two cased boreholes, one a producing well and the other a CO2 monitoring well were occupied for this survey. The data were collected over a zone of approximately 500 feet at a depth of over 2000 feet. The nominal separation of the two wells is approximately 184 feet. The geology of the surveyed region is virtually flat with little apparent lateral heterogeneity.

A cylindrical piezoelectric bender, was used as the source. We drove the source with a linear upsweep, from 250-2000 Hertz, over 200ms. The hydrophones were programmed

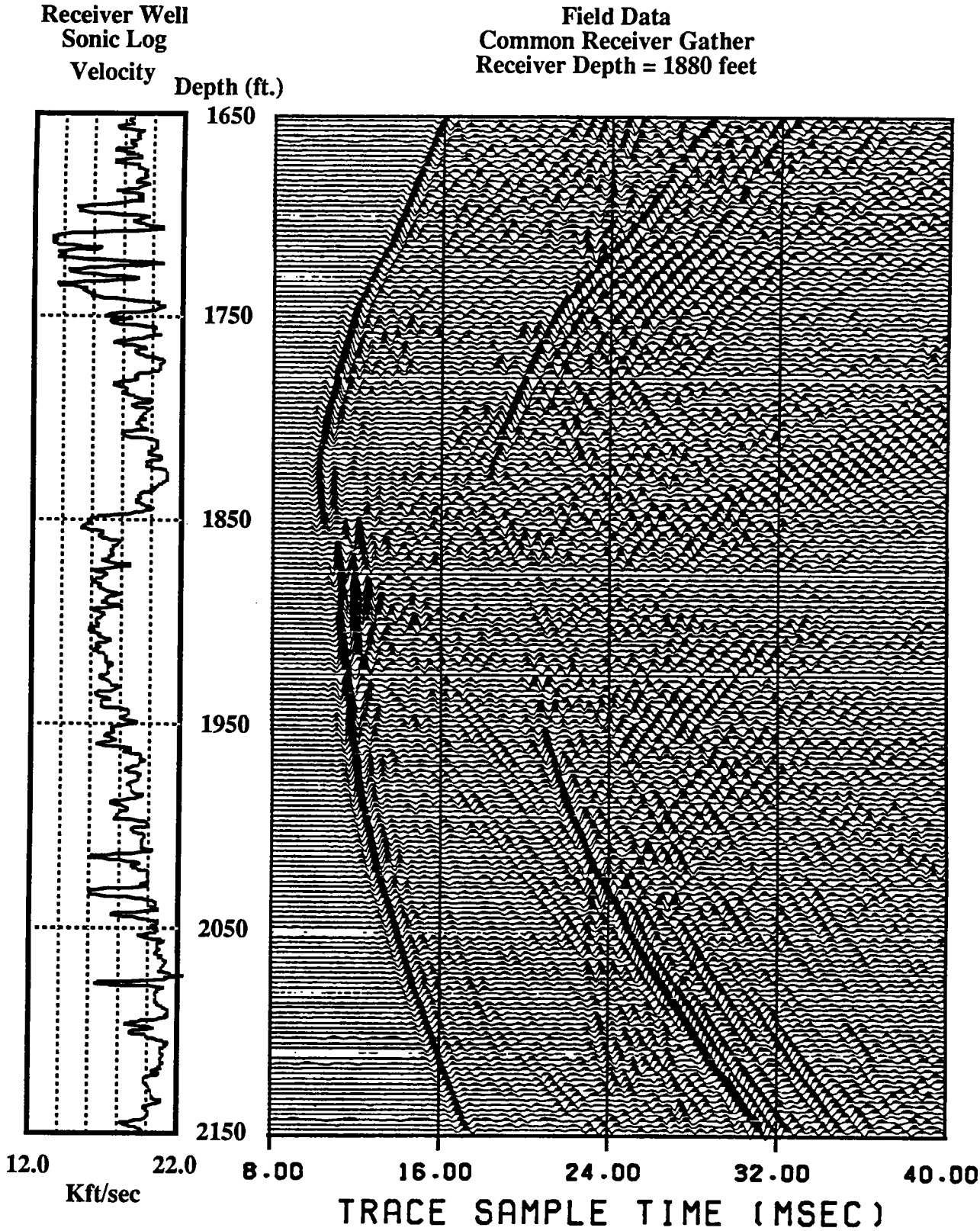

Figure 1) An unprocessed field gather and velocity sonic log from the receiver well. This common receiver gather was collected from a depth of 1880 feet. Source depths were shot over an interval ranging from 2150 - 1650 feet using the technique of "shooting on the fly". The source depth interval is 2.5 feet.

with a 300ms listen time for each sweep. Each shot consisted of a stack of two of these sweeps which were then transmitted digitally uphole. We collected this data using the technique of "shooting on the fly". Using this technique data are collected as common receiver gathers as the source is logged slowly up the hole. Although the source is moving while it is being fired the shot "smear" is only about 2 inches for the winch rate we were using (~500 ft/hr). The source shot interval for each receiver gather is 2.5 feet. For the 500 feet survey this results in 201 traces per receiver gather.

In our wavefield modeling and analysis we study a single receiver gather located in the low velocity reservoir layer at 1880 feet (figure 1) This gather is used because of the large number of converted modes and reflections that result from the velocity contrasts above and below the receiver. In this typical gather seismic energy containing frequencies over the entire 250-2000 Hertz range was recorded (figure 2), although most of the energy is concentrated in the higher frequencies.

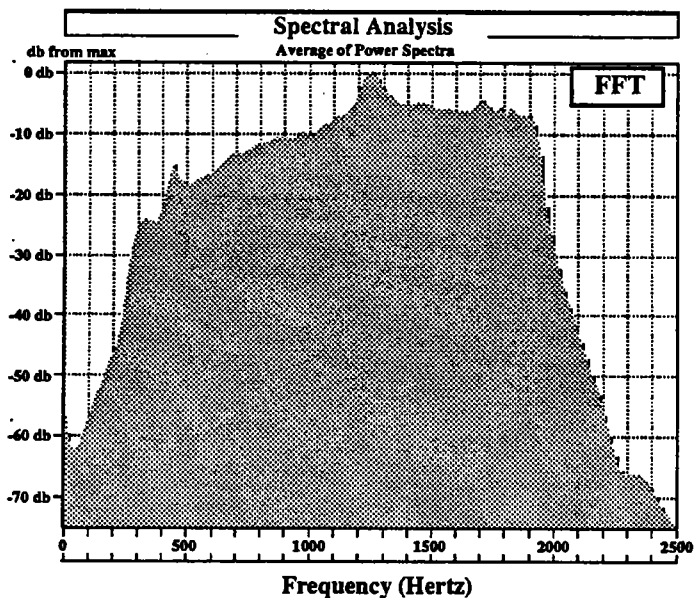

Figure 2) Spectral analysis of common receiver gather at 1880 feet (figure 1). The analysis was done from 0-40ms. A pre-FFT Hanning time window taper with an 80% flat time was used. Spectrum shown is the average of all 201 traces.

WAVEFIELD MODELING

The simulations were run using Sierra Geophysics' viscoelastic seismic profiling program, VESPA (Apsel, 1979). Although this algorithm is fully 3-D it allows only 1D

geologic models. In our case this limitation has minimal consequence due to the 1-D nature of the local geology. Although layers deeper in the surveyed section do exhibit a mild dip, as seen with logs and by reflection imaging (Lazaratos et al, 1992), this has little effect on our ability to match wave modes.

Modeling the Source

Our choice in the manner in which we model the piezoelectric bender source used in the field survey is influenced by several observations. One is that the source length is small compared to the radiated wavefield. The average wavelength is about 20 feet where the active element of the source is only about 3 feet long. Also, the outside diameter of the source is only about 1/4" less than the inside diameter of the casing for this survey This should reduce the amount of energy that escapes into the borehole fluid and maximize the energy transferred directly into the formation. This hypothesis is supported by the low relative amplitude of the tube waves to the direct and reflected arrivals in the field data.

These observations satisfy assumptions made by Heelan (1953) in his work on cylindrical sources. Simply stated Heelan's assumptions were; short relative source length, isolation from borehole fluid , and mechanical coupling to the formation. These assumptions were used in his derivation of an analytical approximation to the far-field radiation pattern created by a cylindrical source in a homogeneous medium. We use these same observations as a basis to use a radial point force, similar to Heelan's source, to model the piezoelectric bender source. We are primarily concerned, in this analysis, with the generation and moveout of various crosswell seismic events and not with absolute amplitudes. For these reasons the radial point force seems a good choice.

Modeling the Receivers

To model our hydrophone receivers we use the radial stress component of the wavefield. In this code the coordinate system is cylindrical so the radial stress component is equal the horizontal stress. The interaction of the seismic wavefield on the receiver borehole is complicated with conversions of shear to compressional waves being the most difficult to predict. As our hydrophone is basically a pressure transducer it seems reasonable that the pressure inside a borehole might be best approximated by the orthogonal stress to the outside of the casing.

The Geologic Model

The geologic model was created using blocked data from the sonic shear and compressional well logs. A shear sonic log was run only in the receiver well so the blocked logs from this well were used for our 1-D model. Rock density was also used in our calculations and was incorporated from the wireline well logs. Figures 3 and 4 show the unblocked sonic and density logs and their blocked counterparts used as the 1-D model. The simulations shown in this paper were created using a geologic model with 200 distinct layers ranging in thickness from 6 inches to several feet.

Results of the Wavefield Simulation

The results of our simulation (figure 5) tie well with the raw field data (figure 1) and a number of events are shared by the two. The arrival times of these events are also predicted very well considering the crudeness of our velocity model and that no attempt is made to model borehole deviations in our simulation. The relative amplitudes of the various events also seem well modeled by our choices for source and receivers. The degree to which our synthetic and field data agree suggest that the borehole effect is not very large for the piezoelectric bender source and hydrophone combination under the conditions they were run. Certainly the high velocities encountered eliminated the possibility of certain modes, such as the Mach wave (Meredith, 1990).

The lack of any unexplainable wave modes of significant amplitude is certainly encouraging. We can develop processing techniques and algorithms confident that our subtle manipulations are not overwhelmed by unaccounted for large amplitude wave modes. Wavefield processing and imaging of this dataset can be found in Lazaratos et al (1992) and Rector et al (1992).

WAVEFIELD ANALYSIS

Since a number of seismic events are successfully modeled by the wavefield simulation we are encouraged to take the next step and to identify these events. Our modeling program permits us to build up the wavefield piece by piece and to separate different seismic modes as we go. Figures 6-21 document this decomposition of the full wave field and provide additional information about the source of some events.

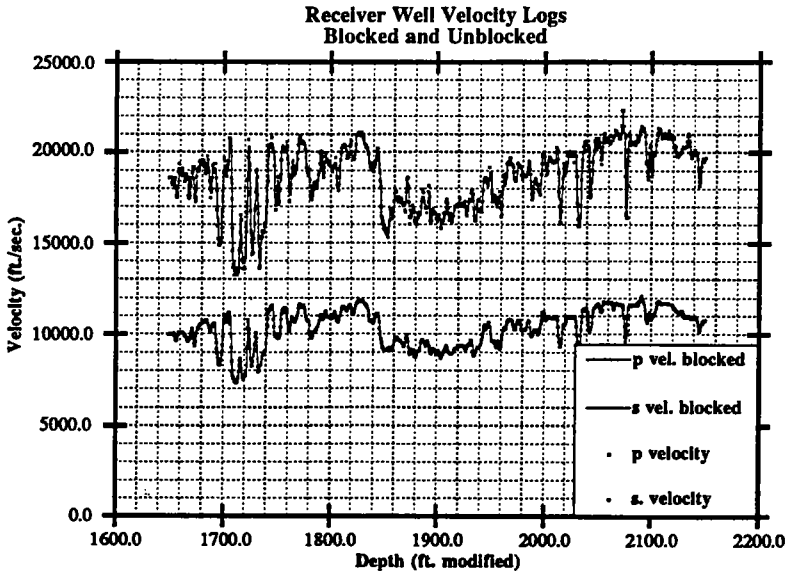

Figure 3) The plot show compares the p and s-wave sonic well logs with their blocked counterparts used in the wavefield simulations. The sonic logs are blocked into 200 layers preserving much of the high frequency content of the original well logs.

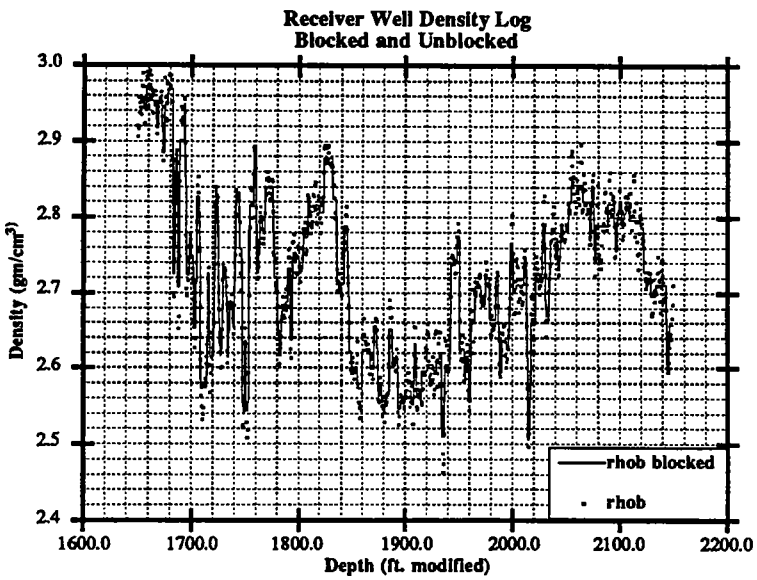

Figure 4) The plot show compares the density well log with its' blocked counterpart used in the wavefield simulations. The density log blocking follows the structure of the velocity log blocking.

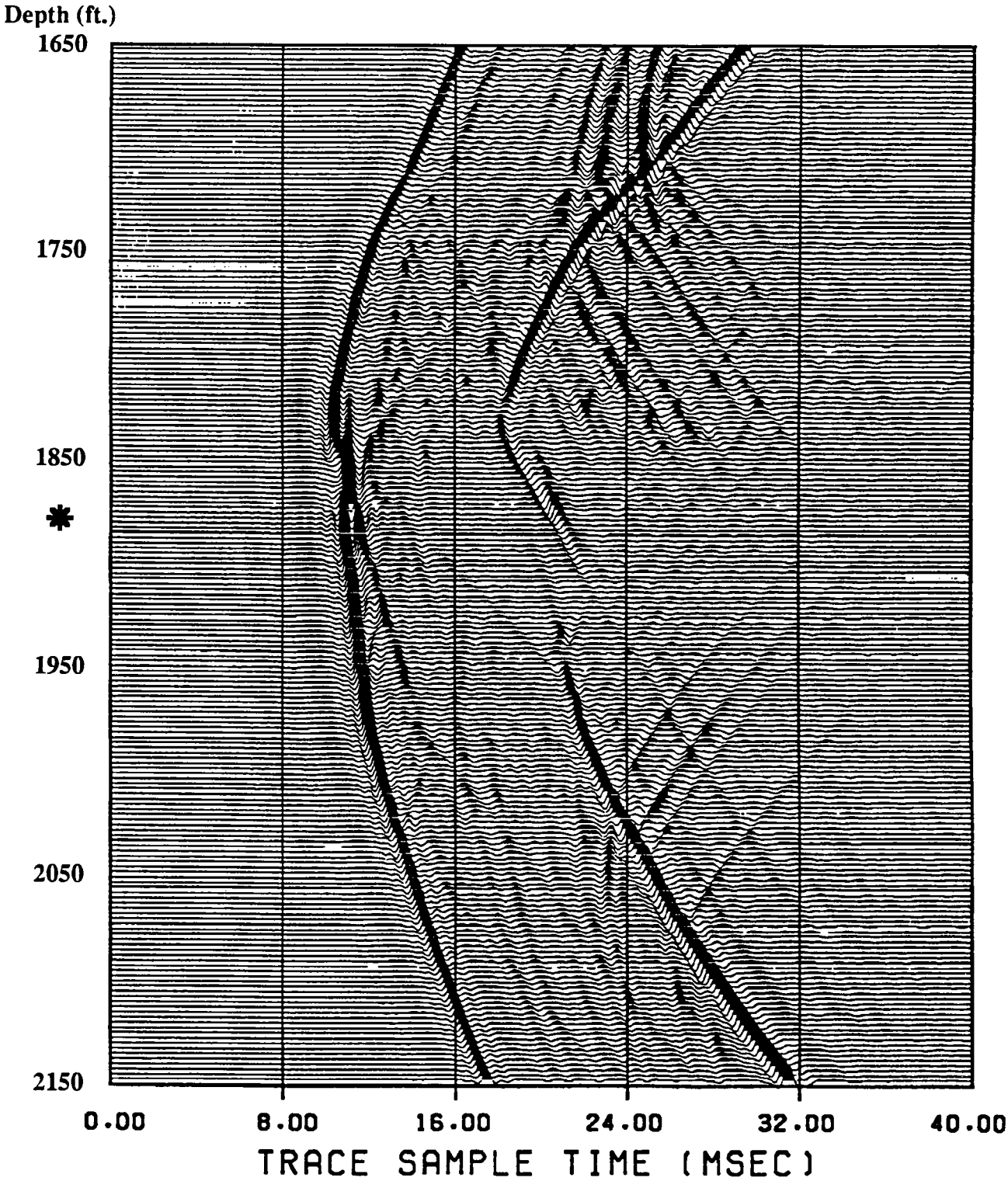

Figure 5) The results of our crosswell simulation. The source is modeled using a radial (horizontal) point force and the hydrophone receivers are modeled using the radial stress component. The 1-D velocity model was created using the receiver well sonic p-wave and s-wave well logs, and the density well log, blocked into 200 layers.

Wavefield Decomposition

The most basic run of our simulation software permits us to simulate primary arrivals, with head waves and primary reflections. Using a radial point force and the horizontal stress component to simulate the source and receivers (as we did in the wavefield simulation) we simulate our primary mixed wavefield (figure 6). This wavefield is mixed in the sense that both p and s waves are permitted. In this seismogram we can observe direct p and s waves, p and s reflections, and to lesser extent headwaves. We can further reduce this record by adding to the radial stress component the vertical and tangential stress components. Together these components make up the isotropic part of the wavefield effectively removing all shear waves (figure 7). By comparing these two seismograms p and s wave events are easily identified by noting which events remain or are eliminated after combining the isotopic elements of the stress field. Figures 8 and 9 repeat this procedure using an explosive source instead of the radial point force. These two records are basically identical since an explosive source generates no shear energy (and no conversions are yet allowed). This fact will be useful later in determining the history of certain events.

In figures 10 and 12 we repeat our simulation except now we allow conversions in our record. We can isolate the conversion energy in these seismograms by subtracting the appropriate primary mode record from these records. From figure 10 we subtract figure 6 and from figure 12 we subtract figure 7. We are left with two converted wavefield records, mixed (figure 11) and p-wave only (figure 13). Given these records we can identify many sublinear events in figure 11 originating from the direct p arrival that are not present in figure 13. These are p-s converted reflections and transmissions. Many of these p-s transmitted conversions are apparent in the field data. In addition many sub-hyperbolic events with similar asymptotic moveout to the direct p-wave arrival are evident in both figure 11 and 13. These are s-p converted and transmitted arrivals. Again, many similar events can also be found in the field record.

In figures 14-17 we perform the same analysis except now we analyze the multiple modes. Figure 15 contains mixed p and s-wave multiple events. Through comparison with figure 17 we can identify shear multiple events which are suggested in the field data. Note that the p-wave multiple events have very nearly the same moveout as the s-p converted events seen in figure 13. They can be differentiated by the minute difference in their moveouts. The moveout of the s-p conversions decreases at farther offsets where the moveout of the multiple reflections increases slightly at farther offsets. Note that the moveout of the shear multiples is very similar to both the moveout of the s-wave reflections

and the moveout of the s-p converted reflections. This suggests that moveout based filters will have some difficulty discerning these events, at least in CSG and CRG space.

Finally we study explosion generated conversions. The importance of these records is in studying the genesis of the various p-wave conversions. We saw before in figure 13 the large number of semi-hyperbolic events with moveouts paralleling the direct p arrival. We know these are s-p conversions but we may wish to know if they originate from direct s-wave energy or if the s-wave energy had its beginning as p-wave energy. As the 3-D explosive source generates no s-wave energy s-p conversion events in common between figures 21 and 13 must be at least p-s-p converted modes. Upon close study of these figures we find several events which fit this criteria but none which unmistakably apply to the field data.

CONCLUSIONS

In figure 22 we label many of the identifiable wave modes in our field gather. Even in this case where tube wave energy did not contribute heavily to the seismic record we find the crosswell wavefield quite complicated. Nevertheless, we find that with reasonable completeness, we can model a great number of these modes with simple shot, receiver, and geologic models. The absence of source and receiver boreholes in our survey did not result in any major differences between our synthetic gather and the field record. This however is undoubtedly due to many special survey conditions. We might not always be so lucky in avoiding many of the overpowering seismic modes so often present in crosshole seismic data. But, if the proper processing and acquisition techniques can be developed, crosswell data offers a wealth of information in its many reflected, transmitted and converted modes.

ACKNOWLEDGMENTS

The authors are grateful to the Gas Research Institute for supporting this research and to Chevron Oil Field Research Company for providing the field site and co-sponsoring this study at Stanford.

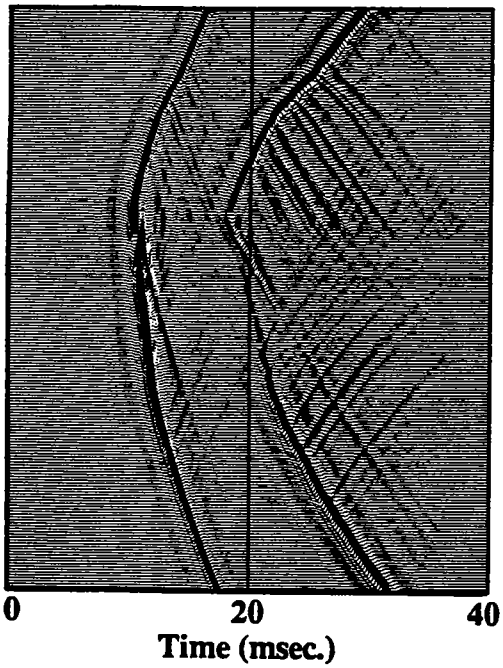

Figure 6) Primary arrivals calculated with a horizontal point force as the source and the isotropic stress components as receivers.

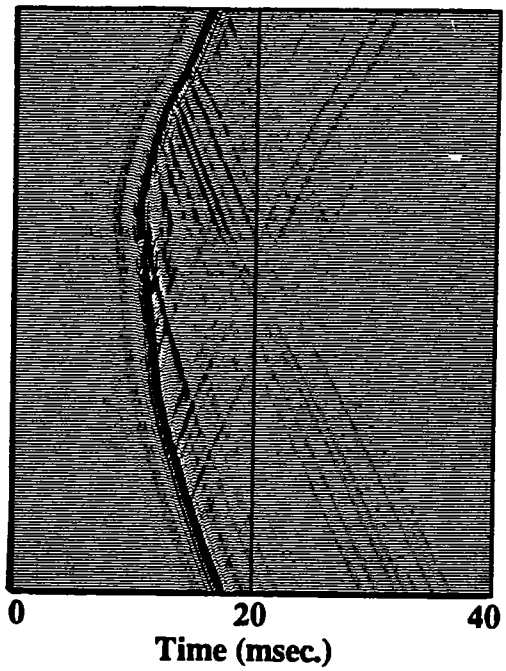

Figure 7) Primary arrivals calculated with a horizontal point force as the source and the radial stress component as receivers.

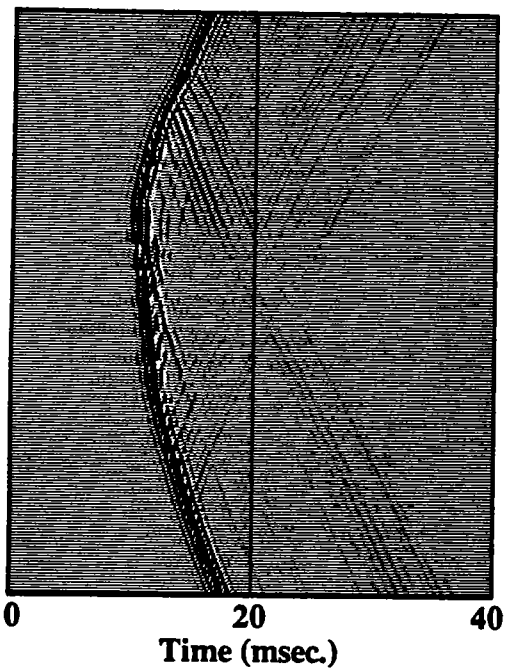

Figure 8) Primary arrivals calculated with an explosive source and the isotropic stress components as receivers.

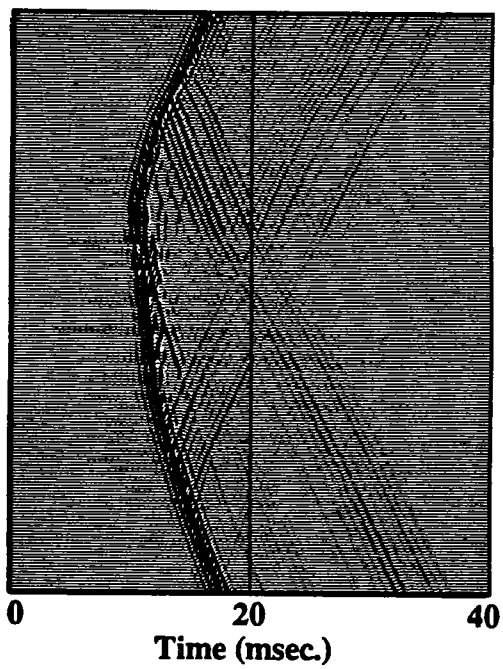

Figure 9) Primary arrivals calculated with a an explosive source and the radial stress component as receivers.

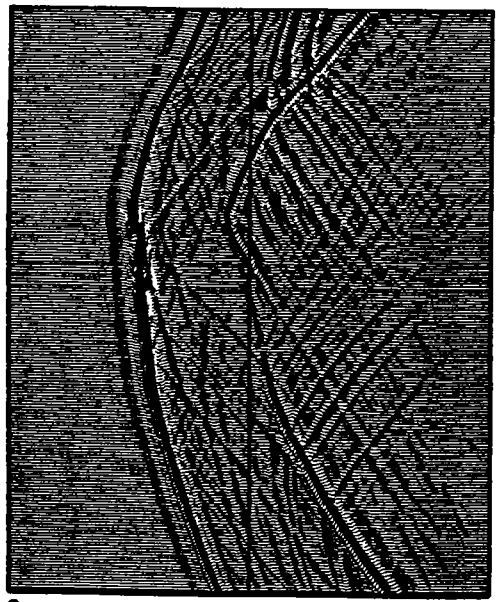

Figure 10) Primary arrivals + conversions calculated with a horizontal point force as the source and the radial stress component as receivers.

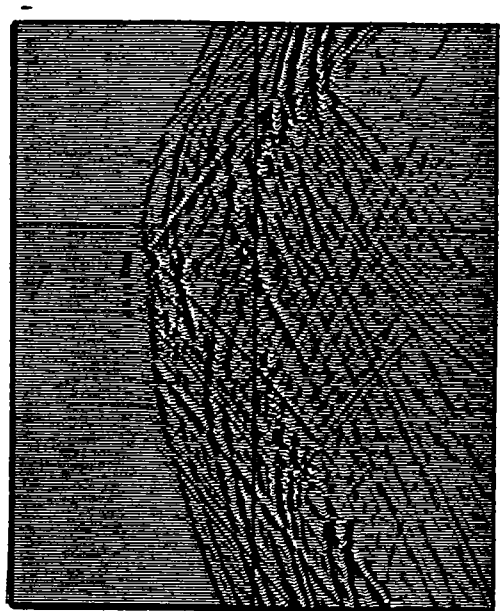

Figure 11) P and S wave conversions only. This wavefield is the difference of figure 10 and figure 6.

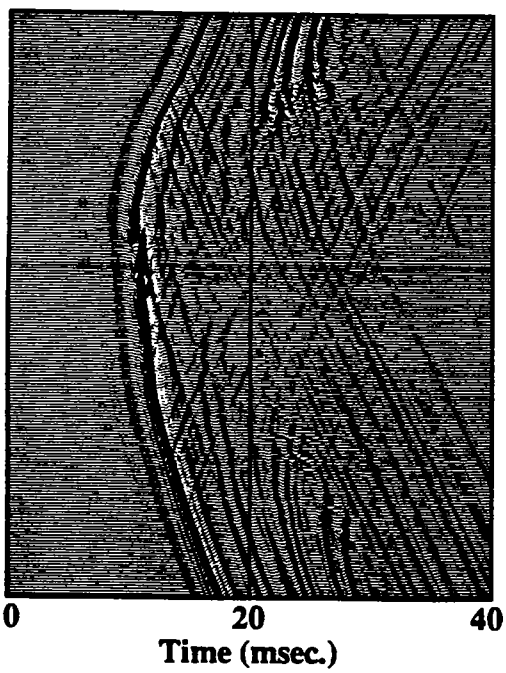

Figure 12) Primary arrivals + conversions calculated with a horizontal point force as the source and the isotropic stress components as receivers.

Figure 13) P-wave conversions only. This wavefield is the difference of figure 12 and figure 7.

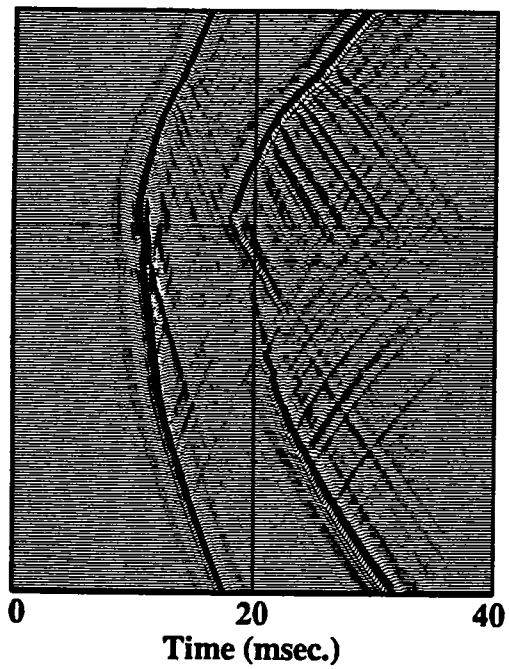

Figure 14) Primary arrivals + multiples calculated with a horizontal point force as the source and the radial stress component as receivers.

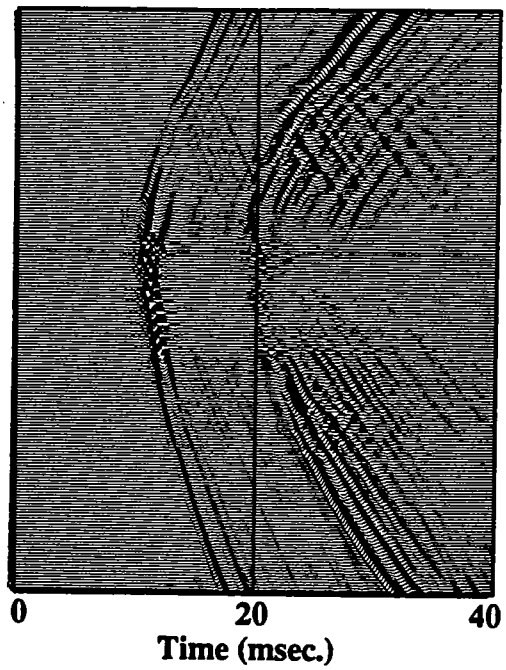

Figure 15) P and S wave multiples only. This wavefield is the difference of figure 14 and figure 6.

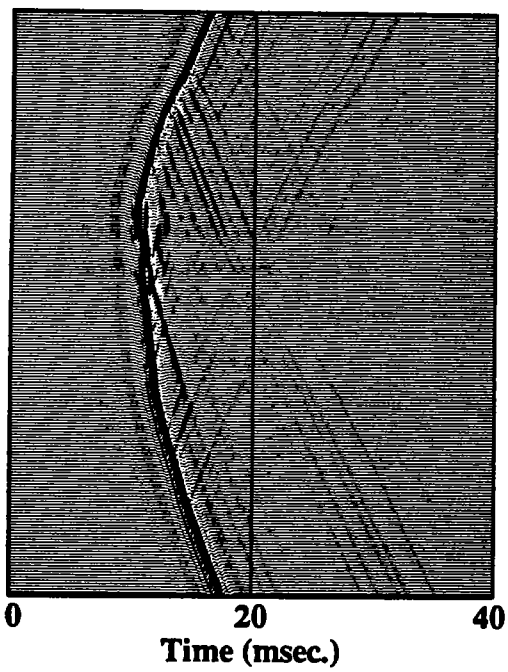

Figure 16) Primary arrivals + multiples calculated with a horizontal point force as the source and the isotropic stress components as receivers.

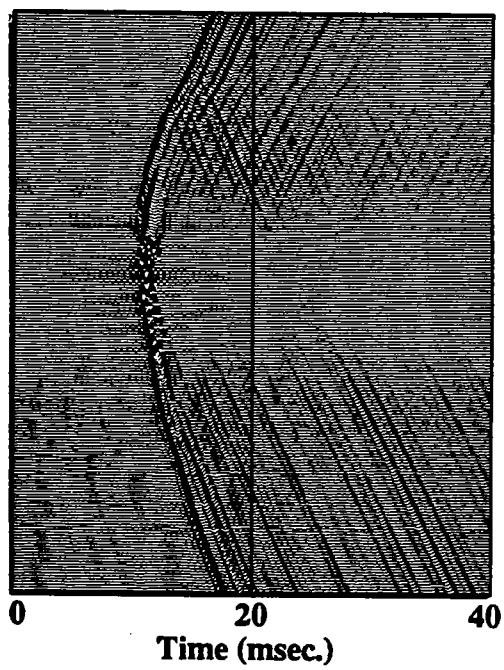

Figure 17) P-wave multiples only. This wavefield is the difference of figure 16 and figure 7.

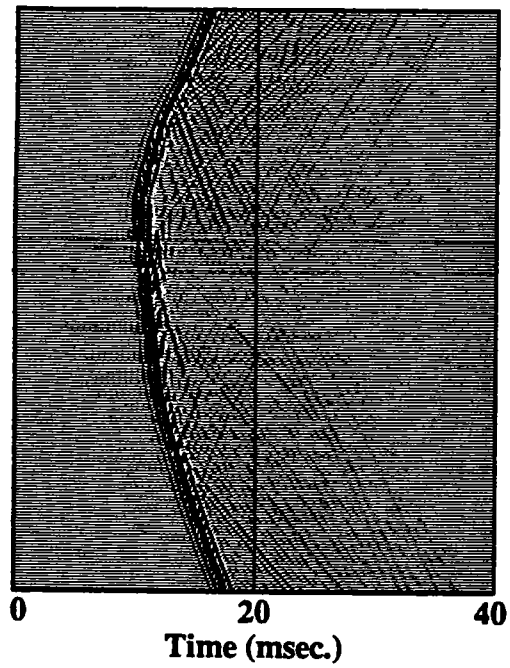

Figure 18) Primary arrivals + conversions calculated with an explosive source and the radial stress component as receivers.

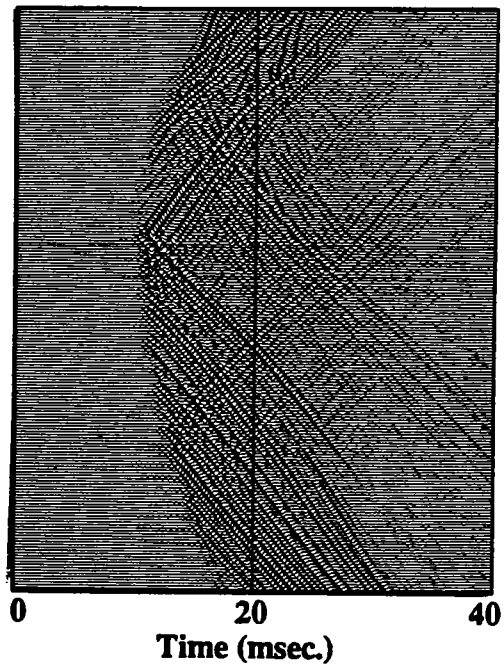

Figure 17) P and S wave conversions only. This wavefield is the difference of figure 18 and figure 8.

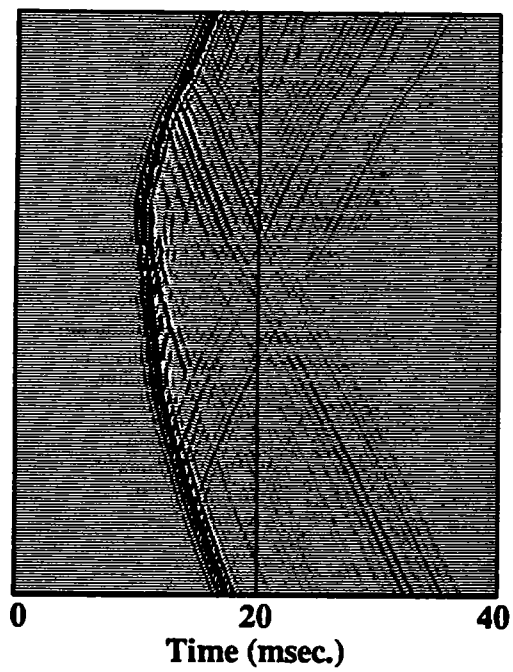

Figure 20) Primary arrivals + conversions calculated with an explosive source and the isotropic stress components as receivers.

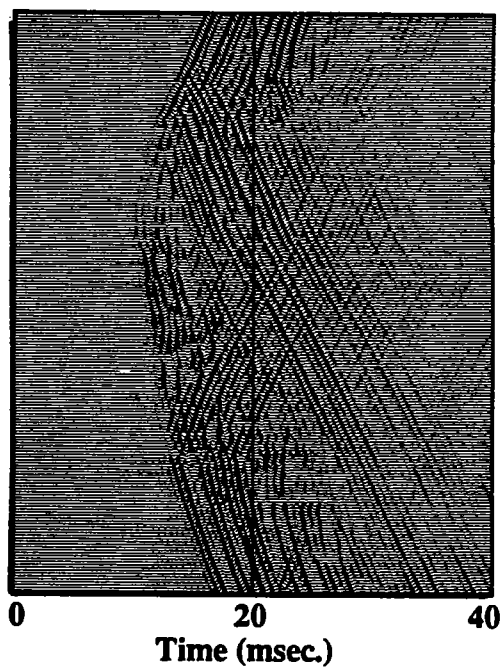

Figure 21) P-wave conversions only. This wavefield is the difference of figure 20 and figure 9.

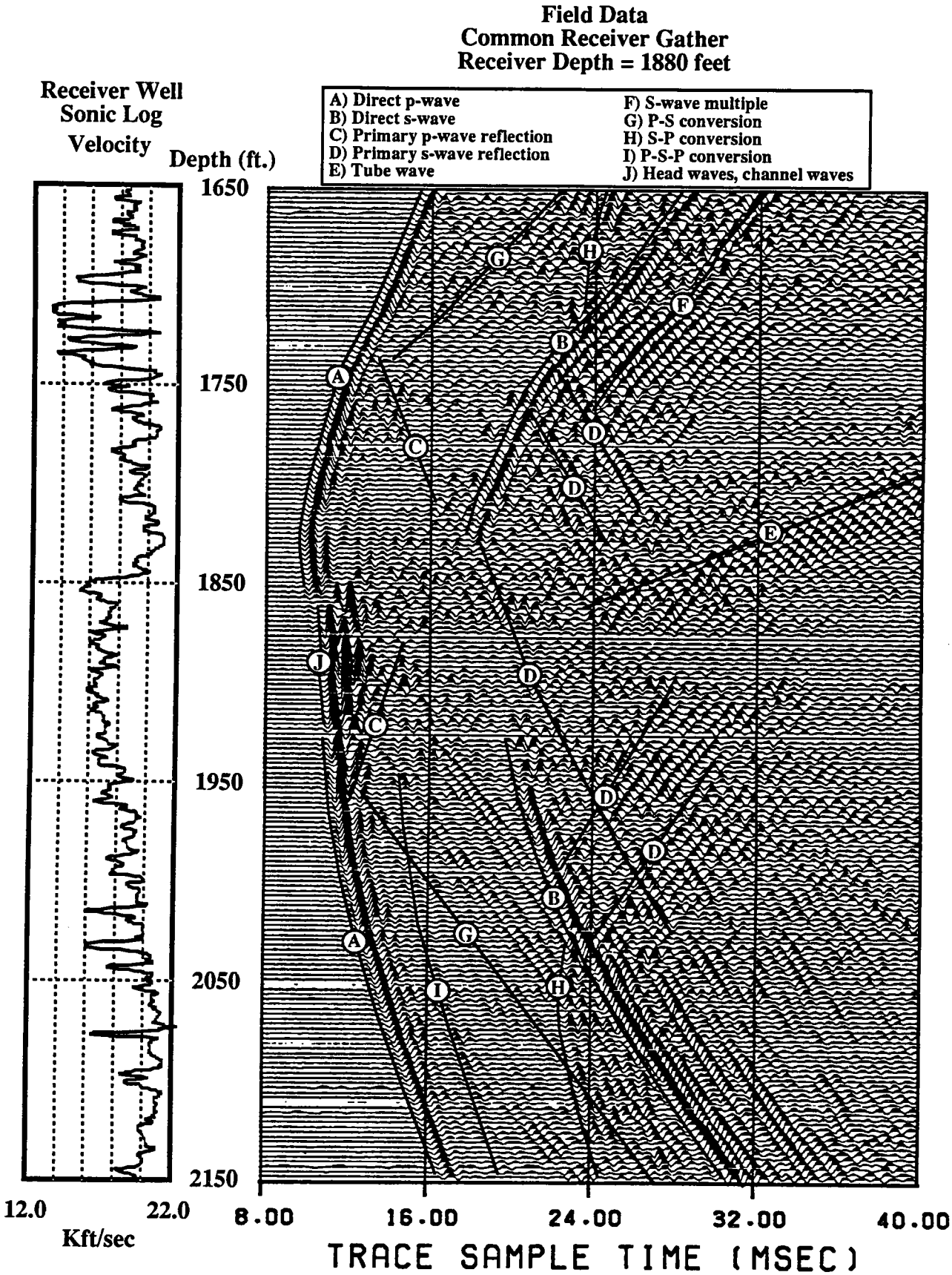

Figure 22) This figure is an interpretation of some of the many wave modes present in the common receiver gather shown in figure 1.

REFERENCES

Apsel, R.J., 1979, Dynamic Green's Functions for Layered Media and Application to Boundary-Value Problems, Ph.D. Thesis, University of California at San Diego.

Heelan, P., 1953b, Radiation from a Cylindical Source of a Finite Length, *Geophysics, 18,* 685-696, 1953b

Harris, J.M., 1992, High Resolution Imaging of a West Texas Carbonate Reservoir: Part 1 - Project Overview, and Data Acquisition, STP-3, paper A.

Lazaratos, S.K., Rector, J.W., Harris, J.M., Van Schaack, M.A., 1992, High Resolution Imaging of a West Texas Carbonate Reservoir: Part 5 - Reflection Imaging STP-3, paper E.

Rector, J.W., Lazaratos, S.K., Harris, J.M., Van Schaack, M.A., 1992, High Resolution Imaging of a West Texas Carbonate Reservoir: Part 4 - Pre-Processing and Wavefield Separation, STP-3, paper D.

Van Schaack, M.A., Harris, J.M., Lazaratos, S.K., Rector, J.W., 1992, High Resolution Imaging of a West Texas Carbonate Reservoir: Part 3 - Tomography STP-3, paper C.

PAPER C

HIGH RESOLUTION CROSS-WELL IMAGING OF A WEST TEXAS CARBONATE RESERVOIR

Part 3 – Traveltime Tomography

Mark Van Schaack, Jerry Harris, James Rector III#, and Spyros Lazaratos
Seismic Tomography Project

ABSTRACT

We have collected two crosswell seismic datasets of nearly 40,000 traces each in a West Texas carbonate oilfield. In this paper we discuss the tomographic processing of the first survey. In this survey, data were collected at 2.5 foot intervals in both the source and receiver wells. The surveyed zone is about 500 feet in extent with the primary target being the approximately 100 foot thick Permian-aged Grayburg formation. The offset between the two wells is nominally 184 feet. We collected the crosswell data using the technique of "shooting on the fly" where data is collected at constant intervals as the source is "logged" over the surveyed zone.

The cylindrical piezoelectric bender source provided ample signal strength and high quality data were collected with a very good signal to noise ratio containing frequencies from 250-2000 Hertz. Wavefield analysis of field data has shown that the surveyed zone can be approximated fairly well with a 1-D velocity model (Van Schaack et al, 1992). Using this 1-D model and a simplistic approximation for the source and receiver we created a synthetic dataset paralleling our field data. This synthetic dataset is used as a guide to optimize our tomographic inversion processing stream. The ability to refine our processing stream using feedback from the inversion of the synthetic survey in combination with quality field data has made possible a very low residual velocity tomogram. The tomogram converges with a traveltime residual of less than 100us and ties very well with the velocities of the sonic well logs in the vicinity of the borehole. The resolution is good and a response from a number of 10-20 foot thick beds can be seen in this comparison.

Now with the University of California, Berkeley

INTRODUCTION

Traveltime tomography has been in use as a tool for imaging velocity structure between wells for a number of years now. Great strides have been made in the development of inversion algorithms as is evident by the great number of techniques now being used. Despite this, many times differences between well log and tomogram velocities, and/or structures within the tomogram, are inexplicable in light of the known geology. This is because the ability of traveltime tomography to accurately image velocities is adversely affected by a number of factors.

Some of the many factors which can lead to poor tomographic results are limited spectral bandwidth, dispersion, attenuation, measurement errors, and velocity anisotropy. Some of these factors are, unfortunately, a result of the experimental setup itself while others, such as velocity anisotropy, could be handled by more sophisticated inversion algorithms. Work being done to incorporate anisotropy into the inversion process has shown promise (Michelena, 1992). Another important consideration in crosswell tomography is the development of a processing scheme well suited to the data to be inverted. In many cases the inversion process can be drastically improved through the use of synthetic modeling to guide the picking and processing of the field data.

In this paper we discuss the tomographic results of our crosswell experiment. In this experiment, special attention to depth control and other acquisition parameters was emphasized to meet the requirements of both crosswell reflection imaging and traveltime tomography (see Harris et al, 1992, for full experiment and site description). As the lithology of the surveyed zone is known to be largely isotropic, we expect a good tie between the sonic well log velocities and the tomography velocities near the well. We find after processing that we do get a very good tie with the well logs and that a number of thin beds are imaged by the tomogram.

FIELD DATA

The crosswell data were collected at a producing carbonate field in West Texas. Two cased boreholes, one a producing well and the other a CO2 monitoring well, were used for this survey. Figure 1 illustrates the geometry of the acquisition. Source coverage extends over 500 feet. Due to hardware problems and time constraints the receiver well coverage is slightly less. The nominal separation of the two wells is approximately 184 feet.

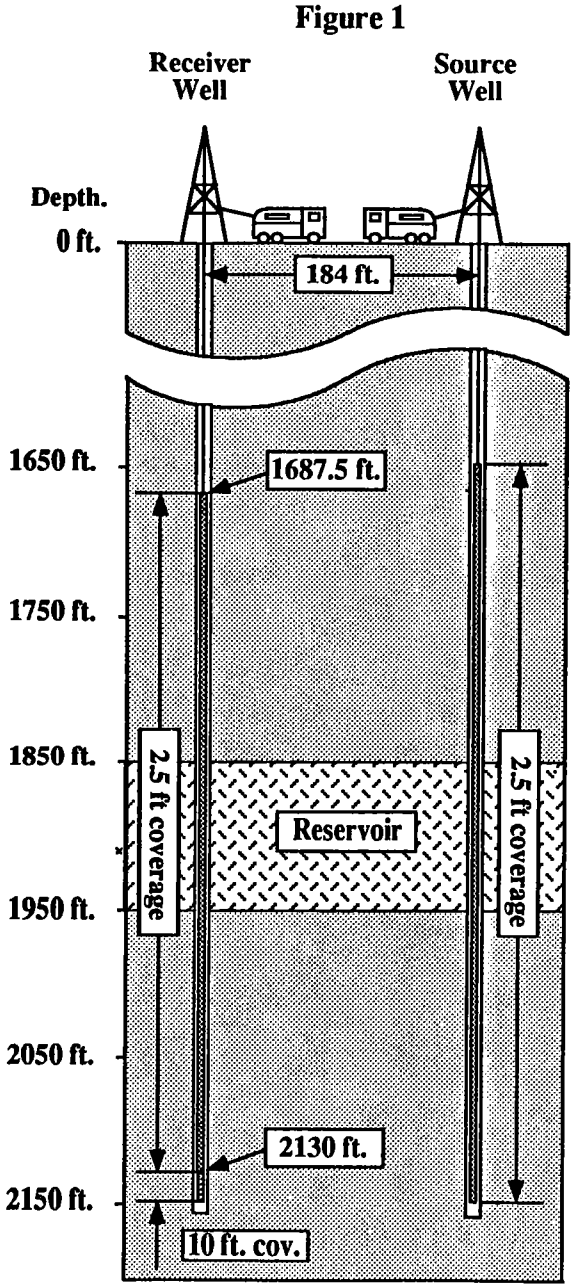

Figure 1. Schematic view of crosswell field acquisition geometry. Note the receiver well coverage is slightly different than the source well coverage.

Figure 2. Typical receiver gather from the field survey. The receiver depth is 1880 feet in this gather. The source depths range from 2150-1650 feet. Individual trace gain used.

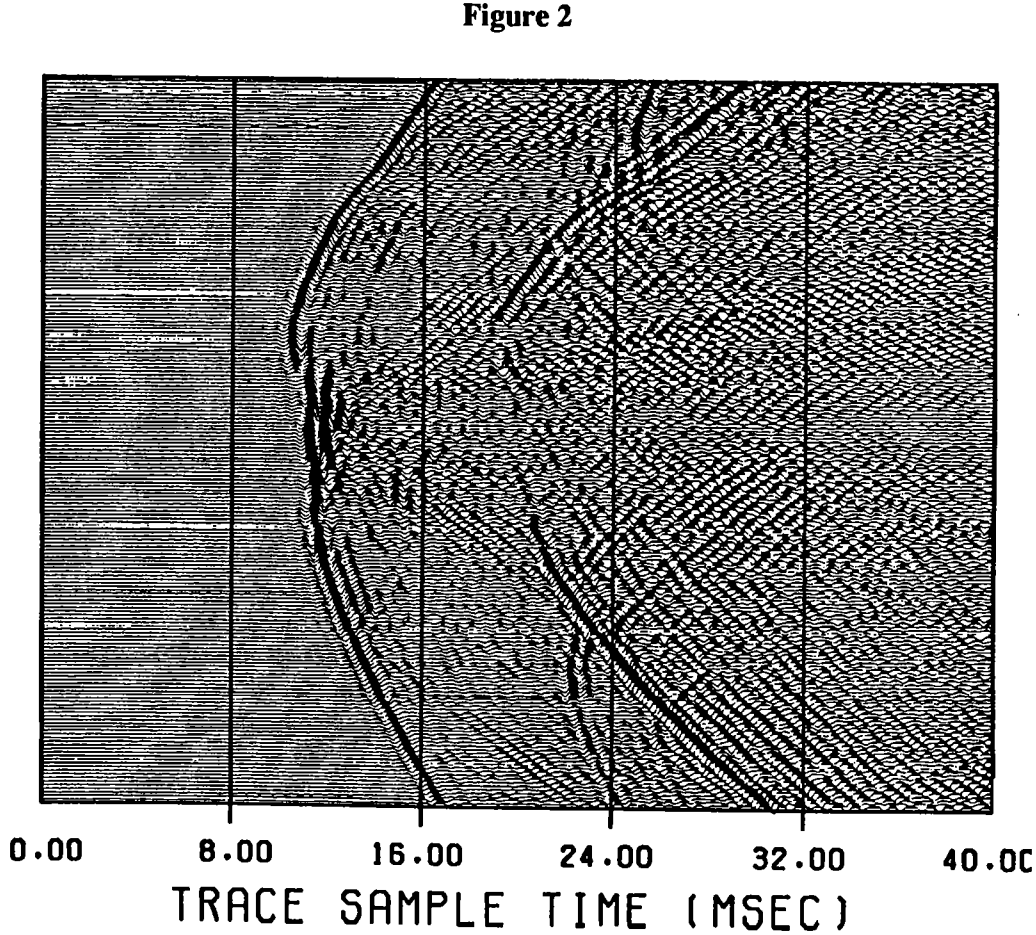

The data were acquired using a cylindrical piezoelectric bender source swept from 250-2000 Hertz over 200ms. This source is well suited to the deep hard rock conditions encountered in this survey and provided high signal to noise level data (figure 2) containing frequencies over the entire 250-2000 Hertz bandwidth. The receiver string consisted of 5-7 OAS deep ocean hydrophones.

For this survey we used the technique of "shooting on the fly". When "shooting on the fly" data are collected as fans of receiver gathers. For each group of receiver fans the receiver string is positioned in the hole and set up for acquisition. The source is then "logged" up the well. As the source moves continuously up the well it receives a trigger pulse from the depth system. For our survey a 2.5 foot shot interval was used. The trigger consists of a variable number of sweeps separated by a short listening time. Although the source is not stopped for these shots the smear effect was less than 2 inches for the two sweeps and winch rate used in our acquisition. One advantage of this technique is that the relative depth interval of the source is very regular due to its' constant movement under steady tension. Following the completion of the source run the receivers are repositioned and the same process is repeated. Additional details regarding the acquisition parameters, and hardware can be found in Harris (1992).

Following data editing and the definition of the wellbore geometries, first break p-wave traveltimes were picked from the field data. Although hand picking nearly 40,000 traces may seem a daunting task, first pass picking was accomplished in one 3 hour session. The general philosophy for this first cut picking was to pick on first arriving energy without trying to decipher direct arrivals from headwaves and the other various modes. The primarily flat, laterally homogeneous, nature of the surveyed zone can be easily interpreted, even before inversion, from the travel time picks (figure 3). In the pick map this 1-D nature manifests itself as symmetry about the zero offset diagonal (source depth = receiver depth). For comparison see figure 4 which is the pick map from a 1-D synthetic survey modeled after the field survey.

CROSSWELL SIMULATION

The purpose of our crosswell simulation is to aid us in the development of an optimal processing scheme for our field data. Analysis of the crosswell field data (Van Schaack et al, 1992) has revealed that the surveyed zone can be approximated quite well using a simple 1-D velocity model. We take the approach that a processing scheme is more easily developed using synthetic data. Parameters can be adjusted to maximize resolution and

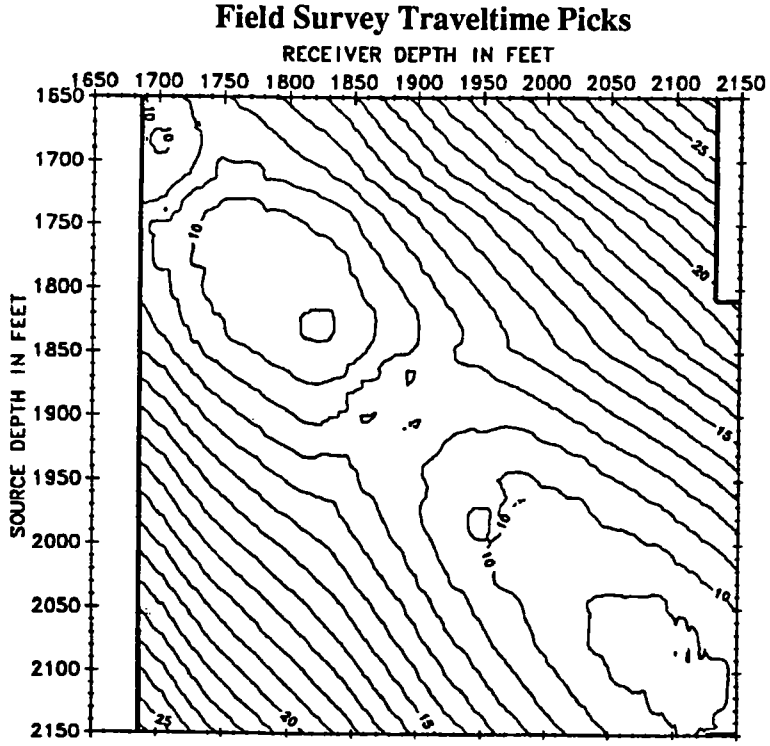

Figure 3) Field data pick map. Note the symmetrical nature of the picks about the axis where receiver depth equals source depth. This is indicative of the 1-D nature of the velocity structure over the surveyed zone.

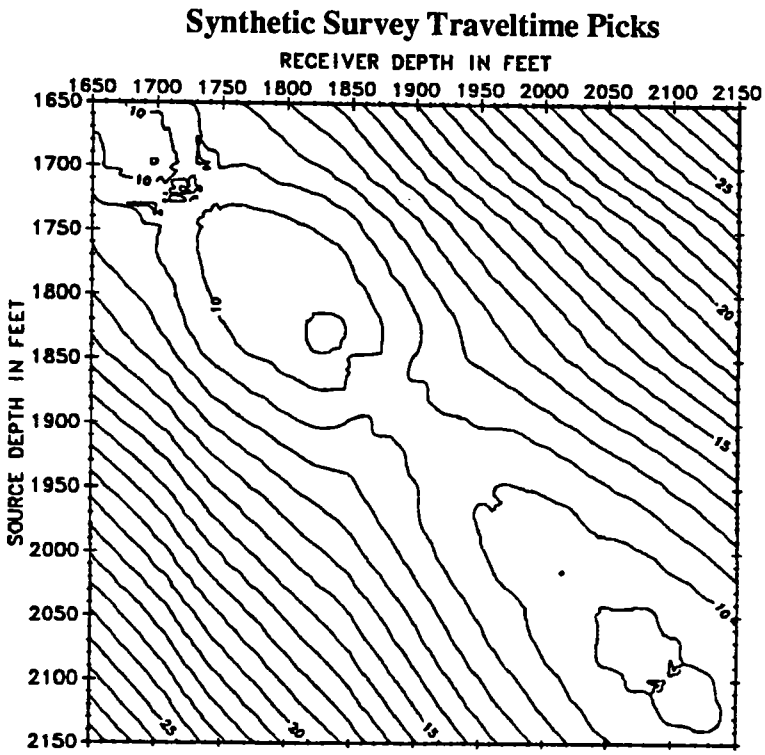

Figure 4) Synthetic data pick map. This provides a 1-D comparison for figure 3. The data here is picked using the peak amplitude of the first arriving energy.

minimize artifacts in an objective fashion since these criteria can be measured directly. If the velocity structure of the simulation is similar to the true velocity structure the optimized processing scheme should prove ideal to invert the field data. In addition the synthetic tomogram can provide a guide in interpretation of the field tomogram.

The velocity model used in our simulation was created using a finely blocked sonic well log from the receiver well of our field survey. As with the our wavefield modeling, the source and hydrophone receivers were simulated using a radial point force and radial (horizontal) stress respectively. Field parameters were used wherever possible in the simulation. The source and receiver increment of our simulation is 2.5 feet, as with the field survey, Since well deviations in our field survey were quite moderate straight wellbores, 184 feet apart, were used to approximate the field geometry (figure 5).

Although this simulation was certainly simpler than the collection of the field data it took nearly 15 times longer to do (approximately 30 computer-days). For the purpose of expediency and simplicity the most basic calculations were performed. Our modeling program allows the separate calculation of a number of different wave modes. We simplified the calculated wavefield and sped up computation time by ignoring conversions and multiples. The simulated wavefield data include only direct p and s-waves, head waves and primary reflections (figure 6).

To further reduce calculation time a frequency bandwidth of 200-1250 Hertz was used instead of the 250-2000 Hertz bandwidth used in the field. Over 40,000 traces were calculated making the coverage almost identical to our field survey. Picking of the synthetic data was done in the same fashion as with the field data.

OPTIMIZATION OF INVERSION PARAMETERS

Traveltime picks were inverted using the STRINGS inversion code (Harris et al, 1990). This algorithm is an iterative method. Algebraic reconstruction techniques are powerful and effective. In fact, with the computing power at our disposal and our large datasets, they are crucial.

In a STRINGS inversion traveltimes calculated through a starting model are compared to measured traveltimes. Residuals are computed through the difference in these two traveltimes to calculate a correction to the starting model. The model is then updated and used as the starting model for the next iteration. This process is carried on through subsequent iterations until the residual reaches an acceptable level. Parameterization of the starting model, bin size, pixelation, smoothing, number of rays, number of backprojections, maximum aperture and the differential ray length have the largest effect on both whether the

Figure 5

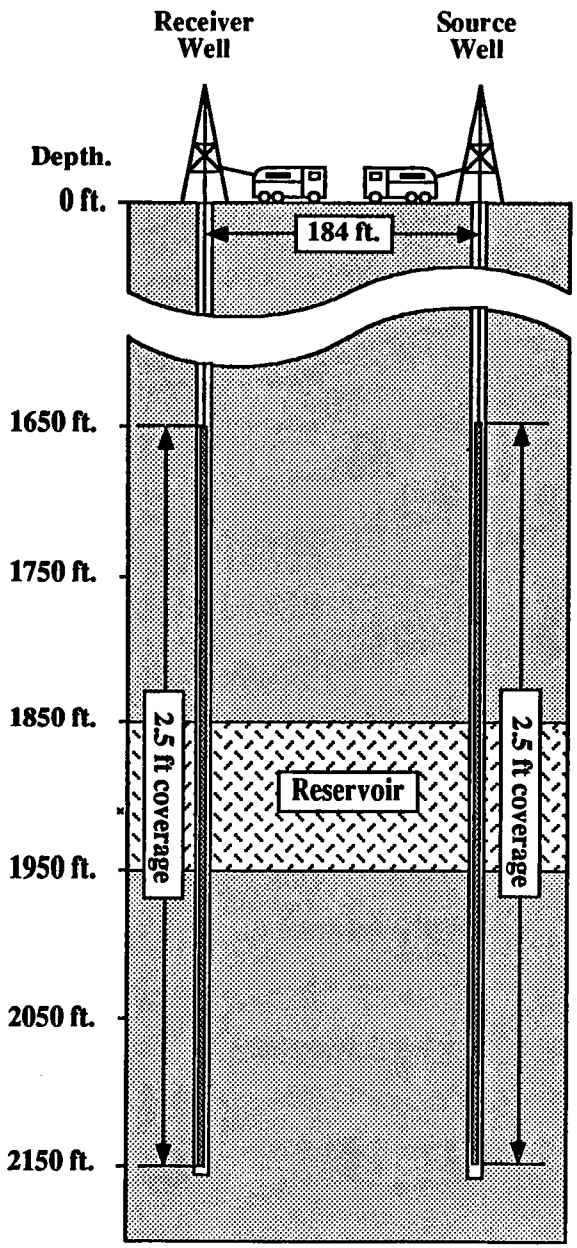

Figure 5. Schematic view of crosswell simulation geometry. The geometry is identical to the field survey with the exception that the receiver well coverage is now the same as the source well coverage.

Figure 6. A common receiver gather crosswell simulation. The receiver depth is 1880 feet in this gather. The source depth range from 2150-1650 feet. Individual trace gain used.

Figure 6

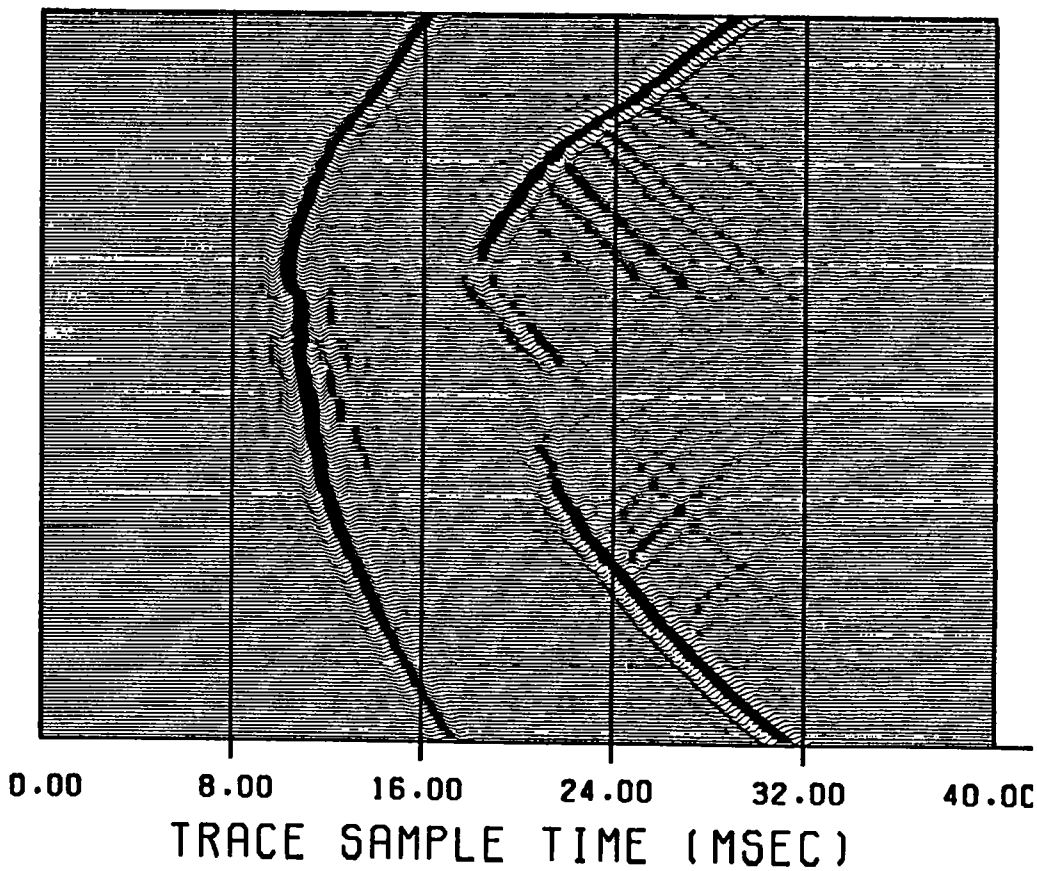

inversion converges to an acceptable residual and the speed at which it does converge. There are a number of other parameters in STRINGS primarily used in the identification and rejection of dubious data that also can have a large effect on the quality of the inversion.

Initial Iterations

Reasonable values can be estimated for many of the above parameters based on the survey geometry. We have developed a number of rules of thumb which work reliably on the simpler synthetics we test our inversion routines on. Due to the non-linear nature of the tomographic inversion problem some parameters are best estimated through trial and error. Unfortunately, parameters that are ideal for one survey geometry and geology may not be so good for another. It is these parameters that we estimate using our synthetic dataset.

The basic philosophy in our processing flow is to calculate a rough velocity model based on the known geometry then to use this as a starting model for our final iterations. The 1-D nature of our synthetic dataset and field data suggests we initially use the STRINGS code to calculate a 1-D solution. This is can be done easily by adjusting the bin size and smoothing parameters. The first 3 iterations of our processing flow are parameterized to calculate a 1-D solution to our dataset. Following these calculations the bin size and smoothing parameters are slowly reduced until by the 6 iteration the final bin and smoothing parameters are reached. The inversion is then run until convergence. Figure 7 shows the rate of convergence for several different inversions run on our synthetic dataset.

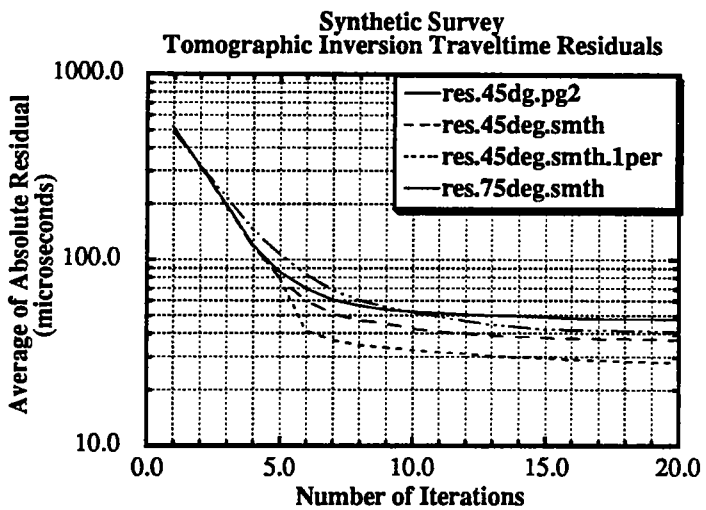

Figure 7) Travel time residual versus iteration number for several of the processing flows studied

These different processing flows can all be seen to reach a stable residual error after about 15 iterations.

Advantages of Traveltime Pick Smoothing

A large degree of experimentation was performed using these data. The results of four processing streams illustrate several important points. The most important part of any inversion, of course, is the data. We noted while picking the synthetic data that peak amplitudes did not move out smoothly. The moveout is affected by interfering direct and reflected arrivals giving the pick moveout a staircase-like appearance. We found after convergence of our tomographic inversion this moveout was very faithfully matched when synthetic times were displayed over picked data. Our inversion routine is not designed to take into account such wave phenomena as phase interference. This suggested that the source of some of the 2-D artifacts we were seeing in the inversion of the synthetic data might be a result of the adjustment of the velocity model to reproduce the staircased picks.

To study the effect of the irregular picks on the tomographic image we ran an identical inversion with the traveltime picks smoothed over a 10 foot window in both CSG and CRG space using a 2-D Hanning filter. The convergence of this second inversion can be compared to the first in figure 7. The curve res45dg.pg2 documents the convergence of the inversion using the unsmoothed picks. Curve res.45deg.smth documents the convergence of the second inversion using the identical processing flow but with smoothed picks. We can see the average residual using the smoothed picks is nearly 15 percent better after 20 iterations.

A second surprising benefit of smoothing the traveltime picks is that in some areas the resolution of the tomographic has actually been improved! This is can be seen in figures 8 and 9. Figure 8 shows a 10 foot smoothed version of the input 1-D velocity model (pvel.blocked (21 pt smooth)) and three vertical slices from the velocity tomogram. 45deg.1 corresponds to the tomogram velocity at the receiver well. 45deg.184 corresponds to the tomogram velocity at the source well. 45deg.92 corresponds to a slice of the tomogram taken right down the middle. Nomenclature for figure 9 follows the same logic. The tomographic inversion using the smoothed pick data actually comes much closer to matching the velocity of the slow layer at ~1720 feet. Over the rest of the image the velocities are fairly well matched except the very top and bottom where the velocities are affected by artifacts.

Some Effects of Inversion Pick Rejection

A second important inversion parameter is what we call the "bounds". This parameter is set to avoid incorporating raypath traveltimes outside a certain window of what is expected. Setting the bounds at 5% eliminates rays shot in the inversion whose calculated traveltimes fall outside of a 5% window of the field measured traveltimes. This is a particularly useful feature in the STRINGS program since source-receiver raypath linking is not used. This helps reject raypaths who may have taken indirect paths, such as guided rays and reflected rays. The processing flow used in figures 9 and 10 allows a very loose value for the bounds of 25% for the first 5 iterations and a tighter 5% for the remaining iterations. This is done so that not too many rays are rejected in the early phase of the inversion when primarily a 1-D model is being calculated.

A comparison of figures 9 and 10 illustrates the effect of setting the bounds too tight. Both inversions use smoothed traveltime picks but the resolution seen in the tomogram velocities of figure 10 is similar to that seen in figure 8. The same low velocity bed at 1720 feet provides a good indicator of the resolution. At most other depths the resolutions of the different flows appear more alike.

Effects of Aperture

The previous inversions were run with a maximum allowed aperture of +/- 45 degrees. One advantage in using less of the far offset data is that the effects of mild anisotropy can be minimized. Also, there will exist a larger vertical zone in the middle of the survey with uniform ray coverage. Our experience is that a large number of artifacts are due to change raypath coverage. For this reason we interpolate missing data if necessary. Techniques being developed to extrapolate data to minimize inversion problems near the top and bottom edges of the tomogram show promise.

Figure 11 describes the results of increasing the maximum aperture. The maximum straight line ray angle for our synthetic survey is about 70 degrees. We set the maximum a little higher, 75 degrees, to account for the possibility of bending rays. A maximum coverage of +/- 75 degrees insures that virtually all the data can be used. A comparison of figure 11 to its low angle related inversion, figure 9, shows a mild decrease in resolution as seen by the 1720 foot slow bed. One benefit of using the higher angles is that the velocities in the middle of the tomogram, curve 75deg.smth.92, lie much closer to the model velocities

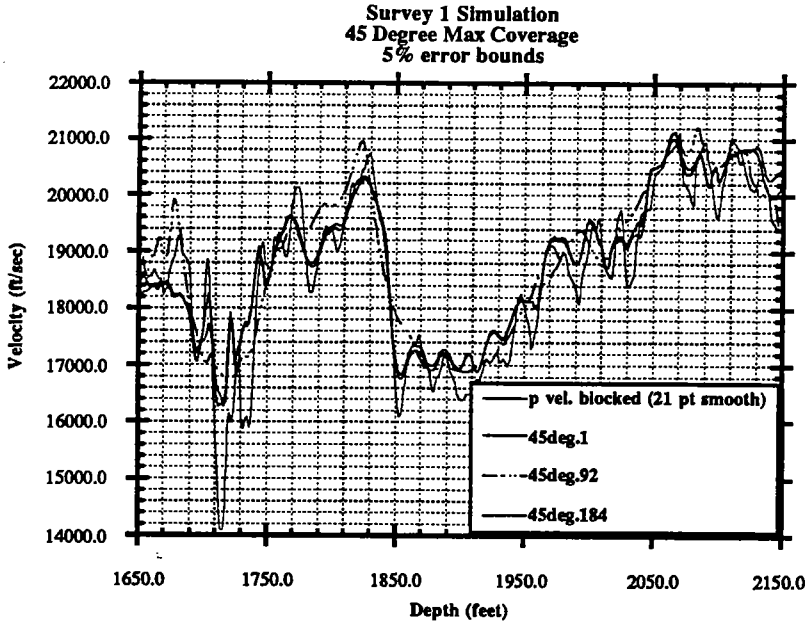

Figure 8) The above plot shows a 10 ft. smoothed version of the blocked 1-D velocity model used to create the synthetic survey, p vel. blocked. The remaining three curves are slices of the velocity tomogram at the receiver well, the source well and the halfway point; curves 45deg.1, 45deg.184, and 45deg.92 respectively. Angular coverage is limited to +/- 45 degrees and the ray rejection bounds is set at 5% of the measured traveltime. Fifteen iterations were run in this inversion.

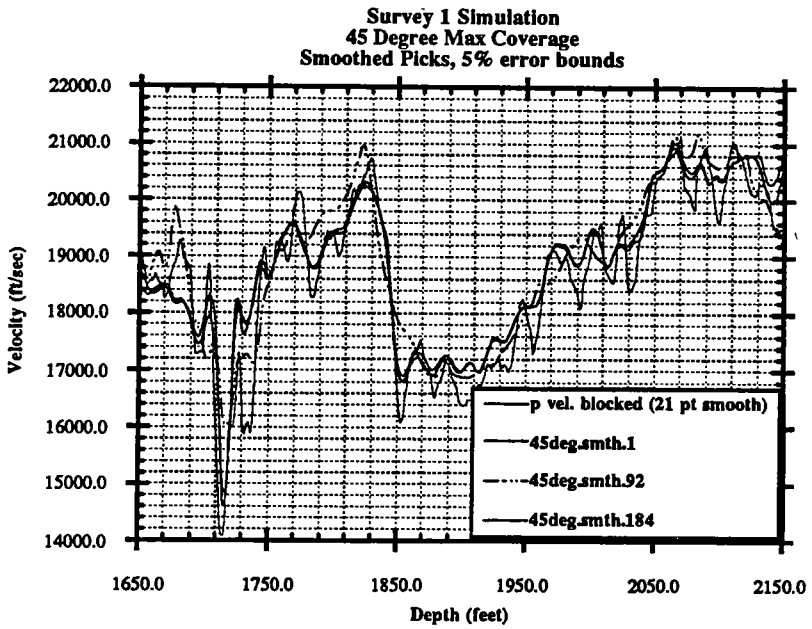

Figure 9) The above plot shows the same comparison as figure 8. The processing is identical except the inversion was performed using traveltime pick data smoothed in shot and receiver space with a 5 point 2-D Hanning filter. Note the increase in resolution at 1720 feet.

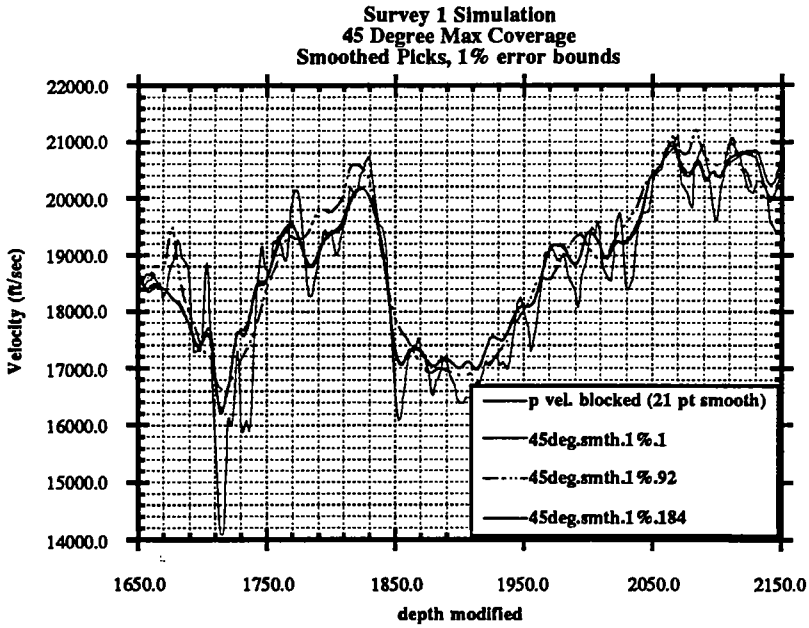

Figure 10) The above plot demonstrates a slight loss of resolution when the traveltime error rejection bounds is set too low. This can be seen in the low velocity layer at ~1720 feet. The processing is identical to figure 9 except the bounds has now been set at 1%.

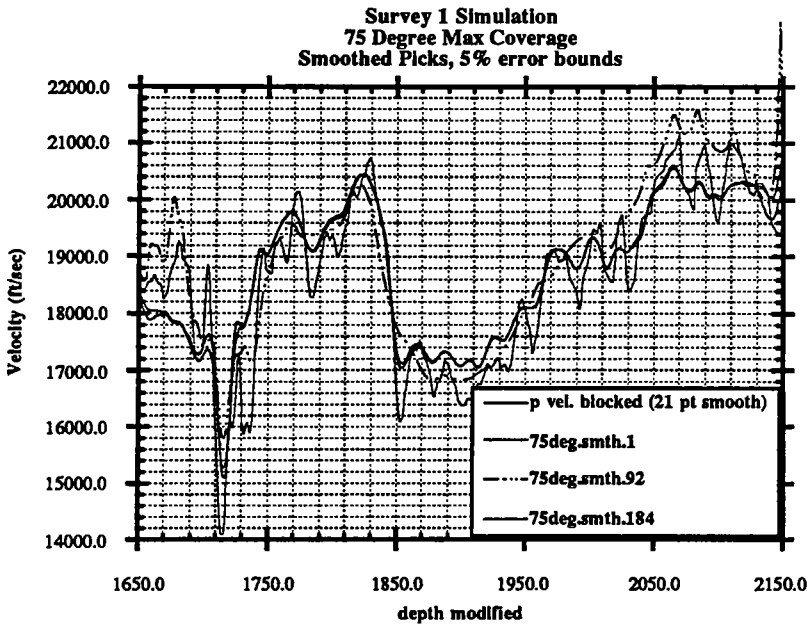

Figure 11) The above plot demonstrates that increased angular coverage can lead to more reliable velocity estimates in the interwell region. Processing parameters are identical to those of figure 9 except the maximum allowed angular ray coverage is now set at +/- 75 degrees. Note that artifacts have increase near the top and bottom edges of the image

and the tomogram velocities at the edge of the image. In particular an improvement can be seen between 1800 and 1850 feet. As expected, artifacts near the edge of the tomogram are worse using increased aperture. If the zone of interest is sufficiently near the middle of the survey, as it is in our field survey, the increased resolution should be worth the price of the edge effects.

INVERSION OF THE FIELD DATA

Application of the inversion routines designed using the synthetic survey resulted in velocity images that tied well with the sonic logs. As might be expected, the inversion of the real data resulted in some artifacts not predicted by the synthetic inversions. In particular, the processing flow using +/- 75 degree coverage, that produced the best results in the inversion of the synthetic data, produced an image with high angle artifacts from our field data. These artifacts tend to dominate the more subtle features in the reservoir section that we are most interested in imaging.

Figure 12 shows the result of our best inversion. This inversion was made using smoothed traveltime picks, a +/- 45 degree aperture of coverage, and a 1% error rejection bounds. The average magnitude of the traveltime residual for this result is approximately 30 microseconds for the over 28,000 rays used in each backprojection. Figures 13a & b illustrate the tie of the tomogram velocities in the near well region to the local sonic logs. The accuracy with which the velocities have been matched parallels the equivalent synthetic inversion, figure 10. The resolution seems very nearly equal in these two inversions which suggests our data collection errors must be of a low magnitude.

Figure 14 shows the results of our synthetic inversion. This velocity image was created using the identical processing stream as that used to invert the field data, figure 12. This synthetic image provides us a basis with which to interpret our field tomogram. The synthetic tomogram shows relatively few artifacts of large magnitude. In particular, artifacts seen in the reservoir region are the result of velocity variations of only about 1%. The tie of the field survey to the smoothed well logs in the reservoir zone is also around 1%. This gives us the confidence to interpret larger perturbations to the velocity field as being the result of true velocity variations. Several low velocity structures between 1875 and 1925 feet suggest heterogeneities within the reservoir present even within the relatively small area surveyed.

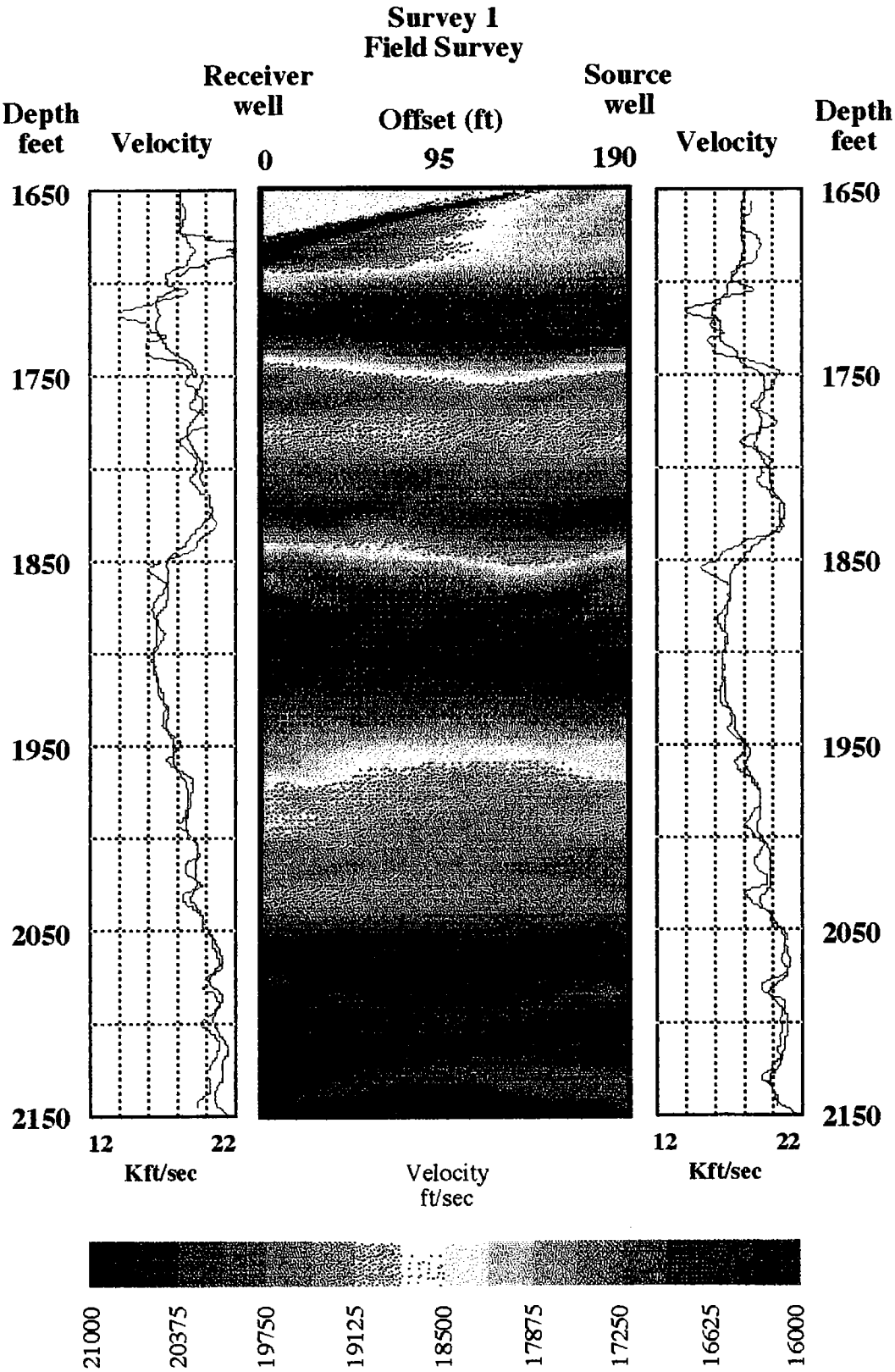

Figure 12) Inversion results of West Texas field data. Velocity curves included are 10 foot smoothed sonic logs (black) and tomogram velocities 5 feet inside image. This inversion was run 15 iterations and has an average absolute traveltime residual of ~35 microseconds.

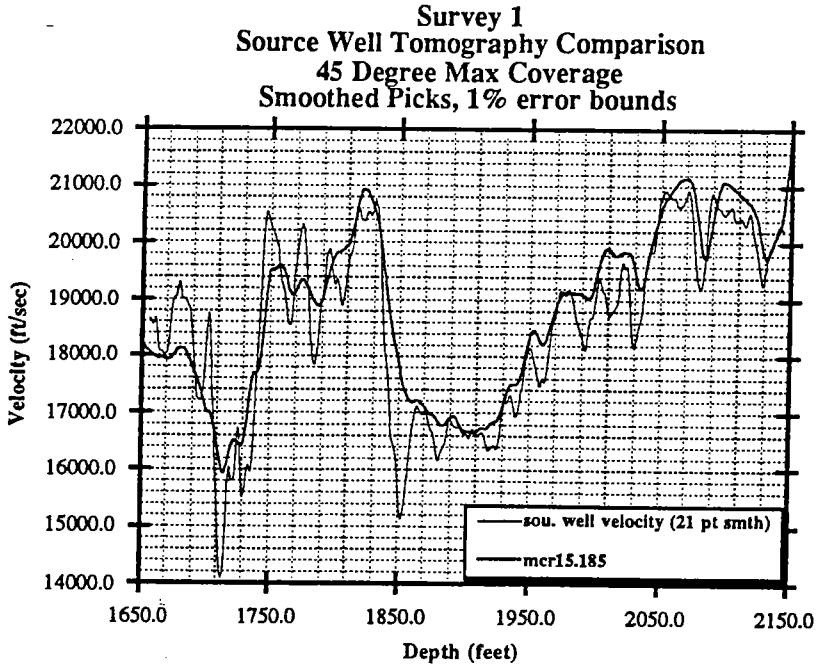

Figure 13a) This figure shows the results of a 15 iteration inversion of the field data. The thin solid line is a 10 foot smoothed version of the source well sonic log. The thick line displays a vertical slice of the tomogram image taken 5 feet inside the boundary on the source well side

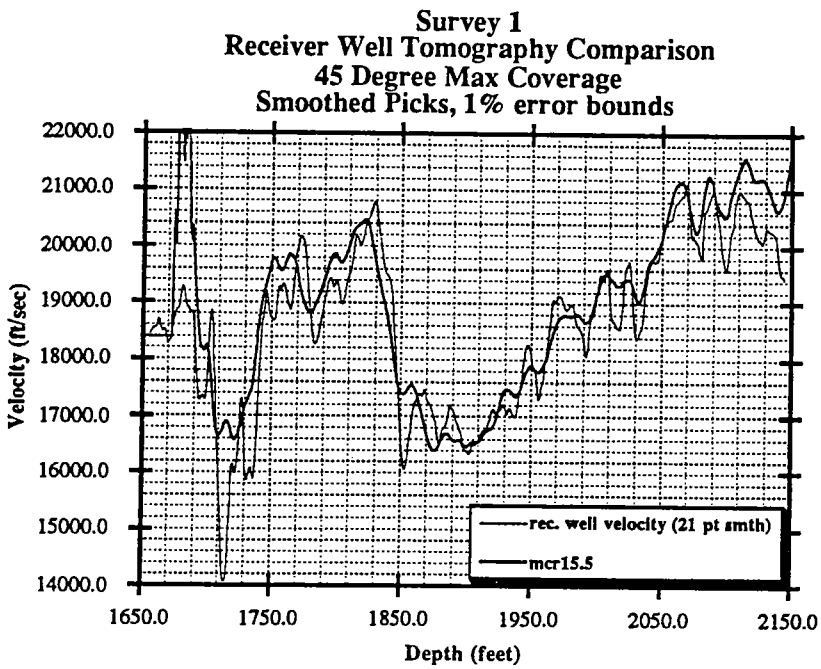

Figure 13b) This figure shows the results of a 15 iteration inversion of the field data. The thin solid line is a 10 foot smoothed version of the receiver well sonic log. The thick line displays a vertical slice of the tomogram image taken 5 feet inside the boundary on the receiver well side.

REFERENCES

Harris, J.M., Lazaratos, S.K., Michelena, R.J., 1990, Tomographic String Inversion, STP-1, paper B.

Harris, J.M., 1992, High Resolution Imaging of a West Texas Carbonate Reservoir: Part 1 - Project Overview, and Data Acquisition, STP-3, paper A.

Lazaratos, S.K., Rector, J.W., Harris, J.M., Van Schaack, M.A., 1992, High Resolution Imaging of a West Texas Carbonate Reservoir: Part 5 - Reflection Imaging STP-3, paper E.

Michelena, R.J., 1992, Traveltime Tomography in Azimuthally Anisotropic Media, STP–3, paper G.

Rector, J.W., Lazaratos, S.K., Harris, J.M., Van Schaack, M.A., 1992, High Resolution Imaging of a West Texas Carbonate Reservoir: Part 4 - Pre-Processing and Wavefield Separation, STP-3, paper D.

Van Schaack, M.A., Harris, J.M., Lazaratos, S.K., Rector, J.W., 1992, High Resolution Imaging of a West Texas Carbonate Reservoir: Part 2 - Wavefield Modeling and Analysis, STP-3, paper B.

PAPER D

HIGH RESOLUTION CROSS-WELL IMAGING OF A WEST TEXAS CARBONATE RESERVOIR
Part 4 - Pre-processing, Wavefield Analysis

James W. Rector III#, Spyros K. Lazaratos, Jerry M. Harris, Mark Van Schaack
Seismic Tomography Project

ABSTRACT

A well to well seismic survey was acquired in a West Texas oil field in 1991. This cross-well field experiment was acquired in a manner that permitted P-P and S-S reflection arrivals to be extracted from the complex total wavefield. In this paper and the following one, we discuss the extraction and the imaging of the reflection arrivals for the cross-well seismic data. This paper focuses on the wavefield separation and deconvolution of the data. Although reflections are barely distinguishable in the raw data, through adaptive multichannel filters applied in the domains of common source, receiver and vertical offset, we are able to produce reflection wavefields that are highly continuous, with a minimum amount of Rieber mixing. The techniques used in this work require data volumes and associated data filtering operations that are several orders of magnitude larger than those encountered in conventional VSP data analysis. In many respects, this aspect makes data manipulations more similar to conventional surface seismic processing than to VSP processing. The high quality of the S-S reflections imaged from single component borehole hydrophone data in this experiment may reduce the use of multicomponent sources and receivers for some cross-well applications.

Now with the University of California, Berkeley

INTRODUCTION

Several authors have recently proposed using cross-well reflection arrivals to image the subsurface between two boreholes (Lazaratos et al, 1991 and Stewart and Marchisio, 1991). Well-to-well imaging with reflections holds several advantages over more conventional transmission tomography techniques. First and foremost, reflections provide an image of horizons at and below the well bottom, where the target (i. e. the reservoir) is typically located. Transmission tomography is limited to zones above the well bottom. Figure 1 shows the zone imaged with transmission tomography compared to the zone imaged with reflections for a single common source gather assuming horizontal reflectors in a constant-velocity earth. (A reciprocal common receiver gather would yield a zone of coverage that is mirrored across a vertical line at the midpoint between the two wells.) Note that only the reflection arrivals image a significant horizontal portion of the subsurface near the bottom of the well and below.

This paper is the first of two papers that discuss the reflection image processing performed on cross-well seismic data acquired at a West Texas oil field. The extraction of P-P and S-S reflections through wavefield separation and deconvolution are summarized in this paper. Through adaptive multichannel filtering applied in common source, receiver and offset domains, reflected arrivals can be identified that correspond closely with interfaces inferred from S and P velocity logs.

FULL WAVEFIELD ANALYSIS

The data acquisition parameters for this cross-well seismic data set are discussed in Paper A. In the processing and analysis presented here, we will focus on the survey conducted between wells spaced 175 ft (53m). This survey, was acquired at 2.5 ft (.76 m) source and receiver intervals, substantially finer than the 10 to 20 ft (3 to 6 m) intervals commonly used in cross-well tomography surveys. The depth sampling interval was designed to allow the data to be wavefield separated, extracting reflected arrivals though moveout-based multichannel filters. With coarser sampling intervals, the slower arrivals such as the tube wave and the shear waves are substantially aliased in the frequency range of interest (300 to 2000 Hz).

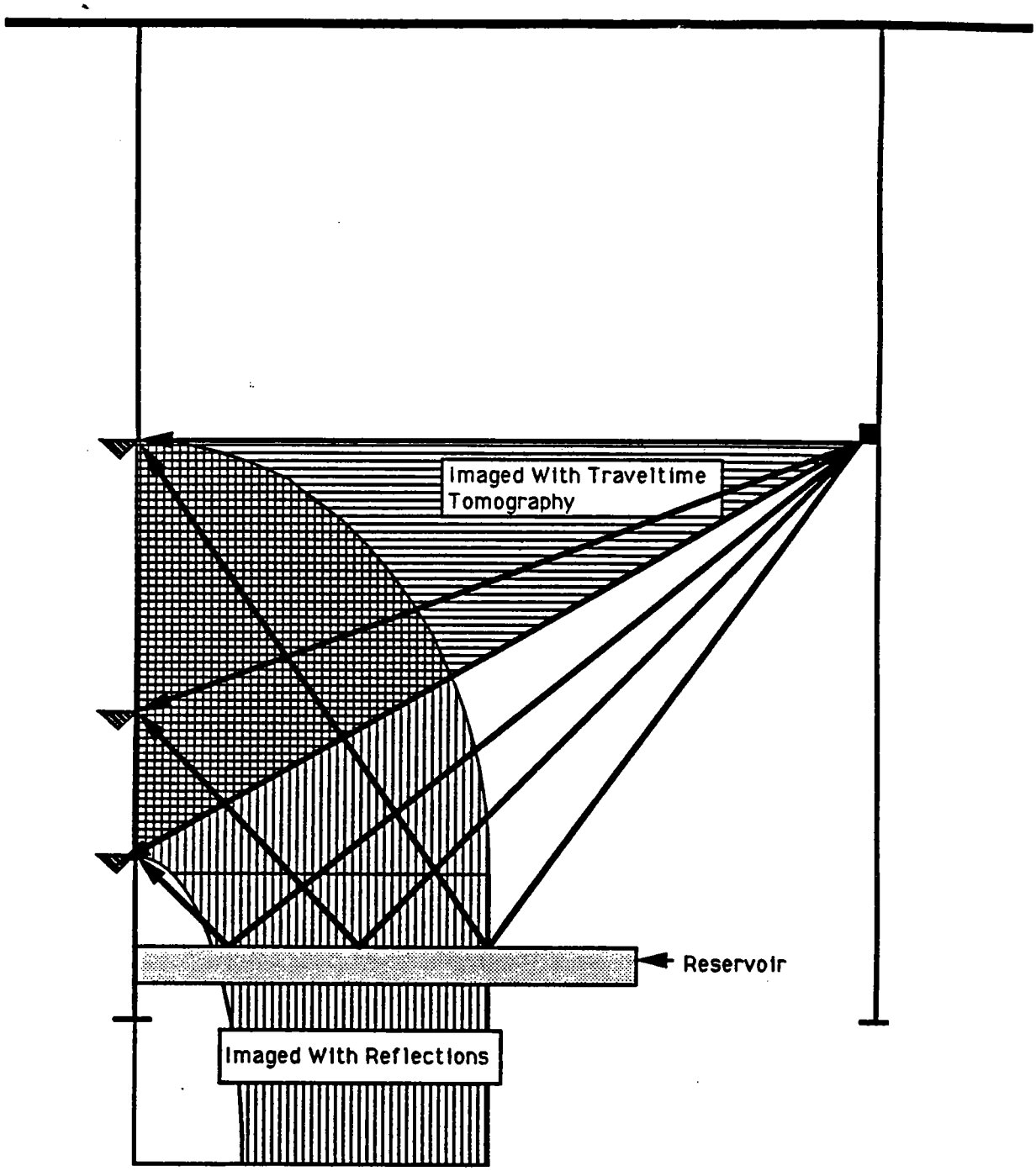

Figure 1: Subsurface region imaged with crosswell traveltime tomography compared with region imaged with crosswell reflections for a single common shot gather.

Figure 2 is a typical common receiver gather. For the data shown in Figure 2, the hydrophone was located at a depth of 1904 ft (581 m), just below the top of the reservoir, and the piezoelectric source depths ranged from 1701 ft to 2101 ft (825 to 947 m). P and S-wave sonic logs from the source well are also shown. The data in Figure 2 are displayed after normalizing each trace to its maximum amplitude. P and S direct and reflected arrivals, down and upgoing P and S reflections, and converted arrivals can all be identified based on their moveout and time delay characteristics (Rector et al, 1992).

The disappearance of the shear wave in the center of the section, at small vertical source/receiver offsets, is consistent with the radiation pattern of the piezoelectric source, which can be modeled like an airgun as a radially-directed force applied to the fluid in the source well. Lee et al (1984) showed that the radiation from this type of source produces highly focused shear wave lobes with maximum radiation at +- 45 degrees, and no shear waves radiated horizontally. The P-waves on the other hand have a more uniform radiation pattern, with the largest amplitudes directed horizontally. Shear waves can be recorded by a hydrophone receiver in a borehole because a radial stress that creates a response on the hydrophone is produced by the shear body wave for every incoming direction except the radial.

Another way to view the data is in common vertical offset space. In common offset space, the source to receiver straight line distance is constant, and the direct arrival times emulate velocity variations with depth rather than path length variations. Figure 3 is a common offset display (the offset corresponds to a straight ray angle of 63 degrees with respect to the vertical. Note that the P and S direct arrivals have similar small moveouts in this domain. The dip in arrival times in the center of the section corresponds to an area where the direct arrival was primarily traveling in the lower velocity reservoir rocks. Also note that the reflections have roughly twice as much moveout in this domain as in common receiver space.

WAVEFIELD SEPARATION

Figure 4 is a flow chart illustrating the major steps used to extract P to P reflections form the total wavefield.. A similar sequence was used to extract the S to S reflections. In the first stage of wavefield separation the direct arrival (Either P or S) was aligned as in conventional VSP wavefield separation (Hardage, 1985). A multichannel filter (filter #1)

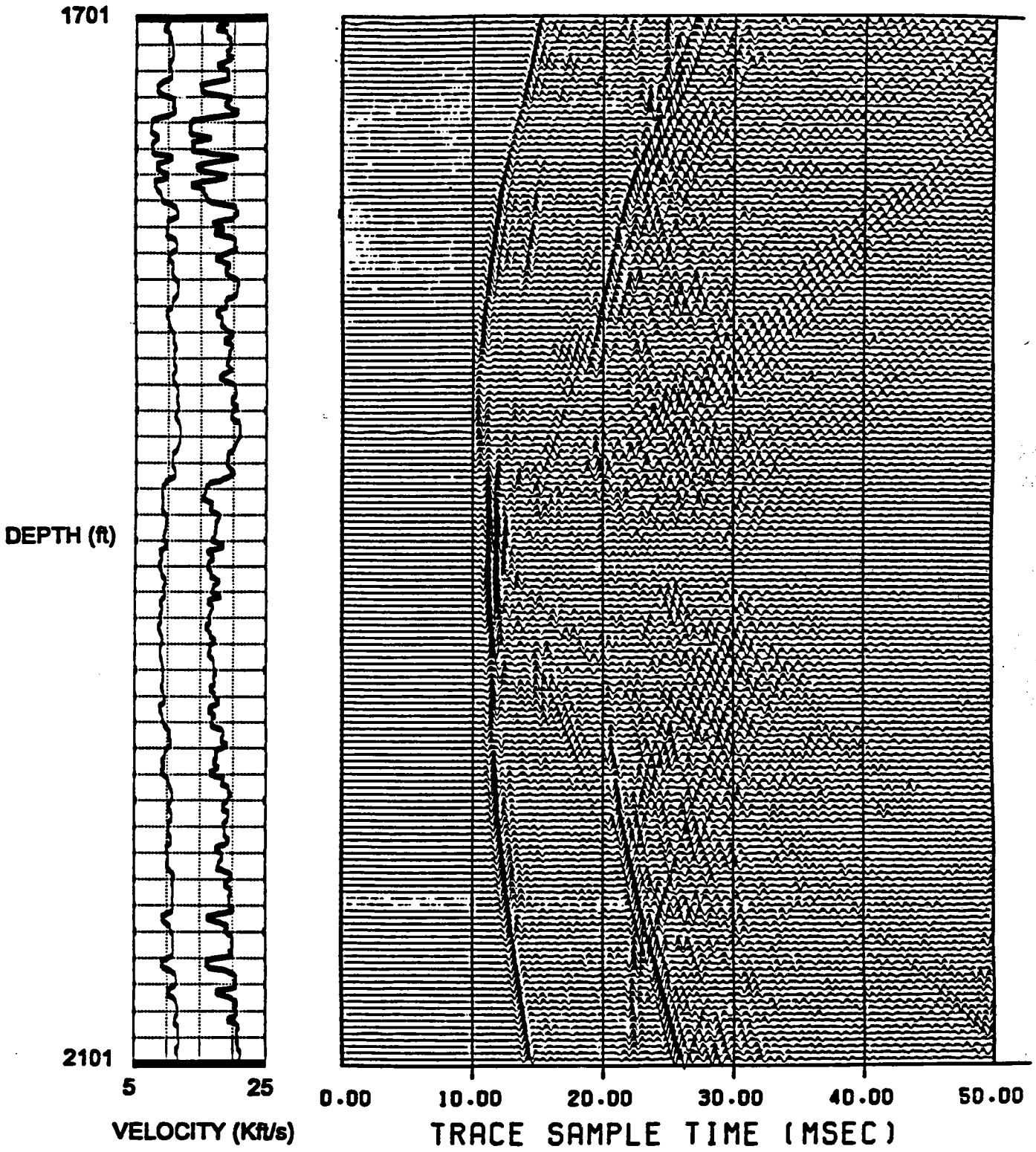

Figure 2: A typical common receiver gather from the West Texas well-to-well experiment. The receiver depth was 1904 ft, just below the top of the reservoir (the bottom of the reservoir was around 1964 ft). Source positions between 1701 ft and 2101 ft every 2.5 ft are shown.

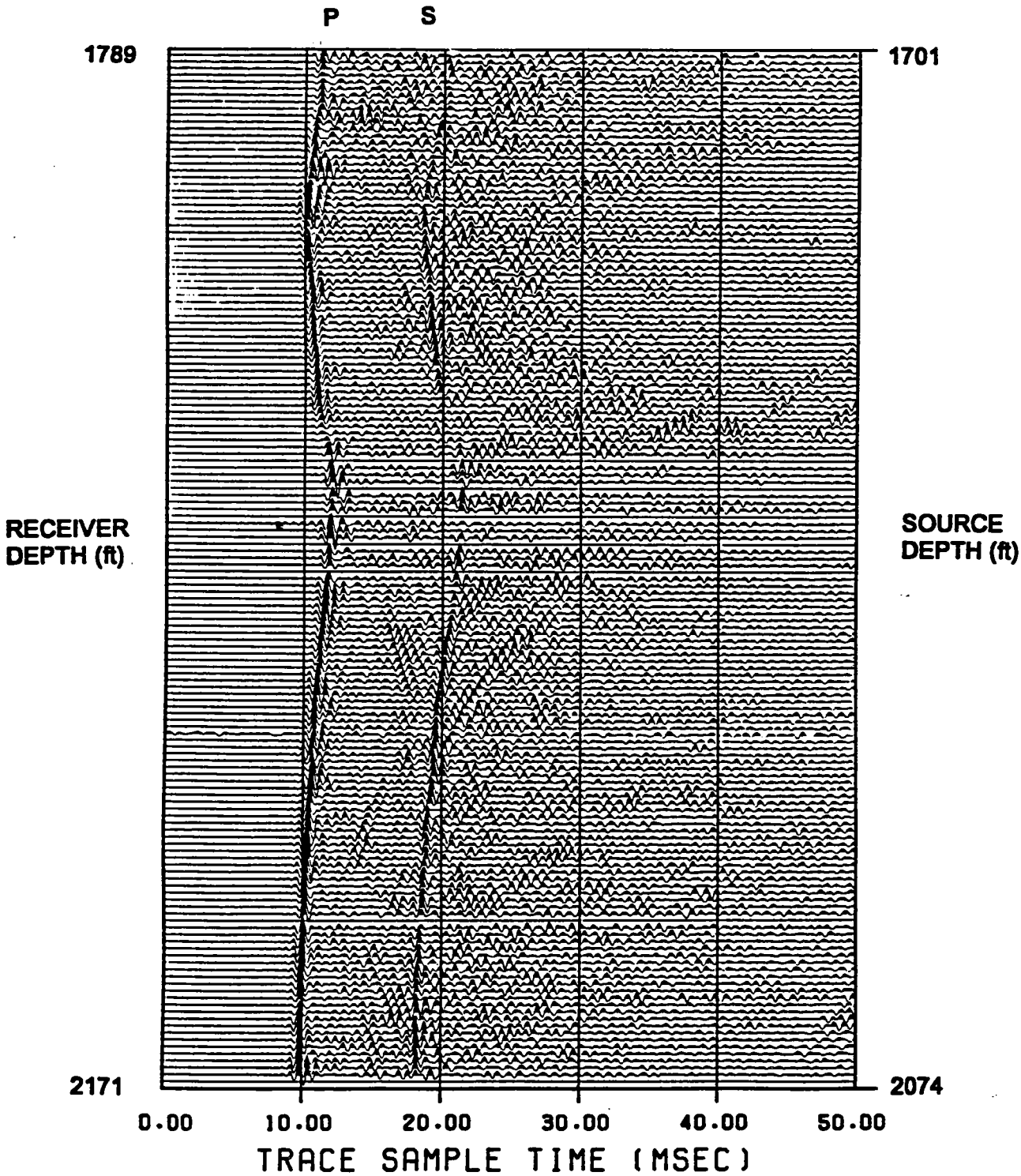

Figure 3: A common vertical offset display (source depth - receiver depth = -90 ft). Variations on the P and S direct arrival times correspond with velocity variations observed in the well logs.

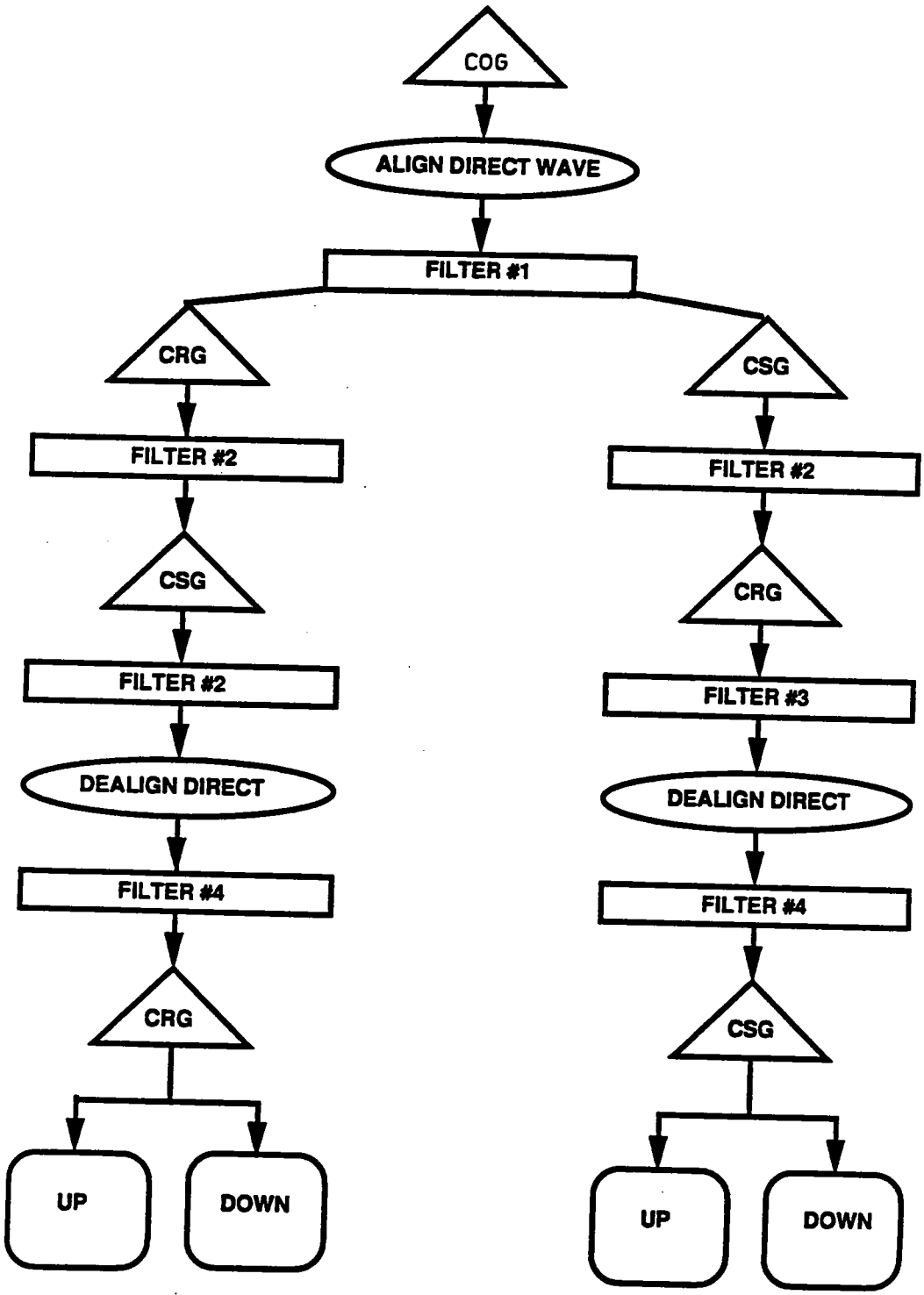

Figure 4: Wavefield separation processing flow used to extract crosswell reflections. Triangles are sorts, rectangles are multichannel filters, and ellipses are time aligning operations.

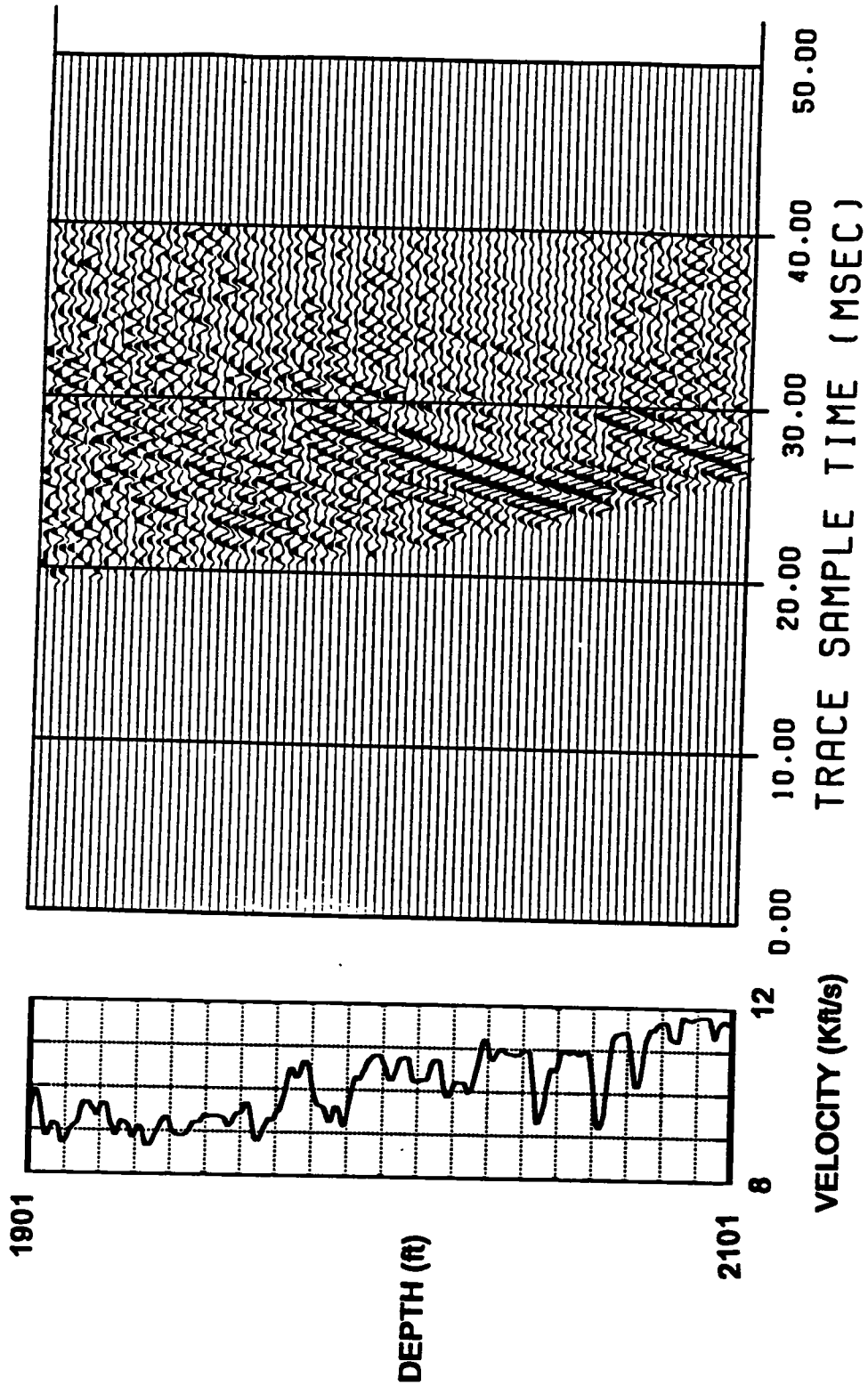

Figure 5: Upgoing S-wave reflection wavefield for the data displayed in Figure 2.

designed to attenuate zero moveout arrivals was then applied to the data. Although any type of multichannel filter (i e median, mean, *f-k*, τ-*p*, etc) could have been applied, we used a trace mix that was then subtracted from the premixed data. The length of the mix was chosen to avoid removing any primary reflection energy in the frequency band of interest (300 to 2000 Hz).

At this point notice that the data processing sequence branches. Two copies of the original data set were made: one sorted into common receiver gathers, the other sorted into common source gathers. Filter # 2 was used to attenuate reflections coming from horizontal locations near the common variable (source or receiver) borehole. This filter was also applied as a simple trace mix and subtraction. Then filter #3 was used to enhance reflections coming from locations hear the common variable well. The multichannel filter was applied as a trace mix *without* subtraction. After applying filters #2 and #3 we have two residual data sets. The one on the left side of the flowchart contains up and downgoing reflections from the half-plane on the side of the *source* well. The one on the right contains up and downgoing reflections from the half-plane on the side of the *receiver* well. Through several tests we observed that it was preferable to adaptively guide the filter pass and reject band using the direct arrival time pick rather than applying a general 2-D pie slice filter. We believe that the adaptive tuning of the filter using the direct arrival time was more important to the process than the type of multichannel filter applied.

In the final stage of wavefield separation the up and downgoing reflections were separated using *f-k* velocity fan filters (in filter #4). By passing positive moveout arrivals we were able to extract downgoing primary reflections and by passing negative moveout arrivals we extracted upgoing reflections. Potentially, up and downgoing wavefield separation at this stage could be further improved with a more data dependent filter like the previous multichannel filters that were applied. Using a similar processing sequence with adaptive multichannel filters based on the shear wave direct arrival we isolated the shear wave reflections.

Figure 5 is a common receiver gathers after applying the sequence outlined in Figure 4 to enhance S-S upgoing reflections from horizontal locations hear the source well. These common receiver gathers correspond to the lower half of the total wavefield data shown in Figure 2. Note the excellent coherency of the upgoing reflections. Also note the minimal Rieber mixing produced. Applying wavefield separation filters using multiple sorting domains allows us to apply much milder filters than those that would be required for up

and downgoing wavefield separation of VSP data, where only one sorting domain (Common source) is available.

After extracting the up and downgoing reflection arrivals, these data subsets were deconvolved. The deconvolution was performed using an operator derived from the transmission wavefield, similar to deconvolution of VSP reflection wavefields (Hardage, 1985). We obtained an estimate of the transmission wavefield by applying filter # 1 as a pass of the direct arrival rather than a rejection. Then simple predictive deconvolution using a 1 ms gap and a 10 ms operator length was applied.

The entire pre-imaging process was performed on all common receiver gathers, common source gathers, and common offset gathers (approximately 200 of each), yielding data subsets that were then imaged. The wavefield separation and deconvolution processing sequence represents roughly four times the number of operations required in a typical VSP processing sequence. However, in VSP we a generally dealing with only one common source gather and only one upgoing P reflection wavefield. To process all gathers and extract all reflection wavefields required about 7,500 times the amount of processing required for a single offset VSP. We performed this processing in 3 days using the ProMAX surface seismic processing system mounted on a standard UNIX workstation. Contractor processing quotes for a VSP data set of this magnitude were several hundred thousand dollars.

CONCLUSIONS

Through appropriate acquisition techniques and through the use of adaptive multichannel filtering techniques, P-P and S-S cross-well reflections were extracted from the complex total wavefield of arrivals recorded at a West Texas well-to-well field experiment. The total wavefield displays were dominated by P to S transmission and converted arrivals and exhibited relatively weak reflection signals. The data processing consisted of wavefield separation and deconvolution applied in a variety of sorting domains. The volume of data processed and the number of operations performed were between two and four orders of magnitude greater than a typical VSP, making the analysis more akin to multifold common depth point surface seismic processing than to VSP processing.

ACKNOWLEDGMENTS

This work was supported by the sponsors of the Stanford Tomography Project, the Gas Research Institute, the David and Lucille Packard Foundation, and Chevron Oil Field Research Corporation.

REFERENCES

Hardage, B. A., 1985, Vertical seismic profiling: part A: principles, Pergamon Press.

Lazaratos, S. K. , Rector, J. W., Harris, J. M., Van Schaack, M., 1991, High resolution imaging using cross-well reflection data, Presented at the 61st Ann. Inter. Mtg of SEG, Expanded Abstracts,1,150-153

Lee, M. W., Balch, A. H., and Parrot, K. R., 1984, Radiation from a downhole airgun source, Geophysics, 49,1, 27-36.

Rector, J. W., Lazaratos, S. K., Harris, J. M., and Van Schaack, M., 1992, Extraction of reflections from cross-well wavefields, To be presented at the 62nd Ann. Mtg. of SEG, New Orleans.

Stewart, R., and Marchisio, G., 1991, Cross-well seismic imaging using reflections, Presented at the 61st Ann. Mtg. of SEG, Expanded Abstracts, 375-378.

PAPER E

HIGH RESOLUTION IMAGING OF A WEST TEXAS CARBONATE RESERVOIR

Part 5 - Reflection Imaging

Spyros K. Lazaratos, James W. Rector III, Jerry M. Harris, and Mark Van Schaack
Seismic Tomography Project

ABSTRACT

Stacking is perhaps the most important procedure in surface seismic data processing. It is also extremely significant for cross-well reflection imaging. Big improvements in the signal-to-noise ratio of the reflection events can be achieved through appropriate use of the fold. Yet, stacking high-frequency, wide-angle reflections is not trivial. With wavelengths of a few ft, small misalignments due to velocity or geometric errors can produce destructive interference and actually degrade the events. Also, the spatial bandwidths of images produced from different angles of incidence differ significantly, something that further complicates processing.

In this paper we present an imaging sequence that allowed us to produce high-quality stacked sections from a large cross-well dataset. A very good tie was achieved at both wells. Heterogeneities inside a 100-ft thick reservoir as well as an uncomformity and a small pinchout were successfully imaged, with both P and S waves and resolution of a few ft. Imaging with these data was the computational equivalent of imaging with 1516 offset VSPs.

INTRODUCTION

In recent years, several authors (Baker and Harris, 1984; Beydoun et al., 1988; Iverson, 1988; Abdalla et al., 1990; Beckey et al., 1991; Stewart and Marchisio, 1991; Lazaratos et al., 1991) advocated the use of reflections recorded in cross-well data for imaging the area between wells. For most of the real-data studies, a very small number of data gathers—or even a single gather—were used for imaging.

Compared to these previous studies, the data volume used for the work presented in this paper is enormous. As we are going to explain below, we imaged with the equivalent of 1516 offset VSPs. Such a large data volume creates new domains for multichannel filtering of the cross-well data, as explained in Rector et al. (1992a) and Rector et al. (1992b). Further, it allows us to use the fold to improve the signal-to-noise ratio through stacking. Cross-well data are so complicated and rich in different modes that both improvements (better processing and stacking) are necessary to produce high-quality images. A numerical modeling analysis revealing the complexity of the cross-well data used in this study, can be found in Van Schaack et al. (1992b).

In Lazaratos et al. (1991) we achieved a good tie at the well, even though we used a single gather for imaging. Yet, we were not able to reliably image away from the wells, due to poor signal-to-noise ratio. In this study, we demonstrate that, with large data volumes, appropriate processing and stacking of multiple gathers, reliable well-to-well sections can be produced from cross-well reflections.

DESCRIPTION OF THE DATA

A description of the geology and the data acquisition is given in Harris et al. (1992).

The wavefields used for imaging were the P to P and S to S primary reflections. Unlike the direct P and S arrivals, these events are often invisible in the raw data and need to be enhanced and separated by appropriate processing. The processing sequence used for this study is discussed in detail in a companion paper (Rector et al., 1992a). As illustrated in Figure 1, for each reflection mode (P-P, S-S), we have two types of reflection wavefields: upgoing and downgoing. Upgoing reflections (reflections that are upgoing as they are received) are produced by interfaces below the source/receiver. Downgoing reflections (reflections that are downgoing as they are received) are produced by interfaces above the source/receiver. Both upgoing and downgoing reflections were used for imaging.

For every reflected wavefield (P upgoing, P downgoing, S upgoing, S downgoing), there is a further subdivision, also illustrated in Figure 1. As explained in Rector et al. (1992a), the data are processed in both the common source and common receiver domains. Processing in common source gathers (CSG) optimally enhances reflections generated at reflection points between the receiver well and halfway the distance between wells. Processing in common receiver gathers (CRG) optimally enhances reflections generated at reflection points between the source well and halfway the distance between wells.

This dataset consisted of 201 common source gathers and 178 common receiver gathers. From each gather—common source or common receiver—we extracted four separate wavefields: P upgoing, P downgoing, S upgoing, S downgoing. So, we ended up with 804 common source gathers and 712 common receiver gathers, a total of 1516 gathers, 758 for each mode (P or S). All these gathers were taken through the imaging sequence.

THE IMAGING SEQUENCE

The processing sequence improves the signal-to-noise ratio for the reflection events. Further improvements can be achieved by further processing after imaging and by taking advantage of the data redundancy—the fold—through stacking. To produce an optimal stacked section, one has to deal with the fact that, when imaging with high-frequency cross-well reflections, the quality of the final stack is extremely sensitive to small differences in the positioning of the events as they are imaged with individual gathers. Such differences can be due to an inaccurate velocity model or geometric errors, like well deviation and errors in the positioning of sources and receivers. Dipping reflectors, possibly dipping out of the plane of the wells, will also have residual move-

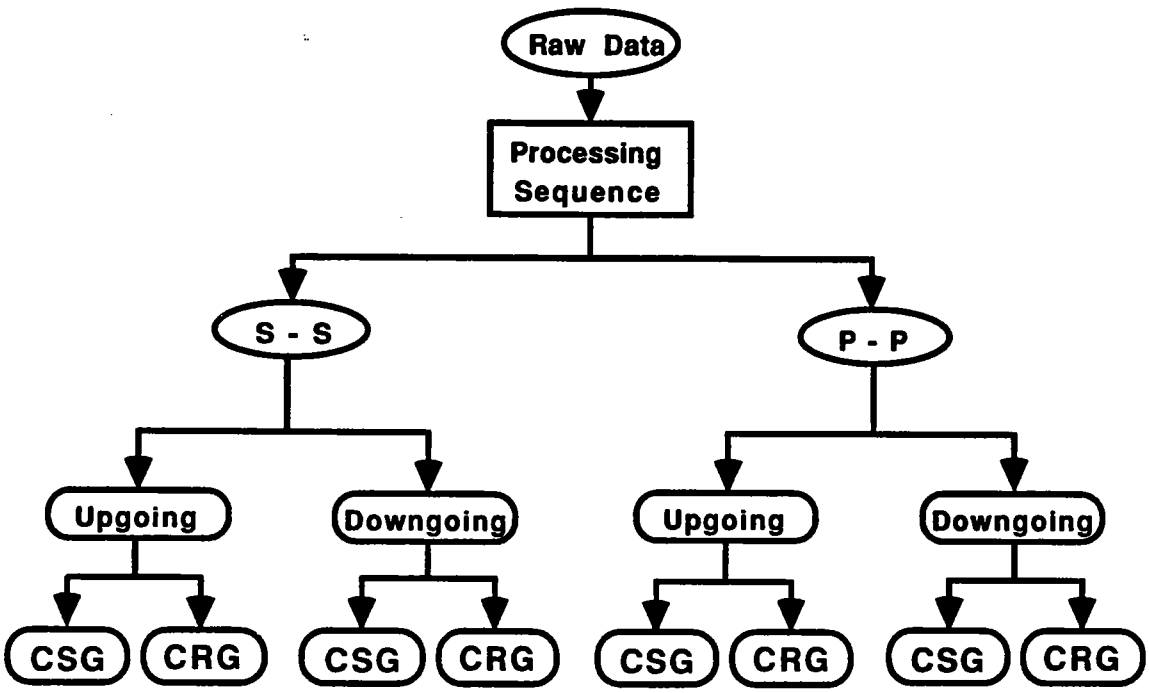

Figure 1: Wavefields used for imaging. After processing, the P to P and S to S reflections are extracted from the raw data. For each reflection mode, the data are further separated into upgoing and downgoing wavefields which are processed as both common source and common receiver gathers.

out after imaging, if not properly handled by the imaging algorithm. For wavelengths of around 5 ft, mispositionings of 2 or 3 ft can significantly affect the final stack. In this paragraph we outline a sequence that allows us to optimally align and stack reflections. This sequence will be briefly described in this paragraph. A complete step-by-step exposition and analysis will be included in Lazaratos (1992).

The imaging sequence flowchart is shown in Figure 2. First the data are imaged in depth with the VSP-CDP mapping algorithm (Wyatt and Wyatt, 1984). A brief description of our particular implementation can be found in Lazaratos et al. (1991). The velocity model used for this step was a 1-D model derived from the tomogram shown in Van Schaack et al. (1992b). This algorithm can only handle a single dip for a particular image location and, in that sense, it is less general than full aperture migration algorithms. In fact, it is more similar conceptually to the normal moveout procedure. Yet, it has the significant advantage that, exactly because it is a point-to-point mapping rather than an integral operator, it does not alter the character of the data by smearing noise along its impulse response. Migration will produce significant smear when applied to aperture-limited cross-well data. This smear often makes it difficult to distinguish signal from noise.

After mapping, the data can be stacked without any further processing to produce what we define as a brute stack. The brute stack is useful to give us a first idea of the structure and major reflectors. Generally, though, it will be sub-optimal due to the imperfect alignment problems mentioned above. It will also tend to be lower resolution, dominated by the wide-angle reflections.

To produce a final stack that is higher quality than the brute stack we first transform our data cube to a new coordinate system as indicated in Figure 3. The original mapped data cube consists of common source or common receiver gathers mapped in depth. Hence the three dimensions of the cube are the depth and horizontal coordinate of the reflection points and a coordinate that identifies the gather, like the depth of the source (when imaging a common source gather) or the receiver (when imaging a common receiver gather). After a transformation based on ray tracing, this last coordinate can be replaced by the ray parameter. After this transformation, the data can be sorted and examined in constant ray parameter gathers. For this work we did this transformation assuming straight raypaths and not taking into account velocity variations. So, essentially we used straight-ray constant angle of incidence gathers. It is important to make clear that the straight ray assumption was just used here for the purpose of resorting the data, which had been previously mapped to the correct depths and reflection points by an accurate ray tracing algorithm. The transformation to the new coordinates is just a new way of looking at the data, so, assumptions made here in no way affect the final stack.

The constant ray parameter gathers (straight ray angle of incidence here) proved very useful in our analysis of the dataset. The main benefit was that the identification of coherent events was much simpler in these gathers than it was in either mapped common source/common receiver gathers or common reflection point gathers. The physical reason for this is that the constant ray parameter gathers are much more stationary than other types of gathers. It can be shown that the stretch of the wavelet during the VSP-CDP mapping essentially depends on the ray parame-

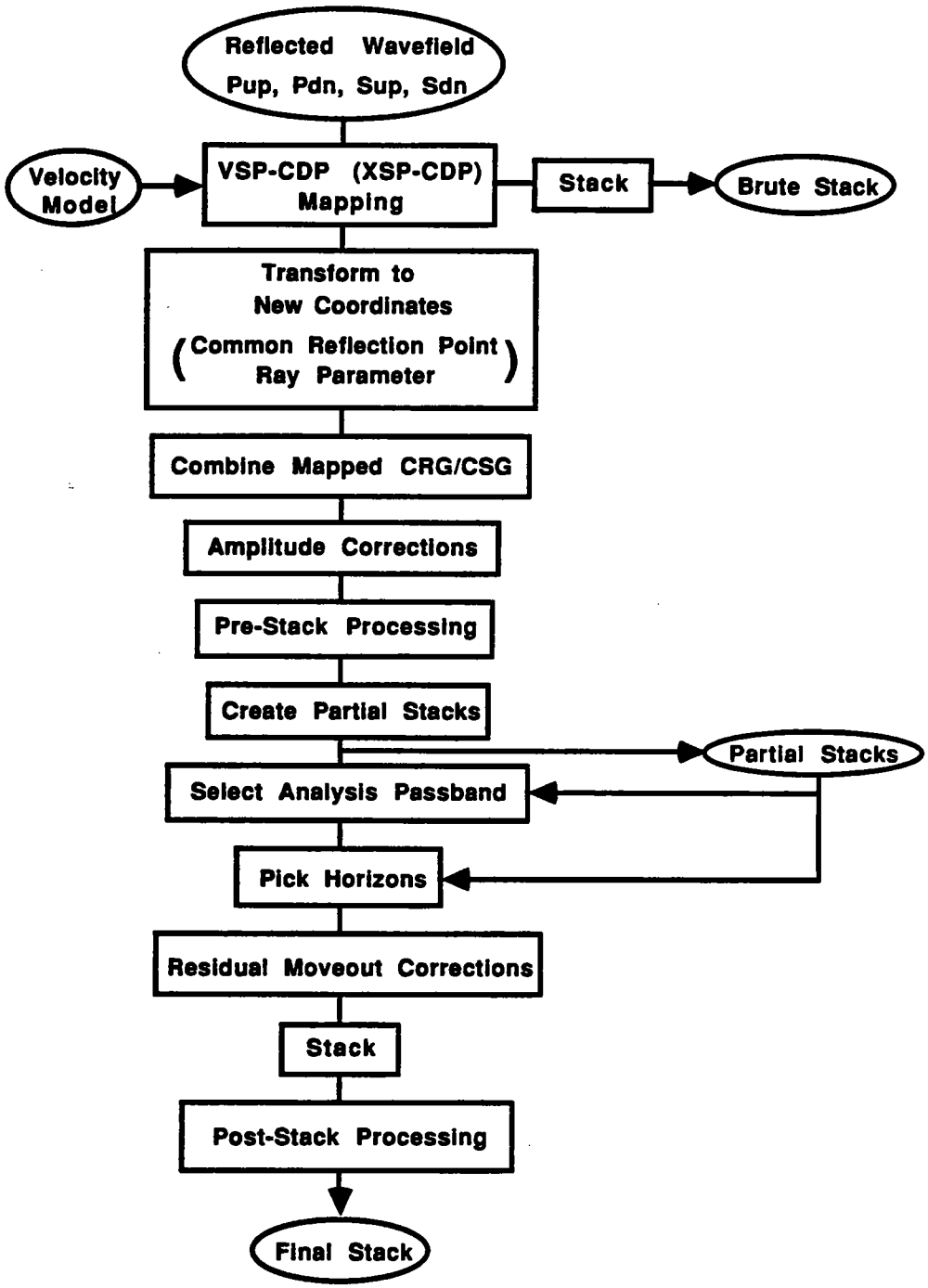

Figure 2: Imaging sequence flowchart.

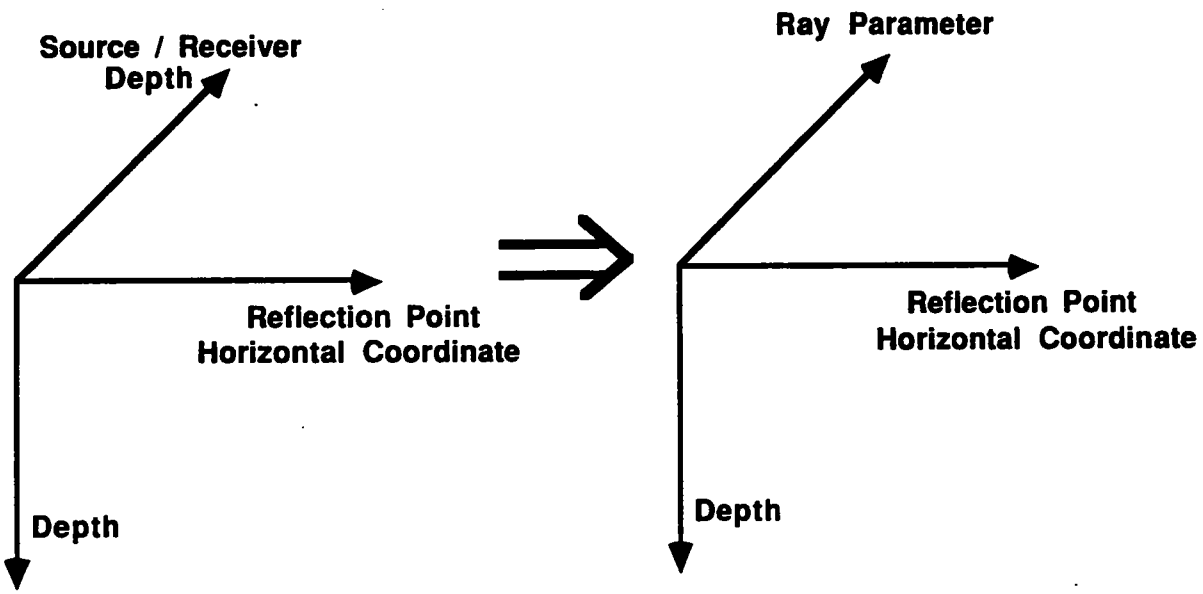

Figure 3: Transformation of the mapped data cube to new coordinates.

ter. So, for constant ray parameter gathers, the wavelet is constant for the whole section. For mapped common source or common receiver gathers, we have a different effective wavelet at every point in the image. Also, the constant ray parameter gathers are much less sensitive to radiation pattern, geometric spreading and attenuation effects than are other types of gathers. Although these amplitude effects change as ray parameter changes, they are roughly constant for each particular value of ray parameter.

As mentioned in the previous section, the data have been processed in two ways: in common source gathers and common receiver gathers. The first sort is used to best enhance reflections generated at reflection points between the receiver well and halfway the distance between wells. The second one is used to best enhance reflections generated at reflection points between the source well and halfway the distance between wells. At this stage—after the transformation to the new coordinates—the data are combined to produce well-to-well constant ray parameter gathers. This step includes interactive editing and selection of the optimal parts imaged with each of the two sorts.

Next we apply amplitude corrections. In this case these were a straight-ray geometric spreading correction and a radiation pattern correction based on theoretical expressions given by Heelan(1953) and Schoenberg (1986). The reason for making these corrections was not to attempt a detailed amplitude interpretation but rather to roughly equalize the contributions to the final stack of reflections recorded at different angles of incidence. A more detailed analysis should include transmission losses and attenuation efects. Even the rough corrections were helpful though. We noticed that without them, the wide angles of incidence tended to dominate the P-wave image, while for the S waves the effect was less significant because the range of angles we used was smaller.

At this stage the ray parameter gathers can be further processed to eliminate obvious noise. Bandpass and F-K filtering both global and local as well as muting of noise-affected parts were interactively applied.

To further improve our ability to identify events, we then perform partial stacks (stacks over limited range of ray parameters). The optimal size of the ray parameter range used in the partial stacks can be defined by sorting and displaying the data in common reflection point supergather form (several neighbouring reflection point locations for each ray parameter).

The final steps of the sequence address the problem of event misalignment between gathers. At first one might be tempted to think that if our velocity model and geometry assumptions were exactly correct, the different ray parameter gathers should be exactly identical, except perhaps for slightly different coverage or amplitude effects. Yet, as we mentioned above, this is not true. Different ray parameters correspond to an effectively different wavelet, because of different stretch during the mapping. So, effectively, each ray parameter gather produces an image of the reflectors that lies in a different wavenumber band. To compare the different gathers and test to what extent they agree, we first need to find a passband common for all ray parameter gathers.

After the ray parameter gathers have been filtered to the same passband, they can

finally be compared for misalignment of events. Our method consists of two steps. First, we identify and pick horizons. This is done on constant ray parameter gathers, which, as mentioned before, are very appropriate for identifying coherent events. The picks are also displayed and edited on common reflection point gathers. Then, based on the picked horizons, we apply a global stretching transformation that aligns all gathers to a reference.

This last procedure is conceptually similar to a normal moveout correction. In standard surface seismic data processing we apply normal moveout to transform non-zero-offset gathers to a zero-offset gather. The zero offset gather is our reference in that case and the transformation is based on picked velocities under the hyperbolic moveout approximation.

In our case, the transformation is defined based on the picked horizons. The reference model cannot of course be the normal incidence gather, since normal incidence reflections are not recorded in cross-well data. We can either use the brute stack as a reference—as we did here—or use one particular ray parameter gather or the best partial stack.

The important point is that this transformation only solves the coherency problem. Events that are imaged at slightly different positions from different angles of incidence are aligned at a common position so that they can be coherently stacked. Yet, if the events do not map to exactly the same position as we change angle of incidence, it means either that our velocities are wrong or that there are geometric errors in our data. This in term implies that, not only our stack is not optimal but, at the same time that our final image could be slightly wrong. To use again the analogy with surface seismic, we have solved the stacking problem but not the time-to-depth conversion problem. What needs to be done eventually is to use the deviations of our events from gather to gather in order to estimate consistent statics corrections and corrections to the velocity model.

On the other hand, given a good tomogram, like the one we had in this case, we can expect that the brute stack will be mostly accurate on the average, although not perfectly coherent. Also, we can use the logs to make our final conversion to accurate depths.

After applying residual moveout corrections, we stack and perform some post-stack processing operations to produce the final stack: we select the passband that is best for our interpretation and tie the section to the logs.

RESULTS

The results of imaging with P to P and S to S reflections are shown in Figures 4 and 5 respectively. The part of the image between 1700 ft and 2000 ft was produced from downgoing reflections. The part below 2000 ft was produced from upgoing reflections. The P-wave sonic logs and synthetics for both source and receiver wells are also shown. The synthetics shown here are just bandpass filtered versions of the logs, phase shifted by 90 degrees. The spectrum of the filter applied to the logs was an average of the spectra of our image traces. To make the synthetics compatible with the data, we reversed the sign of the synthetic for the downgoing reflection part. This

is based on the fact that, for small contrasts (although not for post-critical reflections or big contrasts), the reflection coefficient for a wave incident on an interface from below has the same value as the reflection coefficient for incidence from above but opposite signs (Aki and Richards, 1980). Unfortunately, a shear velocity log was only available for one of the wells. For this reason we used the P logs to generate synthetics for the shear waves, choosing of course a different passband. For the single shear log that we had, we noticed that, although of course the P and S velocities are different, the structure was essentially identical.

In any case, it is important to point out that these synthetics are basically qualitative. Our purpose in using them was mainly to identify events rather than exactly model amplitudes. An exact normal-incidence synthetic introducing the density logs to calculate impedances would not be appropriate either. Given our cross-well geometry we cannot make the assumption that the final stack represents normal incidence reflectivity, since normal incidence reflections are not recorded in this geometry. Also, it should be mentioned that, for the range of incidence angles recorded here (20-80 degrees), the variation in the reflection coefficient as a function of the angle of incidence can be dramatic. So, making an exactly accurate log-based synthetic for our recording geometry is certainly not trivial and we consider it beyond the scope of this paper.

Overall the coherency of both P and S-wave images and the tie with the logs are very good. The large reflectors at depths of about 1750, 1850, 1950 and 2050 ft correlate well with the boundaries between the major layers shown in the tomogram in Van Schaack et al. (1992b). The S-wave image shows higher resolution. This is due to the fact that the S-wave is slower than the P-wave and, at the same time, the frequency content for the S-wave is not significantly lower than the frequency content for the P-wave.

As it is described in Harris at al. (1992), the target of this experiment was a reservoir between about 1850 and 1950 ft. The P and S wave images of the reservoir zone are shown in Figures 6 and 7 at a larger scale. Notice the large number of events inside the reservoir indicating vertical heterogeneity. Layers with thicknesses of the order of 5 ft produce significant coherent events at our frequencies of investigation. Although both P and S images tie well at the two wells, there is slightly more curvature in the shear result between 1900 and 1950 ft. This could be due to a slightly incorrect velocity.

In Figure 8 we show the result of stacking the P and S wave images of the reservoir zone. This was done to enhance coherent events that appear on both images. Notice the apparent zonation with some parts appearing very coherent and others much less so. At this point we have no explanation for this result.

Another interesting feature easily seen in Figures 4 and 5 is the angular uncomformity at a depth of 2050 ft. Larger scale plots are shown in Figures 9 and 10. This feature is located close to the bottom of the wells for which the tomogram suffers from limited view artifacts.

Finally, a small pinchout is shown in Figures 11 and 12. It occurs at around 1770 ft and is clearly visible on the S wave image. The logs support the fact that there is lateral variation at this depth range. Although the P-wave image indicates some

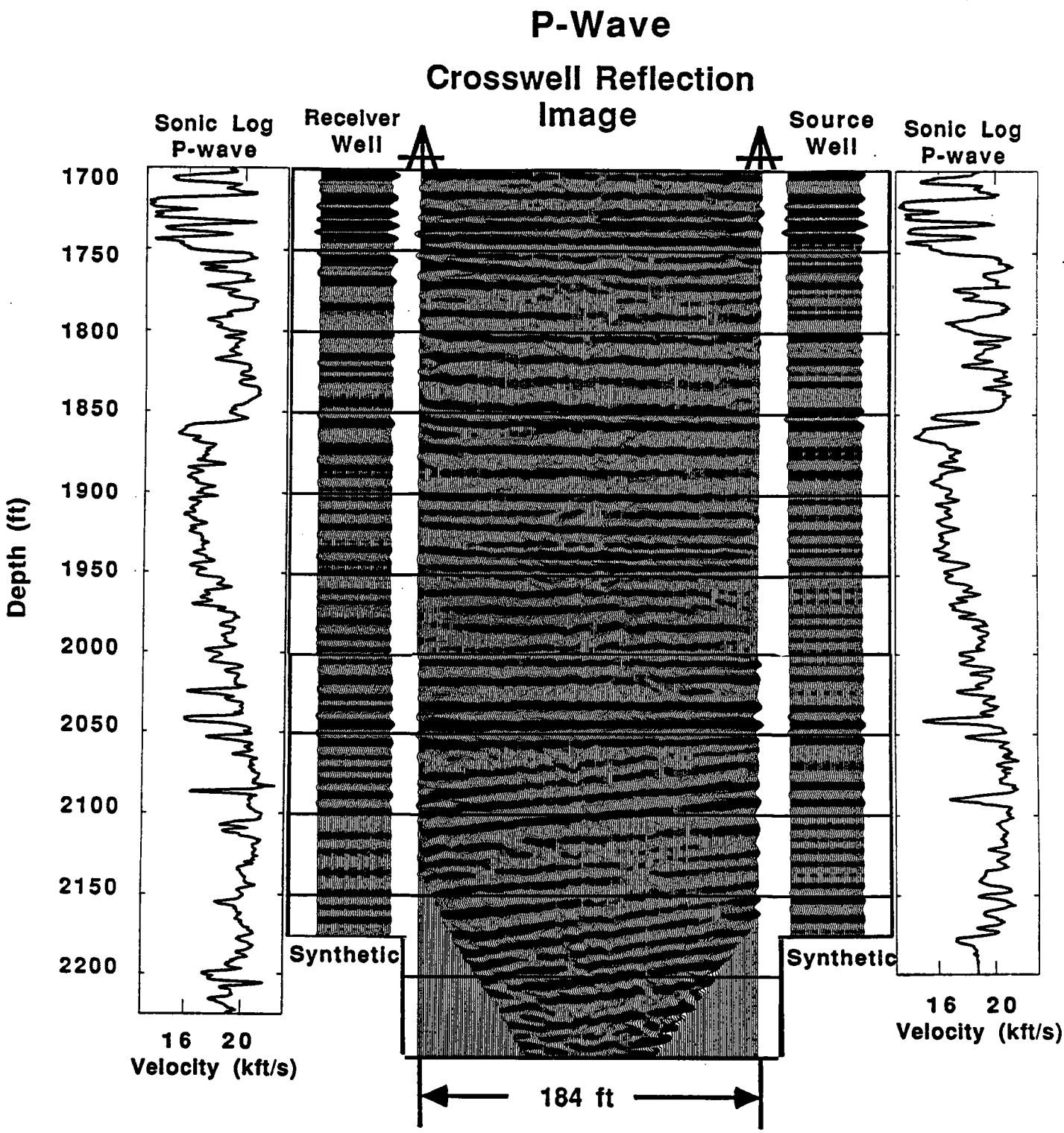

Figure 4: Result of imaging with P to P reflections. The P-wave sonic logs and synthetics for both source abd receiver wells are also shown.

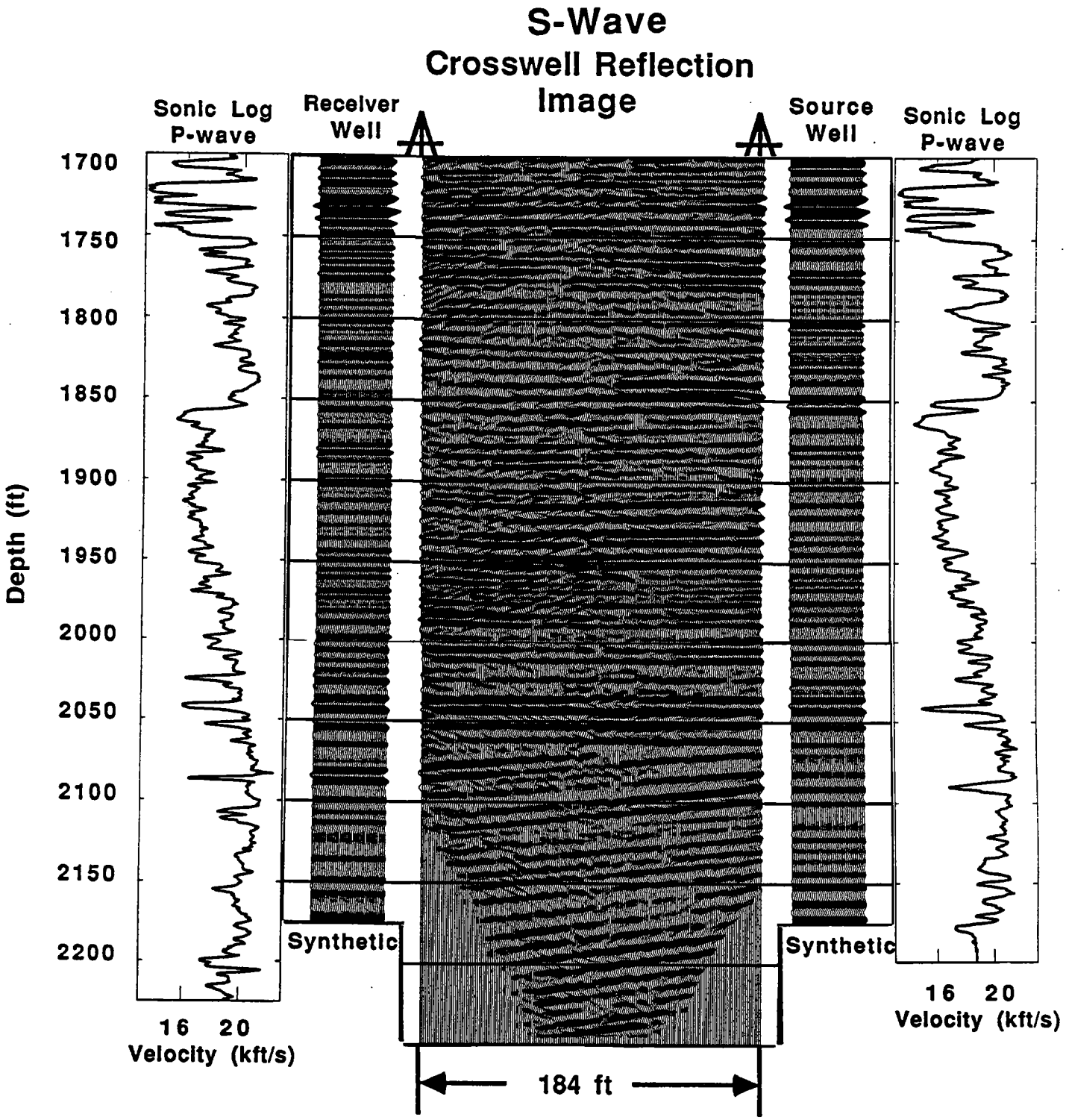

Figure 5: Result of imaging with S to S reflections. The P-wave sonic logs and synthetics for both source abd receiver wells are also shown.

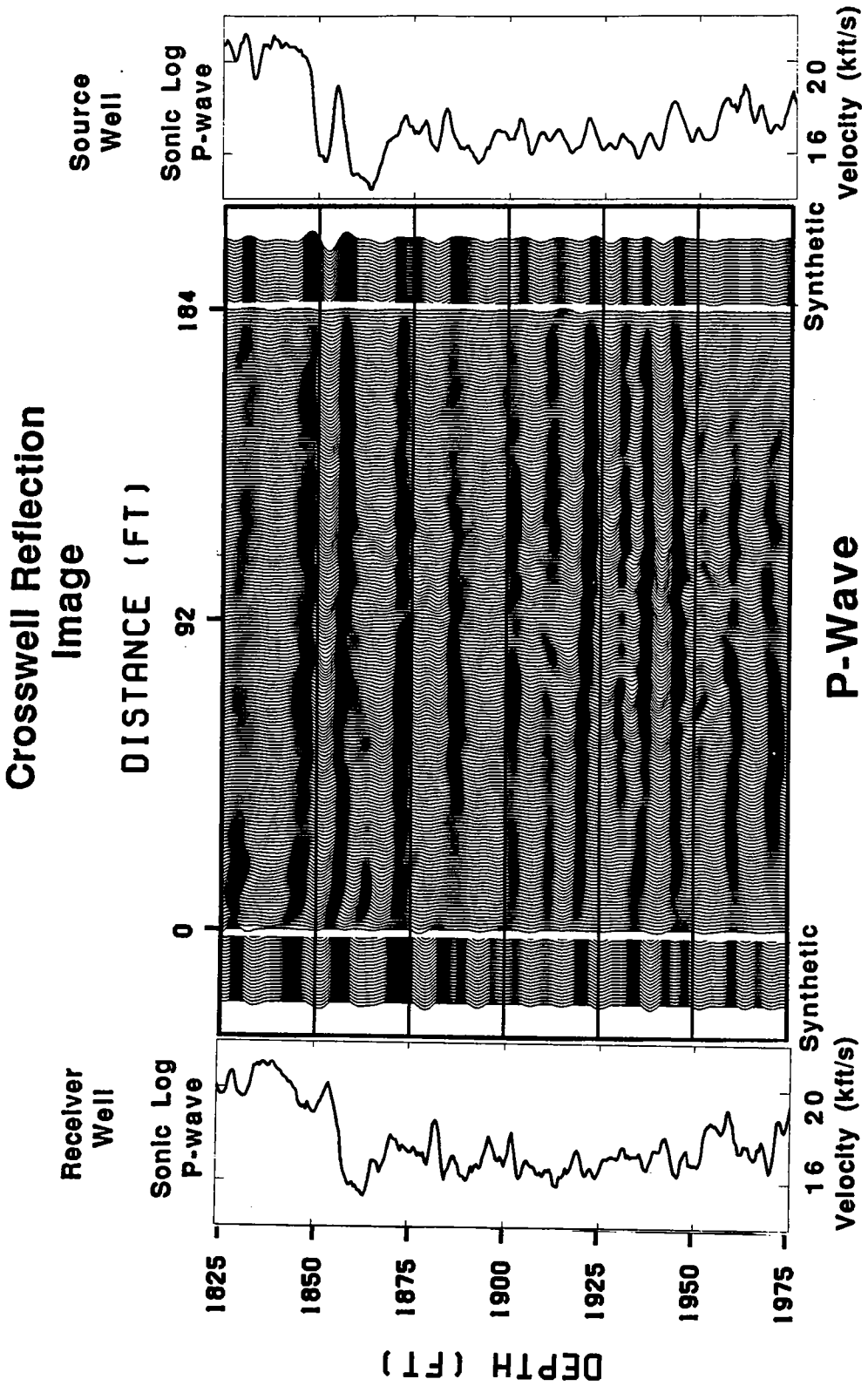

Figure 6: Image of the reservoir with P to P reflections

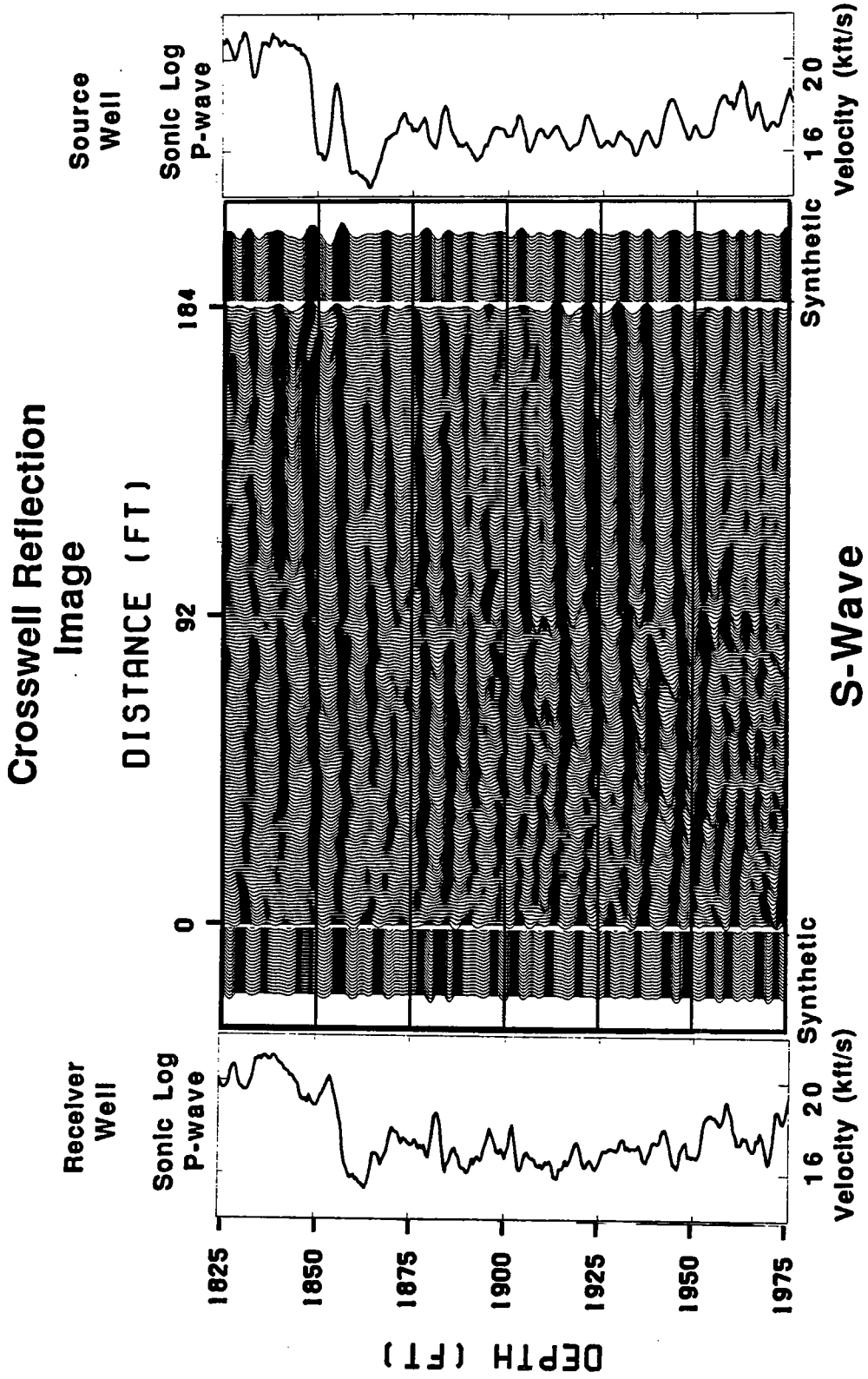

Figure 7: Image of the reservoir with S to S reflections

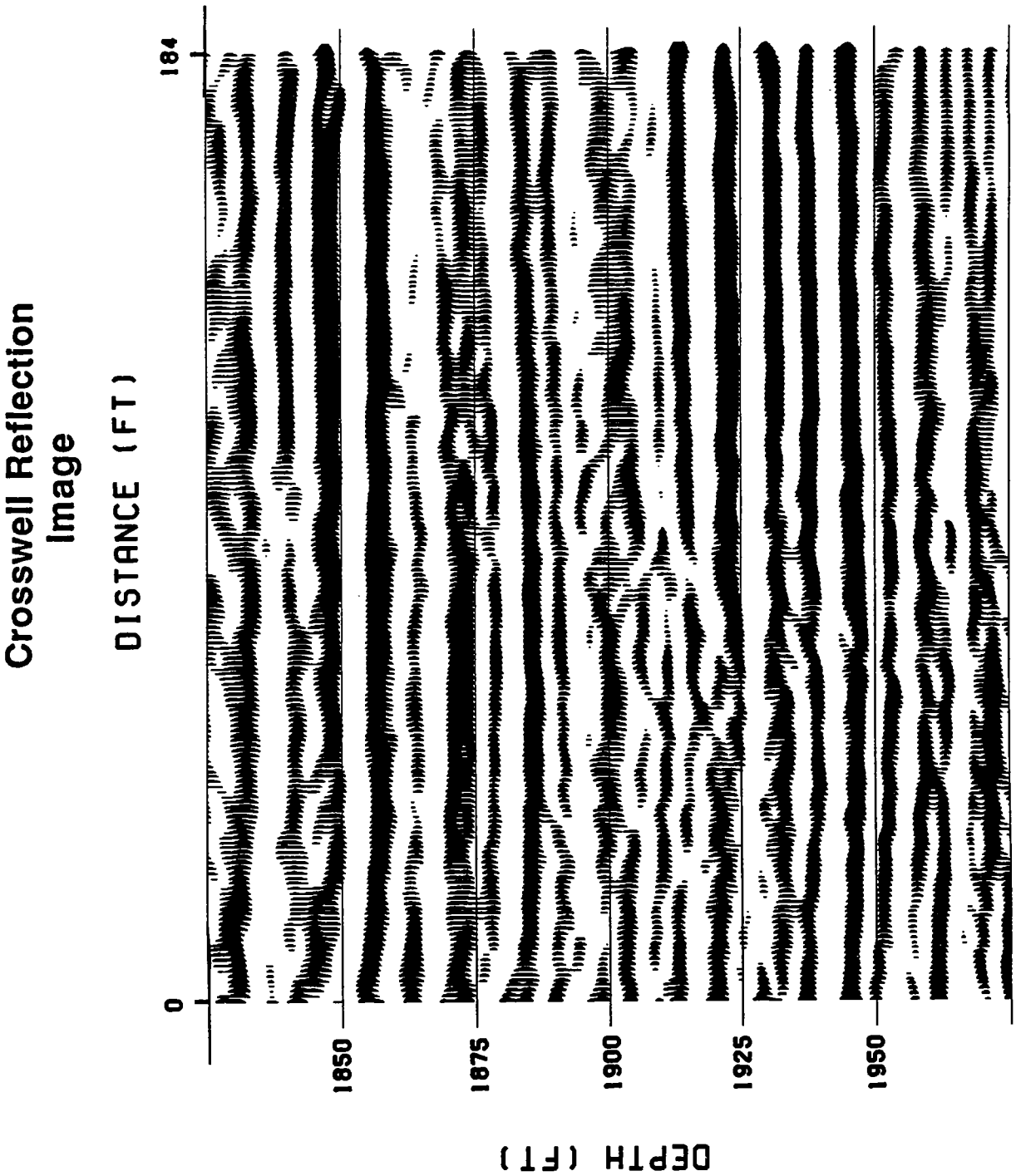

Figure 8: Result of stacking the P to P and S to S images of the reservoir. Notice the apparent zonation with some parts appearing very coherent and others much less so.

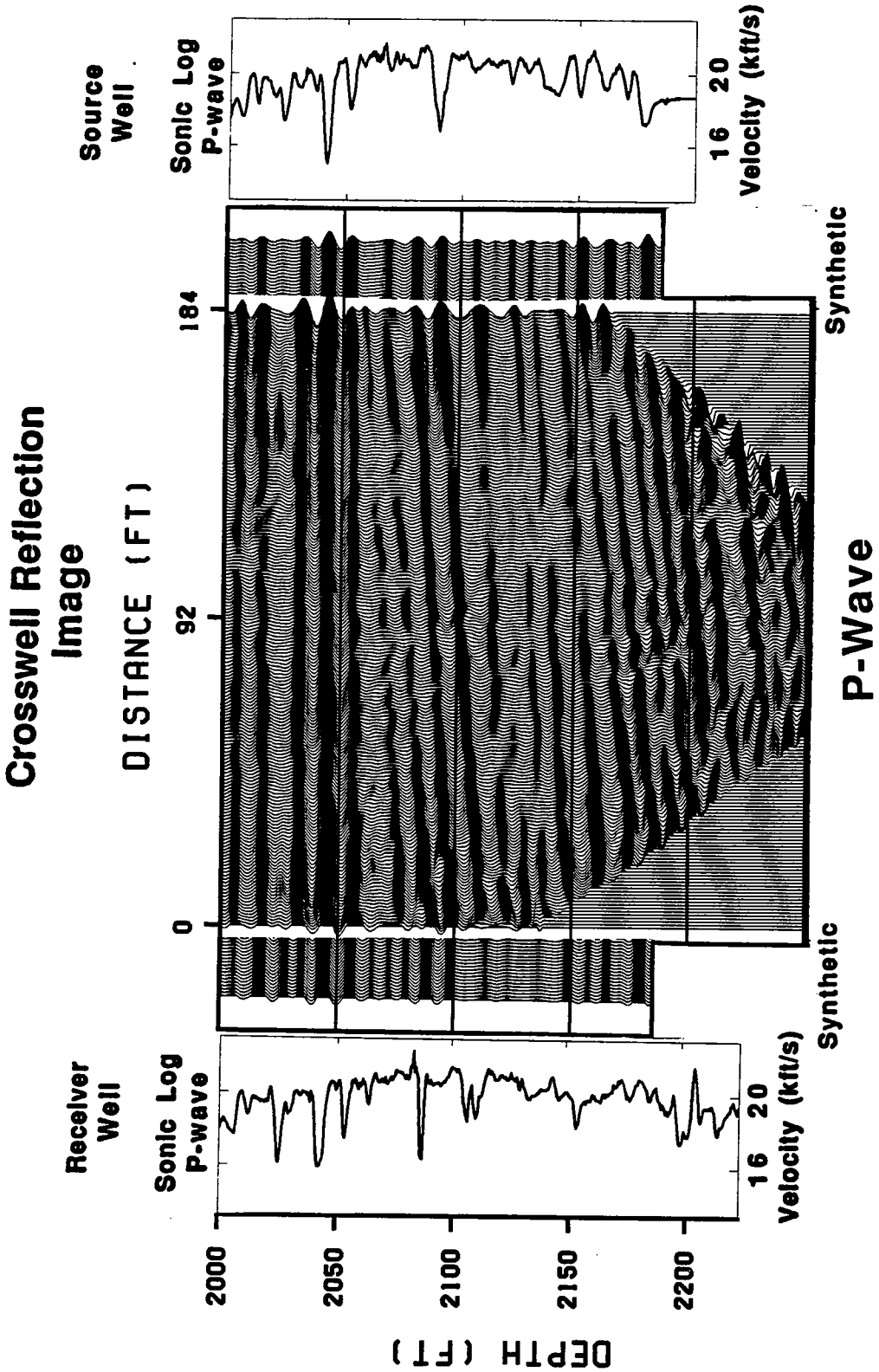

Figure 9: An angular uncomformity imaged with P to P reflections

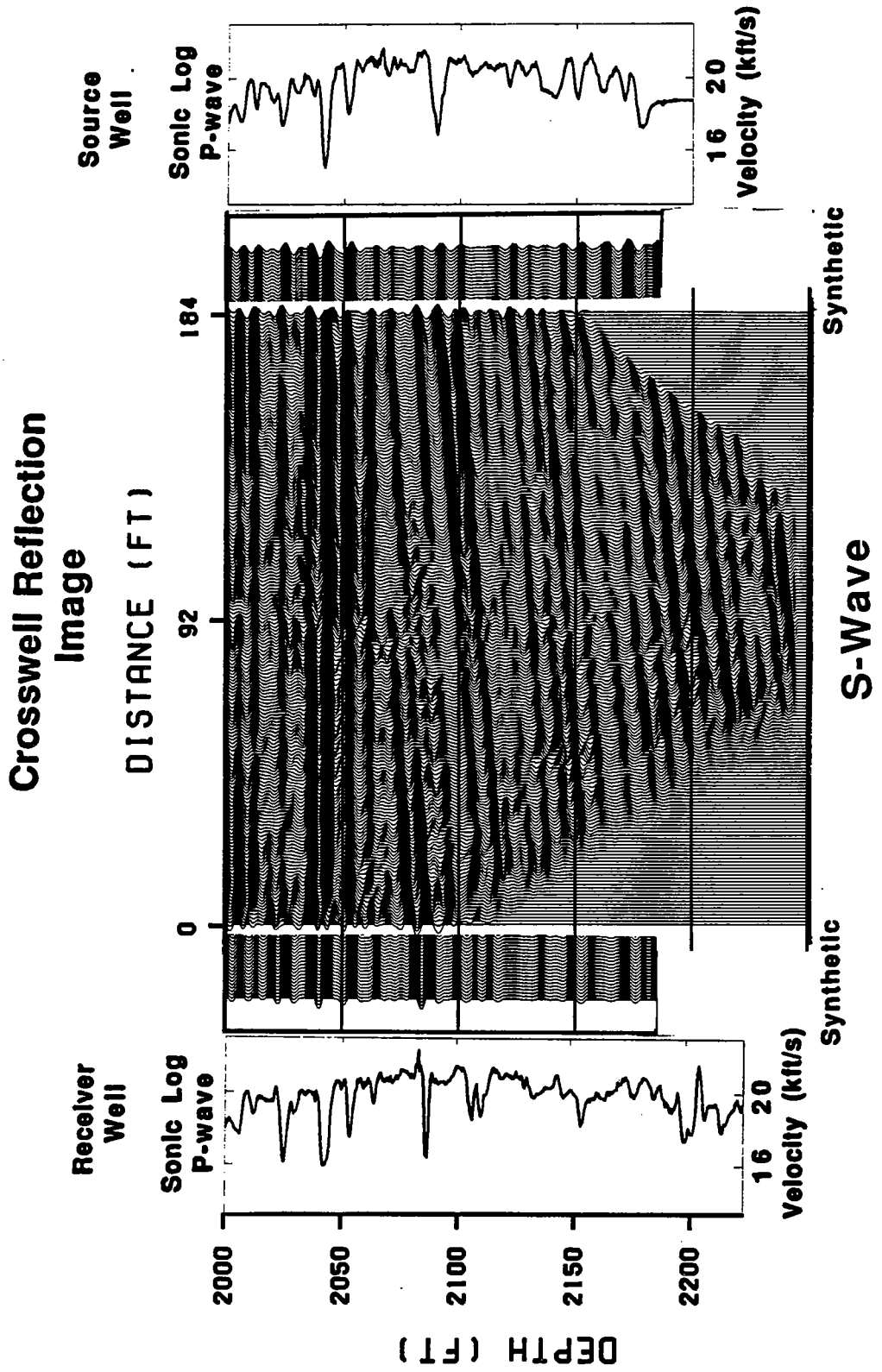

Figure 10: An angular uncomformity imaged with S to S reflections

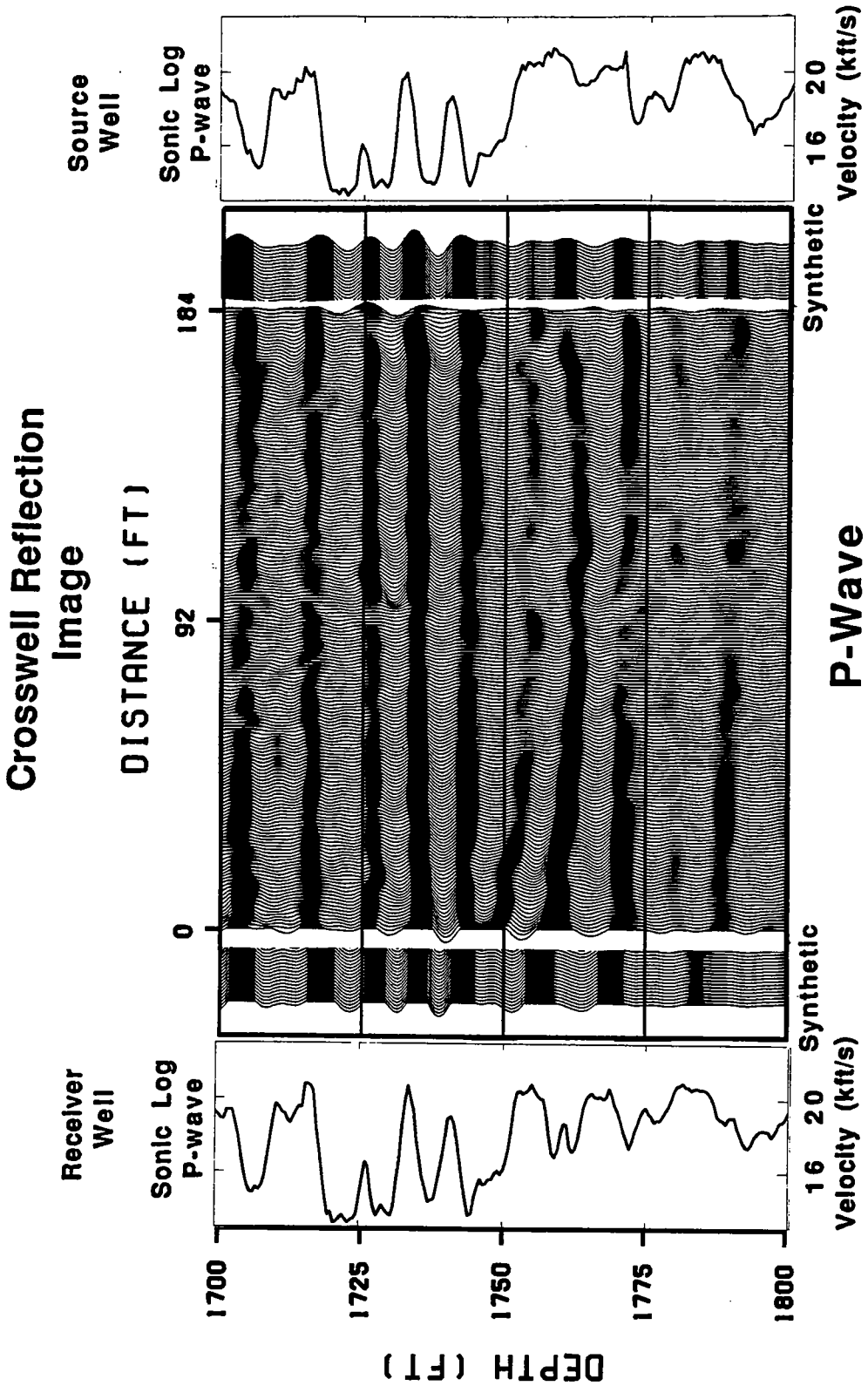

Figure 11: Image of a small pinchout with P to P reflections. The feature is not really resolved.

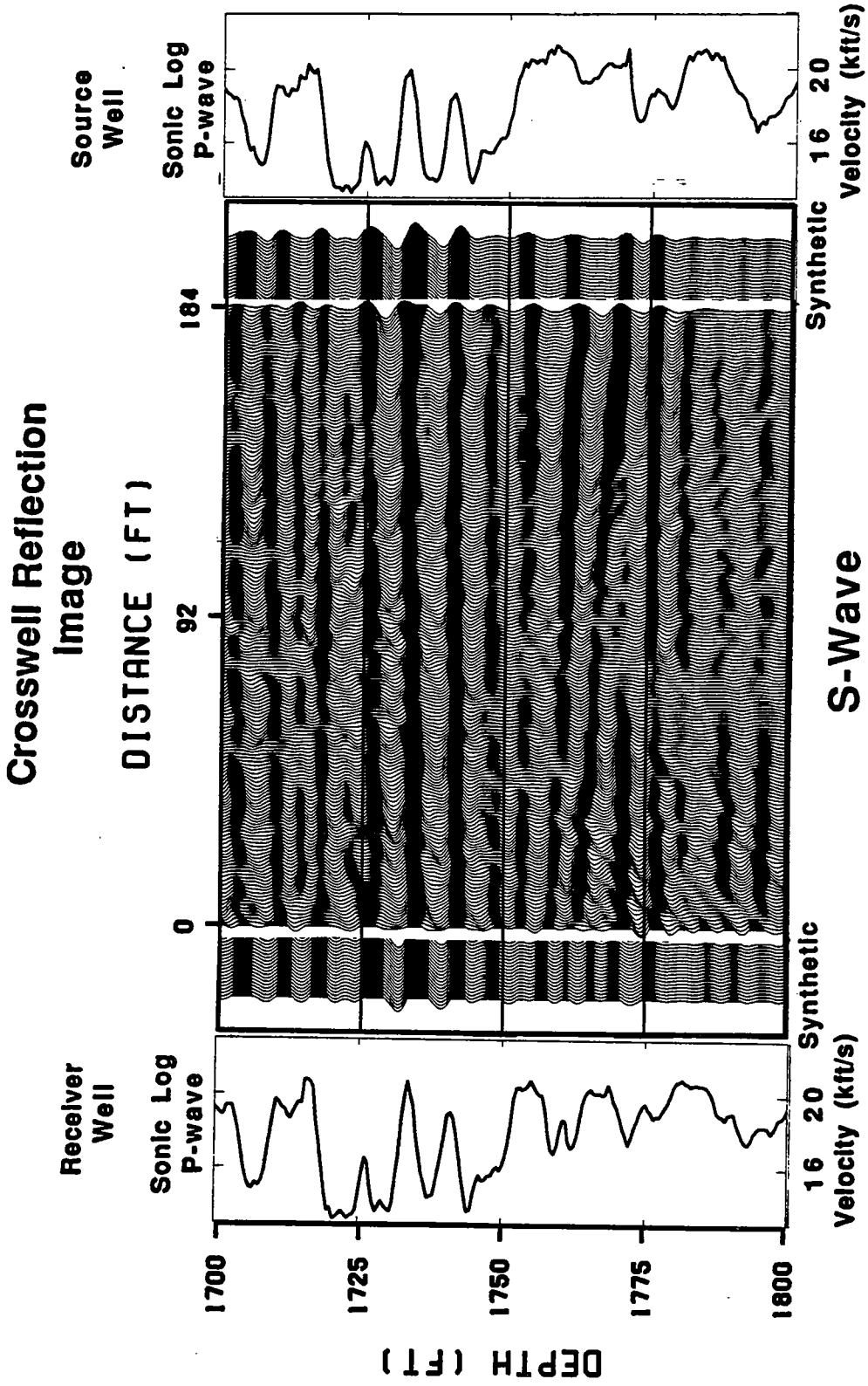

Figure 12: Image of a small pinchout with S to S reflections. The higher resolution of the S to S reflections allows us to see the feature.

lateral variation, the interpretation of the pinchout would not have been easy without the higher-resolution S-wave image. The thickness of the pinching-out layer at the receiver well is less than 10 ft.

CONCLUSIONS

We proposed an imaging sequence for cross-well data and showed results from a large cross-well dataset. We were able to image heterogeneities inside a 100-ft reservoir, an angular uncomformity and a small pinchout with both P and S waves.

Imaging these data required computational effort equivalent to imaging 1516 offset VSPs. Appropriate use of fold was a critical factor for producing high-quality well-to-well images from cross-well reflections.

With increasing data volumes, cross-well reflection processing and imaging becomes more and more similar (in terms of computational effort) to the processing and imaging of surface seismic data, although the geometry is more similar to the VSP geometry. These large data volumes are necessary for reliable high resolution imaging of reservoirs.

ACKNOWLEDGEMENTS

The authors would like to acknowledge the support of the Chevron Oil Field Research Company and the Gas Research Institute (GRI).

REFERENCES

Abdalla, A. A., Stewart, R. R., and Henley, David, C., 1990, Traveltime Inversion and Reflection Processing of Cross-Hole Seismic Data: paper BG2.8 presented at the 1990 Annual Meeting of SEG, San Francisco, Sep.23 - 27.

Aki, K., and Richards, P. G., 1980, Quantitative Seismology, Theory and Methods, Volume 1: Freeman and Co., New York

Baker, L. J., and Harris, J. M., 1984, Cross-Borehole Seismic Imaging: paper BHG2.2 presented at the 1984 Annual Meeting of SEG, Atlanta, Dec.2 - 6.

Beckey, M., Bernet-Rollande, J. O., Laurent, J., and Noual, G., 1991, Imaging reflectors in a crosswell seismic experiment: paper B025 presented at the 1991 Annual Meeting of EAEG, Florence, May 26 - 30.

Beydoun, W. B., Delvaux, J., Mendes, M., Noual G., and Tarantola, A., 1988, Practical Aspects of an Elastic Migration / Inversion of Crosshole Data for Reservoir Characterization: A Paris Basin Example: Geophysics **54**, 1587 - 1595

Harris, J. M., Nolen-Hoeksema, R., Rector, J. W., Van Schaack, M., and Lazaratos, S. K., 1992, High Resolution Imaging of a West Texas Carbonate Reservoir - Part 1: Project Overview and Data Acquisition, Paper A, this volume

Heelan, P., 1953, Radiation from a cylindrical source of finite length, Geophysics **18**, 685 - 696

Iverson, W. P., 1988, Crosswell Logging for Acoustic Impedance: Pet. Tech. J., 75 -

82

Lazaratos, S. K., Rector, J. W., Harris, J. M., and Van Schaack, M., 1991, High-Resolution Imaging with Cross-Well Reflection Data: paper BG4.4 presented at the 1991 Annual Meeting of SEG, Houston, Nov. 10 - 14

Lazaratos, S. K., 1992, Cross-Well Reflection Imaging, Ph.D. thesis in preparation

Rector, J. W., Lazaratos, S. K., Harris, J. M., and Van Schaack, M., 1992a, High Resolution Imaging of a West Texas Carbonate Reservoir - Part 4: Pre-processing and Wavefield Separation, Paper D, this volume

Rector, J. W., Lazaratos, S. K., Harris, J. M., and Van Schaack, M., 1992b, Wavefield Separation of Cross-Well Seismic Data, Paper L, this volume

Schoenberg, M., 1986, Fluid and solid motion in the neighborhood of a fluid-filled borehole due to the passage of a low-frequency elastic plane wave, Geophysics **51**, 1191 - 1205

Stewart, R., R., and Marchisio, G., 1991, Cross-well Seismic Imaging Using Reflections: paper D/P1.4 presented at the 1991 Annual Meeting of SEG, Houston, Nov. 10 - 14

Van Schaack, M., Harris, J. M., Rector, J. W., and Lazaratos, S. K., 1992a, High Resolution Imaging of a West Texas Carbonate Reservoir - Part 2: Wavefield Modeling and Analysis, Paper B, this volume

Van Schaack, M., Harris, J. M., Rector, J. W., and Lazaratos, S. K., 1992b, High Resolution Imaging of a West Texas Carbonate Reservoir - Part 3: Traveltime Tomography, Paper C, this volume

Wyatt, K. D., and Wyatt, S. B., 1984, Determining subsurface structure using the vertical seismic profiling: In Toksoz, M. N., and Stewart, R. R., Eds, Vertical Seismic Profiling: Advanced Concepts, Geophysical Press

PAPER F

HIGH RESOLUTION CROSS-IMAGING OF A WEST TEXAS CARBONATE RESERVOIR

Part 6 – Core Analysis

Richard C. Nolen-Hoeksema

ABSTRACT

A core analysis program was conducted to provide supporting data to a crosswell demonstration field experiment (DFE) carried out by the Stanford University Seismic Tomography Project. The DFE is being conducted to demonstrate the use of crosswell seismic tomography for reservoir characterization and monitoring the seismic effects of CO_2 flooding. This report examines the core-analysis results to see if it is feasible to identify seismic property changes in response to CO_2 flooding.

The contrast between a CO_2-swept zone and an unswept zone averages a small 2% if one uses P-wave velocities (v^*_p). The contrast is somewhat better for P-wave and bulk-wave impedances, averaging 3% and 4.5%, respectively. The best contrast comes from the bulk moduli (K*) where the estimated contrast averages about 8%.

INTRODUCTION

A pilot project is being conducted in a West Texas carbonate reservoir to evaluate the performance of a hybrid CO_2-injection scheme. The Stanford University Seismic Tomography Project (STP) is a participant in this project through a demonstration field experiment (DFE) to investigate the use of crosswell seismic tomography for (1) reservoir characterization and (2) monitoring CO_2 injection. Stanford University conducted two

crosswell seismic surveys in December 1991 between wells A and B and between wells A and C. We reported these crosswell seismic results last year [STP-3, 1992]. Herein, I report core-analysis results in support of the STP project—this is Part 6 of 6 reports.

Well A was drilled as an observation well for the CO_2-injection pilot project. The well was drilled to a depth of 3260 feet. A total of 285 feet of 3.25-inch diameter, unoriented core was cut between 2,775 and 3,060 feet. The principal pay interval in well A is the D5 unit of the Grayburg formation and was cored between 2,863 and 2,947 feet. Minor secondary pay zones were also cored above and below the D5 unit, in the E and M Grayburg units, respectively. The top of the San Andres formation was cored at a depth of 3,038 feet.

In this report, I describe the core-analysis programs, ultrasonic velocity data, and methods I used to estimate sonic and seismic properties from core data. I extend the sonic-log matching calculations to estimate the effects of CO_2 flooding on the seismic properties of the Grayburg formation. These estimates suggest that the contrast between a CO_2-swept zone and an unswept zone is a small 2% if one uses P-wave velocities. The contrast is somewhat better for P-wave and bulk-wave impedances, being 3% and 4.5%, respectively. The best contrast comes from the bulk moduli where the estimated contrast is about 8%.

CORE ANALYSIS PROGRAMS

Routine Full-Diameter Core Analysis

Core Laboratories in Midland, Texas, did routine full-diameter core analysis of the core. This consisted of taking 6-inch long full-diameter samples from each foot of core. Core Laboratories cleaned the samples using a low-temperature toluene-CO_2 extraction method. The low temperature (less than 104°F or 40°C) minimized dehydration of the gypsum ($CaSO_4 \cdot 2H_2O$) that is in the rock. Fluid saturations were determined from the fluids collected during core cleaning. After each sample was cleaned and dried, porosity, permeability, and grain density were determined. This first porosity measurement is referred to as the "low temperature porosity".

After these measurements were made, the core samples were heated to drive off the water of hydration in the gypsum. After the samples cooled, a second porosity measurement was made. This second porosity, referred to as the "high temperature porosity", is greater than the low-temperature porosity. Estimates of gypsum content come

from the high-temperature porosity, assuming the increase in porosity (i.e., pore volume) results from volume lost by gypsum caused by dehydration.

Routine Core Analysis of Plug Samples

We selected vertical plugs from 16 locations, based on core-to-log gamma-ray correlations, log data (density, neutron, sonic), and hand-specimen examination. We cut mostly vertical plugs to favor the dominant propagation direction of sonic-log signals. We also wanted a few horizontally oriented plugs to capture some aspect of P-wave anisotropy. So at 4 locations we selected horizontal plugs cut from the same stratigraphic horizon as their companion vertical plugs. As we wanted to sample both reservoir and non-reservoir zones, nine plug locations were in reservoir zones and seven locations were in non-reservoir zones. These data appear in Table 1.

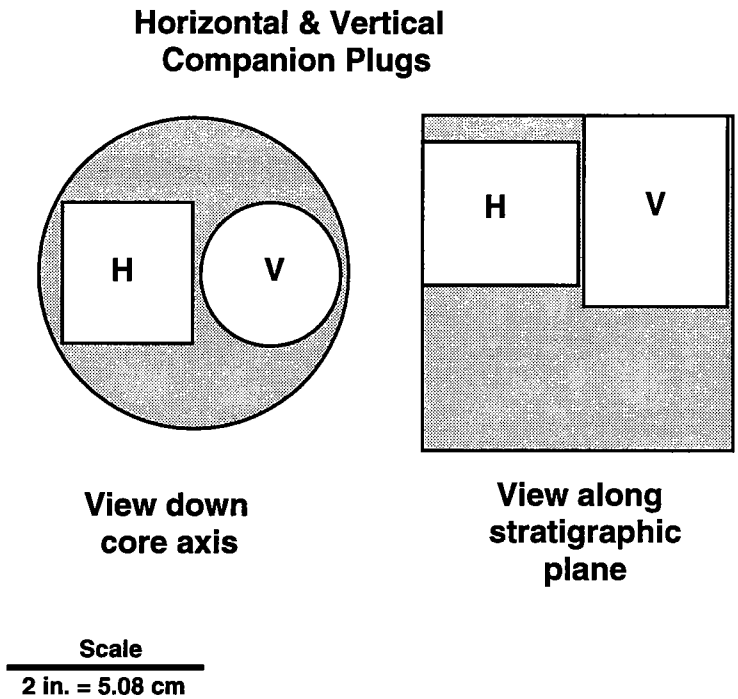

Sketch of how horizontal and vertical companion plugs were cut.

The plugs were 1.5 inches in diameter and 1.5 to 2.0 inches long. The horizontal plugs were shorter than the vertical plugs because of the core's small diameter.

As with the full-diameter samples, Core Laboratories cleaned the plugs using a low-temperature oil extraction method.

After drying the plugs, Core Laboratories determined the porosity, permeability and grain density, all at room temperature and pressure conditions. Bulk volume (V_b) was measured using Archimedes' principle, whereby each sample was immersed to a common depth in mercury. Grain volume (V_g) was measured using a helium pycnometer. Pore volume (V_p) was calculated $V_p = V_b - V_g$. Porosity (ϕ) was calculated $\phi = V_p/V_b$. The dry weight (W_{dry}) was measured. Assuming dry weight equals the weight of the grains (W_g), grain density (ρ_g) was calculated $\rho_g = W_{dry}/V_g$. Steady-state permeability to air was measured. Dry bulk density (ρ_d) is:

$$\rho_d = \frac{W_{dry}}{V_b} = (1-\phi)\rho_g. \tag{1}$$

Saturated bulk density (ρ^*) is:

$$\rho^* = \rho_d + \phi \cdot \rho_f = \rho_d + \phi \cdot \sum_i S_i \rho_i \tag{2}$$

where ρ_f is the fluid density, S_i is the pore-volume fraction or saturation of the *i*-th fluid component, and ρ_i is the density of the *i*-th fluid component.

These data appear in Table 1. Porosity ranges from 0.3 to 22.1 percent. Steady-state permeability to air ranges from less than 0.01 to 66.7 mD. (Note that Core Laboratories' steady-state permeameter cannot resolve permeabilities below 0.01 mD, so there is an artificial floor of 0.01 mD to the permeability values. Rocks with permeabilities below 0.01 mD are considered effectively impermeable to fluid flow.) Grain density ranges from 2.72 to 2.88 g/cm^3.

Figure 1 is a plot of permeability versus porosity for the 20 plug samples. Figure 2 is a plot of vertical permeability versus porosity from the full-diameter measurements and is shown for comparison with Figure 1. Figure 1 is a very limited data set. It shows a semi-log linear trend. A truer picture is given by Figure 2, which shows a weak trend with tremendous scatter in the data. This scatter reflects the significantly heterogeneous nature of these dolomitic rocks. Plug pairs 6 and 8 are from the Grayburg D5 reservoir zone and illustrate this heterogeneity. The pairs were collected side-by-side within the same stratigraphic horizon, yet their porosities differ significantly within the pair.

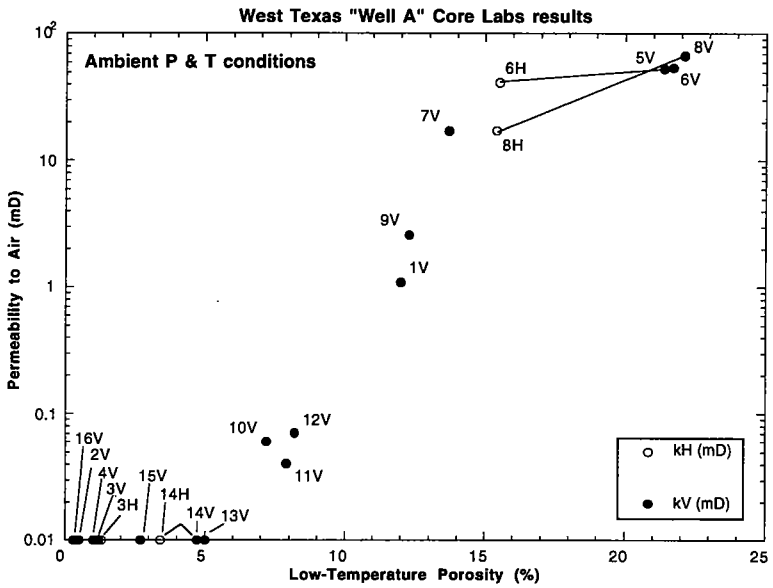

Figure 1

Figure 1: Permeability versus porosity for the 20 plug samples.

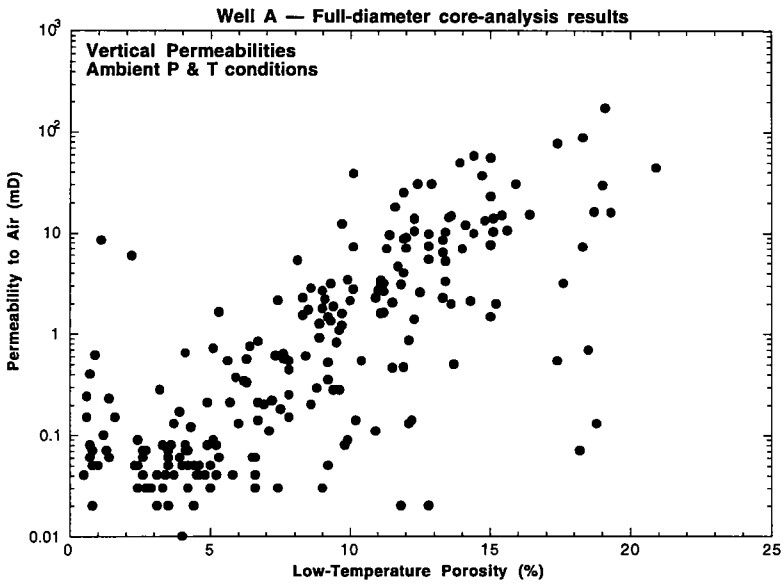

Figure 2

Figure 2: Vertical permeability versus porosity from the full-diameter measurements, shown for comparison with Figure 1.

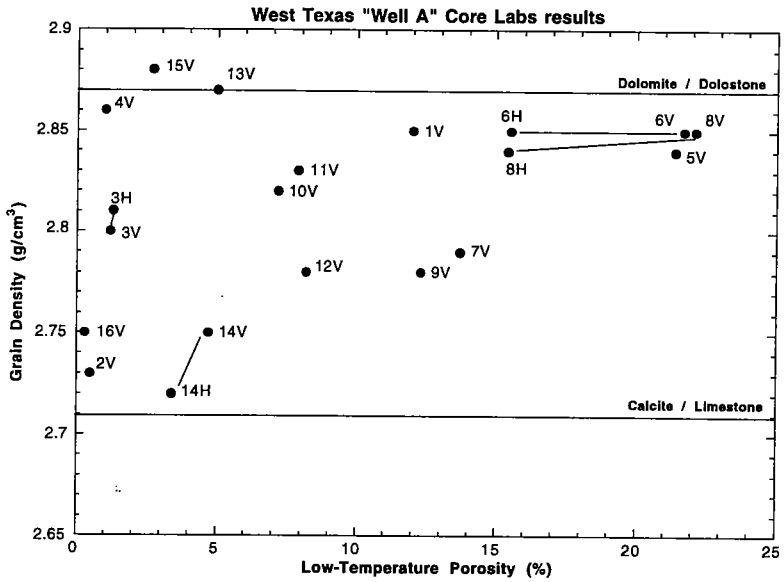

Figure 3

Figure 3: Grain density versus porosity for the 20 plug samples.

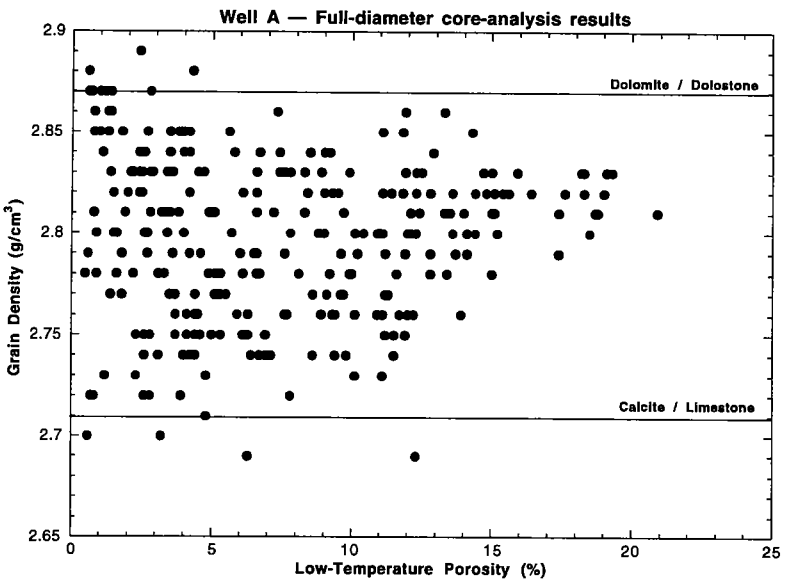

Figure 4

Figure 4: Grain density versus porosity from the full-diameter measurements, shown for comparison with Figure 3. There is no relationship between grain density and porosity.

Figure 3 is a plot of grain density versus porosity for the 20 plug samples. The plug pairs are identified by connecting lines. Figure 4 is a plot of grain density versus porosity from the full-diameter measurements and is shown for comparison with Figure 3. Figure 3 is a very limited data set. Comparison with Figure 4 indicates there is no relationship between grain density and porosity. As expected, grain density and porosity are intrinsic rock properties that are independent of one another.

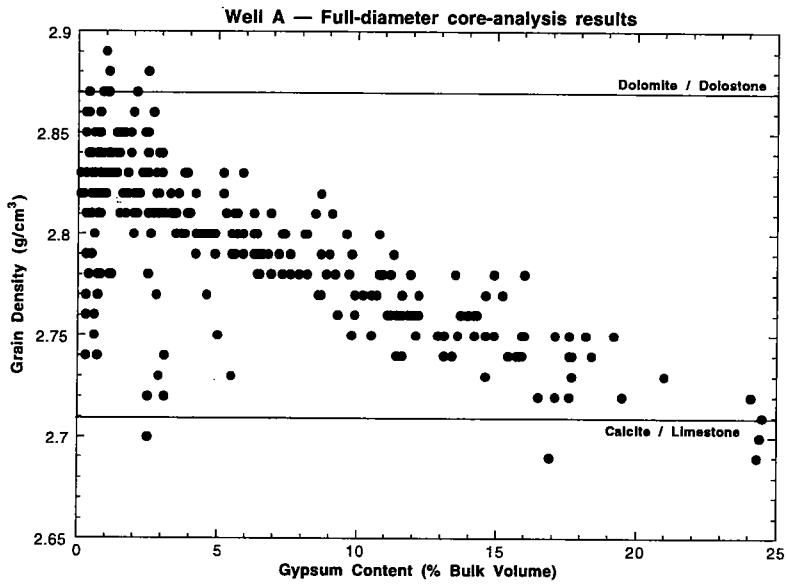

Figure 5

Figure 5: Grain density versus gypsum content from the full-diameter measurements, shown for comparison with Figures 3 and 4. There is a definite decrease in grain density with increasing gypsum content.

Figure 5 is a plot of grain density versus gypsum content from the full-diameter measurements and is shown for comparison with Figures 3 and 4. The grain densities for pure calcite and dolomite are indicated for comparison. As expected, there is a definite relation of decreasing grain density with increasing gypsum content. Grayburg formation deposition occurred as shallow-shelf carbonate muds [Ward et al., 1986], primarily limestone, which has a grain density of 2.71 g/cm^3. After deposition, secondary dolomitization converted the rocks to dolostone, which has a grain density of 2.87 g/cm^3. Following dolomitization the rocks were commonly cemented with anhydrite (ρ_g = 2.96 g/cm^3) and gypsum (ρ_g = 2.31 g/cm^3). If the primary cement was anhydrite, then an increase in the grain-volume fraction of anhydrite would cause the overall grain density to increase above 2.87 g/cm^3. On the other hand, if the primary cement was gypsum, then an

increase in the grain-volume fraction of gypsum would cause the overall grain density to decrease below 2.87 g/cm^3. Figure 5 shows a definite decrease in grain density with increasing gypsum content. Gypsum appears to be the primary cement in these rocks.

Ultrasonic Measurement Program

The 20 plugs were sent to Verde GeoScience for ultrasonic velocity measurements, after completion of the measurements by Core Laboratories. Compressional (P) and two independent, orthogonally polarized shear (S1, S2) velocities were measured. As the plugs and the core were not oriented, no attempt was made to align the shear polarizations to any planar features in the core. Shear velocities reported here are averages of S1 and S2. The central frequency for the P and S ultrasonic transducers was 1 MHz. The plugs were measured dry (pores filled with air) and fully saturated with oil-field brine. The dry and saturated measurements were made at 4 differential pressures ($P_{diff} = P_{confining} - P_{pore}$): 1000, 2000, 3000, and 5000 psid. For the dry measurements the pore pressure was 0 psig and for the saturated measurements the pore pressure was 1000 psig. Resolution of the first-break picks was ±0.01 μsec. Precision of the P and S velocities was conservatively ±0.5%.

Compressional velocity (v_p), shear velocity (v_{s1}, v_{s2}, avg. v_s), v_p/v_s ratio, dynamic bulk modulus (K), dynamic shear moduli (G), and dynamic Young's modulus (E) were tabulated in the Verde GeoScience report. I have plotted all the data for each plug sample in Appendix A.

Ultrasonic Velocities

In this paper, I concentrate on the velocity measurements made at a differential pressure of 2000 psid (13.8 MPa). The West Texas reservoir is at a depth of about 3000 feet. The lithostatic stress gradient in the area is about 1 psi/ft and the reservoir pressure is about 1000 psig. Therefore, it is most appropriate to examine the velocities in this data set that were measured at 2000 psid. Table 2 lists these data.

Figures 6 and 7 are graphs of velocity versus porosity for the P-wave and S-wave velocities, respectively. In each figure, the open circles are the dry data and the filled circles are the saturated data. The dashed and solid best-fit lines are for dry and saturated data, respectively. The best-fit lines show that the velocities clearly decrease with increasing porosity.

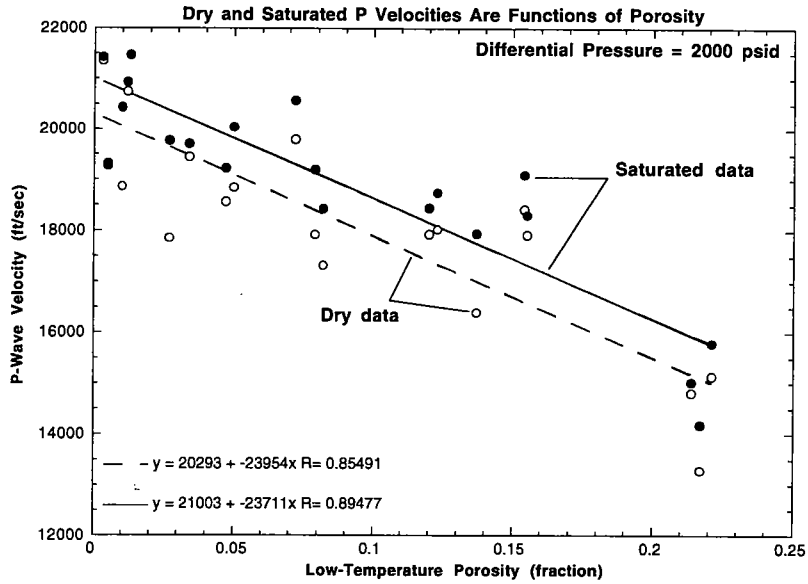

Figure 6

Figure 6: P-wave velocity versus porosity.

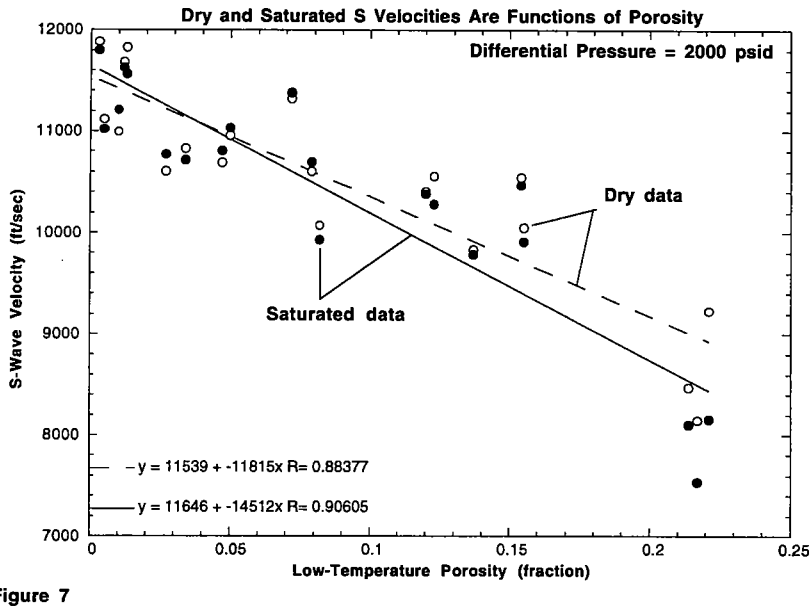

Figure 7

Figure 7: S-wave velocity versus porosity.

Figure 8 is a graph of $\Delta v = (v_{sat}-v_{dry})/v_{dry}$ versus porosity for both P and S velocities. It shows the effect of 100% replacement of air by oil-field brine. There is an average 4.2% increase in P-wave velocity and an average 1.5% decrease in S-wave velocity, when the rocks are saturated with brine as compared to when the rocks are dry (Table 2).

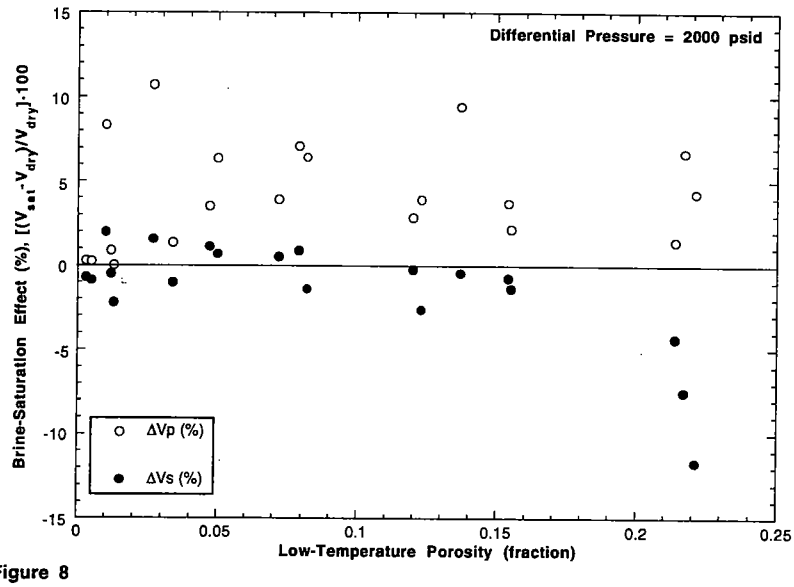

Figure 8: $\Delta v = (v_{sat}-v_{dry})/v_{dry}$ versus porosity for both P and S velocities, showing the effect of 100% replacement of air by oil-field brine.

The saturated P-wave velocity

$$v^*_p = \sqrt{\frac{K^*+(4/3)G^*}{\rho^*}} \qquad (3a)$$

is affected by brine saturation through the saturated-rock bulk modulus (K*) and bulk density (ρ*). At a constant saturation, the effect of brine saturation on P waves ($|\Delta v|_p$) is highest in low-porosity rocks because the density effect is smallest and the effect of pore-fluid substitution on pore stiffness is largest. As porosity increases, the density effect increases and the bulk-modulus effect decreases.

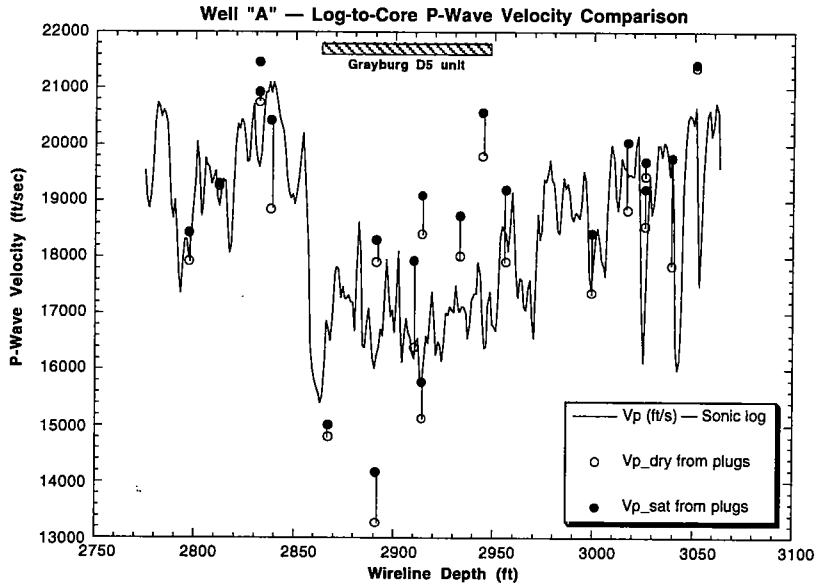

Figure 9

Figure 9: Comparison of ultrasonic core and sonic-log P-wave velocities.

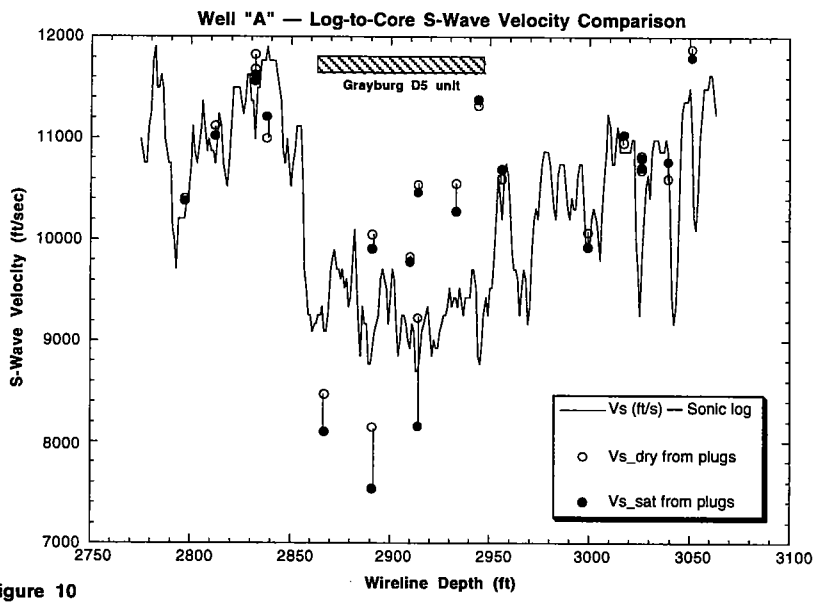

Figure 10

Figure 10: Comparison of ultrasonic core and sonic-log S-wave velocities.

For saturated S-wave velocities,

$$v^*_s = \sqrt{\frac{G^*}{\rho^*}} \quad , \tag{3b}$$

replacement of air by brine does not affect the shear modulus (G*) but causes the saturated bulk density (ρ*) to increase. The density effect gets larger as porosity increases, which causes v^*_s to decrease and the magnitude of the brine effect on S waves ($|\Delta v|_s$) to increase (Figure 8).

Figures 9 and 10 compare the ultrasonic core velocities to the sonic-log velocities for P and S waves, respectively. For the most part, ultrasonic velocities are higher than sonic-log velocities. There is more mismatch in the data within the main reservoir zone between 2860 and 2950 feet than there is above and below this zone. The two data sets generally follow each other and correlate with a linear coefficient of best-fit (r^2) of about 0.5. Some mismatch is expected. The two measurements sampled different paths, path lengths, and scales of heterogeneities. Using a velocity range of 10,000–20,000 ft/sec (3,048–6,096 m/sec), the ultrasonic transducers have a resonant frequency of 1 MHz and produce signals with 0.12–0.24 in. (0.3–0.6 cm) wavelengths. These are "point" measurements over path lengths of 8–16 wavelengths (i.e., 2-inch long plugs), affected by inch-scale heterogeneities (e.g., plug pairs 6H & 6V and 8H & 8V). In contrast, sonic logs have resonant frequencies about 15–20 kHz and produce signals with 0.5–1.3 ft (15–40 cm) wavelengths. Using a velocity range of 10,000–20,000 ft/sec (3,048–6,096 m/sec), they measure path lengths of 8 feet or more (8–16 wavelengths) and are affected by heterogeneities of several inches to feet. The mismatch between the ultrasonic and well-log velocities is attributable, in part, to these factors.

SEISMIC AND SONIC VELOCITIES

Ultrasonic P-wave velocities are affected by fluid effects because of scattering, solid-fluid inertial effects, and grain-scale local flow effects [e.g., Mavko and Jizba, 1991]. Velocities in saturated rock measured at ultrasonic frequencies are often faster than velocities measured at lower seismic and sonic frequencies. Velocities in dry rock are largely insensitive to the frequency of measurement. Gassmann's [1951] equation relates the saturated-rock bulk modulus (K*) to the dry-rock bulk modulus (K_d). It applies at low frequencies where scattering, solid-fluid inertial effects, and grain-scale local flow effects are negligible. Seismic and sonic frequencies typically lie within this low-frequency band.

Therefore, my approach has been to use the dry ultrasonic data and Gassmann's equation to estimate the effects of fluid saturation on measurements at seismic and sonic frequencies.

Gassmann's [1951] equations are low-frequency (i.e., zero-frequency) estimates of the fluid-saturated moduli, when the dry-frame moduli, mineral moduli, fluid moduli, and porosity are known. The saturated bulk modulus (K*) is given by

$$K^* = K_d + K_p = K_d + \frac{\left(1 - \frac{K_d}{K_m}\right)^2}{\frac{\phi}{K_f} + \frac{1-\phi}{K_m} - \frac{K_d}{K_m^2}} \tag{4a}$$

where K_d is the dry-frame bulk modulus, K_m is the mineral bulk modulus, K_f is the fluid modulus, K_p is the bulk modulus of the fluid-filled pore space, and ϕ is porosity. The shear modulus is assumed to be unaffected by saturation, so

$$G^* = G_d \tag{4b}$$

where G* is the saturated-rock shear modulus and G_d is the dry-frame shear modulus.

Estimation of Sonic Velocities from Core Measurements

To estimate the sonic-log velocities, I wanted to take advantage of the full-diameter core samples. These samples were selected every foot of the core. I used the following basic procedure:

1) Estimate the mineral moduli (K_m & G_m) from the grain-density measurements on the plug samples (Appendix B).
2) From measurements of dry-rock ultrasonic velocities, density and porosity on the plug samples, obtain linear least-squares regression fits to dry-rock moduli (K_d & G_d) versus porosity (ϕ). These fits have the form: $K_d/K_m = f(\phi)$ and $G_d/G_m = f(\phi)$.
3) Estimate the mineral moduli (K_m & G_m) from the grain-density measurements on the full-diameter core samples (Appendix B).
4) Apply the $K_d/K_m = f(\phi)$ and $G_d/G_m = f(\phi)$ linear-regression fits obtained in Step 2 to the full-diameter-core estimates of mineral moduli to obtain estimates of the dry-rock moduli (K_d & G_d) for each foot of core.

5) Use Gassmann's equations 4a and 4b to obtain estimates of the low-frequency, saturated-rock moduli (K* & G*) for each foot of core.
6) Calculate saturated-rock densities (ρ^*) using equations 1 and 2.
7) Calculate the saturated-rock velocities (v^*_p & v^*_s) using equations 3a and 3b.

For brine, I used density $\rho_f = 1.028$ g/cm^3 based on measurements of the reservoir brine, bulk modulus $K_f = 2.5$ GPa, and velocity = 5116 ft/sec (1560 m/sec) [Long and Chierici, 1961; Carmichael, 1989, p. 469].

I explored three methods to estimate the grain moduli, K_m and G_m, from the grain-density information. I call these three methods the dolomite-calcite transform, the dolostone-limestone transform, and the core-constrained transform. Details about these transforms are given in Appendix B. In this section, I only discuss the results and how they compare to the open-hole sonic logs from Well A.

Using the dolomite-calcite transform, I assumed the principal mineral components of the Grayburg formation were calcite and dolomite. Assuming a two-phase system, the transform estimates the mineral modulus M_m using

$$M_m = M_1 + \int_0^{X_2} \frac{\partial M_m}{\partial X_2} dx_2' = M_1 + \frac{\partial M_m}{\partial X_2} X_2 \quad ; \quad X_1 + X_2 = 1, \tag{5a}$$

where M_m is the desired estimate of the effective mineral modulus (K_m or G_m), X_1 and X_2 are the grain-volume fractions of pure end-member phases 1 and 2, and M_1 and M_2 are mineral moduli of phase 1 and 2. X_1 and X_2 vary from 0 to 1. The quantity $\partial M_m/\partial X_2$ is presumed constant and equal to $(M_2–M_1)$. One can think of equation 5a as being the grain-density weighted arithmetic average between the mineral moduli M_1 and M_2 of the pure end-member phases 1 and 2

$$\begin{aligned} M_m &= M_1 + w(M_2 - M_1) \quad ; \quad 0 \le w \le 1 \\ &= M_1 + \frac{(\rho_g - \rho_1)}{(\rho_2 - \rho_1)}(M_2 - M_1) \end{aligned} \quad , \tag{5b}$$

where w is the weighting factor and is equal to X_2, ρ_1 and ρ_2 are the grain densities of the pure end-member phases 1 and 2, and ρ_g is the measured grain density. Here, the grain-density weighting factor (w) is the mineral fraction of dolomite (phase 2). When compared to the sonic logs, this method resulted in saturated velocities that were too high (Figure 11). This dolomite-calcite transform method does not take into account the lower mineral moduli

of the other mineral components in the Grayburg formation, that is, anhydrite, gypsum and quartz [Ward et al., 1986].

Using the dolostone-limestone transform, I assumed the principal rock components of the Grayburg formation were limestone and dolostone. I used equation 5 again, except that now phase 1 was limestone and phase 2 was dolostone. This technique gave a good fit to the sonic logs (Figure 12). In this dolostone-limestone approach the mineral moduli were generally lower than those for dolomite-calcite approach. These lowered moduli capture some of the effects of the other mineral components in the Grayburg formation.

I tried a third method to estimate K_m and G_m, the core-constrained method (Appendix B). I used the full-diameter core measurements to try to estimate the grain-volume fractions of dolomite, calcite, anhydrite, gypsum, and quartz silt. This core-constrained method produced a good fit to the P-wave sonic log (Figure 13), but the fit to the S-wave log was less satisfactory than the when using the dolostone-limestone method (cf. Figure 12). The core-constrained method produces a better fit to the well logs than the dolomite-calcite method (compare Figures 11 & 13). The core-constrained transform method suffered because I did not have reliable quantitative estimates of the mineral fractions in these rocks. The best way to estimate mineral moduli is to use quantitative mineralogy obtained from petrographic and geochemical analyses (e.g., mineral modal analyses).

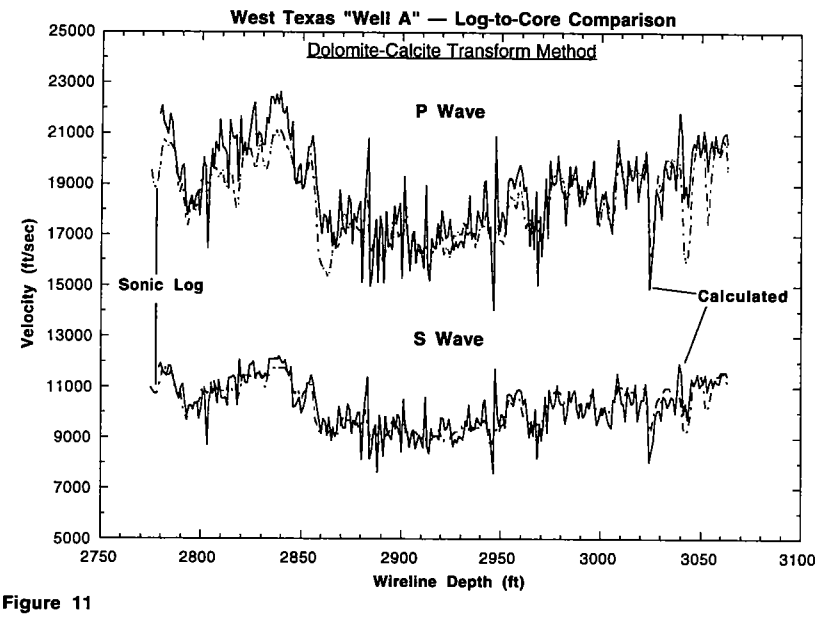

Figure 11

Figure 11: Log-to-core comparison of sonic velocities. Core velocities were calculated using mineral moduli estimated by the dolomite-calcite transform method.

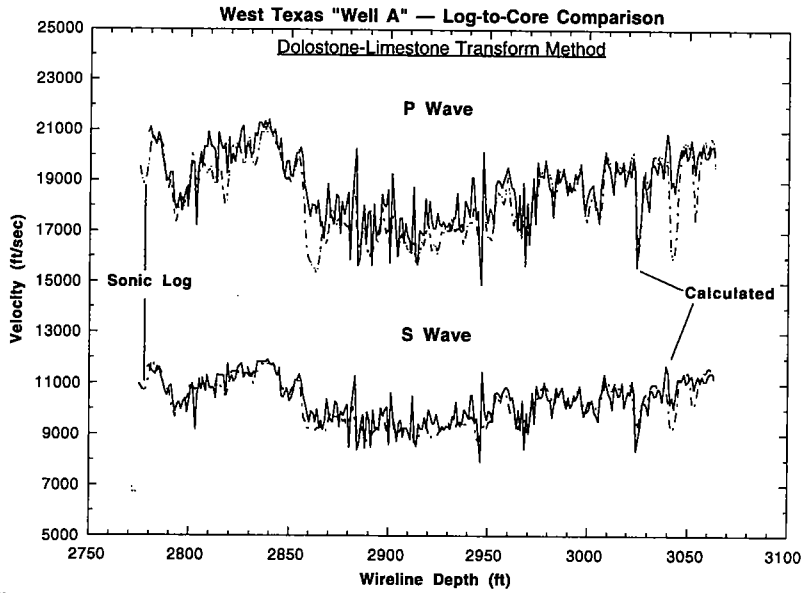

Figure 12

Figure 12: Log-to-core comparison of sonic velocities. Core velocities were calculated using mineral moduli estimated by the dolostone-limestone transform method.

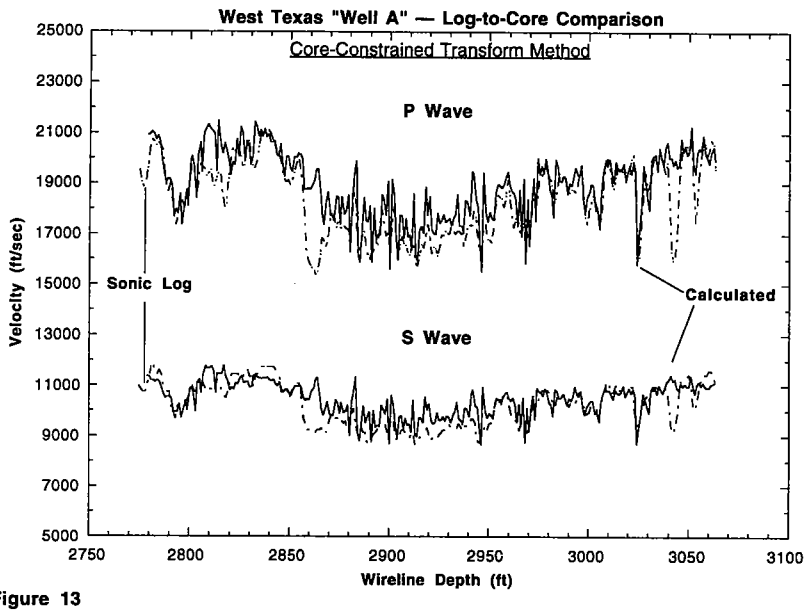

Figure 13

Figure 13: Log-to-core comparison of sonic velocities. Core velocities were calculated using mineral moduli estimated by the core-constrained transform method.

I use the dolostone-limestone method in the rest of this report. It is easy to use, it appears to capture the overall characteristics of the mineralogy, and the resulting fit to both P- and S-wave sonic logs is good (correlation coefficient, r = +0.84; coefficient of determination, $r^2 = 0.71$).

THE BRINE EFFECT — 100% REPLACEMENT OF AIR BY BRINE IN THE PORE SPACE

Table 2 shows that 100% replacement of air by brine in the plug samples produced a measured average v_p increase of 4.18% (range = 0 to 10.71%) and an average v_s decrease of -1.45% (range = -11.68 to +1.98%). For these measured data, there is a very weak (r = 0.13, $r^2 = 0.02$) positive correlation between Δv_p and ϕ and a strong (r = -0.71, $r^2 = 0.51$) negative correlation between Δv_s and ϕ.

I used Gassmann's [1951] equation to estimate the low-frequency "brine effect" (i.e., 100% replacement of air by brine in the pore space). Table 4 shows that the Gassmann equation predicts an average v_p increase of 1.98% (range = -1.13 to 7.48%) and an average v_s decrease of -1.81% (range = -0.05 to -4.75%). There is a weak (r = -0.48, $r^2 = 0.23$) negative correlation between Δv_p and ϕ and a very strong (r = -0.99, $r^2 = 0.99$) negative correlation between Δv_s and ϕ. These negative correlations between Δv and porosity result from the increase in rock density when brine replaces air in the pore space (equations 3a & 3b).

Figure 14 is a comparison of P-wave velocities in brine-saturated and air-saturated (i.e., dry) rocks. This plot was generated using the dry moduli (K_d and G_d) obtained to match the sonic logs (Figure 12). Both air- and brine-saturated v_p's were calculated using these moduli. The lines in Figure 14 were drawn to help visualize the magnitude of the brine effect; the 1:1 line indicates when $v^*_p = v_{pdry}$ and the other lines indicate when v^*_p is 2.5% and 5% greater than v_{pdry}. On average, the brine-saturated velocities are 1.4% higher than the air-saturated velocities (range = 0.03 to 4.9%). The curvature in the data reflects the sensitivity of v_p to changes in fluid content at low porosities (high v_p) and the decreased sensitivity of v_p at high porosities (lower v_p) that results from the opposing density effect (cf. equation 3a). This v_p* versus v_{pdry} relation can be approximated by the exponential relation:

$$v^*_p\,(\text{ft/s}) = 5920\exp\left(6.22\times10^{-5}v_{pdry}\right)$$
$$v^*_p\,(\text{km/s}) = 1.80\exp\left(0.204v_{pdry}\right) \quad \ldots\ r^2 = 0.994.$$

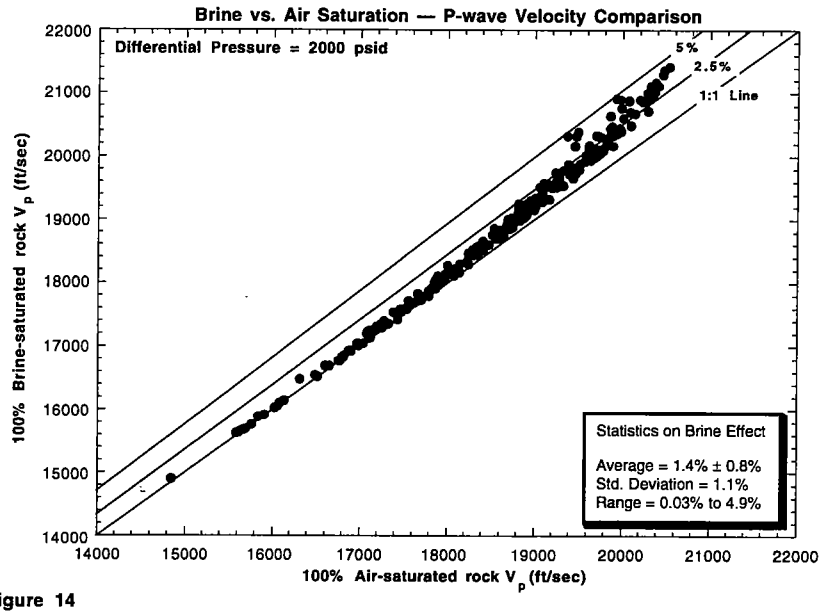

Figure 14

Figure 14: Comparison of P-wave velocities in brine-saturated versus air-saturated rocks. This plot was generated using the dry moduli (K_d and G_d) obtained to match the sonic logs in Figure 12.

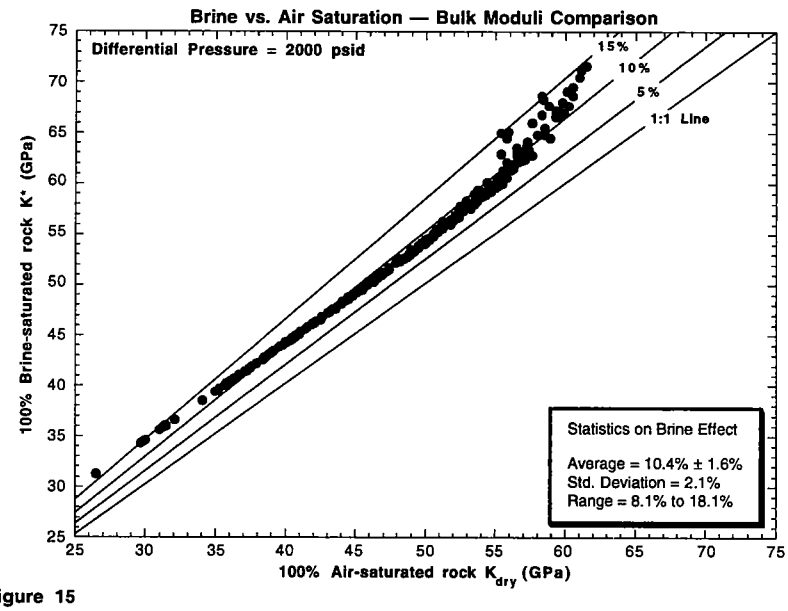

Figure 15

Figure 15: Comparison of saturated versus dry bulk moduli, K* versus K_d. This plot was generated using the dry bulk modulus (K_d) obtained to match the sonic logs in Figure 12.

Another way to look at these data is to compare the saturated versus dry bulk moduli, K* versus K_d (Figure 15). Here the effect of changes in fluid content is quite clear. On average, K* is 10.4% higher than K_d—the average deviation is 10.4 ± 1.6% and the brine effect ranges from 8.1 to 18.1%. The curvature in these data reflects the interaction between the strongest effect of decreasing sensitivity of K* (or $K_p = K^* - K_d$; equation 6a) to changes in fluid content (K_f) with increasing porosity, the intermediate effect of increasing sensitivity of K* with decreasing K_d (i.e., K_d/K_m), and the small effect of increasing sensitivity of K* with increasing K_m. This K* versus K_d relation can be approximated by the exponential relation:

$$K^*(\text{GPa}) = 18.4 \exp\left(2.17 \times 10^{-2} K_d\right) \ldots r^2 = 0.994.$$

As suggested by the average brine effects in Figures 14 and 15, the bulk moduli are more sensitive to changes in fluid content than P-wave velocities. This suggests that to detect the effects of fluid substitution we should be monitoring changes in moduli rather than changes in velocity (e.g., CO_2 flooding of a previously waterflooded reservoir).

Comparisons between Mineral Moduli Estimation Methods

These estimates of the brine effect will depend on the mineral moduli (equation 4a). For example had I used higher mineral moduli, such as those from the dolomite-calcite transform method, these estimates of the effect of brine would have been larger. The tables below give summary statistics of the brine effect for the three methods used to estimate the mineral moduli (Appendix B).

Summary Statistics on Effect of 100% Replacement of Air by Brine on P-wave Velocities
Comparison by mineral moduli estimation method

	Dolomite-Calcite	Dolostone-Limestone	Core Constrained
Average	3.2 ± 1.1%	1.4 ± 0.8%	2.0 ± 0.9%
Std. Deviation	± 1.4%	± 1.1%	± 1.2%
Range	1.1% to 8.5%	0.03% to 4.9%	0.4% to 5.7%

Summary Statistics on Effect of 100% Replacement of Air by Brine on Bulk Moduli
Comparison by mineral moduli estimation method

	Dolomite-Calcite	Dolostone-Limestone	Core Constrained
Average	17.3 ± 2.7%	10.4 ± 1.6%	12.8 ± 2.2%
Std. Deviation	± 3.7%	± 2.1%	± 2.9%
Range	12.2% to 30.8%	8.1% to 18.1%	9.4% to 25.5%

In these tables, the brine effects are expressed using

$$\Delta v_p(\%) = \left(\frac{v^*_p - v_{pdry}}{v_{pdry}} \right) \cdot 100 \qquad \text{and} \qquad \Delta K(\%) = \left(\frac{K^* - K_d}{K_d} \right) \cdot 100$$

for P-wave velocities and bulk moduli, respectively. The dolomite-calcite transform method resulted in the largest estimates of the brine effect. The dolostone-limestone transform resulted in the smallest estimates. The core-constrained method yielded intermediate estimates, which overlapped some with the dolostone-limestone estimates. I believe the most appropriate estimates of the brine effect are those represented by the dolostone-limestone and core-constrained transforms. I use the dolostone-limestone transform here.

ESTIMATES OF CO_2 EFFECTS ON SEISMIC VELOCITIES

The operating temperature in the West Texas reservoir is close to 88°F (31°C). Reservoir fluid pressures range from about 900 psig (6.2 MPa) to about 1200 psig (8.3 MPa) [pers. comm., Paul Griffith, Company reservoir engineer, 1992]. So, I estimated the fluid properties at these reservoir conditions.

The oil in the reservoir is a light oil with API gravity = 30–32° API (≈0.87 g/cm^3). At 88°F, the measured isothermal compressibilities (β_T) of the oil is 5.00×10^{-6} psi^{-1} (0.73 GPa^{-1}) at 900 psig and 4.85×10^{-6} psi^{-1} (0.70 GPa^{-1}) at 1200 psig [pers. comm., Paul Griffith, 1992]. The corresponding isothermal bulk moduli ($K_T = 1/\beta_T$) are 1.38 GPa at 900 psig and 1.42 GPa at 1200 psig. The associated viscosities for this oil are 2.47 cP at 900 psig and 2.50 cP at 1200 psig [pers. comm., Paul Griffith, 1992]. I estimate the P-wave velocity for this oil (v_{poil}) to be 1395 m/sec (4577 ft/sec) at 900 psig and 1405 m/sec (4610 ft/sec) at 1200 psig [Wang, 1988]. Using oil density ρ_{oil} = 0.87 g/cm^3, I estimated the corresponding adiabatic (isentropic) bulk moduli ($K_S = \rho_{oil} \cdot v_{poil}^2$) to be 1.69 GPa at

900 psig and 1.72 GPa at 1200 psig. These reservoir oil properties are summarized in the table below.

Oil Properties Used to Estimate Effects of CO_2

T (°F)	P (psig)	K_T (GPa)	Viscosity (cP)	v_{poil} (m/s)	K_{Soil} (GPa)
88	900	1.38	2.47	1395	1.69
88	1200	1.42	2.50	1405	1.72

The reservoir temperature of 88°F (31°C) is right at the critical temperature for pure CO_2. This is the temperature above which pure CO_2 is always in a vapor phase. The reservoir pressures of 900–1200 psig (6.2–8.3 MPa) span across the critical pressure for pure CO_2, which is 1070 psia (7.4 MPa). For West Texas reservoirs, the critical pressure is a good estimate of the minimum miscibility pressure (MMP), above which CO_2 can effectively extract hydrocarbons from crude oil to produce CO_2-hydrocarbon mixtures that are miscible with the oil [pers. comm., F. M. Orr, 1992; Orr and Taber, 1984].

Properties of CO_2 Used in CO_2 Effect Calculations

T (°F)	P (psig)	ρ_{CO2} (g/cm^3)	v_{pCO2} (m/s)	K_{SCO2} (GPa)
88	900	0.19	210	0.008
88	1200	0.70	190	0.025

I used the analytical equation of state given by Bender [1970; pers. comm., Maurice Stadler, Stanford University, 1992] to estimate the density of pure CO_2 . I used the data tabulated by Hilsenrath et al. [1955, 1960] and Vargaftik [1975] to estimate the P-wave velocities of pure CO_2.

To estimate the effects of CO_2 flooding on seismic velocities, I assumed a pre-CO_2, waterflooded reservoir with a water-to-oil ratio of 53% to 47% [pers. comm., Paul Griffith and Brett Newton, Company reservoir engineers, 1992]. After CO_2 has swept through a zone, I assumed a water-oil-gas mixture of 16%–8%–76%. I used the arithmetic average of these fluid components to calculate the densities of these fluid mixtures (ρ_f):

$$\rho_f = \sum_i S_i \rho_i \qquad (6)$$

where S_i is the pore-volume fraction or saturation of the *i*-th fluid component, and ρ_i is the density of the *i*-th fluid component. I used Wood's [1930] isopressure relation for fluid mixtures to calculate the bulk moduli of the fluid mixtures (K_f):

$$K_f = \left[\sum_i \frac{S_i}{K_i} \right]^{-1} \tag{7}$$

where again S_i is the pore-volume fraction or saturation of the *i*-th fluid component, and K_i is the bulk modulus of the *i*-th fluid component. Wood's relation applies when (1) the pressure within each fluid component is the same, (2) the fluid mixture is a multi-component fluid such as gas bubbles in brine or a mixture of oil and brine, and (3) there has been no dissolution of one component in another such as gas dissolved in oil. The properties of these fluid mixtures are given below:

Properties of Fluid Mixtures Used in CO_2 Effect Calculations

T, P	Fluid Property	pre-CO_2 injection (53% oil, 47% brine)	post-CO_2 injection (16% oil, 8% water, 76% CO_2)
88°F, 900 psig	ρ_f	0.94 g/cc	0.37 g/cc
	K_f	1.99 GPa	0.011 GPa
88°F, 1200 psig	ρ_f	0.94 g/cc	0.75 g/cc
	K_f	2.02 GPa	0.033 GPa

These fluid properties were substituted into equations 2, 3 and 4 to estimate the seismic rock properties of pre-CO_2 and post-CO_2 injection conditions. The contrast between these conditions is summarized in the tables below and is shown in Figures 16–19.

Summary Statistics on Effect of CO_2 Injection on P-wave Velocities

Comparison by reservoir conditions

	88 °F, 900 psig	88 °F, 1200 psig
Average	-1.5 ± 0.5%	-2.1 ± 0.3%
Std. Deviation	± 0.7%	± 0.5%
Range	-0.7% to -4.2%	-1.5% to -4.2%

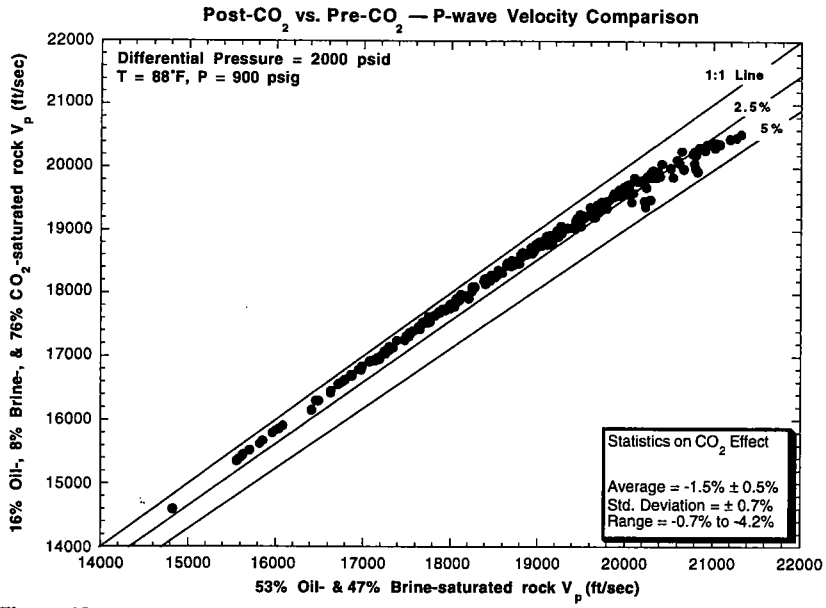

Figure 16

Figure 16: Comparison of P-wave velocities under post-CO_2 versus pre-CO_2 conditions at T = 88°F and P = 900 psig. K_d and G_d were obtained to match the sonic logs in Figure 12.

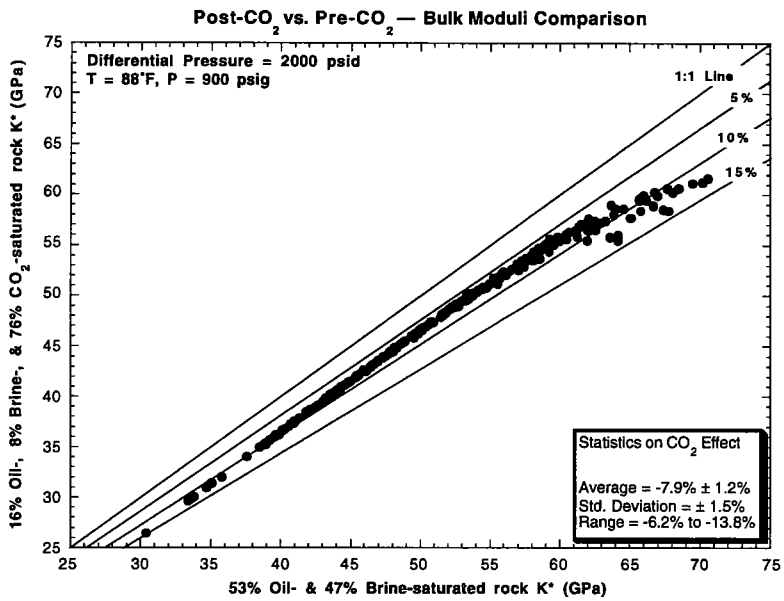

Figure 17

Figure 17: Comparison of bulk moduli under post-CO_2 versus pre-CO_2 conditions at T = 88°F and P = 900 psig. K_d was obtained to match the sonic logs in Figure 12.

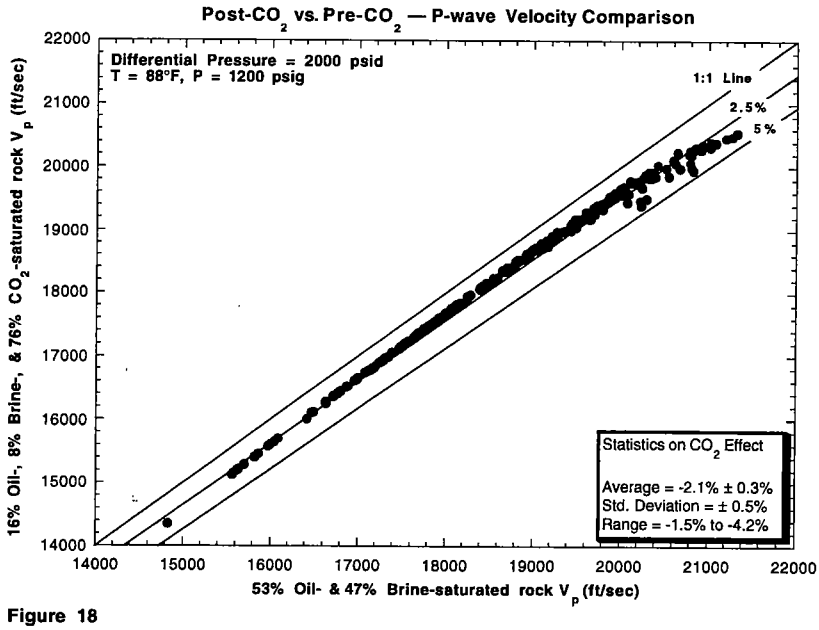

Figure 18

Figure 18: Comparison of P-wave velocities under post-CO_2 versus pre-CO_2 conditions at T = 88°F and P = 1200 psig. K_d and G_d were obtained to match the sonic logs in Figure 12.

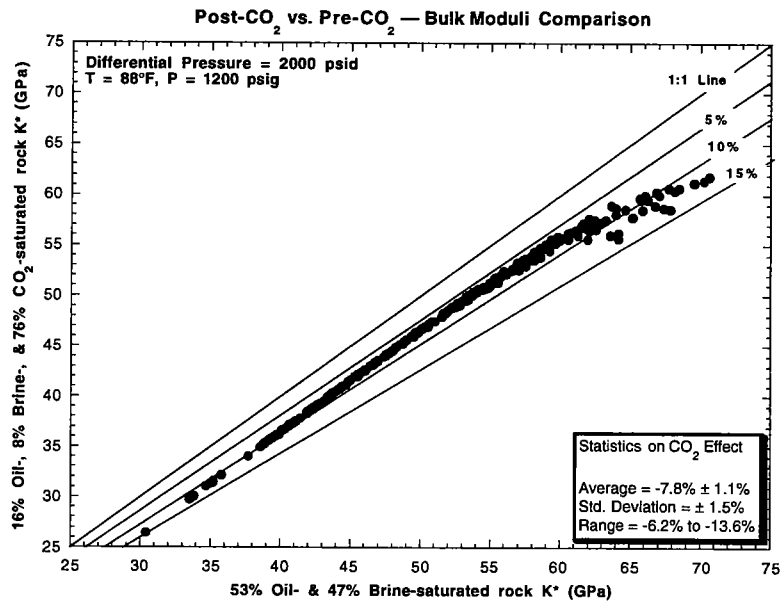

Figure 19

Figure 19: Comparison of bulk moduli under post-CO_2 versus pre-CO_2 conditions at T = 88°F and P = 1200 psig. K_d was obtained to match the sonic logs in Figure 12.

Summary Statistics on Effect of CO_2 Injection on Bulk Moduli
Comparison by reservoir conditions

	88 °F, 900 psig	88 °F, 1200 psig
Average	-7.9 ± 1.2%	-7.8 ± 1.1%
Std. Deviation	± 1.5%	± 1.5%
Range	-6.2% to -13.8%	-6.2% to -13.6%

The contrasts are expressed using

$$\Delta v^*_p(\%) = \left(\frac{v^*_{post-CO2} - v^*_{pre-CO2}}{v^*_{pre-CO2}} \right) \cdot 100$$

$$\Delta K^*(\%) = \left(\frac{K^*_{post-CO2} - K^*_{pre-CO2}}{K^*_{pre-CO2}} \right) \cdot 100$$

for P-wave velocities and bulk moduli, respectively. The estimated contrast between pre- and post-CO_2 conditions is a small -2% for P-wave velocities and a larger -8% for bulk moduli. These results emphasize the suggestion that to detect the effects of fluid displacement efforts might be made to monitor changes in moduli rather than changes in velocity (e.g., CO_2 flooding of a previously waterflooded reservoir).

For completeness, let's look at the effect of CO_2 on the P-wave impedance (Z^*_p)

$$Z^*_p = \rho^* v^*_p = \sqrt{\rho^* \left[K^* + (4/3) G^* \right]}. \quad (8)$$

The table below gives the estimated contrast between pre- and post-CO_2 conditions. The -3% contrast is better than for P-wave velocities but less than for bulk moduli.

Summary Statistics on Effect of CO_2 Injection on P-wave Impedance
Comparison by reservoir conditions

	88 °F, 900 psig	88 °F, 1200 psig
Average	-3.2 ± 0.6%	-2.6 ± 0.4%
Std. Deviation	± 0.8%	± 0.5%
Range	-2.2% to -6.4%	-1.9% to -4.8%

The bulk-wave (K-wave) impedance (Z^*_k)

$$Z^*_p = \rho^* v^*_k = \sqrt{\rho^* K^*} \qquad (9)$$

is more sensitive than Z^*_p but to estimate it requires information on S-wave properties. The table below gives the estimated contrast between pre- and post-CO_2 conditions as being about -4.5%.

Summary Statistics on Effect of CO_2 Injection on Bulk-wave (K-wave) Impedance
Comparison by reservoir conditions

	88 °F, 900 psig	88 °F, 1200 psig
Average	-4.8 ± 0.8%	-4.2 ± 0.7%
Std. Deviation	± 1.0%	± 0.8%
Range	-3.6% to -8.9%	-3.3% to -7.3%

CONCLUSIONS

The P-wave velocity contrast between a CO_2 swept zone and an unswept zone is likely to be small, about a 2% contrast. In comparison, the bulk-modulus contrast is about 4 times larger, about a 8% contrast. This suggests that if we want to monitor CO_2 flooding effects using seismic data we should consider monitoring bulk-modulus changes rather than P-wave velocity changes.

Monitoring P-wave impedance contrasts would be somewhat better than monitoring P-wave velocity contrasts, because the inverse effects of bulk modulus and density for velocity (cf. equation 3) become multiplicative for impedance (cf. equation 8). The K-wave impedance (equation 9) provides a somewhat better impedance contrast.

In order of decreasing sensitivity to changes in fluid content, the seismic properties are:

$$K^* \geq Z^*_k \geq Z^*_p \geq v^*_p.$$

The two most sensitive properties (K^* and Z^*_k) require obtaining S-wave information along with P-wave data, in order for them to be evaluated. However, this should not present an insurmountable problem for crosswell seismic data acquisition. Crosswell P-wave and S-wave data have already be obtained in this West Texas field [e.g., STP-3, 1992].

In this report, I have assumed that the fluids exist as distinct phases and do not dissolve in or become miscible with one another. The reservoir oil is a live oil, i.e., it contains gas

in solution. So the seismic properties of this oil and the unswept zone will be lower than estimated here. During CO_2 flooding under minimum miscibility pressure (MMP) conditions, CO_2-hydrocarbon mixtures become miscible with the crude oil. So the seismic properties of the CO_2-swept zones will be lower than estimated here. Generally, however, I would expect the contrast between a CO_2-swept and an unswept zone to be about the same magnitude as estimated here. More complex calculations could be carried out to provide more accurate estimates of the seismic contrast, provided the fluid phase-behavior data are available.

ACKNOWLEDGMENTS

We thank Chevron Oil Field Research Company (now Chevron Petroleum Technology Company) for providing the field site and co-sponsoring this study with Stanford University. We thank Verde GeoScience, Inc., and Core Laboratories, Inc., for conducting the core measurements. We also thank the Gas Research Institute and the Packard Foundation for their continuing support of the Seismic Tomography Project (STP) at Stanford University.

REFERENCES

Bender, E., 1970, "Equations of state exactly representing the phase behavior of pure substances," Proceedings of the Fifth Symposium on Thermophysical Properties, American Society of Mechanical Engineers, pp. 227–235.

Carmichael, R. S., 1989, "CRC Practical Handbook of Physical Properties of Rocks and Minerals," CRC Press, Inc.

Gassmann, F., 1951, "Über die elastizität poröser medien," Vierteljahrsschrift der Naturforschenden Gesellschaft in Zürich, v. 96, pp. 1–23.

Hilsenrath, J., et al., 1955, 1960, "Tables of thermal properties of gases," Circular 564, National Bureau of Standards, Washington, D.C.

Hill, R. W., 1952, "The elastic behavior of a crystalline aggregate," Proc. Phys. Soc. London, Series A, v. 65, pp. 349–354.

Long, G., and G. Chierici, 1961, "Salt content changes compressibility of reservoir brines," Petroleum Engineering, (July 1961), pp. B25–B31.

Mavko, G., and D. Jizba, 1991, "Estimating grain-scale fluid effects on velocity dispersion in rocks," Geophysics, v. 56, no. 12, pp. 1940–1949.

Orr, F. M., Jr., and J. J. Taber, 1984, "Use of carbon dioxide in enhanced oil recovery," Science, v. 224, no. 4649, pp. 563–569.

STP-3, 1992, Seismic Tomography Project, Volume 3, No. 1, July 1992.

Vargaftik, N. B., 1975, "Tables on the thermophysical properties of liquids and gases," Hemisphere Publishing Co., Washington, D.C.

Wang, Zhijing, 1988, "Wave velocities in hydrocarbons and hydrocarbon saturated rocks—With applications to EOR monitoring," Ph.D. Dissertation, Geophysics Department, Stanford University.

Ward, R. F., C. G. St. C. Kendall, and P. M. Harris, 1986, "Upper Permian (Guadalupian) facies and their association with hydrocarbons—Permian Basin, west Texas and New Mexico," American Association of Petroleum Geologists Bulletin, v. 70, no. 3, pp. 239–262.

Wood, A. D., 1930, "A textbook of sound," G. Bell and Sons, London.

Table 1
Results from Core Laboratories
West Texas "Well A"

Sample Number	Approximate Wireline Log Depth (feet)	Core-Gamma Log Depth (feet)	Reservoir (R) or Non-Reservoir (NR) Rock	Stratigraphic Interval	Permeability		Low-Temperature Porosity (fraction)	Grain Density (g/cc)
					Horizontal (mD)	Vertical (mD)		
1V	2,797.0	2,794.1	R	E to D5		1.08	0.120	2.85
2V	2,810.5	2,807.1	NR	E to D5		<0.01	0.005	2.73
3H	2,831.0	2,826.5	NR	E to D5	<0.01		0.013	2.81
3V	2,831.0	2,826.5	NR	E to D5		<0.01	0.012	2.80
4V	2,837.0	2,833.1	NR	E to D5		<0.01	0.010	2.86
5V	2,868.0	2,865.1	R	D5 to M		53.10	0.214	2.84
6H	2,890.0	2,887.1	R	D5 to M	41.10		0.155	2.85
6V	2,890.0	2,887.1	R	D5 to M		53.90	0.217	2.85
7V	2,910.0	2,907.9	R	D5 to M		16.90	0.137	2.79
8H	2,914.0	2,911.8	R	D5 to M	17.00		0.154	2.84
8V	2,914.0	2,911.8	R	D5 to M		66.70	0.221	2.85
9V	2,933.0	2,928.9	R	D5 to M		2.56	0.123	2.78
10V	2,944.0	2,940.1	R	D5 to M		0.06	0.072	2.82
11V	2,956.0	2,951.9	NR	M to S.		0.04	0.079	2.83
12V	2,999.0	2,997.1	R	M to S.		0.07	0.082	2.78
13V	3,016.0	3,013.9	NR	M to S.		0.01	0.050	2.87
14H	3,026.0	3,024.1	R	M to S.	<0.01		0.034	2.72
14V	3,026.0	3,024.1	R	M to S.		<0.01	0.047	2.75
15V	3,038.5	3,034.5	NR	M to S.		<0.01	0.027	2.88
16V	3,048.5	3,044.5	NR	San Andres		<0.01	0.003	2.75

Table 2
Ultrasonic Velocities Measured at 2000 psid Differential Pressure
West Texas "Well A"

Sample No.	Approx. Wireline Depth (feet)	Res. (R) or Non-Res. (NR)	Stratigraphic Interval	Porosity (fraction)	Perm. (mD)	Grain Density (g/cc)	Dry Measurements		Brine-Saturated Measurements		Measured Brine Effect	
							Vp (ft/s)	Vs (ft/s)	Vp (ft/s)	Vs (ft/s)	ΔVp	ΔVs
1V	2,797.0	R	E to D5	0.120	1.08	2.85	17926	10407	18436	10382	2.85%	-0.24%
2V	2,810.5	NR	E to D5	0.005	0.01	2.73	19263	11117	19309	11019	0.24%	-0.88%
3H	2,831.0	NR	E to D5	0.013	0.01	2.81	21466	11823	21466	11563	0.00%	-2.20%
3V	2,831.0	NR	E to D5	0.012	0.01	2.80	20744	11683	20929	11625	0.89%	-0.50%
4V	2,837.0	NR	E to D5	0.010	0.01	2.86	18853	10992	20428	11210	8.35%	1.98%
5V	2,868.0	R	D5 to M	0.214	53.10	2.84	14809	8471	15022	8103	1.44%	-4.34%
6H	2,890.0	R	D5 to M	0.155	41.10	2.85	17914	10049	18305	9910	2.18%	-1.38%
6V	2,890.0	R	D5 to M	0.217	53.90	2.85	13289	8146	14179	7535	6.70%	-7.50%
7V	2,910.0	R	D5 to M	0.137	16.90	2.79	16397	9830	17944	9786	9.43%	-0.45%
8H	2,914.0	R	D5 to M	0.154	17.00	2.84	18414	10546	19094	10467	3.69%	-0.75%
8V	2,914.0	R	D5 to M	0.221	66.70	2.85	15136	9231	15785	8153	4.29%	-11.68%
9V	2,933.0	R	D5 to M	0.123	2.56	2.78	18027	10556	18735	10280	3.93%	-2.61%
10V	2,944.0	R	D5 to M	0.072	0.06	2.82	19794	11320	20569	11379	3.92%	0.52%
11V	2,956.0	NR	M to S.A.	0.079	0.04	2.83	17923	10603	19193	10695	7.09%	0.87%
12V	2,999.0	R	M to S.A.	0.082	0.07	2.78	17319	10073	18431	9932	6.42%	-1.40%
13V	3,016.0	NR	M to S.A.	0.050	0.01	2.87	18842	10957	20042	11033	6.37%	0.69%
14H	3,026.0	R	M to S.A.	0.034	0.01	2.72	19444	10828	19705	10716	1.34%	-1.03%
14V	3,026.0	R	M to S.A.	0.047	0.01	2.75	18558	10686	19213	10807	3.53%	1.13%
15V	3,038.5	NR	M to S.A.	0.027	0.01	2.88	17856	10602	19769	10768	10.71%	1.57%
16V	3,048.5	NR	San Andres	0.003	0.01	2.75	21363	11882	21421	11797	0.27%	-0.72%
Column Averages				0.089	12.63	2.81	18167	10490	18899	10358	4.18%	-1.45%

Table 3
Dry Ultrasonic Velocities Measured at 2000 psid Differential Pressure
West Texas "Well A"

Sample No.	Approx. Wireline Depth (feet)	Res. (R) or Non-Res. (NR)	Stratigraphic Interval	Porosity (fraction)	Perm. (mD)	Grain Density (g/cc)	Dry Density (g/cc)	Dry Measurements				
								Vp (ft/s)	Vs (ft/s)	Bulk, Kd (GPa)	Shear, Gd (GPa)	P-Wave, Pd (GPa)
1V	2,797.0	R	E to D5	0.120	1.08	2.85	2.50	17926	10407	41.16	25.20	74.76
2V	2,810.5	NR	E to D5	0.005	0.01	2.73	2.71	19263	11117	52.00	31.16	93.54
3H	2,831.0	NR	E to D5	0.013	0.01	2.81	2.77	21466	11823	70.62	35.97	118.59
3V	2,831.0	NR	E to D5	0.012	0.01	2.80	2.77	20744	11683	63.90	35.12	110.73
4V	2,837.0	NR	E to D5	0.010	0.01	2.86	2.83	18853	10992	51.13	31.79	93.52
5V	2,868.0	R	D5 to M	0.214	53.10	2.84	2.23	14809	8471	25.66	14.89	45.51
6H	2,890.0	R	D5 to M	0.155	41.10	2.85	2.41	17914	10049	41.73	22.62	71.89
6V	2,890.0	R	D5 to M	0.217	53.90	2.85	2.23	13289	8146	18.25	13.74	36.56
7V	2,910.0	R	D5 to M	0.137	16.90	2.79	2.41	16397	9830	31.30	21.60	60.11
8H	2,914.0	R	D5 to M	0.154	17.00	2.84	2.41	18414	10546	42.66	24.87	75.82
8V	2,914.0	R	D5 to M	0.221	66.70	2.85	2.22	15136	9231	23.85	17.60	47.31
9V	2,933.0	R	D5 to M	0.123	2.56	2.78	2.44	18027	10556	39.99	25.26	73.67
10V	2,944.0	R	D5 to M	0.072	0.06	2.82	2.61	19794	11320	53.63	31.11	95.11
11V	2,956.0	NR	M to S.A.	0.079	0.04	2.83	2.60	17923	10603	41.43	27.18	77.67
12V	2,999.0	R	M to S.A.	0.082	0.07	2.78	2.55	17319	10073	39.00	24.03	71.05
13V	3,016.0	NR	M to S.A.	0.050	0.01	2.87	2.73	18842	10957	49.40	30.42	89.97
14H	3,026.0	R	M to S.A.	0.034	0.01	2.72	2.63	19444	10828	54.13	28.62	92.29
14V	3,026.0	R	M to S.A.	0.047	0.01	2.75	2.62	18558	10686	46.79	27.81	83.86
15V	3,038.5	NR	M to S.A.	0.027	0.01	2.88	2.80	17856	10602	43.95	29.24	82.93
16V	3,048.5	NR	San Andres	0.003	0.01	2.75	2.75	21363	11882	68.40	36.02	116.42
Column Averages				0.089	12.63	2.81	2.56	18167	10490	44.95	26.71	80.57

Table 4
Comparison of Measured-vs.-Gassmann Brine Effect at 2000 psid
West Texas "Well A"

Sample No.	Porosity (fraction)	Grain Density (g/cc)	Dry Measurements		Brine-Saturated Measurements		Measured Brine Effect		Dry P-wave Modulus (GPa)	Dry Shear Modulus (GPa)	Dry Bulk Modulus (GPa)	Grain Bulk Modulus (GPa)	Gassmann Brine		Gassmann-predicted Brine Effect	
			Vp (ft/s)	Vs (ft/s)	Vp (ft/s)	Vs (ft/s)	ΔVp	ΔVs					Vp (ft/s)	Vs (ft/s)	ΔVp	ΔVs
1V	0.120	2.85	17926	10407	18436	10382	2.85%	-0.24%	74.76	25.20	41.16	78.31	17992	10159	0.37%	-2.38%
2V	0.005	2.73	19263	11117	19309	11019	0.24%	-0.88%	93.54	31.16	52.00	73.14	20654	11106	7.22%	-0.09%
3H	0.013	2.81	21466	11823	21466	11563	0.00%	-2.20%	118.59	35.97	70.62	76.54	21506	11795	0.18%	-0.24%
3V	0.012	2.80	20744	11683	20929	11625	0.89%	-0.50%	110.73	35.12	63.90	76.46	21061	11657	1.53%	-0.23%
4V	0.010	2.86	18853	10992	20428	11210	8.35%	1.98%	93.52	31.79	51.13	78.89	20264	10972	7.48%	-0.18%
5V	0.214	2.84	14809	8471	15022	8103	1.44%	-4.34%	45.51	14.89	25.66	78.04	14877	8083	0.46%	-4.58%
6H	0.155	2.85	17914	10049	18305	9910	2.18%	-1.38%	71.89	22.62	41.73	78.61	17747	9732	-0.93%	-3.15%
6V	0.217	2.85	13289	8146	14179	7535	6.70%	-7.50%	36.56	13.74	18.25	78.26	13714	7767	3.20%	-4.66%
7V	0.137	2.79	16397	9830	17944	9786	9.43%	-0.45%	60.11	21.60	31.30	75.75	16674	9555	1.69%	-2.80%
8H	0.154	2.84	18414	10546	19094	10467	3.69%	-0.75%	75.82	24.87	42.66	78.16	18206	10216	-1.13%	-3.13%
8V	0.221	2.85	15136	9231	15785	8153	4.29%	-11.68%	47.31	17.60	23.85	78.61	15179	8792	0.28%	-4.75%
9V	0.123	2.78	18027	10556	18735	10280	3.93%	-2.61%	73.67	25.26	39.99	75.58	18059	10292	0.18%	-2.50%
10V	0.072	2.82	19794	11320	20569	11379	3.92%	0.52%	95.11	31.11	53.63	76.95	19814	11163	0.10%	-1.39%
11V	0.079	2.83	17923	10603	19193	10695	7.09%	0.87%	77.67	27.18	41.43	77.42	18307	10441	2.14%	-1.53%
12V	0.082	2.78	17319	10073	18431	9932	6.42%	-1.40%	71.05	24.03	39.00	75.36	17753	9910	2.50%	-1.62%
13V	0.050	2.87	18842	10957	20042	11033	6.37%	0.69%	89.97	30.42	49.40	79.31	19273	10856	2.29%	-0.92%
14H	0.034	2.72	19444	10828	19705	10716	1.34%	-1.03%	92.29	28.62	54.13	72.79	19729	10757	1.47%	-0.65%
14V	0.047	2.75	18558	10686	19213	10807	3.53%	1.13%	83.86	27.81	46.79	74.11	19026	10589	2.52%	-0.90%
15V	0.027	2.88	17856	10602	19769	10768	10.71%	1.57%	82.93	29.24	43.95	79.56	19070	10551	6.80%	-0.48%
16V	0.003	2.75	21363	11882	21421	11797	0.27%	-0.72%	116.42	36.02	68.40	74.29	21613	11876	1.17%	-0.05%
Column Averages			18167	10490	18899	10358	4.18%	-1.45%	80.57	26.71	44.95	76.81	18526	10313	1.98%	-1.81%

Appendix A

Plots of Ultrasonic Data for Each Plug Sample

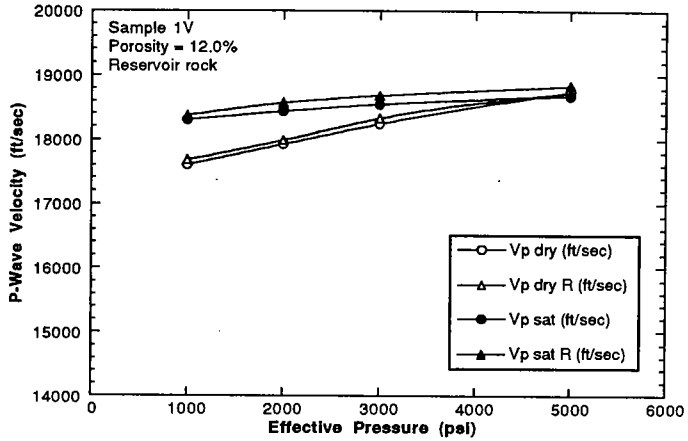
Sample 1V
Porosity = 12.0%
Reservoir rock
P-Wave Velocity (ft/sec)
Effective Pressure (psi)
Vp dry (ft/sec)
Vp dry R (ft/sec)
Vp sat (ft/sec)
Vp sat R (ft/sec)

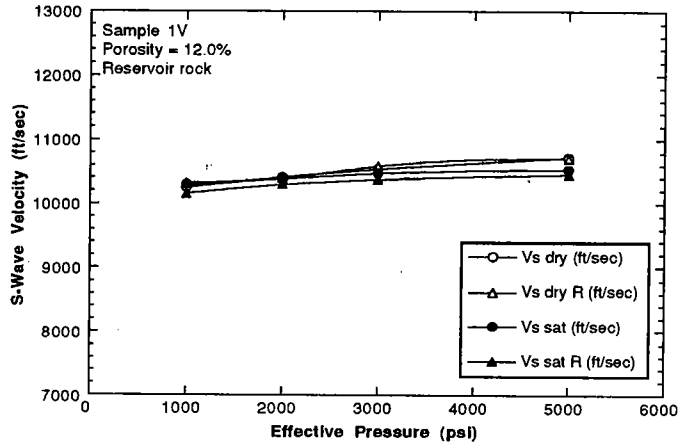
Sample 1V
Porosity = 12.0%
Reservoir rock
S-Wave Velocity (ft/sec)
Effective Pressure (psi)
Vs dry (ft/sec)
Vs dry R (ft/sec)
Vs sat (ft/sec)
Vs sat R (ft/sec)

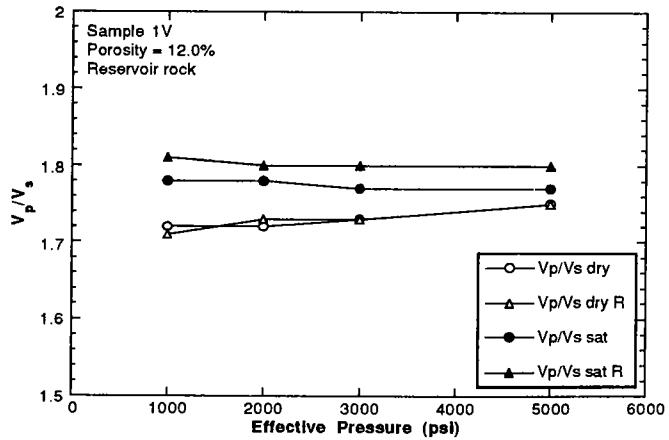
Sample 1V
Porosity = 12.0%
Reservoir rock
Vp/Vs
Effective Pressure (psi)
Vp/Vs dry
Vp/Vs dry R
Vp/Vs sat
Vp/Vs sat R

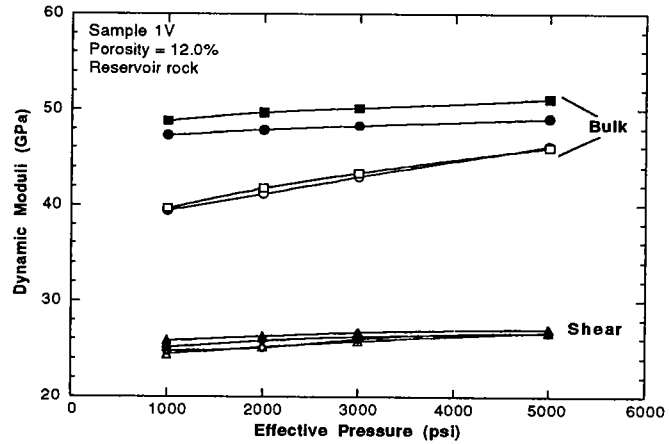
Sample 1V
Porosity = 12.0%
Reservoir rock
Dynamic Moduli (GPa)
Effective Pressure (psi)
Bulk
Shear

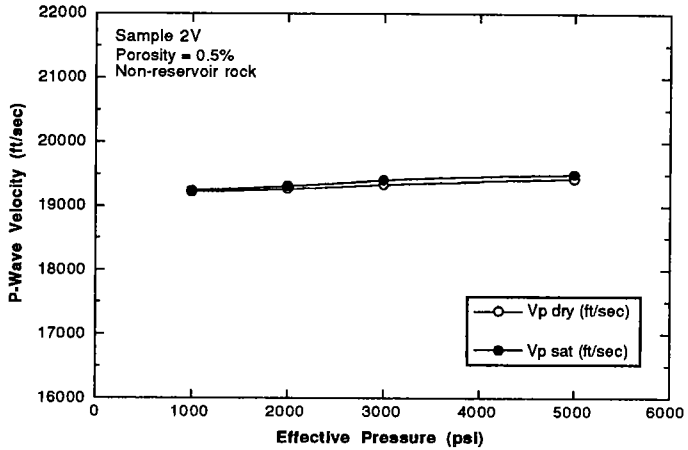
Sample 2V
Porosity = 0.5%
Non-reservoir rock
Vp dry (ft/sec)
Vp sat (ft/sec)
P-Wave Velocity (ft/sec)
Effective Pressure (psi)
22000
21000
20000
19000
18000
17000
16000
0
1000
2000
3000
4000
5000
6000

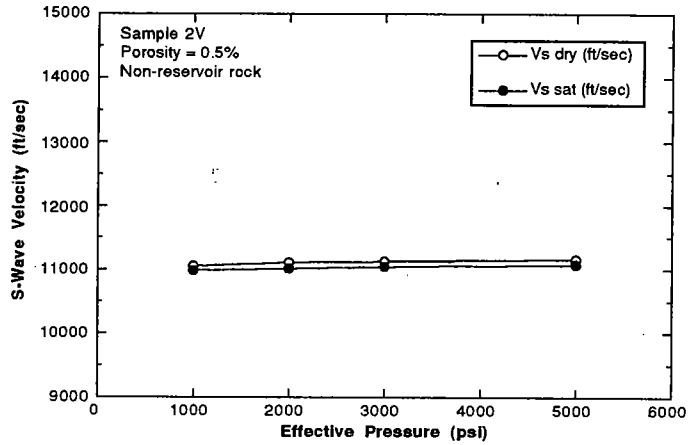
Sample 2V
Porosity = 0.5%
Non-reservoir rock
Vs dry (ft/sec)
Vs sat (ft/sec)
S-Wave Velocity (ft/sec)
Effective Pressure (psi)
15000
14000
13000
12000
11000
10000
9000
0
1000
2000
3000
4000
5000
6000

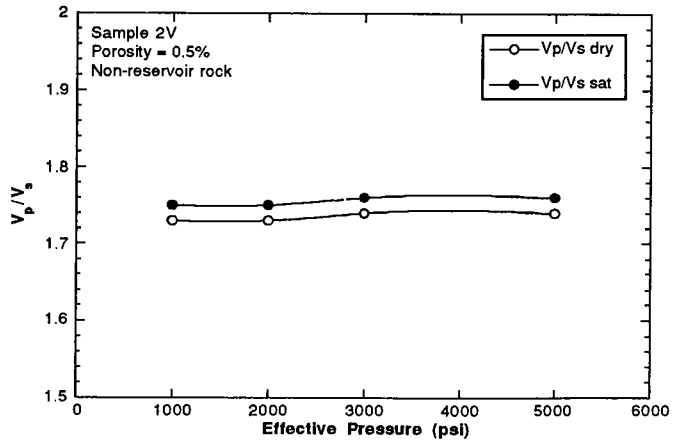
Sample 2V
Porosity = 0.5%
Non-reservoir rock
Vp/Vs dry
Vp/Vs sat
Vp /Vs
Effective Pressure (psi)
2
1.9
1.8
1.7
1.6
1.5
0
1000
2000
3000
4000
5000
6000

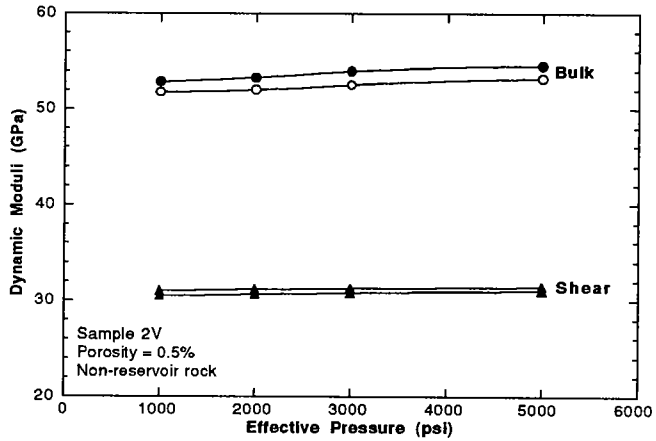
Bulk
Shear
Sample 2V
Porosity = 0.5%
Non-reservoir rock
Dynamic Moduli (GPa)
Effective Pressure (psi)
60
50
40
30
20
0
1000
2000
3000
4000
5000
6000

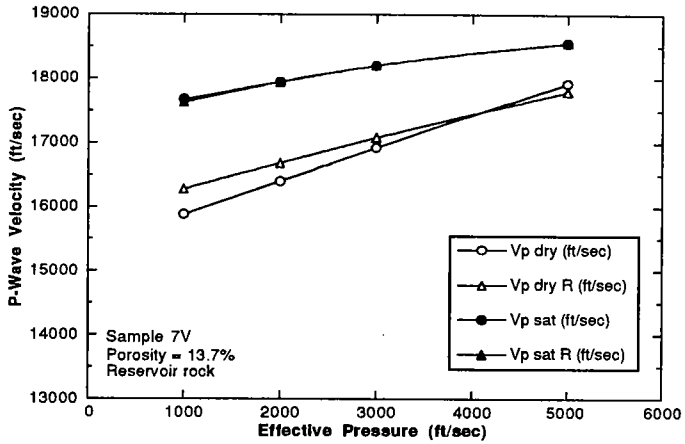
P-Wave Velocity (ft/sec)
Effective Pressure (ft/sec)
Sample 7V
Porosity = 13.7%
Reservoir rock
Vp dry (ft/sec)
Vp dry R (ft/sec)
Vp sat (ft/sec)
Vp sat R (ft/sec)

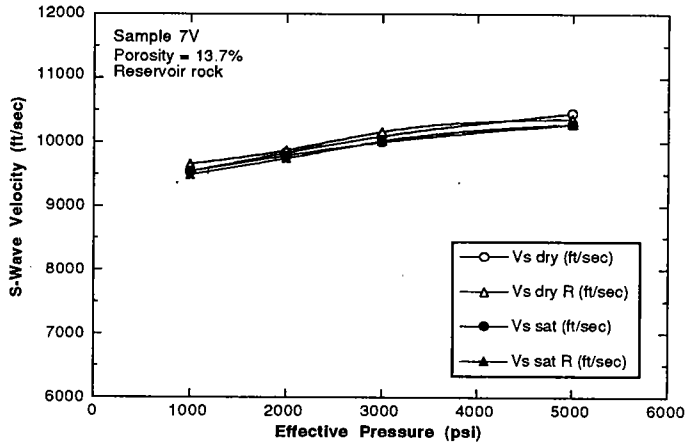
S-Wave Velocity (ft/sec)
Effective Pressure (psi)
Sample 7V
Porosity = 13.7%
Reservoir rock
Vs dry (ft/sec)
Vs dry R (ft/sec)
Vs sat (ft/sec)
Vs sat R (ft/sec)

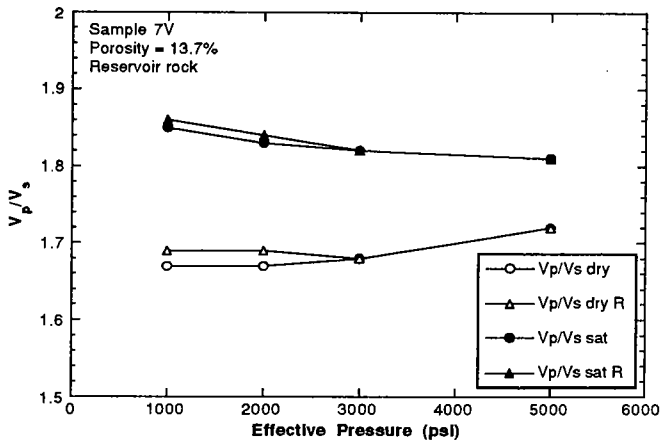
Vp/Vs
Effective Pressure (psi)
Sample 7V
Porosity = 13.7%
Reservoir rock
Vp/Vs dry
Vp/Vs dry R
Vp/Vs sat
Vp/Vs sat R

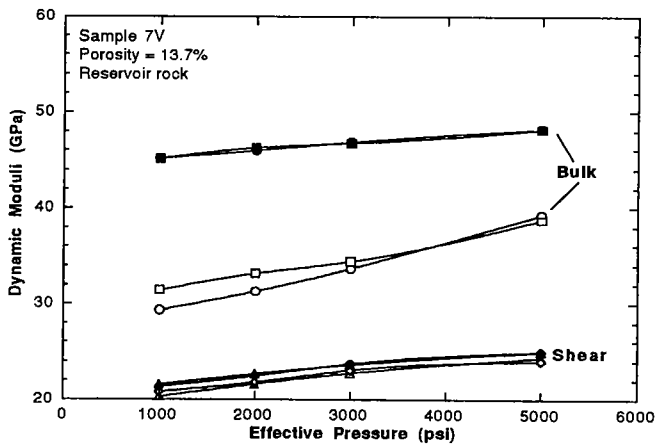
Dynamic Moduli (GPa)
Effective Pressure (psi)
Sample 7V
Porosity = 13.7%
Reservoir rock
Bulk
Shear

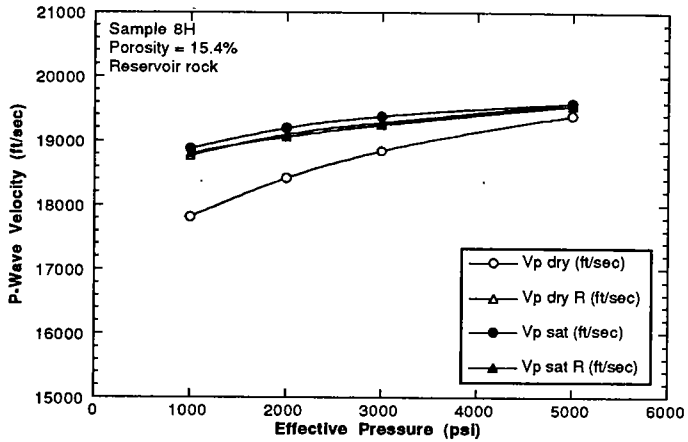
Sample 8H
Porosity = 15.4%
Reservoir rock
P-Wave Velocity (ft/sec)
Effective Pressure (psi)
Vp dry (ft/sec)
Vp dry R (ft/sec)
Vp sat (ft/sec)
Vp sat R (ft/sec)

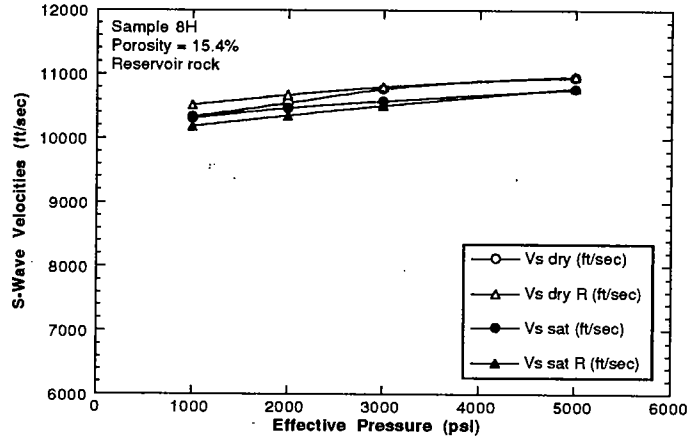
Sample 8H
Porosity = 15.4%
Reservoir rock
S-Wave Velocities (ft/sec)
Effective Pressure (psi)
Vs dry (ft/sec)
Vs dry R (ft/sec)
Vs sat (ft/sec)
Vs sat R (ft/sec)

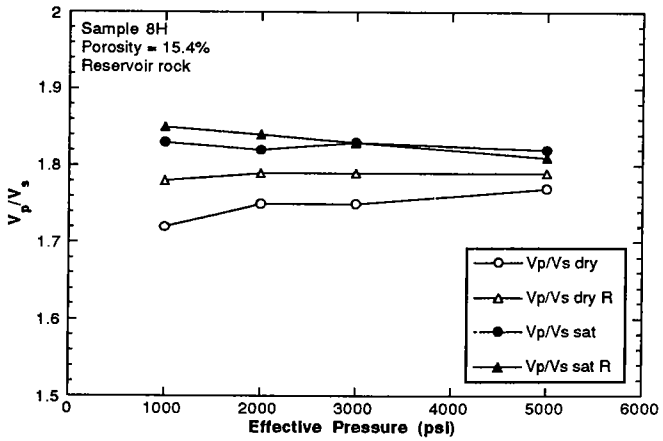
Sample 8H
Porosity = 15.4%
Reservoir rock
Vp/Vs
Effective Pressure (psi)
Vp/Vs dry
Vp/Vs dry R
Vp/Vs sat
Vp/Vs sat R

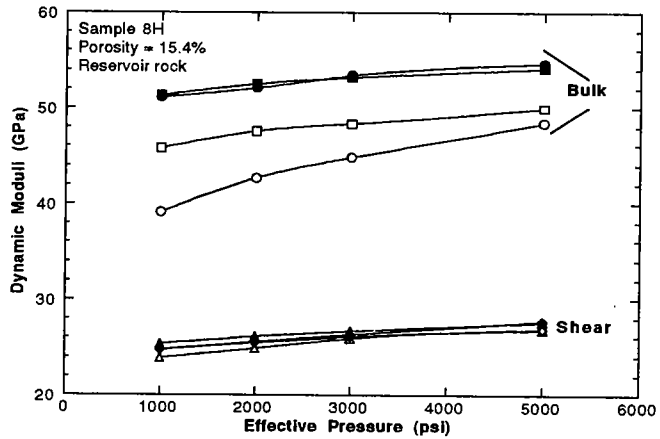
Sample 8H
Porosity = 15.4%
Reservoir rock
Dynamic Moduli (GPa)
Effective Pressure (psi)
Bulk
Shear

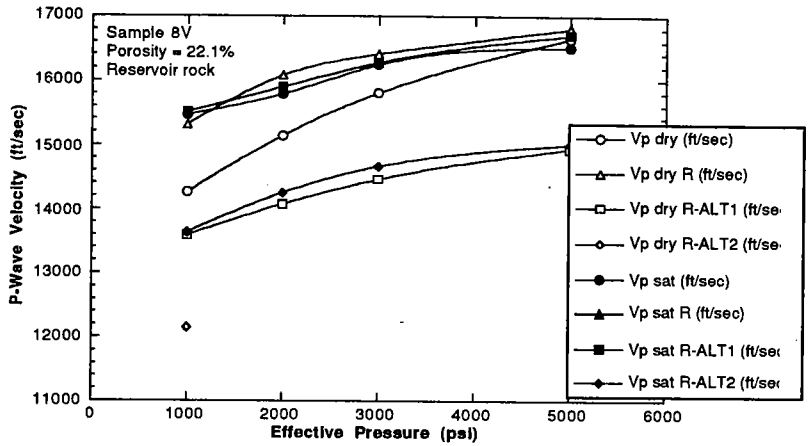
Sample 8V
Porosity = 22.1%
Reservoir rock
P-Wave Velocity (ft/sec)
Effective Pressure (psi)
Vp dry (ft/sec)
Vp dry R (ft/sec)
Vp dry R-ALT1 (ft/se
Vp dry R-ALT2 (ft/se
Vp sat (ft/sec)
Vp sat R (ft/sec)
Vp sat R-ALT1 (ft/se
Vp sat R-ALT2 (ft/se

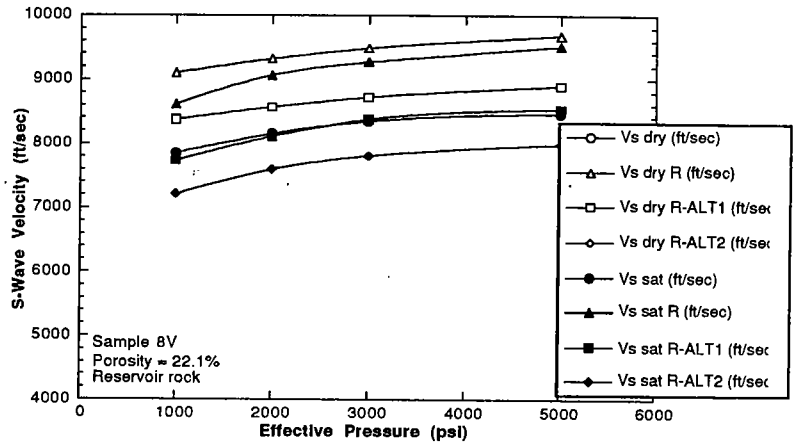
Sample 8V
Porosity = 22.1%
Reservoir rock
S-Wave Velocity (ft/sec)
Effective Pressure (psi)
Vs dry (ft/sec)
Vs dry R (ft/sec)
Vs dry R-ALT1 (ft/se
Vs dry R-ALT2 (ft/se
Vs sat (ft/sec)
Vs sat R (ft/sec)
Vs sat R-ALT1 (ft/se
Vs sat R-ALT2 (ft/se

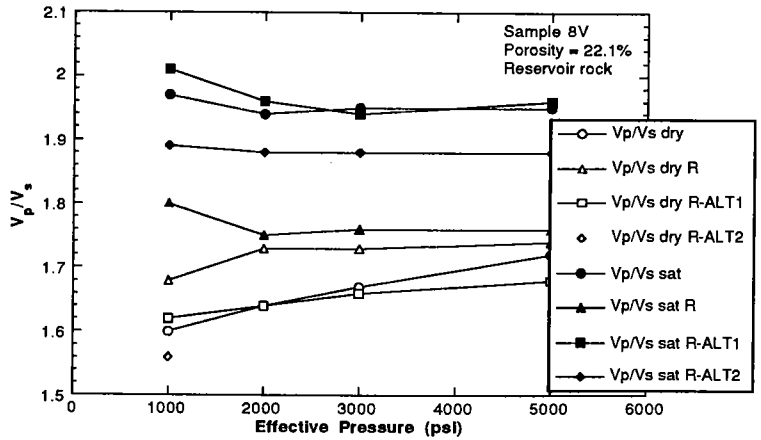
Sample 8V
Porosity = 22.1%
Reservoir rock
Vp/Vs
Effective Pressure (psi)
Vp/Vs dry
Vp/Vs dry R
Vp/Vs dry R-ALT1
Vp/Vs dry R-ALT2
Vp/Vs sat
Vp/Vs sat R
Vp/Vs sat R-ALT1
Vp/Vs sat R-ALT2

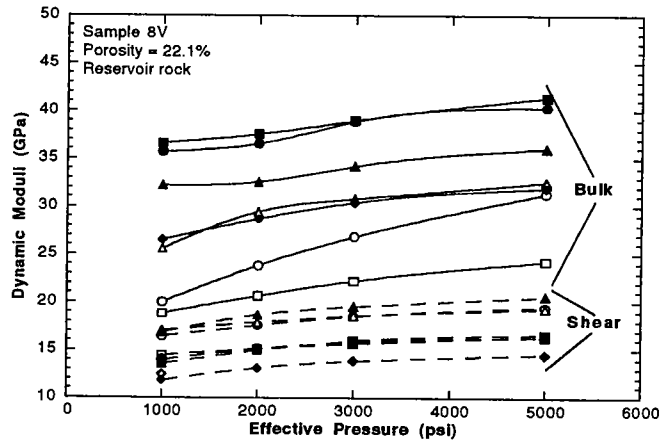
Sample 8V
Porosity = 22.1%
Reservoir rock
Dynamic Moduli (GPa)
Effective Pressure (psi)
Bulk
Shear

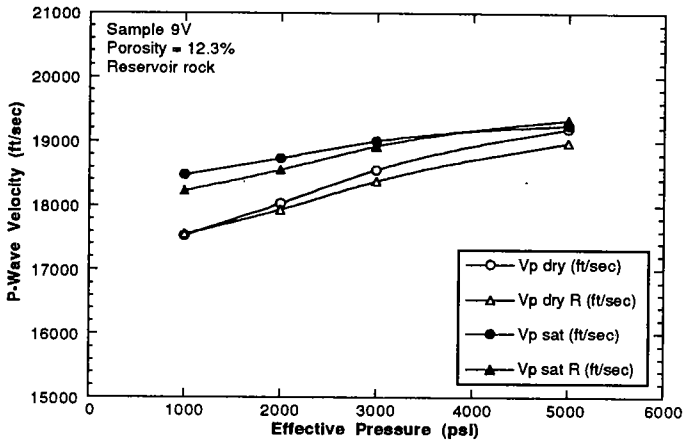
Sample 9V
Porosity = 12.3%
Reservoir rock
P-Wave Velocity (ft/sec)
Effective Pressure (psi)
Vp dry (ft/sec)
Vp dry R (ft/sec)
Vp sat (ft/sec)
Vp sat R (ft/sec)

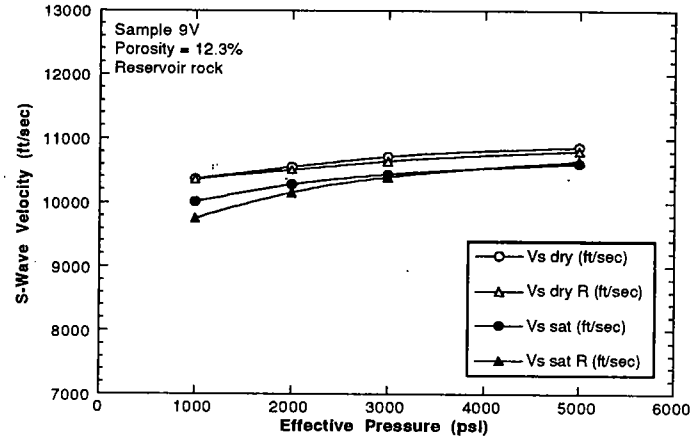
Sample 9V
Porosity = 12.3%
Reservoir rock
S-Wave Velocity (ft/sec)
Effective Pressure (psi)
Vs dry (ft/sec)
Vs dry R (ft/sec)
Vs sat (ft/sec)
Vs sat R (ft/sec)

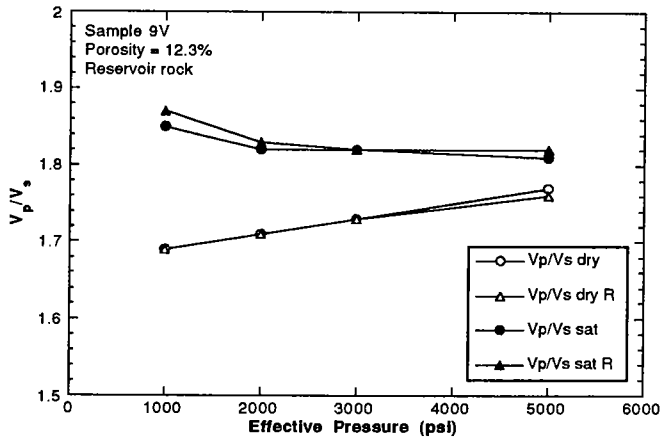
Sample 9V
Porosity = 12.3%
Reservoir rock
Vp/Vs
Effective Pressure (psi)
Vp/Vs dry
Vp/Vs dry R
Vp/Vs sat
Vp/Vs sat R

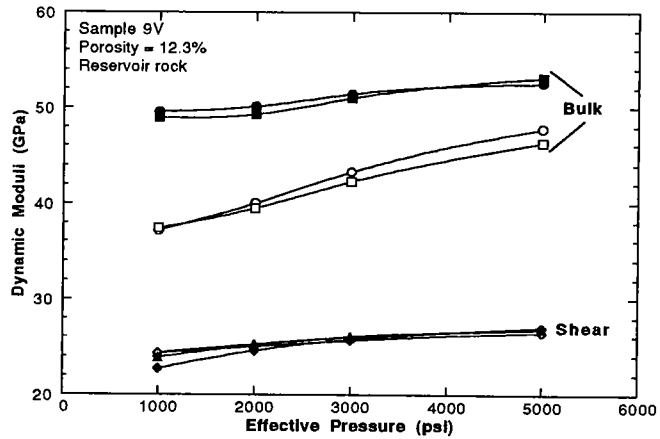
Sample 9V
Porosity = 12.3%
Reservoir rock
Dynamic Moduli (GPa)
Effective Pressure (psi)
Bulk
Shear

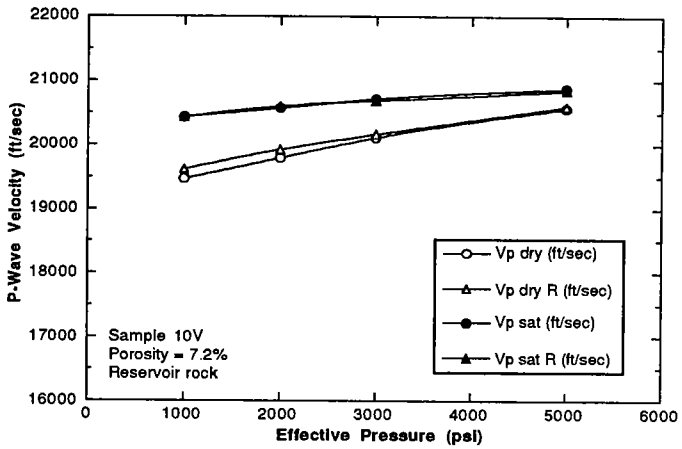
P-Wave Velocity (ft/sec)
Effective Pressure (psi)
Sample 10V
Porosity = 7.2%
Reservoir rock
Vp dry (ft/sec)
Vp dry R (ft/sec)
Vp sat (ft/sec)
Vp sat R (ft/sec)

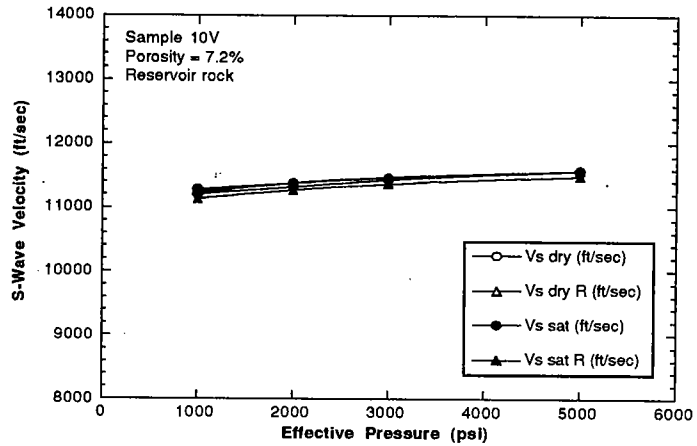
S-Wave Velocity (ft/sec)
Effective Pressure (psi)
Sample 10V
Porosity = 7.2%
Reservoir rock
Vs dry (ft/sec)
Vs dry R (ft/sec)
Vs sat (ft/sec)
Vs sat R (ft/sec)

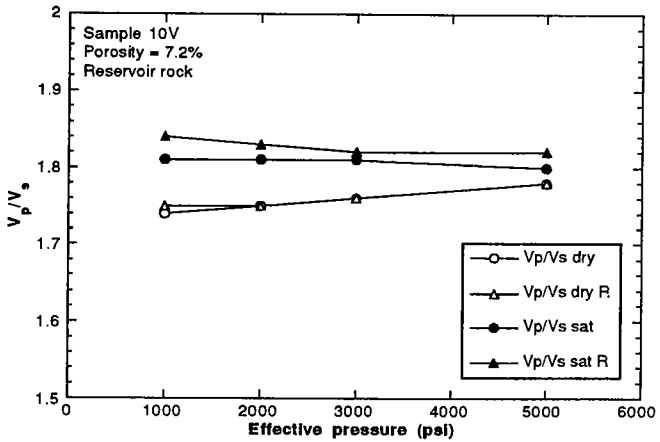
Vp/Vs
Effective pressure (psi)
Sample 10V
Porosity = 7.2%
Reservoir rock
Vp/Vs dry
Vp/Vs dry R
Vp/Vs sat
Vp/Vs sat R

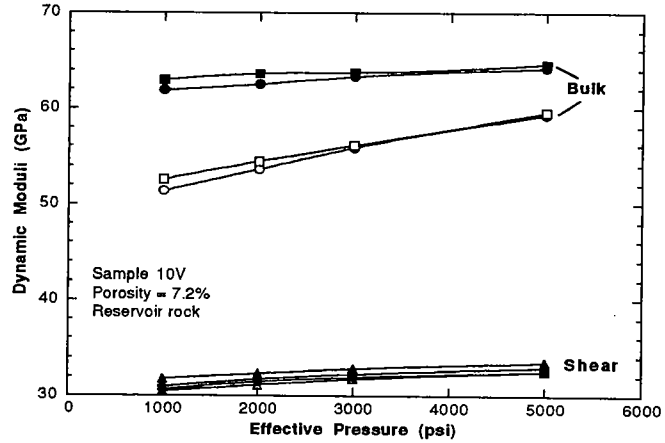
Dynamic Moduli (GPa)
Effective Pressure (psi)
Sample 10V
Porosity = 7.2%
Reservoir rock
Bulk
Shear

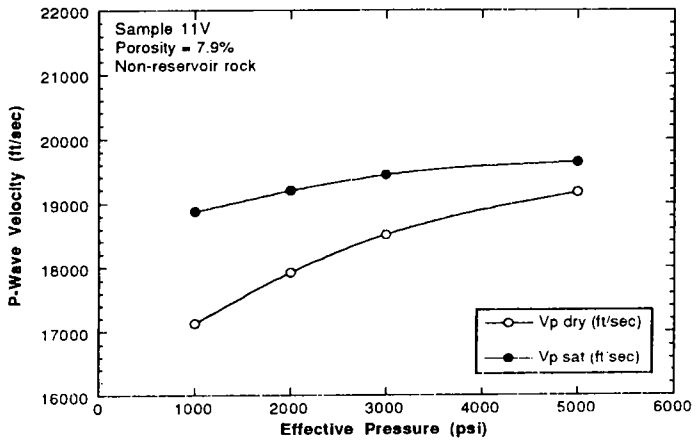
Sample 11V
Porosity = 7.9%
Non-reservoir rock
P-Wave Velocity (ft/sec)
Effective Pressure (psi)
Vp dry (ft/sec)
Vp sat (ft/sec)

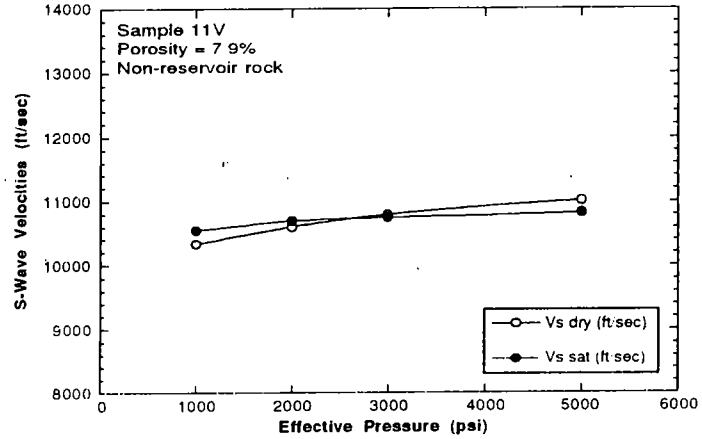
Sample 11V
Porosity = 7.9%
Non-reservoir rock
S-Wave Velocities (ft/sec)
Effective Pressure (psi)
Vs dry (ft/sec)
Vs sat (ft/sec)

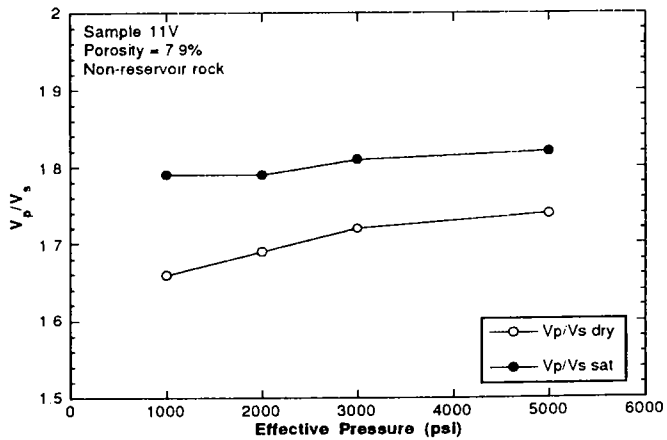
Sample 11V
Porosity = 7.9%
Non-reservoir rock
Vp/Vs
Effective Pressure (psi)
Vp/Vs dry
Vp/Vs sat

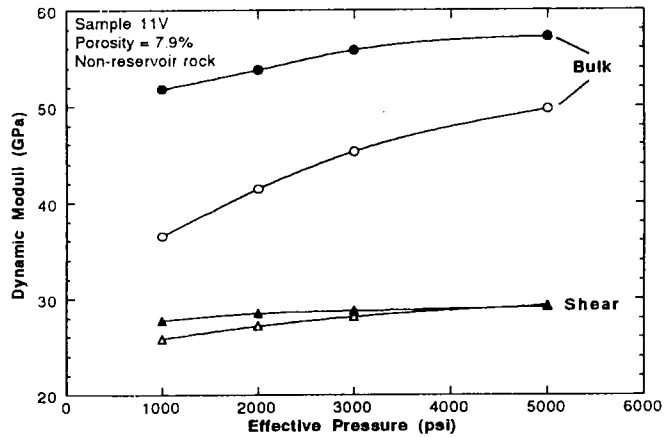
Sample 11V
Porosity = 7.9%
Non-reservoir rock
Dynamic Moduli (GPa)
Effective Pressure (psi)
Bulk
Shear

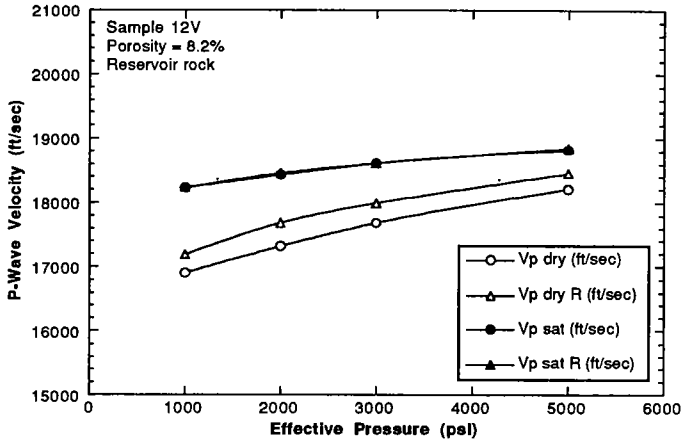
Sample 12V
Porosity = 8.2%
Reservoir rock
P-Wave Velocity (ft/sec)
Effective Pressure (psi)
Vp dry (ft/sec)
Vp dry R (ft/sec)
Vp sat (ft/sec)
Vp sat R (ft/sec)

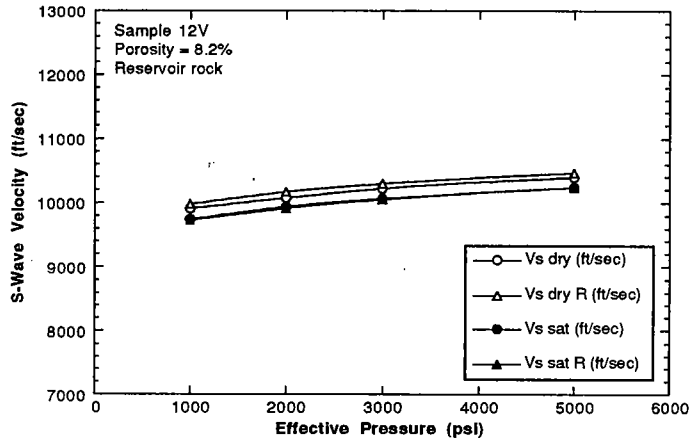
Sample 12V
Porosity = 8.2%
Reservoir rock
S-Wave Velocity (ft/sec)
Effective Pressure (psi)
Vs dry (ft/sec)
Vs dry R (ft/sec)
Vs sat (ft/sec)
Vs sat R (ft/sec)

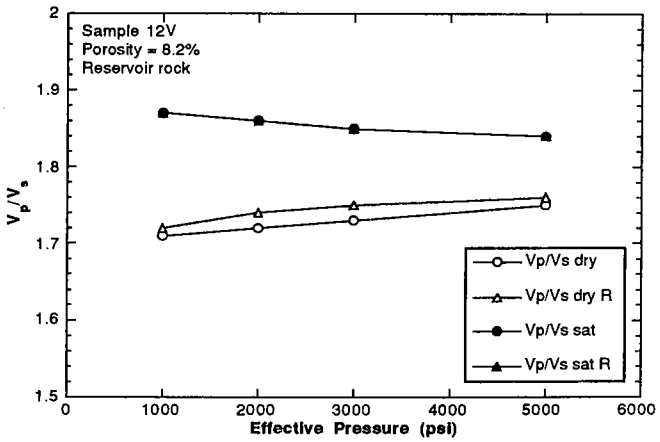
Sample 12V
Porosity = 8.2%
Reservoir rock
Vp/Vs
Effective Pressure (psi)
Vp/Vs dry
Vp/Vs dry R
Vp/Vs sat
Vp/Vs sat R

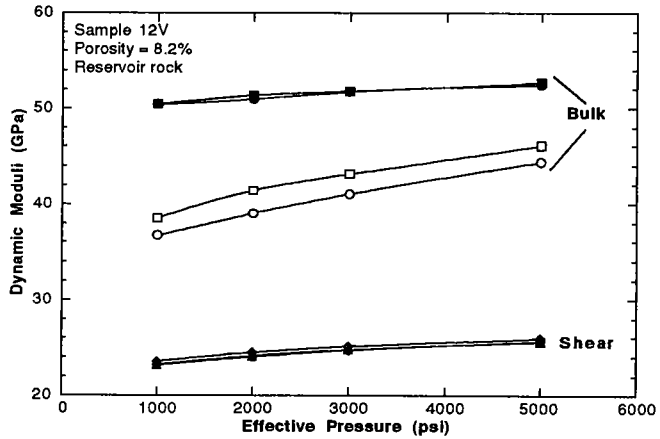
Sample 12V
Porosity = 8.2%
Reservoir rock
Dynamic Moduli (GPa)
Effective Pressure (psi)
Bulk
Shear

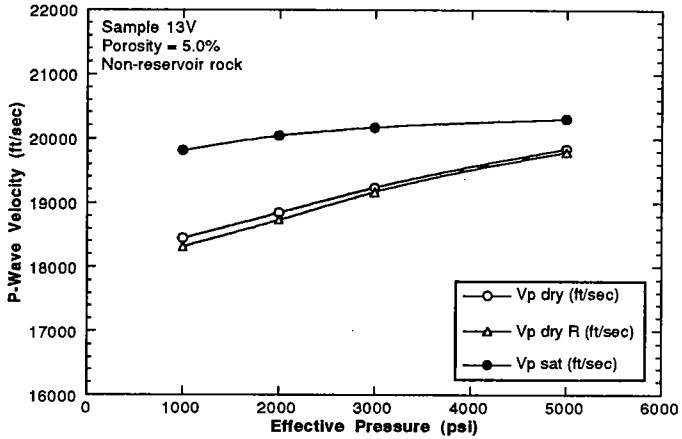
Sample 13V
Porosity = 5.0%
Non-reservoir rock
P-Wave Velocity (ft/sec)
Effective Pressure (psi)
Vp dry (ft/sec)
Vp dry R (ft/sec)
Vp sat (ft/sec)

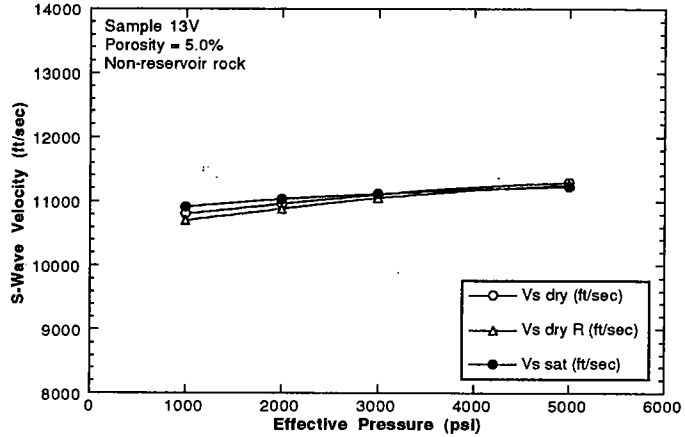
Sample 13V
Porosity = 5.0%
Non-reservoir rock
S-Wave Velocity (ft/sec)
Effective Pressure (psi)
Vs dry (ft/sec)
Vs dry R (ft/sec)
Vs sat (ft/sec)

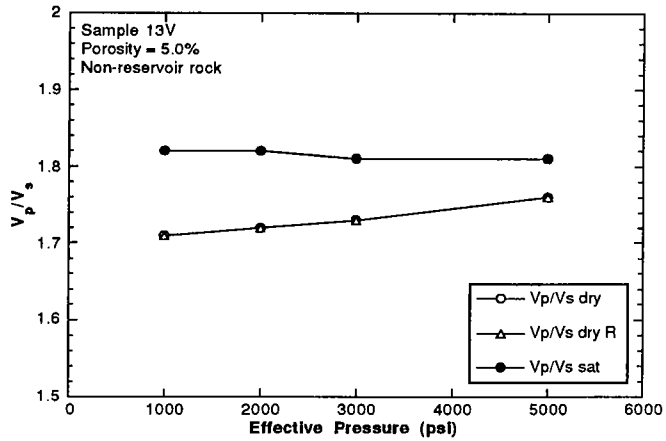
Sample 13V
Porosity = 5.0%
Non-reservoir rock
Vp/Vs
Effective Pressure (psi)
Vp/Vs dry
Vp/Vs dry R
Vp/Vs sat

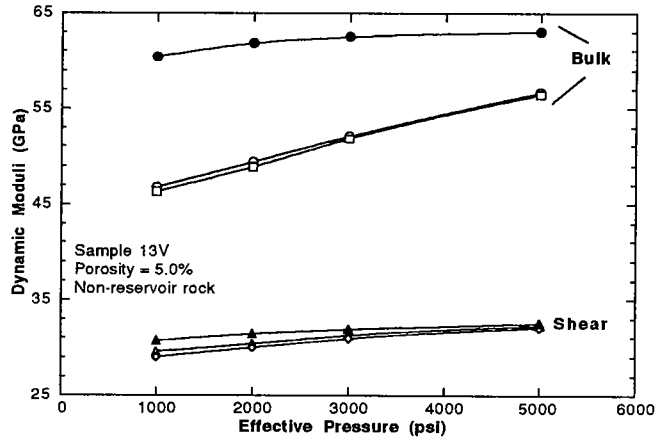
Bulk
Sample 13V
Porosity = 5.0%
Non-reservoir rock
Dynamic Moduli (GPa)
Shear
Effective Pressure (psi)

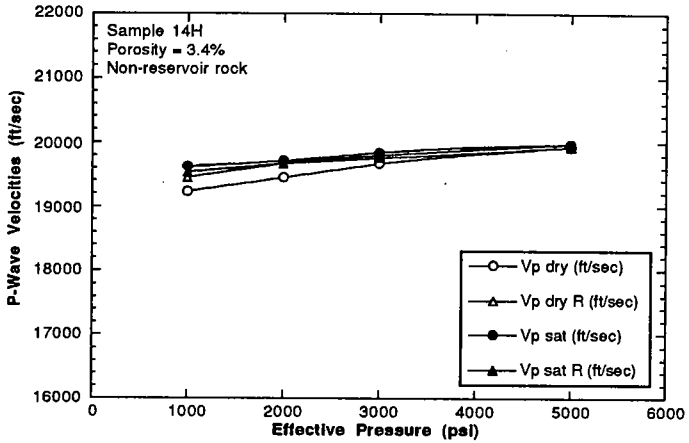
Sample 14H
Porosity = 3.4%
Non-reservoir rock
P-Wave Velocities (ft/sec)
Effective Pressure (psi)
Vp dry (ft/sec)
Vp dry R (ft/sec)
Vp sat (ft/sec)
Vp sat R (ft/sec)

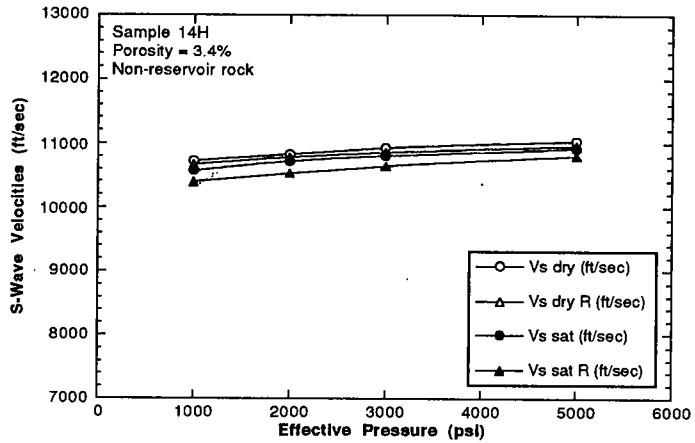
Sample 14H
Porosity = 3.4%
Non-reservoir rock
S-Wave Velocities (ft/sec)
Effective Pressure (psi)
Vs dry (ft/sec)
Vs dry R (ft/sec)
Vs sat (ft/sec)
Vs sat R (ft/sec)

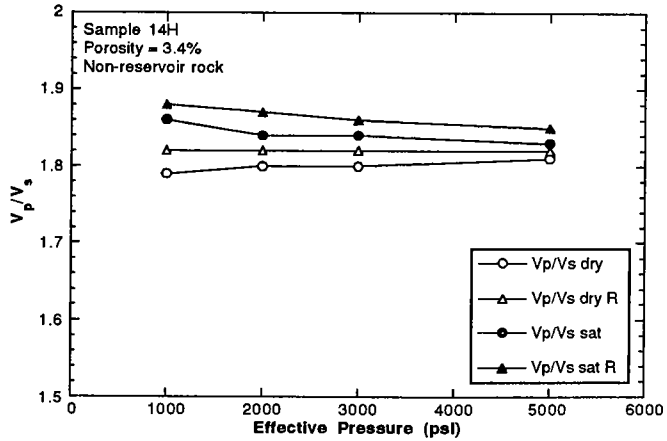
Sample 14H
Porosity = 3.4%
Non-reservoir rock
Vp/Vs
Effective Pressure (psi)
Vp/Vs dry
Vp/Vs dry R
Vp/Vs sat
Vp/Vs sat R

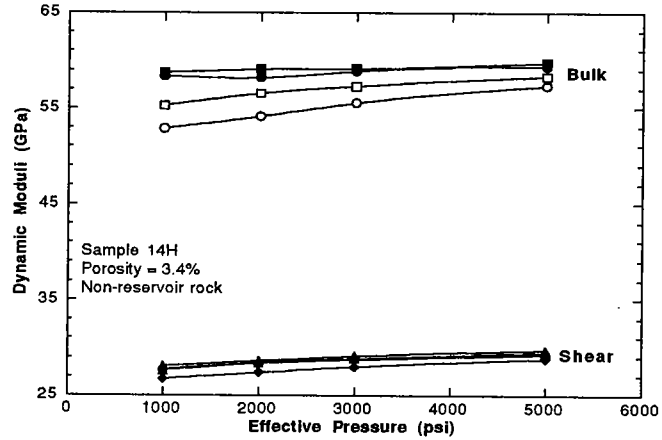
Sample 14H
Porosity = 3.4%
Non-reservoir rock
Dynamic Moduli (GPa)
Effective Pressure (psi)
Bulk
Shear

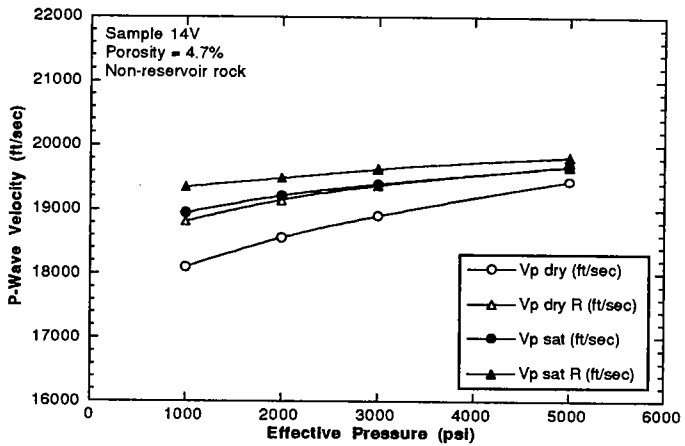
Sample 14V
Porosity = 4.7%
Non-reservoir rock
P-Wave Velocity (ft/sec)
Effective Pressure (psi)
Vp dry (ft/sec)
Vp dry R (ft/sec)
Vp sat (ft/sec)
Vp sat R (ft/sec)

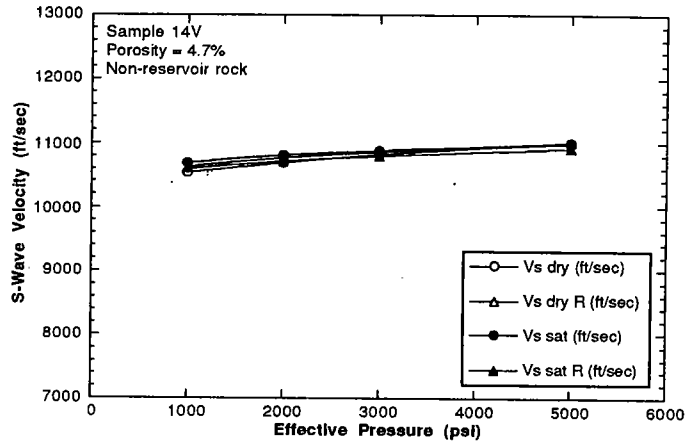
Sample 14V
Porosity = 4.7%
Non-reservoir rock
S-Wave Velocity (ft/sec)
Effective Pressure (psi)
Vs dry (ft/sec)
Vs dry R (ft/sec)
Vs sat (ft/sec)
Vs sat R (ft/sec)

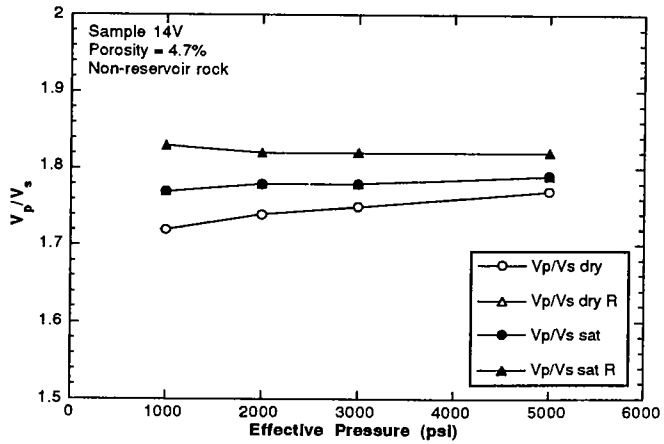
Sample 14V
Porosity = 4.7%
Non-reservoir rock
Vp/Vs
Effective Pressure (psi)
Vp/Vs dry
Vp/Vs dry R
Vp/Vs sat
Vp/Vs sat R

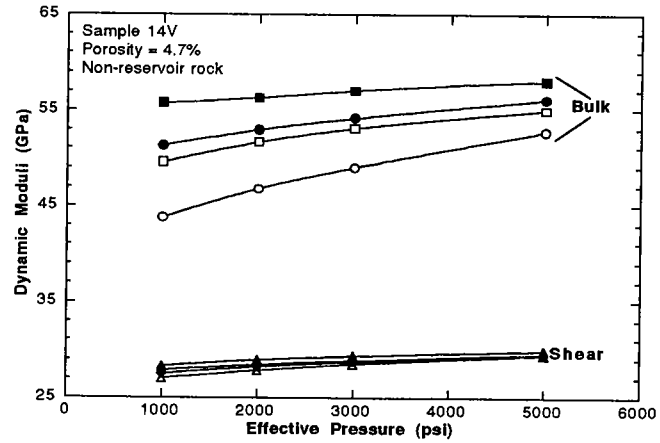
Sample 14V
Porosity = 4.7%
Non-reservoir rock
Dynamic Moduli (GPa)
Effective Pressure (psi)
Bulk
Shear

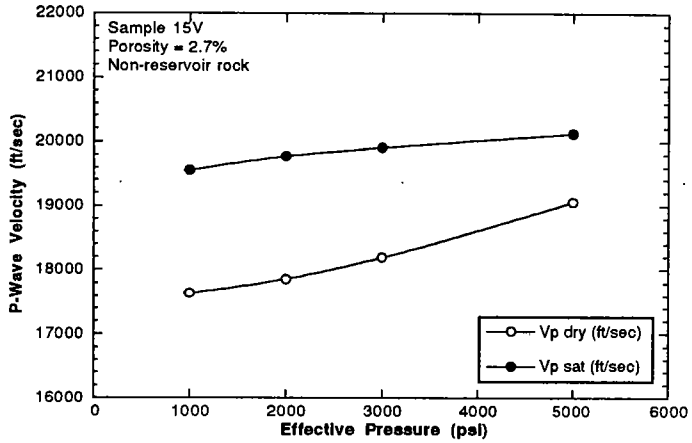
Sample 15V
Porosity = 2.7%
Non-reservoir rock
P-Wave Velocity (ft/sec)
Effective Pressure (psi)
Vp dry (ft/sec)
Vp sat (ft/sec)

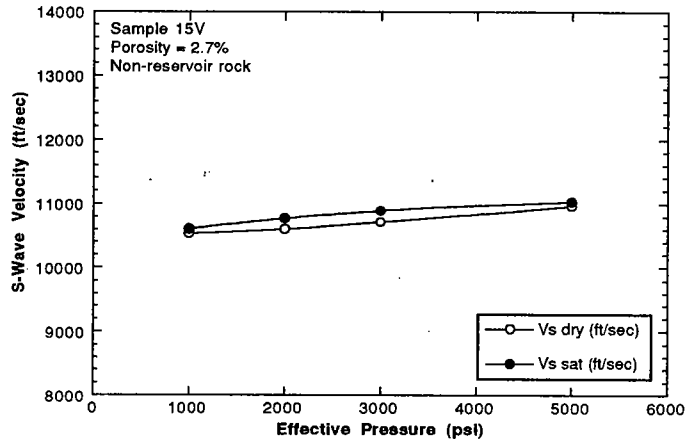
Sample 15V
Porosity = 2.7%
Non-reservoir rock
S-Wave Velocity (ft/sec)
Effective Pressure (psi)
Vs dry (ft/sec)
Vs sat (ft/sec)

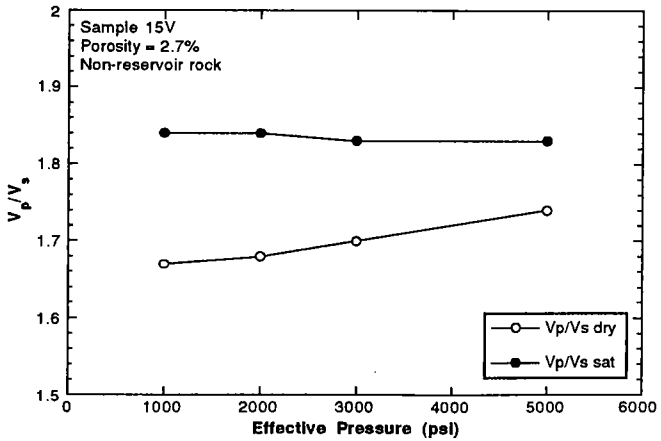
Sample 15V
Porosity = 2.7%
Non-reservoir rock
Vp/Vs
Effective Pressure (psi)
Vp/Vs dry
Vp/Vs sat

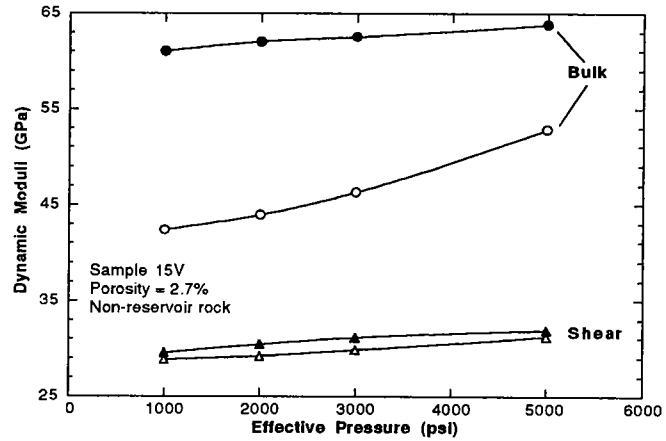
Bulk
Shear
Sample 15V
Porosity = 2.7%
Non-reservoir rock
Dynamic Modull (GPa)
Effective Pressure (psi)

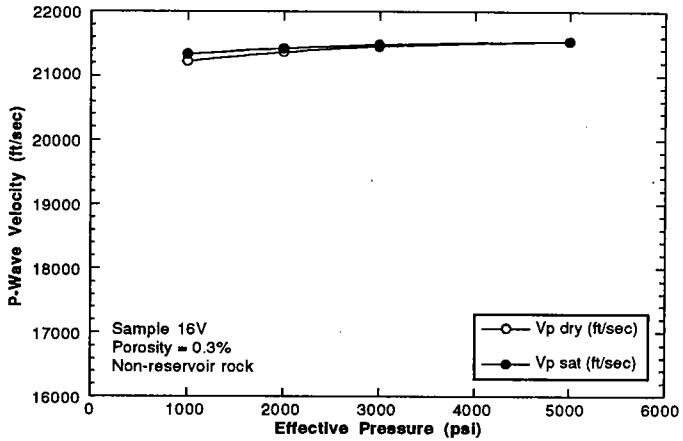
P-Wave Velocity (ft/sec)
22000
21000
20000
19000
18000
17000
16000
0
1000
2000
3000
4000
5000
6000
Effective Pressure (psi)
Sample 16V
Porosity = 0.3%
Non-reservoir rock
Vp dry (ft/sec)
Vp sat (ft/sec)

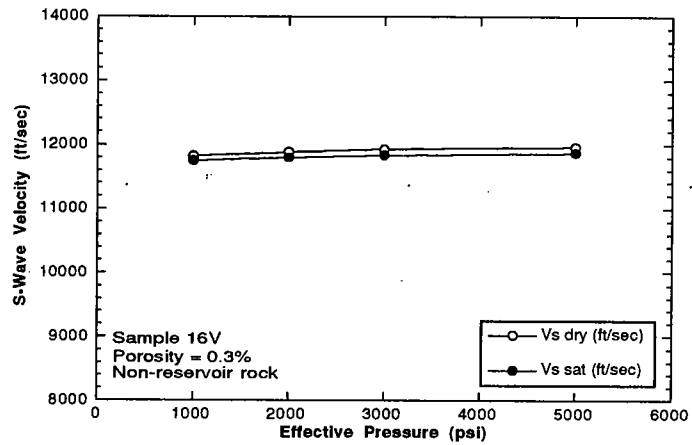
S-Wave Velocity (ft/sec)
14000
13000
12000
11000
10000
9000
8000
0
1000
2000
3000
4000
5000
6000
Effective Pressure (psi)
Sample 16V
Porosity = 0.3%
Non-reservoir rock
Vs dry (ft/sec)
Vs sat (ft/sec)

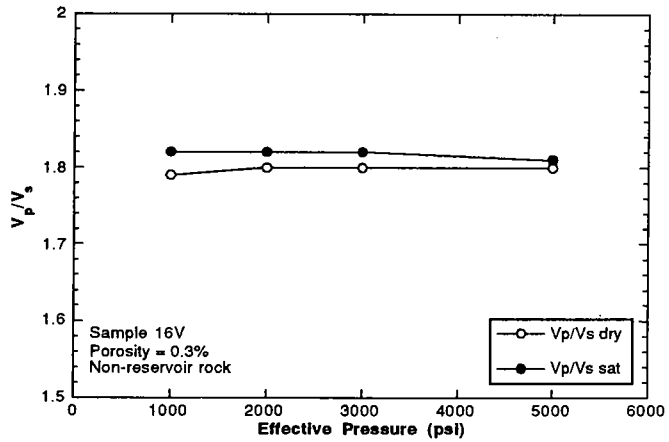
V_p/V_s
2
1.9
1.8
1.7
1.6
1.5
0
1000
2000
3000
4000
5000
6000
Effective Pressure (psi)
Sample 16V
Porosity = 0.3%
Non-reservoir rock
Vp/Vs dry
Vp/Vs sat

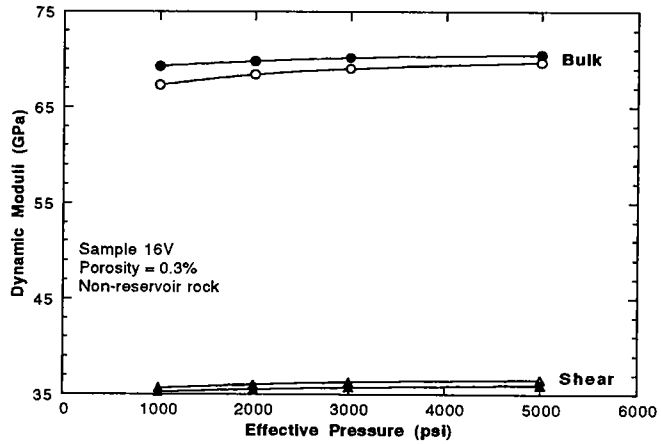
Dynamic Moduli (GPa)
75
65
55
45
35
0
1000
2000
3000
4000
5000
6000
Effective Pressure (psi)
Sample 16V
Porosity = 0.3%
Non-reservoir rock
Bulk
Shear

Appendix B

DOLOMITE-CALCITE TRANSFORM

If we assume the principal minerals of the Grayburg formation are dolomite and calcite, we can estimate the mineral moduli (K_m and G_m) using the following relations:

$$K_m = K_{Clct} + \frac{(K_{Dlmt} - K_{Clct})}{(\rho_{Dlmt} - \rho_{Clct})}(\rho_g - \rho_{Clct}) = 76.7 + 113.125(\rho_g - 2.71) \qquad (B1)$$

$$G_m = G_{Clct} + \frac{(G_{Dlmt} - G_{Clct})}{(\rho_{Dlmt} - \rho_{Clct})}(\rho_g - \rho_{Clct}) = 32.3 + 83.75(\rho_g - 2.71) \qquad (B2)$$

where ρ_g is the measured grain density of the sample, K_{Clct} = 76.7 GPa is the bulk modulus of calcite, K_{Dlmt} = 94.8 GPa is the bulk modulus of dolomite, G_{Clct} = 32.3 GPa is the shear modulus of calcite, G_{Dlmt} = 45.7 GPa is the shear modulus of dolomite, ρ_{Clct} = 2.71 g/cm^3 is the grain (mineral) density of calcite, and ρ_{Dlmt} = 2.87 g/cm^3 is the grain density of dolomite. Accordingly, the grain density (ρ_g) is:

$$\begin{aligned} \rho_g(g/cm^3) &= \rho_{Dlmt} + (\partial\rho_g/\partial X_{Clct})X_{Clct} \\ &= 2.87 - 0.16X_{Clct} \end{aligned} \qquad (B3)$$

where the grain-volume fraction of calcite (X_{Clct}) is:

$$X_{Clct} = \frac{\rho_g - \rho_{Dlmt}}{\rho_{Clct} - \rho_{Dlmt}} = \frac{\rho_g - 2.87}{2.71 - 2.87} \qquad (B4)$$

and

$$X_{Dlmt} + X_{Clct} = 1. \qquad (B5)$$

If mineral composition and porosity (ϕ) were the primary factors controlling the dry-frame moduli (K_d and G_d) of these rocks, then these frame moduli are:

$$\begin{aligned} K_d(\text{GPa}) &= K_m + (\partial K_d/\partial\phi)\phi \\ &= K_{Dlmt} + (\partial K_m/\partial X_{Clct})X_{Clct} + (\partial K_d/\partial\phi)\phi \\ &\approx 94.8 - 18.1X_{Clct} + (\partial K_d/\partial\phi)\phi \end{aligned} \tag{B6}$$

and

$$\begin{aligned} G_d(\text{GPa}) &= G_m + (\partial G_d/\partial\phi)\phi \\ &= G_{Dlmt} + (\partial G_m/\partial X_{Clct})X_{Clct} + (\partial G_d/\partial\phi)\phi. \\ &\approx 45.7 - 13.4X_{Clct} + (\partial G_d/\partial\phi)\phi \end{aligned} \tag{B7}$$

When $X_{Clct} = 0$, then $K_m = K_{Dlmt}$ and $G_m = G_{Dlmt}$. When $X_{Clct} = 1$, then $K_m = K_{Clct}$ and $G_m = G_{Clct}$.

The $(\partial K_d/\partial\phi)$ and $(\partial G_d/\partial\phi)$ coefficients are presumed constant and estimated using $-(K_{Dlmt}/\phi_0)$ and $-(G_{Dlmt}/\phi_0)$ so when ϕ approaches from below the "initial" or "depositional" porosity ϕ_0 the dry moduli of a pure dolomite frame are zero. In reality however, these coefficients depend on pore shape and frame architecture.

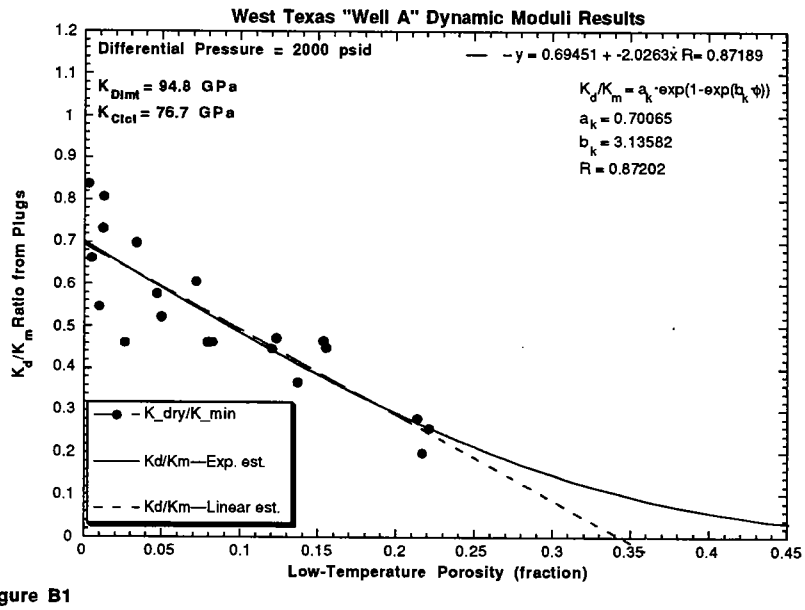

Figure B1: Plot of K_d/K_m vs. low-temperature porosity. Dolomite-calcite transform.

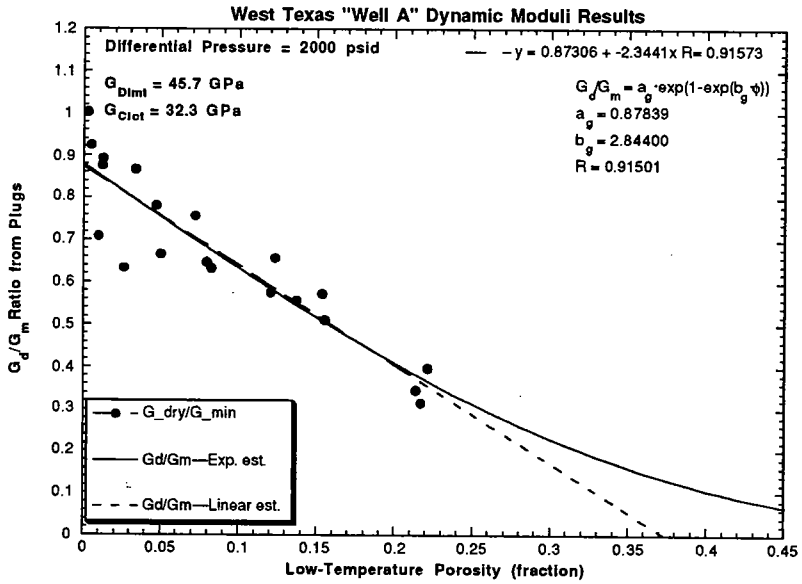

Figure B2: Plot of G_d/G_m vs. low-temperature porosity. Dolomite-calcite transform.

Figures B1 and B2 are plots of K_d/K_m and G_d/G_m, respectively. These plots were generated from the plug data using equations (B1) and (B2) for K_m and G_m, and K_d and G_d calculated from the dry velocity measurements (Table 3). Using the linear least-squares lines from these plots, the frame moduli are:

$$\begin{aligned} K_d(\text{GPa}) &= K_m(\alpha_k - \beta_k\phi) \\ &\approx K_m(0.695 - 2.03\phi) \qquad \ldots \phi_0 = 0.343 \\ &\approx 65.8 - 12.6X_{Clct} - 192.1\phi \end{aligned} \tag{B8}$$

where $\alpha_k = (K_d/K_m)_{\phi=0}$ and $\beta_k = -(\partial K_d/\partial\phi)/K_m = \alpha_k/\phi_0$, and

$$\begin{aligned} G_d(\text{GPa}) &= G_m(\alpha_g - \beta_g\phi) \\ &\approx G_m(0.873 - 2.34\phi) \qquad \ldots \phi_0 = 0.372 \\ &\approx 39.9 - 11.7X_{Clct} - 107.1\phi \end{aligned} \tag{B9}$$

where $\alpha_g = (G_d/G_m)_{\phi=0}$ and $\beta_g = -(\partial G_d/\partial\phi)/G_m = \alpha_g/\phi_0$. These coefficients are lower than the expected theoretical coefficients (i.e., $\alpha_k = \alpha_g = 1$ and $\beta_k = \beta_g = 1/\phi_0$) if

mineral composition (the X_i's) and porosity (ϕ) are the only factors controlling the dry-frame moduli (K_d and G_d) of these rocks. This suggests that the estimates of mineral fractions for the plug samples do not reflect the actual mineralogy. In fact, this dolomite-calcite technique does not reflect the anhydrite, gypsum and quartz contents of these rocks [Harris et al., 1984].

When I used this dolomite-calcite method to generate low-frequency estimates of the saturated-rock velocities to compare to the sonic logs (Figure 11), I found the estimates were generally high.

The exponential curves in Figures B1 and B2 have the form:

$$M_d(\text{GPa}) = M_m \cdot a_j \cdot \exp\left[1 - \exp\left(b_j \cdot \phi\right)\right] \tag{B10}$$

where M_d is the dry modulus (K_d or G_d), M_m is the mineral modulus (K_m or G_m), subscript "j" refers to subscripts "k" or "g" for the K_d and G_d curves in Figures B1 and B2, $a_j = M_d/M_m$, and $b_j = 1/\phi^*$ is the exponent scale factor. When $\phi \rightarrow 0$, then $M_d \rightarrow M_m \cdot a_j$. When $\phi \rightarrow 1$, then $M_d \rightarrow 0$. When $\phi = \phi^* = 1/b_j$, then $M_d = 0.179 \cdot M_m \cdot a_j$.

DOLOSTONE-LIMESTONE TRANSFORM

I explored the possibility that a dolomite-calcite framework was not adequate. If this was true, then we should expect closer agreement between theory and measurement with a different framework composition. If we assume the Grayburg formation is a mix of dolostone and limestone, we can estimate the mineral moduli (K_m and G_m) using the following relations:

$$K_m = K_{Lmst} + \frac{\left(K_{Dlst} - K_{Lmst}\right)}{\left(\rho_{Dlst} - \rho_{Lmst}\right)}\left(\rho_g - \rho_{Lmst}\right) = 72.4 + 43.125\left(\rho_g - 2.71\right) \tag{B11}$$

$$G_m = G_{Lmst} + \frac{\left(G_{Dlst} - G_{Lmst}\right)}{\left(\rho_{Dlst} - \rho_{Lmst}\right)}\left(\rho_g - \rho_{Lmst}\right) = 32.6 + 56.875\left(\rho_g - 2.71\right) \tag{B12}$$

where K_{Lmst} = 72.4 GPa is the bulk modulus of limestone, K_{Dlst} = 79.3 GPa is the bulk modulus of dolostone, G_{Lmst} = 32.6 GPa is the shear modulus of limestone, G_{Dlst} = 41.7 GPa is the shear modulus of dolostone, ρ_{Lmst} = 2.71 g/cm^3 is the grain density of

limestone, and $\rho_{Dlst} = 2.87$ g/cm^3 is the grain density of dolostone. Accordingly, the grain density (ρ_g) is:

$$\begin{aligned}\rho_g(g/cm^3) &= \rho_{Dlst} + (\partial\rho_g/\partial X_{Lmst})X_{Lmst} \\ &= 2.87 - 0.16X_{Lmst}\end{aligned} \tag{B13}$$

where the grain-volume fraction of calcite (X_{Lmst}) is:

$$X_{Lmst} = \frac{\rho_g - \rho_{Dlst}}{\rho_{Lmst} - \rho_{Dlst}} = \frac{\rho_g - 2.87}{2.71 - 2.87} \tag{B14}$$

and

$$X_{Dlst} + X_{Lmst} = 1. \tag{B15}$$

Equations (B13) and (B14) produce the same results as (B3) and (B4). This is because we have not changed the grain densities of the pure end-members.

Again, if mineral composition and porosity (ϕ) were the primary factors controlling the dry-frame moduli (K_d and G_d) of these rocks, then these frame moduli are:

$$\begin{aligned}K_d(GPa) &= K_m + (\partial K_d/\partial\phi)\phi \\ &\approx K_{Dlst} + (\partial K_m/\partial X_{Lmst})X_{Lmst} + (\partial K_d/\partial\phi)\phi \\ &\approx 79.3 - 6.9X_{Lmst} + (\partial K_d/\partial\phi)\phi\end{aligned} \tag{B16}$$

and

$$\begin{aligned}G_d(GPa) &= G_m + (\partial G_d/\partial\phi)\phi \\ &\approx G_{Dlst} + (\partial G_m/\partial X_{Lmst})X_{Lmst} + (\partial G_d/\partial\phi)\phi. \\ &\approx 41.7 - 9.1X_{Lmst} + (\partial G_d/\partial\phi)\phi\end{aligned} \tag{B17}$$

As for the dolomite-calcite estimate, the ($\partial K_d/\partial\phi$) and ($\partial G_d/\partial\phi$) coefficients were estimated so when ϕ approaches from below the "initial" or "depositional" porosity ϕ_0 the dry moduli of a pure dolostone frame are zero.

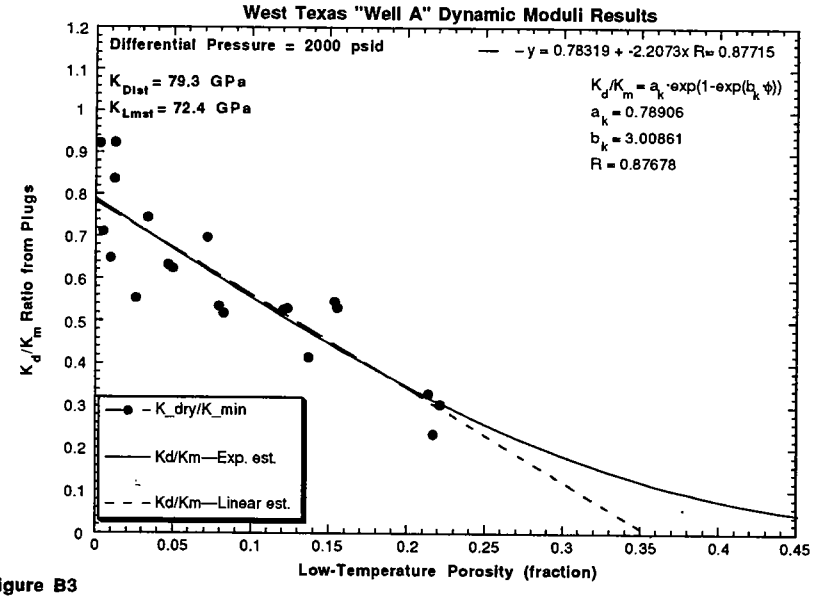

Figure B3

Figure B3: Plot of K_d/K_m vs. low-temperature porosity. Dolostone-limestone transform.

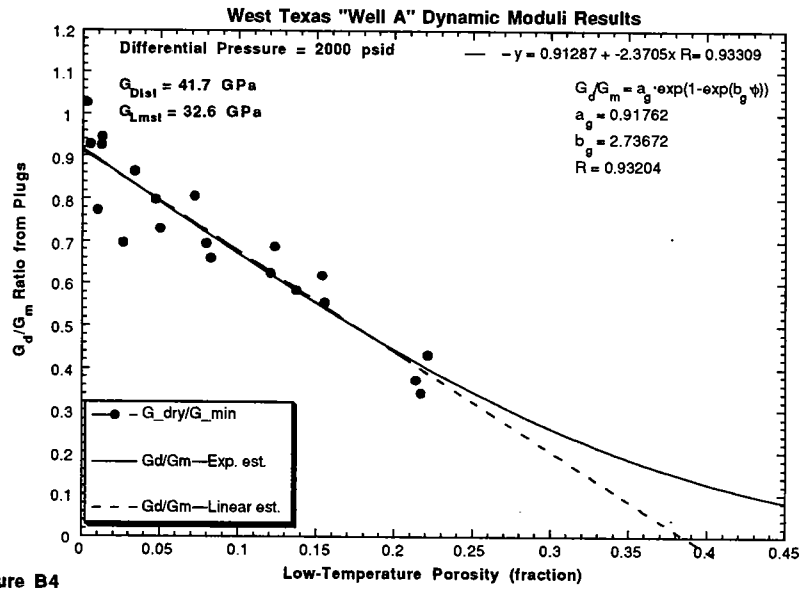

Figure B4

Figure B4: Plot of G_d/G_m vs. low-temperature porosity. Dolostone-limestone transform.

Figures B3 and B4 are plots of K_d/K_m and G_d/G_m, respectively. These plots were generated from the plug data using equations (B11) and (B12) for K_m and G_m, and K_d and G_d calculated from the dry velocity measurements (Table 3). Using the linear least-squares lines from these plots, the frame moduli are:

$$\begin{aligned} K_d(\text{GPa}) &= K_m(\alpha_k - \beta_k\phi) \\ &\approx K_m(0.783 - 2.21\phi) \qquad \ldots \phi_0 = 0.386 \\ &\approx 62.1 - 5.4X_{Lmst} - 160.8\phi \end{aligned} \tag{B18}$$

and

$$\begin{aligned} G_d(\text{GPa}) &= G_m(\alpha_g - \beta_g\phi) \\ &\approx G_m(0.913 - 2.37\phi) \qquad \ldots \phi_0 = 0.385 \\ &\approx 38.1 - 8.3X_{Lmst} - 98.8\phi \end{aligned} \tag{B19}$$

The coefficients are still lower than the expected theoretical coefficients. However, there is closer agreement than for the dolomite-calcite framework case. The ϕ_0 estimates are essentially identical here. This suggests that these dolostone-limestone estimates of mineral fractions are better than the dolomite-calcite estimates. However, the dolostone-limestone framework still may not reflect the actual mineralogy.

When used to generate velocity estimates to compare to the sonic logs (Figure 12), this method resulted in saturated velocities that were closer than those of the dolomite-calcite method (Figure 11).

CORE CONSTRAINED TRANSFORM

Grain Densities

To try to reflect the mineralogy better, I used the full-diameter core measurements of grain density, porosity, gypsum content, and total gamma-ray count to estimate K_m and G_m. I assumed the dominant mineral was dolomite. I constrained the gypsum grain-volume fraction to the core measurements. The total gamma-ray count helped to estimate the quartz silt content in these rocks [Harris et al., 1984], which I assumed varied from 0 to 50 %GV quartz silt. I could not constrain the calcite and anhydrite grain-volume (GV)

fractions using available core data. To obtain an estimate of the grain-volume fractions of these minerals, I started with an estimate (ρ_{Est}) of the grain-density data using

$$\begin{aligned}\rho_{Est} &= \rho_{Dlmt} + \left(\partial\rho_g/\partial X_{Gyps}\right)X_{Gyps} + \left(\partial\rho_g/\partial X_{Qrtz}\right)X_{Qrtz} \\ &= 2.87 - 0.56X_{Gyps} - 0.22X_{Qrtz}\end{aligned} \tag{B20}$$

where ρ_{Dlmt} is the mineral density of dolomite, X_{Gyps} = gypsum grain-volume fraction, and X_{Qrtz} = grain-volume fraction of quartz silt. Positive deviations ($\rho_g > \rho_{Est}$) from this estimate were assumed to result from anhydrite and negative deviations ($\rho_g < \rho_{Est}$) were assumed to result from calcite. Accordingly, the anhydrite mineral fraction (X_{Anhy}) was estimated using

$$\begin{aligned}X_{Anhy} &= \frac{\rho_g - \rho_{Dlmt} + \left(\rho_{Dlmt} - \rho_{Gyps}\right)X_{Gyps} + \left(\rho_{Dlmt} - \rho_{Qrtz}\right)X_{Qrtz}}{\rho_{Anhy} - \rho_{Dlmt}} \\ &= \frac{\rho_g - 2.87 + 0.56X_{Gyps} + 0.22X_{Qrtz}}{0.09}\end{aligned} \quad \ldots \rho_g > \rho_{Est} \tag{B21}$$

and the calcite mineral fraction (X_{Clct}) was estimated using

$$\begin{aligned}X_{Clct} &= \frac{\rho_g - \rho_{Dlmt} + \left(\rho_{Dlmt} - \rho_{Gyps}\right)X_{Gyps} + \left(\rho_{Dlmt} - \rho_{Qrtz}\right)X_{Qrtz}}{\rho_{Clct} - \rho_{Dlmt}} \\ &= \frac{\rho_g - 2.87 + 0.56X_{Gyps} + 0.22X_{Qrtz}}{-0.16}\end{aligned} \quad \ldots \rho_g < \rho_{Est} \tag{B22}$$

Finally the dolomite grain-volume fraction was estimated as

$$X_{Dlmt} = 1 - \left(X_{Clct} + X_{Anhy} + X_{Gyps} + X_{Qrtz}\right). \tag{B23}$$

The grain density is therefore given by

$$\begin{aligned}\rho_g &= \rho_{Dlmt} + \left(\frac{\partial\rho_g}{\partial X_{Clct}}\right)X_{Clct} + \left(\frac{\partial\rho_g}{\partial X_{Anhy}}\right)X_{Anhy} + \left(\frac{\partial\rho_g}{\partial X_{Gyps}}\right)X_{Gyps} + \left(\frac{\partial\rho_g}{\partial X_{Qrtz}}\right)X_{Qrtz} \\ &= 2.87 - 0.16X_{Clct} + 0.09X_{Anhy} - 0.56X_{Gyps} - 0.22X_{Qrtz}\end{aligned} \tag{B24}$$

Grain Moduli

I used Hill's [1952] method to calculate the effective mineral moduli of the rocks from the grain-volume fractions derived from equations (B19) to (B22). Hill's method is:

$$K_m = \frac{1}{2}\left[K_{Voight} + K_{Reuss}\right] = \frac{1}{2}\left[\sum_{i=1}^{M} X_i K_i + \left(\sum_{i=1}^{M} \frac{X_i}{K_i}\right)^{-1}\right] \tag{B25}$$

and

$$G_m = \frac{1}{2}\left[G_{Voight} + G_{Reuss}\right] = \frac{1}{2}\left[\sum_{i=1}^{M} X_i G_i + \left(\sum_{i=1}^{M} \frac{X_i}{G_i}\right)^{-1}\right], \tag{B26}$$

where X_i is the grain-volume fraction of the i-th mineral, K_i and G_i are the mineral bulk and shear moduli of the i-th mineral, and subscripts "Voight" and "Reuss" refer to Voight's [1928] isostrain and Reuss' [1929] isostress averaging techniques.

TABLE B1. Mineral Properties

Mineral	ρ_g (g/cm^3)	K_m (GPa)	G_m (GPa)
Dolomite	2.87	94.8	45.7
Calcite	2.71	76.7	32.3
Anhydrite	2.96	66.5	34.2
Gypsum	2.31	58.0	30.0
Quartz (silt)	2.65	38.0	44.4

Dry-Frame Moduli

To estimate the dry-frame moduli, I used the dry velocity measurements from the 20 plug samples (Table 3). After calculating K_d and G_d, I fit the following relations to these moduli (Figures B5 and B6):

$$\begin{aligned} K_d(\text{GPa}) &= K_m(\alpha_k - \beta_k \phi) \\ &\approx K_m(0.733 - 1.99\phi) \end{aligned} \quad \ldots \phi_0 = 0.368 \tag{B27}$$

and

$$G_d(\text{GPa}) = G_m\left(\alpha_g - \beta_g\phi\right) \quad \ldots \phi_0 = 0.387$$
$$= G_m(0.845 - 2.18\phi) \qquad \text{(B28)}$$

The α and β coefficients are lower than expected if mineral composition (the X_i's) and porosity (ϕ) were the only factors controlling the dry-frame moduli (K_d and G_d) of these rocks. The estimates of $\phi_0 = \alpha/\beta$ differ from one another. This suggests either (1) the estimates of mineral fractions for the plug samples do not reflect the actual mineralogy, (2) the plug sampling was too coarse to capture the full range of mineralogy within the Grayburg formation and for the statistics to reflect expected mineral moduli effects, or (3) factors other than just mineralogy and porosity contribute to the dry-frame moduli.

When used to generate velocity estimates to compare to the sonic logs (Figure 13), this method resulted in a fit comparable to the dolostone-limestone (Figure 12). The two figures differ in the low-velocity zone centered around 2860 feet. This is a high gamma-ray zone and the quartz content may be too low. The dolomite-limestone method (Figure 12) produces an overall better fit to the S-wave sonic data than in Figure 13.

This core-constrained method suffers because I could not estimate the calcite and anhydrite fractions together within the same sample, so the results are somewhat unrealistic. The best way to estimate mineral moduli is to use quantitative mineralogy obtained from petrographic and geochemical analyses (e.g., mineral modal analyses).

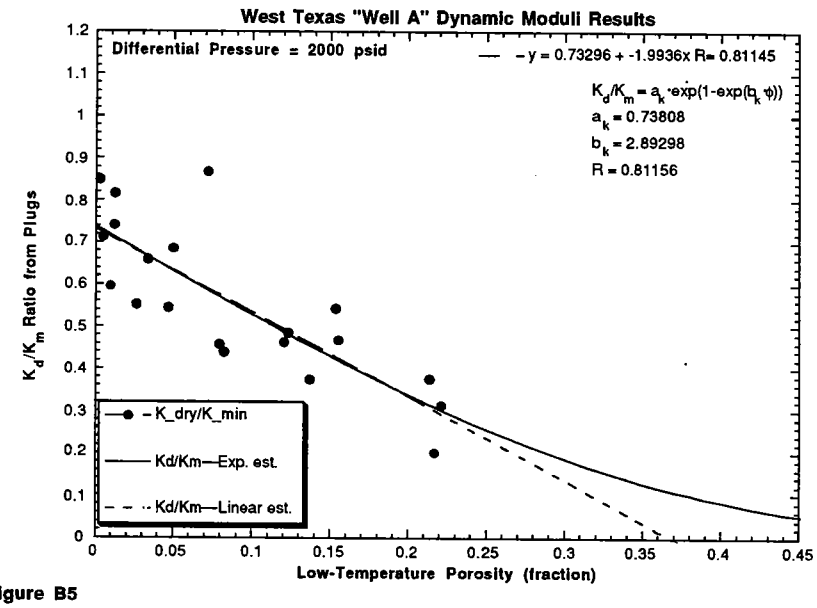

Figure B5: Plot of K_d/K_m vs. low-temperature porosity. Core constrained transform.

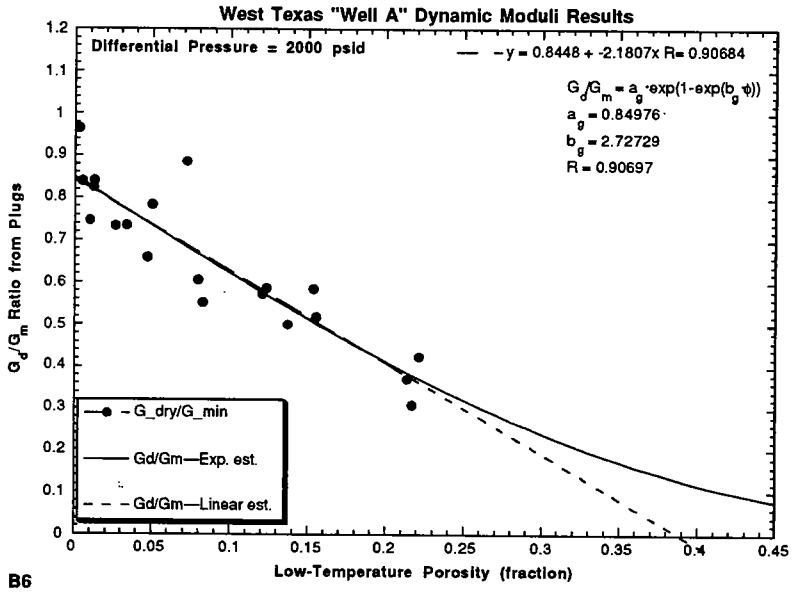

Figure B6

Figure B6: Plot of G_d/G_m vs. low-temperature porosity. Core constrained transform.

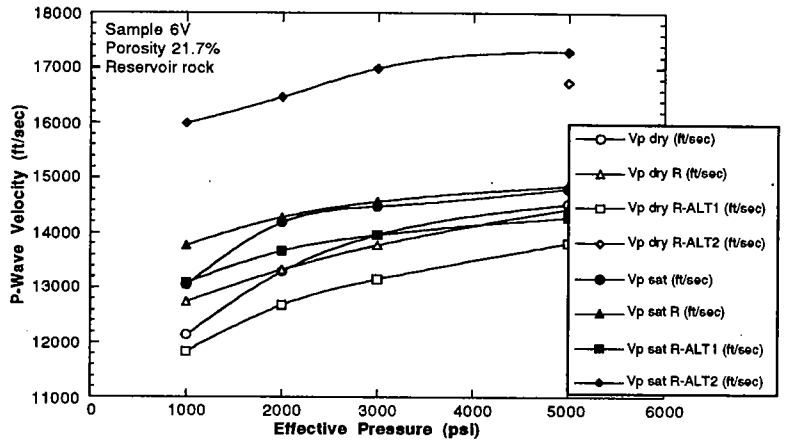
Sample 6V
Porosity 21.7%
Reservoir rock
P-Wave Velocity (ft/sec)
Effective Pressure (psi)
Vp dry (ft/sec)
Vp dry R (ft/sec)
Vp dry R-ALT1 (ft/sec)
Vp dry R-ALT2 (ft/sec)
Vp sat (ft/sec)
Vp sat R (ft/sec)
Vp sat R-ALT1 (ft/sec)
Vp sat R-ALT2 (ft/sec)

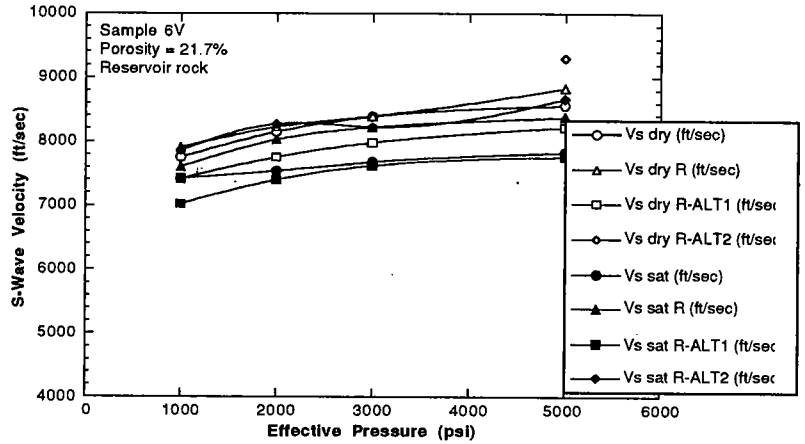
Sample 6V
Porosity = 21.7%
Reservoir rock
S-Wave Velocity (ft/sec)
Effective Pressure (psi)
Vs dry (ft/sec)
Vs dry R (ft/sec)
Vs dry R-ALT1 (ft/sec
Vs dry R-ALT2 (ft/sec
Vs sat (ft/sec)
Vs sat R (ft/sec)
Vs sat R-ALT1 (ft/sec
Vs sat R-ALT2 (ft/sec

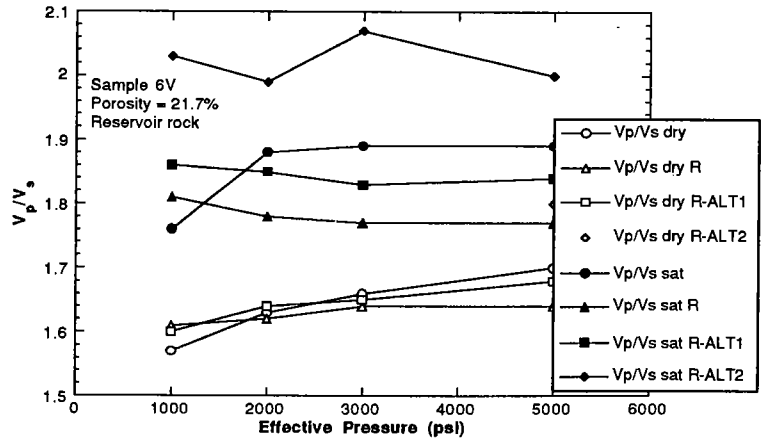
Sample 6V
Porosity = 21.7%
Reservoir rock
Vp/Vs
Effective Pressure (psi)
Vp/Vs dry
Vp/Vs dry R
Vp/Vs dry R-ALT1
Vp/Vs dry R-ALT2
Vp/Vs sat
Vp/Vs sat R
Vp/Vs sat R-ALT1
Vp/Vs sat R-ALT2

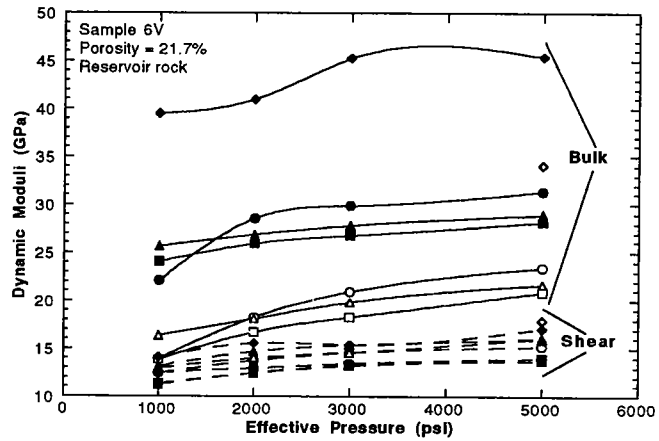
Sample 6V
Porosity = 21.7%
Reservoir rock
Dynamic Moduli (GPa)
Effective Pressure (psi)
Bulk
Shear

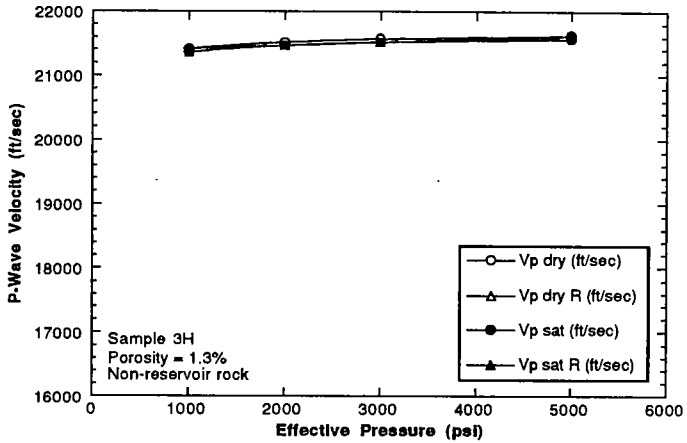
P-Wave Velocity (ft/sec)
Effective Pressure (psi)
Sample 3H
Porosity = 1.3%
Non-reservoir rock
Vp dry (ft/sec)
Vp dry R (ft/sec)
Vp sat (ft/sec)
Vp sat R (ft/sec)

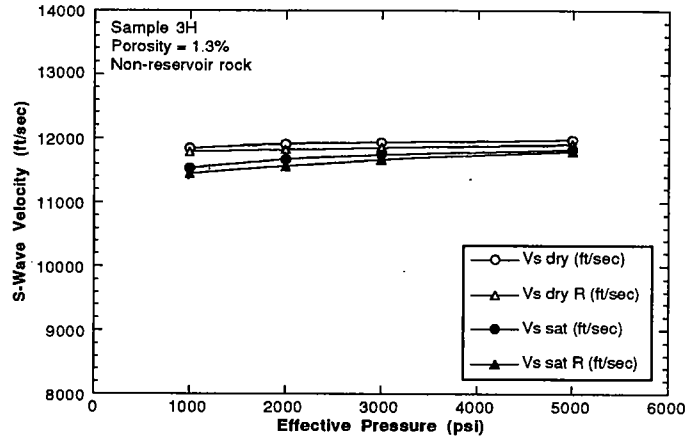
S-Wave Velocity (ft/sec)
Effective Pressure (psi)
Sample 3H
Porosity = 1.3%
Non-reservoir rock
Vs dry (ft/sec)
Vs dry R (ft/sec)
Vs sat (ft/sec)
Vs sat R (ft/sec)

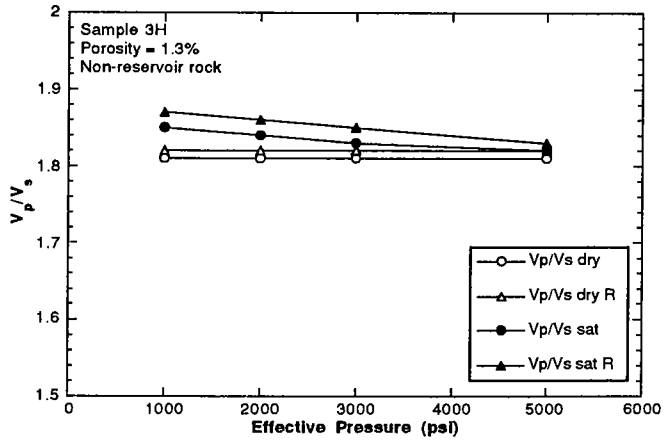
Vp/Vs
Effective Pressure (psi)
Sample 3H
Porosity = 1.3%
Non-reservoir rock
Vp/Vs dry
Vp/Vs dry R
Vp/Vs sat
Vp/Vs sat R

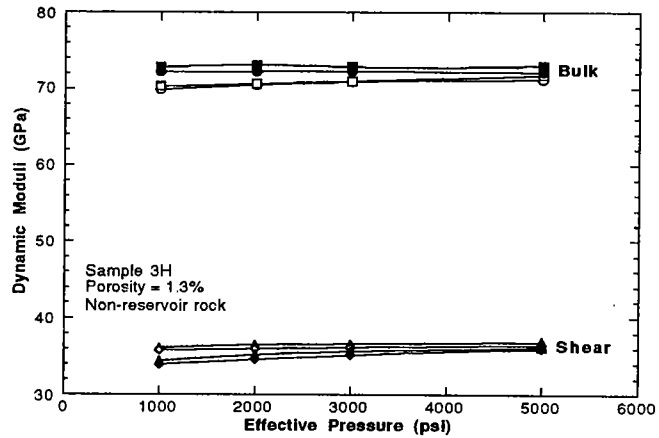
Dynamic Moduli (GPa)
Effective Pressure (psi)
Sample 3H
Porosity = 1.3%
Non-reservoir rock
Bulk
Shear

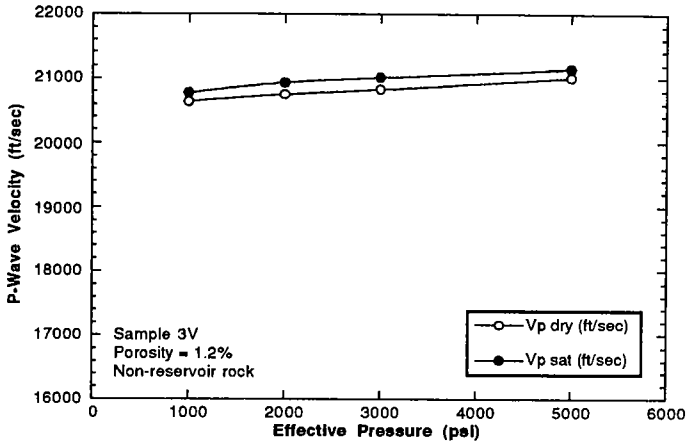
P-Wave Velocity (ft/sec)
22000
21000
20000
19000
18000
17000
16000
0
1000
2000
3000
4000
5000
6000
Effective Pressure (psi)
Sample 3V
Porosity = 1.2%
Non-reservoir rock
Vp dry (ft/sec)
Vp sat (ft/sec)

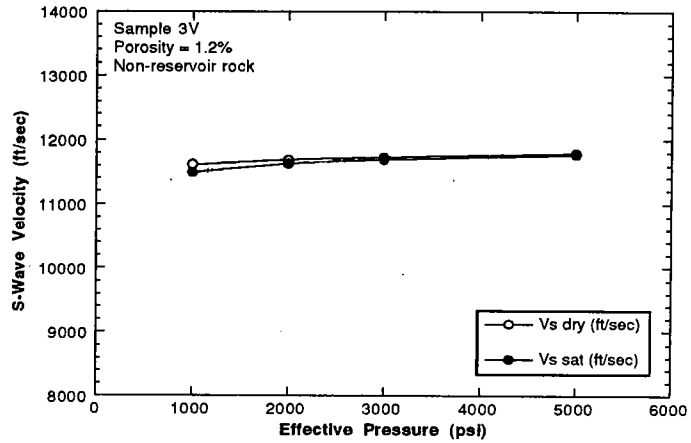
S-Wave Velocity (ft/sec)
14000
13000
12000
11000
10000
9000
8000
0
1000
2000
3000
4000
5000
6000
Effective Pressure (psi)
Sample 3V
Porosity = 1.2%
Non-reservoir rock
Vs dry (ft/sec)
Vs sat (ft/sec)

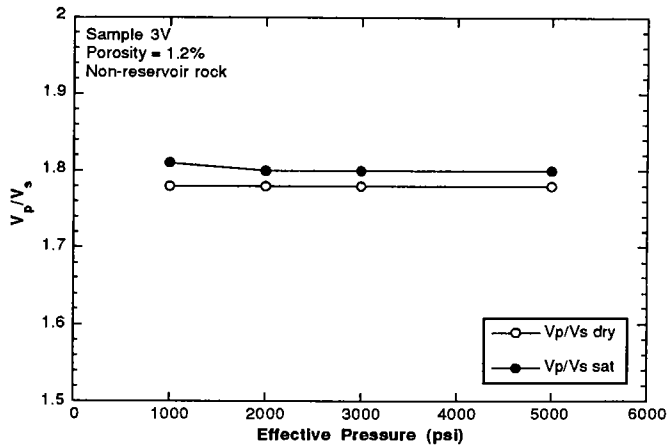
V_p/V_s
2
1.9
1.8
1.7
1.6
1.5
0
1000
2000
3000
4000
5000
6000
Effective Pressure (psi)
Sample 3V
Porosity = 1.2%
Non-reservoir rock
Vp/Vs dry
Vp/Vs sat

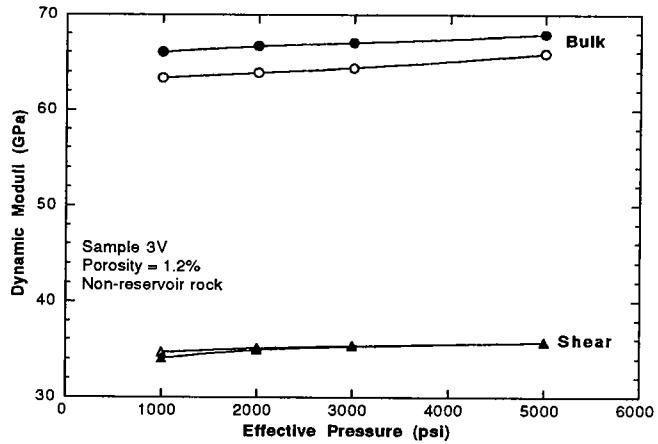
Dynamic Modull (GPa)
70
60
50
40
30
0
1000
2000
3000
4000
5000
6000
Effective Pressure (psi)
Sample 3V
Porosity = 1.2%
Non-reservoir rock
Bulk
Shear

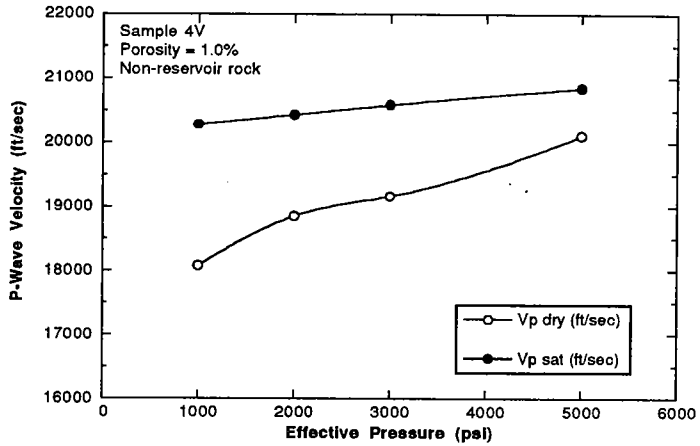
Sample 4V
Porosity = 1.0%
Non-reservoir rock
Vp dry (ft/sec)
Vp sat (ft/sec)
P-Wave Velocity (ft/sec)
Effective Pressure (psi)
22000
21000
20000
19000
18000
17000
16000
0
1000
2000
3000
4000
5000
6000

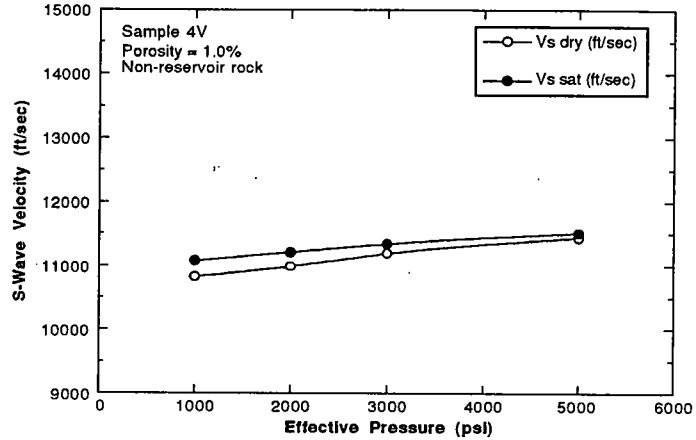
Sample 4V
Porosity = 1.0%
Non-reservoir rock
Vs dry (ft/sec)
Vs sat (ft/sec)
S-Wave Velocity (ft/sec)
Effective Pressure (psi)
15000
14000
13000
12000
11000
10000
9000
0
1000
2000
3000
4000
5000
6000

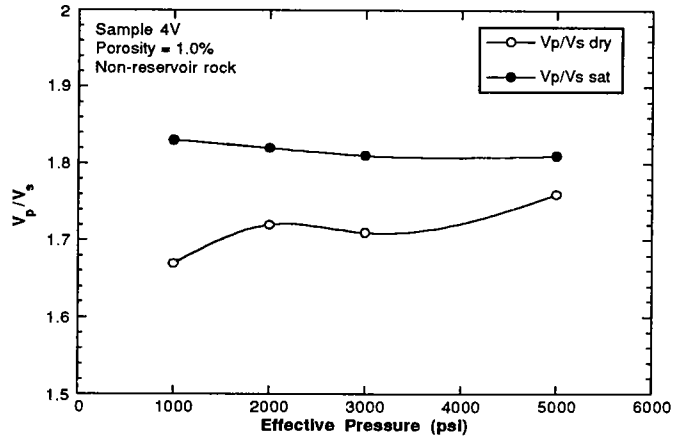
Sample 4V
Porosity = 1.0%
Non-reservoir rock
Vp/Vs dry
Vp/Vs sat
Vp/Vs
Effective Pressure (psi)
2
1.9
1.8
1.7
1.6
1.5
0
1000
2000
3000
4000
5000
6000

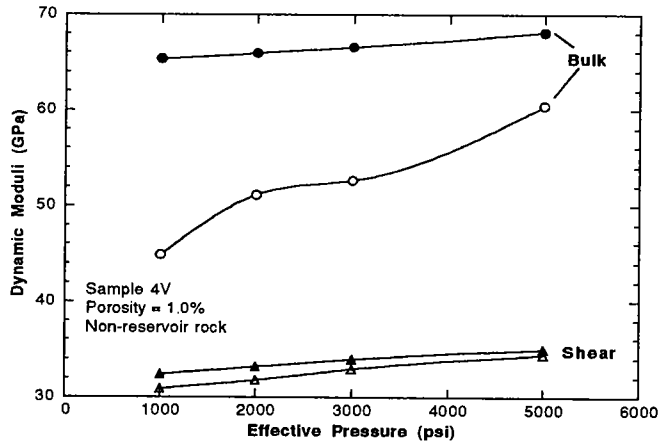
Bulk
Shear
Sample 4V
Porosity = 1.0%
Non-reservoir rock
Dynamic Moduli (GPa)
Effective Pressure (psi)
70
60
50
40
30
0
1000
2000
3000
4000
5000
6000

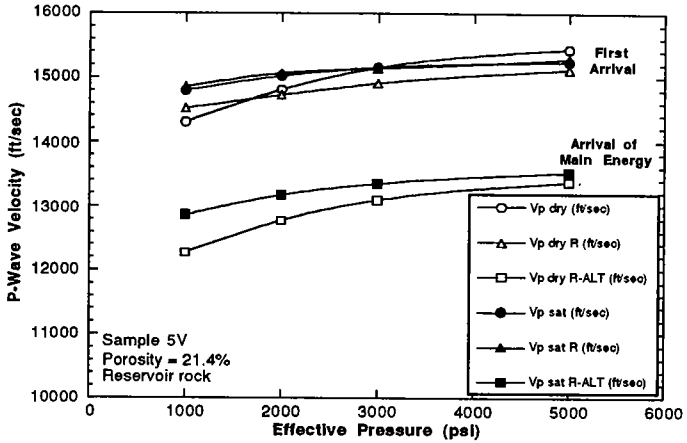
P-Wave Velocity (ft/sec)
Effective Pressure (psi)
First Arrival
Arrival of Main Energy
Vp dry (ft/sec)
Vp dry R (ft/sec)
Vp dry R-ALT (ft/sec)
Vp sat (ft/sec)
Vp sat R (ft/sec)
Vp sat R-ALT (ft/sec)
Sample 5V
Porosity = 21.4%
Reservoir rock

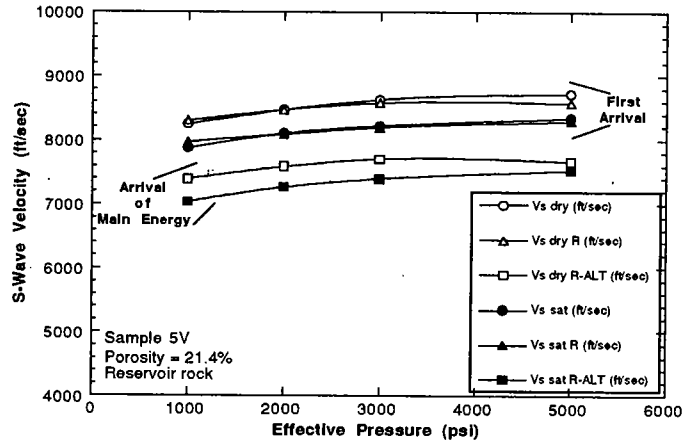
S-Wave Velocity (ft/sec)
Effective Pressure (psi)
First Arrival
Arrival of Main Energy
Vs dry (ft/sec)
Vs dry R (ft/sec)
Vs dry R-ALT (ft/sec)
Vs sat (ft/sec)
Vs sat R (ft/sec)
Vs sat R-ALT (ft/sec)
Sample 5V
Porosity = 21.4%
Reservoir rock

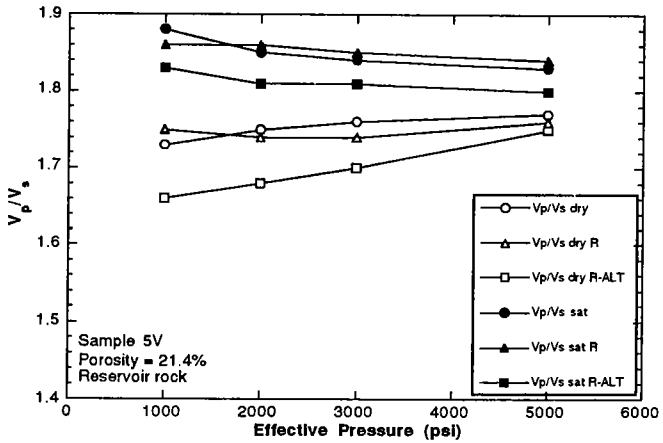
Vp/Vs
Effective Pressure (psi)
Vp/Vs dry
Vp/Vs dry R
Vp/Vs dry R-ALT
Vp/Vs sat
Vp/Vs sat R
Vp/Vs sat R-ALT
Sample 5V
Porosity = 21.4%
Reservoir rock

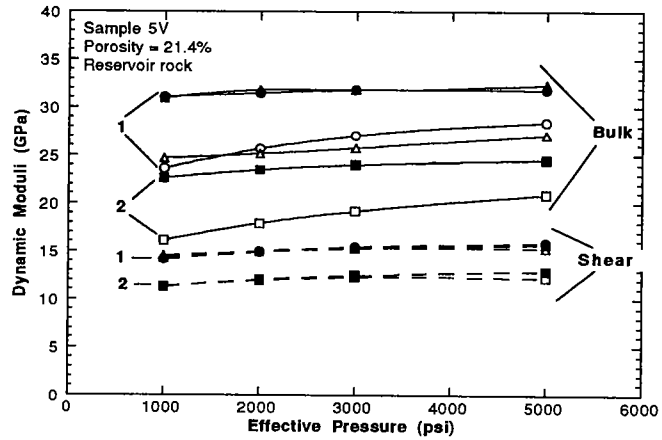
Dynamic Moduli (GPa)
Effective Pressure (psi)
Sample 5V
Porosity = 21.4%
Reservoir rock
Bulk
Shear
1
2
1
2

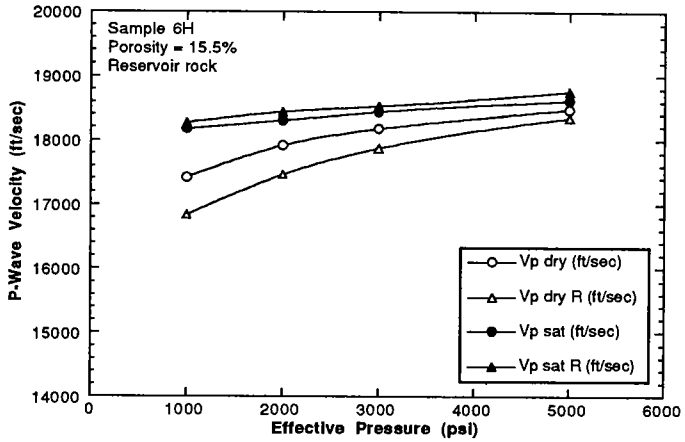
Sample 6H
Porosity = 15.5%
Reservoir rock
P-Wave Velocity (ft/sec)
Effective Pressure (psi)
Vp dry (ft/sec)
Vp dry R (ft/sec)
Vp sat (ft/sec)
Vp sat R (ft/sec)

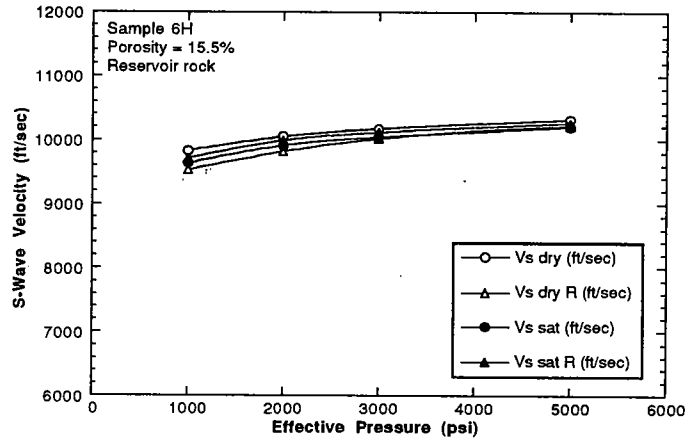
Sample 6H
Porosity = 15.5%
Reservoir rock
S-Wave Velocity (ft/sec)
Effective Pressure (psi)
Vs dry (ft/sec)
Vs dry R (ft/sec)
Vs sat (ft/sec)
Vs sat R (ft/sec)

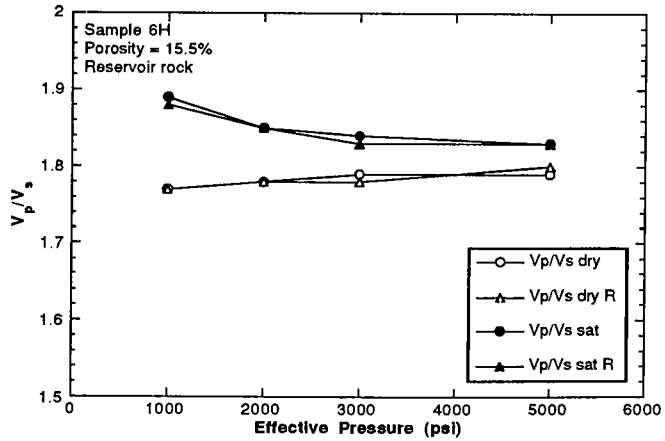
Sample 6H
Porosity = 15.5%
Reservoir rock
Vp/Vs
Effective Pressure (psi)
Vp/Vs dry
Vp/Vs dry R
Vp/Vs sat
Vp/Vs sat R

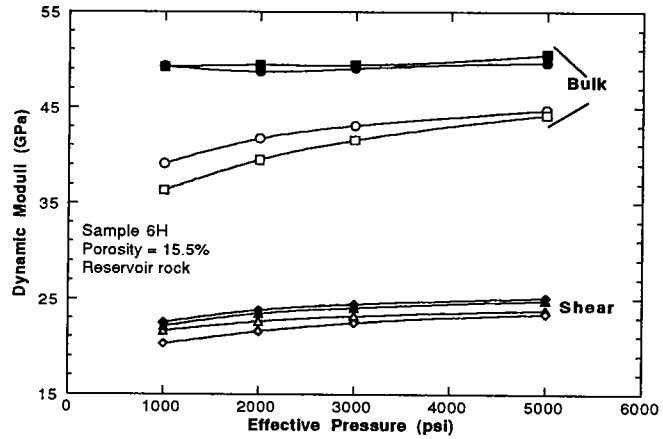
Sample 6H
Porosity = 15.5%
Reservoir rock
Dynamic Modull (GPa)
Effective Pressure (psi)
Bulk
Shear